UNIVERSITÀ DEGLI STUDI DI PADOVA

UNIVERSITÀ DEGLI STUDI DI NAPOLI FEDERICO II

Università degli Studi di Padova

Centro Ricerche Fusione (CRF)

Università degli Studi di Napoli Federico II

Dipartimento di Ingegneria Elettrica e Tecnologie dell'Informazione (DIETI)

JOINT EUROPEAN RESEARCH DOCTORATE IN FUSION SCIENCE AND ENGINEERING

Cycle XXXI

A flexible architecture for plasma magnetic control in tokamak reactors

Coordinator:

Prof. Paolo Bettini

Supervisors:

Prof. Gianmaria De Tommasi

Ph.D. Student: Adriano Mele

Napoli, November 2018

Going after the unknown is always fascinating, I think. It becomes part of your life, this desire to know.

— Mark Oliphant

Nothing in the history of mankind has opened our eyes to the possibilities of science as has the development of atomic power. In the last 200 years, people have seen the coming of the steam engine, the steamboat, the railroad locomotive, the automobile, the airplane, radio, motion pictures, television, the machine age in general. Yet none of it seemed quite so fantastic, quite so unbelievable, as what man has done since 1939 with the atom. There seem to be almost no limits to what may be ahead: inexhaustible energy, new worlds, ever-widening knowledge of the physical universe.

— Isaac Asimov

ABSTRACT

Plasma magnetic control is one of the core engineering issues to be tackled in a fusion device. Over the last years, *model based* approaches have been proposed to face this issue, proving their effectiveness and allowing to reduce the time span needed for control testing and validation.

The first part of this work is intended to give an overview of the subject, from the historical milestones to the underlying physics; the most common techniques for tokamak plasmas electromagnetic modelling and control are also introduced and discussed. After this introduction, a general architecture for plasma magnetic control in tokamaks is proposed. Finally, the proposed solution is applied to the Experimental Advanced Superconducting Tokamak (EAST), where a new plasma magnetic control architecture was developed and implemented during the 2016-2018 experimental campaigns, and to the Japan Torus-60 Super Advanced (JT-60SA) device, which is currently under construction in Japan.

SOMMARIO

Il controllo magnetico è uno dei principali problemi ingegneristici nei reattori a fusione nucleare. Nel corso degli anni, approcci *model-based* si sono imposti all'attenzione della comunità grazie alla loro efficacia e alla possibilità che offrono di ridurre il tempo necessario per il collaudo e la validazione dei sistemi di controllo.

La prima parte di questa tesi fornisce una panoramica sull'argomento, dai principali momenti storici ai concetti fisici alla base della fusione nucleare; le tecniche più comuni di modellistica e controllo elettromagnetici del plasma sono introdotte e discusse. Dopo questa introduzione, viene

proposta una architettura generale per il sistema di controllo magnetico nei tokamak. Infine, la soluzione proposta è applicata ad EAST, per il quale è stato proposto e implementato un nuovo sistema di controllo magnetico durante le campagne sperimentali 2016-2018, e a JT-60SA, attualmente in costruzione in Giappone.

FOREWORD

Over the last century, scientists have looked at nuclear fusion as the holy grail of energy production: clean, sustainable and almost unlimited. Innumerable attempts have been done to tame this source of energy, the most promising being the tokamak reactor. Tokamaks are complex, distributed parameter, highly nonlinear systems, which suffer from several kinds of instabilities. Thus, to push the performances towards the attractive goal of energy production, effective active control strategies become a fundamental requirement. In particular, magnetic control represents a core issue in nuclear fusion, allowing to achieve improved performances in terms of plasma properties and stability. During the past years, *model based* approaches have shown their effectiveness in facing this problem. This is mainly due to two main reasons:

- accurate numerical models of the plasma response usually yield a great improvement in terms of controller performances;
- this kind of approach allows to design and tune the controller mostly offline. Indeed, most of the effort is moved from experimental controllers tuning to the development of reliable modeling and simulation tools; once this task has been accomplished, a very low number of experiments is needed for fine-tuning and validation. This prompts the main advantage of reducing the number of needed technical tests, allowing to use the same time for scientific experiments.

Magnetic control is considered a substantially solved problem in tokamak reactors; however, a generally accepted standard solution to it does not exist. In this view, a proposal for a flexible magnetic control architecture is put forward in this thesis. This architecture provides a sound and flexible

framework for the implementation and validation of all the different magnetic control loops needed on a modern tokamak, and allows to easily integrate additional controllers if needed. It is largely model based, as it relies on the CREATE-L [1] and CREATE-NL [2] equilibrium codes, which have been used over the last years for modeling purposes and for the design of advanced magnetic control solutions on several machines (e. g. JET [3, 4] and TCV [5]). Furthermore, it can be applied to virtually every tokamak, once the modelling tools have been configured properly.

This thesis is organized as follows:

- **Part I** contains an introduction to magnetic confinement nuclear fusion. In particular, **chapter 1** contains a brief chronicle of the historical milestones that led to nuclear fusion as we know it today over the last century. This overview is thought as a homage to the scientists who pioneered this research field and wrote its history, and is not meant to be exhaustive. **Chapter 2**, instead, contains an overview of some of the scientific foundations of magnetic confinement fusion. In particular, in sec. 2.1 some basic notions regarding nuclear fusion are introduced. Sec. 2.2 contains a brief introduction to plasma physics; some of its core aspects are discussed, which underlie the rest of this work. In sec. 2.3 the tokamak configuration for magnetic confinement fusion is described in some detail.

- **Part II** contains an overview of plasma electromagnetic modelling and control. **Chapter 3** is about tokamak axisymmetric modelling. The Grad-Shafranov equation is derived from the ideal Magneto-Hydro-Dynamic (MHD) plasma equilibrium condition and discussed in sec. 3.1. Its resolution by means of Finite Element Method (FEM) techniques is discussed in sec. 3.2.2, while in sec. 3.3 a linearized model for the plasma evolution is derived. Linearized models around a given MHD equilibrium are the starting point for the control design

techniques presented in the rest of the thesis. **Chapter 4** gives an overview of standard plasma magnetic control. **Chapter 5** contains the description of a general plasma magnetic control architecture, whose application to the EAST and JT-60SA tokamaks will be the main topic of Part III.

- **Part III** reports on the results obtained with the proposed control architecture. **Chapter 6** begins with a motivation for the experimental activity carried out at EAST during the 2016-2018 period; then, a brief description of the machine is given in sec. 6.2. The applications of the modelling techniques introduced in chapter 2 to this device is discussed in sec. 6.3. Sec. 6.4 describes the architecture of EAST's plasma magnetic control system. A simulation environment has been set up and validated in order to reproduce the experiments; it has been used extensively for the control design activities described in chapter 7. Simulation results are discussed in sec. 6.4.2. An overview of the modeling and validation activities and of the simulation environment developed for EAST has been published in [6]. **Chapter 7** reports on the experimental activity. New control algorithms for vertical stabilization, Poloidal Field Coils (PFC) current control and plasma current, position and shape control have been proposed and tested, according to the proposed general architecture. Sections 5.1-5.5 each discuss one of the proposed control architecture components. Most of the contents of these sections have been published in [7–11]. Sec. 7.5 reports on preliminary results obtained in simulation for the control of the poloidal flux expansion in the divertor region, originally published in [12]. Finally, sec. 7.6 describes an approach for the estimation of the eddy currents in the tokamak conducting structures and of the plasma shape based on a Kalman filter approach; the results presented in this section have been published in [13]. **Chapter 8** reports on preliminary studies carried out for the design of the plasma magnetic control of the JT-60SA tokamak. A brief description of the machine is

given in sec. 8.1; the adaptation of the proposed architecture to this device is discussed in sec. 8.2, while simulation results are presented in sec. 8.3. The results presented in chapter 8 have been mostly adapted from [14, 15].

In addition to the activities described in this thesis, I had the pleasure of participating in other projects that have not been included in this work. In particular, in collaboration with the CREATE team and in the scope of the activities for the F4E OPE-700 contract, a Graphical User Interface was developed for the generation and manipulation of equilibria and linearized models, which was customized for the EAST, International Thermonuclear Experimental Reactor (ITER) and JT-60SA tokamaks. The interface is thought as a user-friendly tool for tokamak scenario and magnetic control design, optimization and simulation, and includes Simulink libraries specifically designed for magnetic control; these libraries have been used to produce the simulation results of chapter 8. These tools have been installed and tested at the Remote Experimentation Center (Naka, Japan), and have been recently released as a beta version. They were also used to perform preliminary studies on the possibility of exploiting In-Vessel coils "kicks" for Edge Localized Mode (ELM)s triggering at JT-60SA.

Finally, I would like to thank prof. Gianmaria De Tommasi for his contributions in chapter 5 and in section 7.1.2, dr. Antonio Castaldo for those in sec. 6.3 and drs. Doménica Rivera for the work which led to sec. 8.3.2.

Napoli, September 2018

CONTENTS

LIST OF FIGURES

LIST OF TABLES

ACRONYMS

AT Advanced Tokamak

AERE Atomic Energy Research Establishment

ASDEX Axially Symmetric Divertor EXperiment

BA Broader Approach

CNF Controlled Nuclear Fusion

CS Central Solenoid

CCS Cauchy Condition Surface

DEMO DEMOnstration power plant

DN Double Null

DTT Divertor Tokamak Test

EAST Experimental Advanced Superconducting Tokamak

ECRH Electron Cyclotron Resonance Heating

EFC Equilibrium Field Coils

ELM Edge Localized Mode

EOF End Of Flat-top

FEM Finite Element Method

FPPC Fast Plasma Position Coils

HFS High Field Side

IAEA International Atomic Energy Agency

INTOR INternational TOkamak Reactor

ITER International Thermonuclear Experimental Reactor

JET Joint European Torus

JT-60 Japan Torus-60

JT-60U Japan Torus-60 Upgrade

JT-60SA Japan Torus-60 Super Advanced

LCFS Last Closed Flux Surface

LFS Low Field Side

LHRH Lower Hybrid Resonance Heating

LHCD Lower Hybrid Current Drive

LHP Left Half Plane

LSN Lower Single Null

MHD Magneto-Hydro-Dynamic

MIMO Multi-Input-Multi-Output

MISO Multi-Input-Single-Output

MTR Magnetic Thermonuclear Reactor

NBI Neutral Beam Injector

NET Next European Torus

NSTX National Spherical Torus eXperiment

PCS Plasma Control System

PFC Poloidal Field Coils

PID Proportional-Integral-Derivative

PIP Paring Interlacing Property

PLT Princeton Large Torus

PPPL Princeton Plasma Physics Laboratory

QSF Quasi-SnowFlake

RFP Reversed Field Pinch

RHP Right Half Plane

RMSE Root-Mean-Square Error

RWM Resistive Wall Mode

SIMO Single-Input-Multiple-Output

SISO Single-Input-Single-Output

SN Single Null

SOF Start Of Flat-top

SOL Scrape-Off Layer

ST Symmetrical Tokamak

STP Satellite Tokamak Programme

SVD Singular Value Decomposition

TCV Tokamak à Configuration Variable

TFC Toroidal Field Coils

TFTR Tokamak Fusion Test Reactor

TMP Tor s Magnitnym Polem

USN Upper Single Null

VS Vertical Stabilization

W7-X Wendelstein 7-X

XSC eXtreme Shape Controller

ZETA Zero Energy Thermonuclear Assembly

Part I

INTRODUCTION

1

HISTORICAL OVERVIEW

"The beginning in every task is the chief thing. "

— Plato

The idea of nuclear fusion as a viable way to energy production dates back to the year 1920. It was the English scientist Arthur Eddington (1882 – 1944) who first put forward the hypothesis that the large amount of energy needed in order to light up a star could have its origin in fusion reactions of light elements [16]. During the previous couple of years, at the Cavendish Laboratories of Cambridge University, Francis Aston (1877 – 1945) had concocted and built an instrument -his *mass spectrograph*- that could be used to measure the mass of atomic nuclei with extreme accuracy. In this way, he had achieved two breakthrough discoveries: the first was the existence of *isotopes*, a fact that would have not been fully understood until James Chadwick discovered the neutron in 1932; the second was that the mass of these isotopes -in particular those of hydrogen- was not an exact multiple of that of the 'normal' form of the element. In the same way, an helium nucleum was slightly lighter than the sum of four hydrogen ones. At the British Association for Advancement of Science meeting in Cardiff, in 1920, sir Eddington commented on Aston's findings in the following way [17]:

«*Aston has further shown conclusively that the mass of the helium atom is less than the sum of the masses of the four hydrogen atoms which enter into it and in this at least the chemists agree with him. There is a loss of mass in the synthesis amounting to 1 part in 120, the atomic weight of hydrogen being 1.008 and that of helium just 4.00. [...] Now mass cannot be annihilated and the deficit can only represent the mass of the electrical energy*

liberated when helium is made out of hydrogen. If 5% of a star's mass consists initially of hydrogen atoms, which are gradually being combined to form more complex elements, the total heat liberated will more than suffice for our demands, and we need look no further for the source of a star's energy.»

Incidentally, Eddington was the same scientist who, in 1919, guided the expedition to *São Tomé e Prìncipe* that provided the first experimental evidence of Einstein's General Relativity Theory, by measuring the position of some stars in the Torus constellation during a solar eclipse.

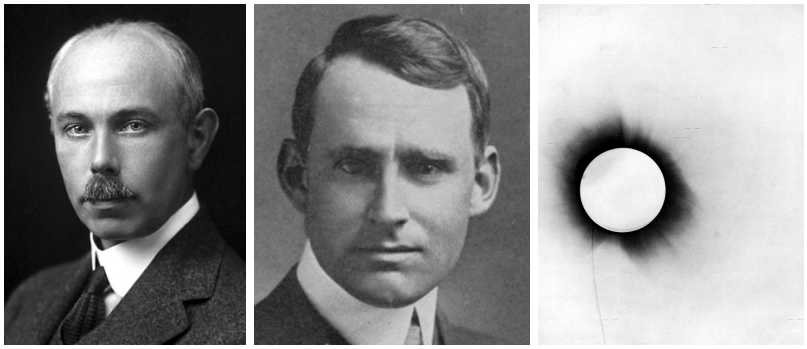

Figure 1: Francis Aston (left).
Sir Arthur Eddington and one of the pictures he took in 1919 (center-right).

However, according to Eddington's calculations fusion reactions would have needed much hotter stars than the one experimentally observed looking at the night sky. A possible solution to this puzzle was found in 1929, when Robert d'Escourt Atkinson (1898 - 1982) and Fritz Houtermans (1903 – 1966) applied the recently discovered phenomenon of quantum tunnelling, which had been formalized by the Russian-American physicist George Gamow (1904 - 1968) just one year before, to nuclear fusion processes in stars. In this way, they demonstrated that fusion reactions could take place at much lower temperatures than the 40 million Kelvin that sir Eddington had initially calculated by means of classic theory [18].

In 1932, at the Cavendish Laboratory of the University of Cambridge, two students of Ernest Rutherford, namely John Cockcroft (1897 – 1967) and Ernest Walton (1903 – 1995), performed the first artificial nuclear dis-

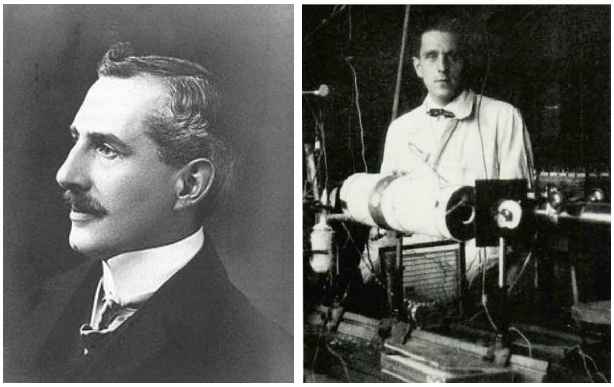

Figure 2: Robert Atkinson and Fritz Houtermans.

integration in history. In their experiments, they used a particle accelerator powered by a generator of their invention -named *Cockcroft-Walton generator* after them- to fire high energy protons into metal targets. Some of the nuclei in the targets were transformed into different elements, and part of their mass were converted into energy during the process. This experiment was performed again, this time in public, at the Royal Institution in 1934. Needless to say, the discovery caught the headlines. An article appeared on the New York Times issue of March 30, 1934 [19] claimed that:

> *«Science has obtained conclusive proof from recent experiments that the innermost citadel of matter, the nucleus of the atom, can be smashed, yielding tremendous amounts of energy and probably vast new stores of gold, radium and other valuable minerals.»*

Turning lead into gold proved to be not as practical as hoped; nevertheless, Cockcroft and Walton won a Nobel Prize in Physics for the "Transmutation of atomic nuclei by artificially accelerated atomic particles" in 1951.

Meanwhile, in 1933, a small amount of heavy water was presented to the Cavendish Laboratory from the American physical chemist Gilbert N. Lewis (the scientist who discovered the covalent bond). Mark Oliphant (1901 – 2000), together with Paul Harteck (1902 – 1985) and Rutherford himself, used the same accelerator to fire deuterium nuclei (called *diplons* by Rutherford) against several targets consisting in metal foils containing deuterium, lithium and other elements [20]. In this way, not only he discovered tritium and 3-helium, but he also noticed that deuterons could be

Figure 3: Walton (inside the detector) operating the Cockcroft-Walton machine, which produced the first laboratory atomic disintegrations in 1932 (left). Rutherford's public demonstration of deuterium nuclei fusion at the Royal Institution in 1934 (right).

made to react with each other, producing particles that had more energy than the original nuclei. The first laboratory nuclear fusion reactions had been obtained.

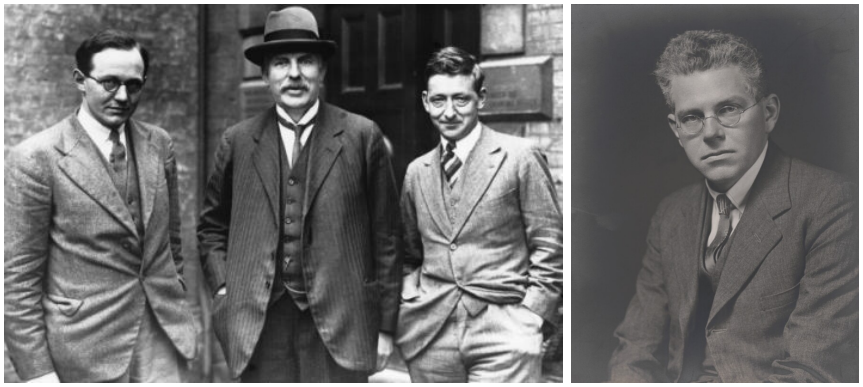

Figure 4: Walton, Rutherford and Cockcroft (left).
Mark Oliphant (right).

Oliphant went on experimenting with other fusion reactions, i. e. deuterons-tritons, deuterons-helions. In particular, the reaction between deuterium and tritium would later become the basis for the hydrogen bomb, an outcome that Oliphant had not foreseen. In an interview published on *Portraits in Science* in 1994, he said [21]:

«We were able to discover two new kinds of atomic species, one was hydrogen of mass 3, unknown until that time, and the other helium of mass 3, also unknown. [...] We were

able to show that heavy hydrogen nuclei, that is to say the cores of heavy hydrogen atoms, could be made to react with one another to produce a good deal of energy and new kinds of atom.[...] Of course, we had no idea whatever that this would one day be applied to make hydrogen bombs. Our curiosity was just curiosity about the structure of the nucleus of the atom, and the discovery of these reactions was purely, as the Americans would put it, coincidental.»

At that point, World War II had come just around the corner. In 1936-37, the main results on nuclear physics obtained until that time were summarized in a series of articles written by Hans Bethe (1906 – 2005), which became widely known as the "Bethe's Bible" [22–24]. Bethe was an incredibly talented theoretical physicist. In 1938, he was invited to the Carnegie Institute and George Washington University's fourth annual Washington Conference of Theoretical Physics. At the beginning, he refused to attend, since the topic did not really appeal to him: the conference was about solar and stellar energy production. He was eventually convinced by Edward Teller (1908 – 2003) to participate. During the conference, Bengt Strömgren challenged the other physicists to give a theoretical explanation of the most recent observations of Sun's temperature, density and chemical composition. By the end of the conference, Bethe came up with a proton-proton reaction cycle. Moreover, he kept studying the subject and later on proposed the CNO-cycle. He wrote two articles, one co-authored by Charles Critchfield on the p-p cycle and the other on the CNO, and sent both to Physical Review. However, after *Kristallnacht*, Bethe's mother decided to move from Germany to the US, and Hans needed 250$ to release her furniture. One of his students discovered that the New York Academy of Sciences was offering a 500$ prize for the best unpublished paper on stellar energy, and so he withdrew the CNO-cycle paper and applied for the prize. Not only he was awarded those 500$, he also won the 1967 Nobel Prize for his work. [25]

In June 1942, in Chicago, and then in July at the University of California, Berkeley, Robert Oppenheimer (1904 – 1967) and Enrico Fermi (1901 – 1954) convened a series of scientific meetings to discuss viable design

concepts for an atomic bomb. Among the participants, the theoretical physicists Hans Bethe himself and Edward Teller and the experimental physicists Emilio Segrè and Felix Bloch are probably some of the most famous names. It was the beginning of the Manhattan Project. The possibility of making a fission device was confirmed during the first of the two conferences. Moreover, during the second one, Teller raised the bar, putting forward the idea -originally proposed by Fermi- that not only a fission device could be actually realized, but it could be used to generate enough energy to trigger deuterium-tritium fusion reactions in a what he called a "super" bomb. This idea would later develop into what we know today as the hydrogen bomb. Despite being initially contrary to the project, Bethe also took part in the H-bomb development. The studies on the *Teller-Ulam configuration* were completed in 1951 (with some help from John von Neumann), and a first full-scale test was performed in 1952, with the drop of *Ivy Mike*. Later on, Hans Bethe would say [26]:

«After the H-bomb was made, reporters started to call Teller the father of the H-bomb. For the sake of history, I think it is more precise to say that Ulam is the father, because he provided the seed, and Teller is the mother, because he remained with the child. As for me, I guess I am the midwife.»

Figure 5: Hans Bethe's, Edward Teller's and Stanislaw Ulam's badges at Los Alamos laboratories.

However, since this work is concerned with Controlled Nuclear Fusion (CNF), let us now put aside the history of thermonuclear weapons to

jump back to the experiments carried out by Oliphant and his colleagues at Cambridge University. These scientists were able to estimate the nuclear cross sections of some fusion reactions, among which the deuterium-tritium turned out to be the most favourable one, reaching a maximum probability of occurrence at the astonishing temperature of about 100 keV (~1 billion Kelvin!). Nevertheless, since the D-T reaction releases a considerable amount of energy, it holds acceptable that only the high-energy tail of the particles' velocity distribution (assumed to be the usual Maxwell-Boltzmann one) reaches these extreme conditions. Furthermore, as we said, quantum tunnelling makes it possible to react also for particles which classically could not. These considerations make the necessary temperature much lower: in 1944 Enrico Fermi calculated that the reactions would be able to self-sustain at about 50 million K [17].

At such high temperatures, materials undergo a transition into a state of matter known as plasma [1]. A plasma is a fully ionized gas, which is hence a very good conductor and is strongly affected by electric and magnetic fields. If enough kinetic energy is provided to the nuclei (e. g. in the form of thermal agitation), they become able to overcome the repulsive Coulomb forces, and hence collide to give rise to fusion events. The main problem, thus, remained that of holding the plasma together (since it has a natural tendency to expand, like any other hot gas) without having it touch any physical wall (since any wall of any material would invariably melt at a hundred million degrees[2]). How could a hot plasma be confined then? A

1 The word 'plasma' comes from Ancient Greek πλασμα, i. e. 'moldable substance', 'jelly'). The first plasma was identified in 1879 by the British chemist and physicist sir William Crookes (1832 – 1919) during some experiments on cathode rays in what is now called a *Crookes tube*. Crookes called it 'radiant matter'; the word 'plasma' was coined by Irving Langmuir (1881 – 1957) in 1928. The idea came from an analogy with blood, since the transport of electrons from thermionic filaments reminded Langmuir of *"the way blood plasma carries red and white corpuscles and germs."*

2 Actually, at the low densities of a fusion plasma, this would not be the case. Although the gas inside the chamber is extremely hot, it is also very rarefied and hence it contains a small amount of heat altogether. However, touching the walls would cool it down, making fusion reactions impossible. On the other hand, the walls would eventually warm up and melt if one tried to keep the plasma hot despite their cooling effect, providing it with enough energy.

potential solution was put forward by the american scientist and inventor Willard Bennett (1903 – 1987). He observed that lightning rods were crushed when a high current flowed into them due to the Lorentz force that arose, and in 1934 he proposed that the same effect could be used to focus a stream of plasma into a thin column [27]. Some years later, this effect was given the name of *pinch effect*.

The idea was actually fairly simple: making a current flow into a plasma cylinder -for instance using two electrodes to apply a driving tension, as in a neon lamp- would have squeezed it, hence contrasting its expansion. Yet, it was not enough: this configuration could not prevent the plasma to escape from the ends of the rod. A natural solution to this problem was then to bend the cylinder into a torus, inducing the current by means of an external magnet. Nowadays, we refer back to this concept as *toroidal pinch*. It was further explored in the UK during the 1940s by George Paget Thomson (1892 – 1975), the son of the Nobel laureate and discoverer of the electron J. J. Thomson. When the Atomic Energy Research Establishment (AERE) was formed at Harwell in 1945, Thomson petitioned its director (John Cockcroft) for funds to build an experimental device; however, his requests were not satisfied. At that time the material concerning nuclear fusion was not classified (since practical military uses were not in view; the reader may recall that the Teller-Ulam design dates to 1951), so Thomson ended up patenting the concept with the South-African crystallographer Moses Blackman (1908 – 1983) in 1947 [28].

In the meanwhile, World War II had come to an end. Later that year, Cockcroft organized a meeting at Harwell with the director of the theoretical physics department Klaus Fuchs (1911 – 1988) to discuss Thomson's ideas. Nonetheless, the concept did not achieve great popularity at the beginning. Thomson passed along his material to two of his students, Stan Cousins (?? - ??) and Alan Ware (1924 - 2010), who built a small vacuum tube at the Imperial College, in which they produced the first (highly un-

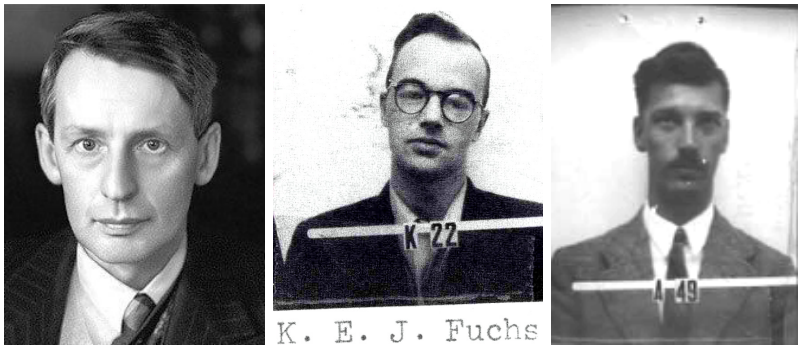

Figure 6: George Paget Thomson (left).
Klaus Fuchs' and James Tuck's badges at Los Alamos (center-right).

stable) kiloampere plasma of history [29]. While continuing to work on the project, Ware and Cousins also involved James Tuck (1910 – 1980), an English physicist who had been a member of the British delegation to the Manhattan Project and had worked with Ulam on an unsuccessful colliding beam fusion system at Los Alamos during the war (in 1944), and Peter Thonemann (1917 - 2017), an Australian theoretical physicist who had come to Oxford in hope to work on fusion devices as a doctorate. Thonemann was eventually directed on different nuclear physics topics, but he kept his interest in the subject. Together with Tuck, he obtained some funding and arranged to build another small device at the Clarendon Laboratory of Oxford University. However, in 1949 -before the machine was finished- Tuck received an invitation from Edward Teller to return to Los Alamos to work on the H-bomb project. He moved back to the US and then to Los Alamos the next year, while Thonemann remained in the UK and went on with his research programme on magnetized plasmas [30]. Tuck brought to the US some informations about the British research on the topic of nuclear fusion. Thonemann, on the other hand, studied ways to form and sustain hydrogen plasmas in glass tori. A current was induced into them as into the secondary of a transformer. These plasmas soon began to show two main kinds of instabilities, which were called 'kinks' and 'sausages' (the formers being more common in toroidal devices, the latters in linear ones). In a summary of the experimental results obtained so far appeared in the pro-

ceedings of the 1965 International Atomic Energy Agency (IAEA) conference held in Culham, Lyman Spitzer described these instabilities as follows [31]:

> *«On the streak pictures of the linear or toroidal discharges that were obtained in those early years one saw clearly the diffuse plasma column, which first contracted to a narrow filament and then started to distort and kink until finally it hit the wall. Under some conditions the plasma was observed to break up into a series of blobs like a string of sausages. Since the behaviour was exactly what the theory had predicted, it took no very great experimental wisdom to conclude that observations had confirmed theory.»*

To tame these instabilities in toroidal devices[3], during the following years two main solution were concocted: the first was to wrap the torus with a conductive metal sheet, which could counteract plasma movements via Lenz's law; the second consisted in encircling the torus with additional coils, in order to add a toroidal magnetic field to the originally purely poloidal one. This field had to be switched on before the plasma discharge, and helped stabilizing the plasma column, while confinement was mainly provided by the pinch current [4]. The application of these ideas resulted in the construction of *stabilized pinches* which showed increased confinement times, and would later develop into the Zero Energy Thermonuclear Assembly (ZETA) machine. [5]

In the meanwhile, however, informations concerning fusion research had been classified, and in the UK research sites had been moved from Universities to safer laboratories. There are at least two reasons for this. The first is that it was thought that the neutrons produced in fusion reactions could provide an efficient way to obtain polonium, which could be used in fission weapons. The second is perhaps to be found in the impression

3 In linear devices, the first attempts made in this concern lead to configurations with a magnetic field minimum (i. e. magnetic mirrors). These will not be covered in this foreword for brevity. The interested reader will find further informations in [31]

4 This concept of a stabilizing magnetic field was pushed further and somehow reversed in the later tokamak desing by Sacharov, where the confinement was mainly provided by a strong external toroidal field, while a smaller current would provide the stabilizing effect. See [32]

5 The term 'Zero Energy' referred to the fact that the machine was intended to produce fusion reactions, but with no net production of energy (see later).

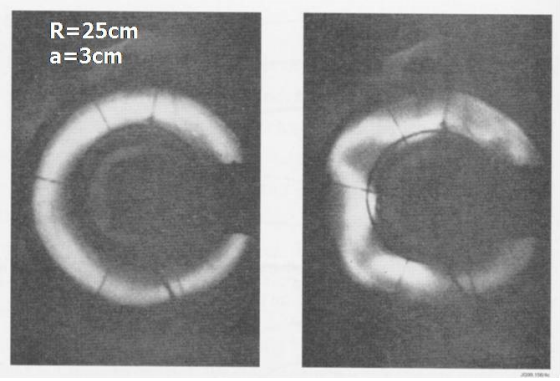

Figure 7: Famous picture of a kink instability in a glass torus at Aldermaston, where the Imperial College team had been moved after fusion research had been classified.

caused by the fact that, in 1950, Klaus Fuchs was prosecuted and sentenced to 14 years of imprisonment (after a trial that last less than 90 minutes) for passing informations on nuclear research to the Soviet Union. This must have been a particularly embarassing discovery since, before going to Harwell, Fuchs had also worked as a theoretical physicist at Los Alamos under Hans Bethe, and had hence passed to the USSR detailed informations about the US research on both fission and fusion weapons. At the time of his imprisonment, it was declared that without his help the USSR would not have been able to develop its own nuclear weapons so rapidly. Although this idea has been put into discussion in more recent times, Hans Bethe once said that Fuchs was the only physicist he knew who had truly changed history [33].

As we said, Jim Tuck had moved from the UK to the US in 1949 to collaborate with the American scientists at Los Alamos. The presence of Tuck in the US acquainted the American researchers with the British efforts on nuclear fusion. [34] In the same period, another remarkable event draw the attention of the Americans to the topic: in 1951, the Argentine President Juan Perón announced that Ronald Richter (1909 - 1991), an Austrian-born physicist working in Argentina at the so-called *Proyecto Huemul*, had succeeded in producing energy from CNF reactions. In March 1951, the US As-

sistant Secretary of Station for Inter-American Affairs Edward Miller was in Argentina to discuss a possible entry of China in the Korean war. However, the emergency eventually cooled down, and President Perón took the opportunity to announce, on March 24th during a press conference at *Casa Rosada*, that:

> *«On February 16, 1951, in the atomic energy pilot plant on Huemul Island [...] thermonuclear experiments were carried out under conditions of control on a technical scale.»*

Soon, according to Perón, energy would have been *«sold in half-litre bottles, like milk»* .

How could Argentina, an underdeveloped and mainly rural country, have achieved such a challenging goal? At that time, neither the US nor the USSR had detonated their first H-bomb yet; thus, it was hardly believable that Argentina had obtained not only nuclear fusion, but *controlled* fusion. It should not come as a surprise, then, that the news was essentially dismissed by the scientific community worldwide. Among the others, George Gamow said [35]:

> *«It seemed to be 95% pure propaganda, 4¾% thermonuclear reactions on a very small scale, and the remaining ¼% probably something better.»*

Actually, short after Richter's experiment, a technician had expressed some doubts on the finding, putting forward the idea that the promising results obtained could depend on a problem in the measurement instruments. But Richter had refused to re-run the experiment, ordering instead the dismantling of the reactor, so that a new one could be built, equipped with a magnetic confinement system. The epilogue of this story is that, after Perón had been deposed in September 1955, the whole affair turned out to be false. Richter was arrested on the night of October 4, 1955, on the accuse of fraud, and spent a short period in jail. A recent estimate places the cost of the Huemul Project close to $300 million in 2003 dollars [36].

But Perón's announcement set something in motion, and the research interest on nuclear fusion suddendly enlivened in other countries as a re-

Figure 8: Ronald Richter and what remains today of the 40-foot-high concrete bunker that housed Richter's experiment.

sponse to the Argentinian news. In 1951, Jim Tuck, the same scientist who had introduced the z-pinch concept at Los Alamos, developed a new confinement configuration under the codename "Project Sherwood". He must have had a bizarre sense of humour: the project name was indeed a joke on his own name and Robin Hood's fellow Friar Tuck, while the device was called *Perhapsatron* due to the fact that it could eventually produce fusion, perhaps. In the same year, the astrophysicist Lyman Spitzer (1914 – 1997) proposed the *Stellarator* concept, and "Project Matterhorn" was born (which was moved to Princeton after declassification, becoming the first seed of today's Princeton Plasma Physics Laboratory (PPPL)). Eventually, in the US a classified programme was launched in 1952-1953, with several groups working on different magnetic confinement solutions. In the UK, the repeated requests for funding of a larger machine were finally accepted, leading to the construction of the ZETA machine, considered to be the first truly large scale fusion experiment. The news of the building of ZETA, in turn, caused the US and even the USSR to reinforce their research programmes in order not to be left behind by the UK.

We will come back to ZETA and to Spitzer's Stellarator later. Now, it's time to turn our attention to one of the most important actors of this brief chronicle, which has been put aside until now: the USSR.

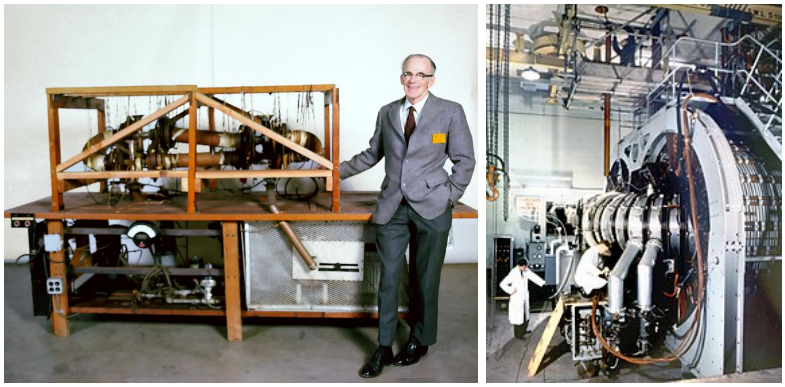

Figure 9: Lyman Spitzer and the Model-A Stellarator, exhibited at Geneva 1958 (left).
The ZETA device at Harwell (right).

The history of nuclear fusion in the Soviet Union set off with a curious anecdote. Oleg Alexandrovich Lavrentiev (1926 – 2011) was a volunteer during the war. He became a sergeant of the Red Army, and after the war he was moved to the Sakhalin Military District. When Oleg was just 15 he had read a book entitled "Introduction to Nuclear Physics", becoming interested in the topic. So, during the military service, he used to spend his free time studying technical and scientifical books from the army's library; with his monthly allowance he also subscribed to the journal *Uspekhi Fizicheskikh Nauk* (Advances in Physical Science). In 1948, he was asked to prepare a lecture on nuclear physics. About this assignment, he said [37]:

«I had a few free days to prepare a lecture. During that period I rethought all the knowledge I'd gained so far. As a result, I've found solutions to the problems I had been battling with for years.»

He decided to write a letter to the Central Committee of the Communist Party of the Soviet Union, asserting that he knew 'the secret of the hydrogen bomb'. An officer was sent from the Kremlin to interrogate him, and an order came to create for him an atmosphere where he could work. Lavrentiev wrote his first article, which was sent to the Central Committee via secret mail in 1950. In the first part of his work, he suggested a possible implementation of a hydrogen bomb, based on lithium-6 deuteride; in the second, he

discussed the exploitation of deuterium nuclei, electrostatically confined, to generate electricity. His letter was sent from Sakhalin island on July 29. By August 18, Andrej Sacharov (1921 – 1989) had reviewed it. Despite some doubts on the design proposed by Lavrentiev, he wrote that [32]:

«The author formulates a very important and not necessarily hopeless problem. [...] At this point, we must not overlook the creative initiative of the author.»

In his review, Andrej Sacharov mentioned a number of problems that should have been addressed and corrected in the prototypical design of Lavrentiev. However, Lavrentiev's letter prompted Sacharov to the idea of exploiting a magnetic field to thermally insulate the hot plasma [38]:

«The first vague ideas on magnetic thermal insulation started to form, while reading his letter and writing the referee report.»

A charged particle in a strong magnetic field moves along a helical trajectory around the field lines. The width of the helix is related to the Larmor radius associated to the particle's motion (i. e. less than $1cm$ for deuterons and less than $1mm$ for electrons for a plasma with $B = 5T$ and $T_p = 50keV$). After a collision -assuming straight field lines- the trajectory of a particle is deviated of a length which is less or equal than one Larmor radius; thus particles diffusion across the magnetic field is greatly reduced, and so is the heat transfer to the reactor walls.

By the time Sacharov's review was signed, Lavrentiev had been demobilized from the army and had enrolled in Moscow University. He also obtained an accelerated graduation from the University, and shortly after he was invited to work at the Kharkiv Physico-Technical Institute, in today's Ucraine, where he remained for the rest of his life. In 1981-1985, a toroidal magnetic trap built at Kharkiv was named ATOLL (Anti-mirror TOroidal Lavrentiev trap, **L**ovushka in Russian) in his honour. In October 1950, Andrej Sacharov and Igor Tamm (1895 – 1971) completed the first evaluations on a Magnetic Thermonuclear Reactor (MTR). We already mentioned that, in order to avoid end-losses in linear pinch devices, one can bend a linear

device into a torus. Particle drifts arise due to the curvature of the magnetic field lines: to compensate this effect, Sacharov proposed to induce a current in the plasma, so that the magnetic field lines would bend into helixes, forming a system of nested magnetic surfaces. Moreover, to keep the plasma in equilibrium, he suggested to house it in a copper vessel; and so, interestingly, at the end the Soviets came up with a design which beared many similarities to the one proposed by Thonemann and the others in the UK a few years earlier [32], despite having followed a completely different route[6]. In 1957, this configuration was baptized *tokamak* [7].

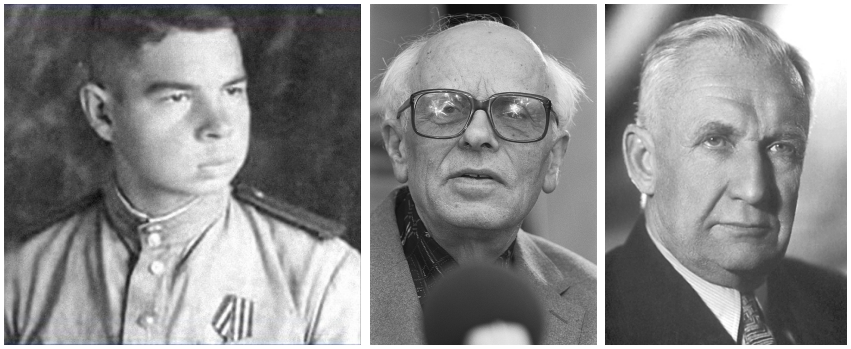

Figure 10: Oleg Lavrentiev, Andrej Sacharov and Igor Tamm.

6 The main difference between a tokamak and a toroidal pinch machine is in the ratio of toroidal field to plasma current/poloidal field. In a toroidal pinch the external toroidal field is much weaker than the poloidal field and only enters the outer layer of the plasma; as opposite, in a tokamak the toroidal field is about 10 times stronger than the poloidal one. As Lev Artsimovich put it [39]: *«The longitudinal field intensity must be many times greater than the intensity of the azimuthal field produced by the current. This constitutes the principal difference between tokamak devices and systems with relatively weak longitudinal fields, such as the well-known English Zeta device»* . This idea is well summarized by the concept of *rotational transform* (ι, i. e. the number of poloidal transits of a field line for a single toroidal transit): magnetic field lines have to be 'twisted' in order to obtain stable plasma configurations. In toroidal pinches and tokamaks, this is obtained by inducing a current in the plasma; in a *stellarator* configuration, instead, a rotational transform is obtained 'statically' by modifying the geometry of the windings. To achieve a stable plasma configuration, the *safety factor* q (i. e. the inverse of ι) must be greater than one, a condition known as the *Kruskal-Shafranov limit*. For instance, in ZETA q had a value of about 1/3. This condition yields a limit on the plasma current density; hence, a higher safety factor was obtained in tokamaks by reducing the pinch current. This, in turn, meant that ohmic heating would not be enough anymore and paved the way to different additional heating methods.

7 The term *tokamak* was coined by Golovin in 1957, as an acronym for the Russian *toroidal'naya kamera s magnitnymi katushkami* — toroidal chamber with magnetic coils. It became of common use after 1958 [32]. In the following, for brevity, we will use it also for tokamak-like experiments built before 1957.

In January 1951, Igor Kurchatov (1903 – 1960), the scientist who had supervised the building of the Soviet atomic bomb, organized a workshop on the MTR. In the following months, while the Russian government was evaluating the idea of starting a more extensive research programme on the topic, something unexpected happened [32]:

«In mid-April, the Minister of the Electric Industry D V Efremov suddenly stormed into Kurchatov's study with a magazine in his hand, which reported successful experiments by someone called Richter in Argentina, who had detected neutrons in gas discharge.»

Kurchatov communicated the news to Lavrentiy Beriya[8], and they suggested to put together a CNF research team, headed by Lev Artsimovich (1909 – 1973) and with Michail Leontovich (1903 – 1981) at the head of the theoretical division[9]. An official resolution was signed by Stalin on May 5, 1951. After some years of feverish investigation, a pilot tokamak, still with a ceramic chamber, was finally built in 1955. It was named Tor s Magnitnym Polem (TMP) (Russian for "Torus with a Magnetic Field"). We will come back to TMP later.

In the meanwhile, cold war had set out, and the danger of an atomic conflict seemed closer than ever. After the drop of Ivy Mike performed by the US in 1952, the USSR tested, just one year later, a H-bomb hundreds of times more powerful. In 1953, the *doomsday clock* reached its closest approach ever to midnight: according to the Bulletin of the Atomic Scientists, humanity was only 2 minutes away from a nuclear catastrophe [10].

8 After the Klaus Fuchs affair and the destruction of Nagasaki and Hiroshima, Stalin had ordered Kurchatov to produce an atomic bomb, and Beriya had been put in direct command of the atomic project, which had been assigned the codename *Arzamas-16*. However, the scientists involved in the project were instructed to test any information coming from the intelligence by themselves, using whatever the spies were able to discover as a benchmark for their own work.

9 Vitalii Shafranov [32] reports a funny story about Leontovich being included in the CNF programme: *«As legend has it, one of Beriya's assistants started to murmur into his ear that Leontovich was a security risk. Beriya replied with a pronounced Georgian accent: "Eef you kepp an aye on heem, he do no hemm" (If you keep an eye on him, he will do no harm)»*

10 Sadly, this shameful goal was achieved again this year. The site of the journal reports [40]: *«In 2017, we saw reckless language in the nuclear realm heat up already dangerous situations and re-*

The atmosphere of that season is well summarised by the famous 'Chance for Peace' speech given by Dwight Eisenhower (1890 - 1969) to the General Assembly of the United Nations on 8 December 1953 [41, 42]:

«I feel impelled to speak today in a language that in a sense is new–one which I, who have spent so much of my life in the military profession, would have preferred never to use. That new language is the language of atomic warfare. [...]

Today, the United States' stockpile of atomic weapons, which, of course, increases daily, exceeds by many times the explosive equivalent of the total of all bombs and all shells that came from every plane and every gun in every theatre of war in all of the years of World War II.

A single air group, whether afloat or land-based, can now deliver to any reachable target a destructive cargo exceeding in power all the bombs that fell on Britain in all of World War II. [...]

But the dread secret, and the fearful engines of atomic might, are not ours alone.

In the first place, the secret is possessed by our friends and allies, Great Britain and Canada, whose scientific genius made a tremendous contribution to our original discoveries, and the designs of atomic bombs.

The secret is also known by the Soviet Union. [...]

The free world, at least dimly aware of these facts, has naturally embarked on a large program of warning and defense systems. That program will be accelerated and expanded. But let no one think that the expenditure of vast sums for weapons and systems of defense can guarantee absolute safety for the cities and citizens of any nation. The awful arithmetic of the atomic bomb does not permit of any such easy solution.»

At that time, Dwight Eisenhower had just taken office, succeeding Henry Truman, while the Korean War – a bloody conflict that had last for 3 years – was coming to an end. It appeared clearly that the US monopoly over nuclear weaponry was doomed to end soon. In this view, Stalin's death, on 5 March 1953, provided the opportunity for rapprochement with the Soviet Union. This was made through the proposal of an International Meeting to discuss viable pacific uses of atomic energy. This conference should have

---

learned that minimizing evidence-based assessments regarding climate and other global challenges does not lead to better public policies.

Although the Bulletin of the Atomic Scientists focuses on nuclear risk, climate change, and emerging technologies, the nuclear landscape takes center stage in this year's Clock statement. Major nuclear actors are on the cusp of a new arms race, one that will be very expensive and will increase the likelihood of accidents and misperceptions. Across the globe, nuclear weapons are poised to become more rather than less usable because of nations' investments in their nuclear arsenals. This is a concern that the Bulletin has been highlighting for some time, but momentum toward this new reality is increasing.»

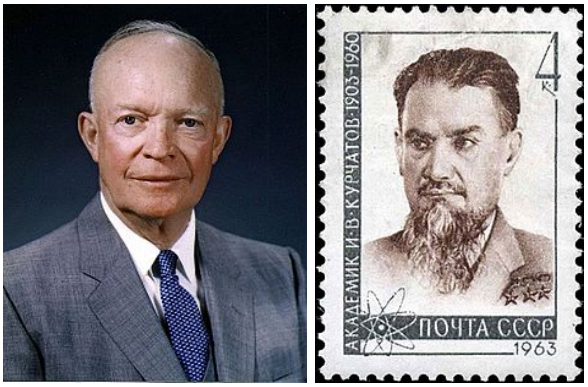

Figure 11: Dwight Eisenhower (left).
A commemorative stamp with a portrait of Igor Kurchatov (right).

been followed by the creation of an International Agency that could become a reference point for the countries collaborating in the project [41]:

«It is not enough to take this weapon out of the hands of the soldiers. It must be put into the hands of those who will know how to strip its military casing and adapt it to the arts of peace. [...]

The United States knows that peaceful power from atomic energy is no dream of the future. That capability, already proved, is here–now–today. Who can doubt, if the entire body of the world's scientists and engineers had adequate amounts of fissionable material with which to test and develop their ideas, that this capability would rapidly be transformed into universal, efficient, and economic usage.

The Governments principally involved, to the extent permitted by elementary prudence, to begin now and continue to make joint contributions from their stockpiles of normal uranium and fissionable materials to an International Atomic Energy Agency. We would expect that such an agency would be set up under the aegis of the United Nations. [...]

Most recently, we have received from the Soviet Union what is in effect an expression of willingness to hold a Four Power Meeting. Along with our allies, Great Britain and France, we were pleased to see that this note did not contain the unacceptable preconditions previously put forward.

As you already know from our joint Bermuda communique, the United States, Great Britain, and France have agreed promptly to meet with the Soviet Union.

The Government of the United States approaches this conference with hopeful sincerity. We will bend every effort of our minds to the single purpose of emerging from that conference with tangible results toward peace–the only true way of lessening international tension[11]*.»*

In 1955, some attempts were made in this direction. In the USSR, Kurchatov convened an All-Union meeting to discuss the progress in fusion re-

11 On the long distance, this speech could perhaps be seen as a propaganda manouver in the wider context of Cold War, aimed at both containing communism's diffusion and reassuring European allies about the risks of a possible nuclear war in Europe.

search obtained all around the country. Yet classified, this meeting was open to a considerably wider public with respect to the previous ones. Later that year, on the 18th of July, a summit was held in Geneva between the leaders of the "Big Four" (USA, URSS, UK and France) which aimed at reducing international tension. One month later, from the 8th to the 20th of August, the first *Atoms for Peace* conference was organized –again in Geneva– by the United Nations.

This conference shed a light of hope on the potential benefits of a peaceful cooperation for the exploitation of atomic energy. It was the biggest scientific meeting the world had ever seen. More than 1000 publications were presented, signifying the official birth of the new field of research of nuclear technologies. Moreover, it was the first time Soviet scientists could take part in a scientific meeting beyond the Iron Curtain. In the opening speech, the chair of the conference, the indian physicist Homi Bhabha, predicted [43]:

> *«A method will be found for liberating fusion energy in a controlled manner within the next two decades.»*

In the general enthusiasm, France published a technology that made possible to reprocess nuclear fuel to obtain polonium, and the URSS accepted to participate in the statute of the forthcoming IAEA.

Figure 12: Commemorative stamp of 1955 Geneva Conference.

At that time, the scientific community were generally confident that fusion could be made also for energy production purposes. In the UK, John

Lawson (1923 – 2008) wrote an article in 1955[12] proposing his famous criterion, which is still used today – in the slightly different form of the *triple product* criterion – to quantify the conditions needed for a reactor to reach ignition (i. e. a regime of self-sustaining nuclear fusion reactions; see section 2.1) [44]. But confining a plasma proved to be a task harder than it might seem, due to the presence of instabilities that were poorly understood at the time. Both theoretical and technical problems arose, making room for a widespread sense of pessimism. The need for a deeper understanding of the mechanisms underlying nuclear fusion and plasma physics was calling for the declassification of the CNF programme.

In April 1956, as a first step towards coperation in the CNF field, Igor Kurchatov (who was an advocate of nuclear disarmament and open fusion research) visited Great Britain (as part of a delegation headed by the Soviet leaders Nikita Khrushchev and Nikolai Bulganin) and gave a lecture at AERE, Harwell, "On the feasibility of the thermonuclear reaction in gas discharge". The lecture, held on April 25, summarised the main results obtained by the soviet researches in pulsed devices now known as *pinches*. From Kurchatov's speech, it was clear that US, UK and USSR were all working on similar solutions to tame nuclear fusion, and were battling with similar problems. At this point, with the Soviets at the same development level in fusion research and willing to share their knowledge, it was clear that declassification would have been of great benefit for scientists on both sides of the Atlantic. Kurchatov also warned his British colleagues that there existed the possibility of getting neutrons production – i. e. fusion reactions – which was not of thermonuclear origin (which was exactly what happened a few years later in the ZETA affair) [13] .

Shortly after, for the first time, a delegation from abroad – made by members of the Swedish Academy of Sciences – was allowed to visit the Kur-

12 The article was declassified in 1957.

13 Already on the 4th July 1952, the group of Nikolai Filippov had detected neutrons in a linear pinch experiment. Further checks, requested by Lev Artsimovich, showed that these neutrons were not thermonuclear in origin at all, and that pinch instabilities did not allow the temperature to increase with the plasma current [32].

chatov Institute. In turn, Hannes Alfvén (1908 – 1995) invited Artsimovich and Golovin to Stockholm for an astrophysics conference, where they gave lectures implicitly related to CNF issues.

Meanwhile, in the UK, the design of the ZETA had been finalized (in early 1956), and the machine was under construction. Research in the field of pinch devices had expanded rapidly in the UK, and by 1954 Thomson had started pressing the government for larger funding, which was eventually granted by the government. When its operation started in summer 1957, with its aluminum torus of more than 3 meters diameter and a foreseen plasma current of 100,000 A (which was soon raised to 900,000 A), ZETA was the biggest fusion device in the world. During the first weeks of experiments, after the current had been raised up to 200,000 A and some deuterium had been mixed to the customary hydrogen gas, many neutrons per pulse were recorded, causing great excitation among the scientists. But the way the measurements would have extrapolated to 'commercial size' reactors strongly depended on the answer to one fundamental question: were these neutrons generated by *thermonuclear* reactions? At that time, the available methods to measure bulk plasma temperature were still rudimentary, making the answer to this question particularly doubtful. From the doppler shift in the lines of some impurities seen in spectrographic measurements, the scientists calculated a plasma temperature of 1 to 5 million K, compatible with the amount of neutrons detected. It seemed that the dream of producing energy out of water had finally been realized. Even though the experiment was top-secret, news of its existence (and of some fabulous results achieved) eventually leaked, and the press started to put Harwell under pressure, asking for more details. In the meanwhile, US and UK had signed an information-sharing agreement, and scientists from both sides were allowed to visit their colleagues' laboratories. A US delegation, including Spitzer, Tuck and Stirling Colgate (physics professor and heir to the Colgate toothpaste family fortune), visited ZETA. After an initial enthu-

siasm for the results that were showed to them, on his way back to America Spitzer noted that something were wrong with the neutrons measurements, as the pulses were too short for the plasma to reach such high temperatures. By taking into accoung the well-known relation between temperature and plasma conductivity, also Colgate reached the same conclusion: the temperature measurements were wrong.

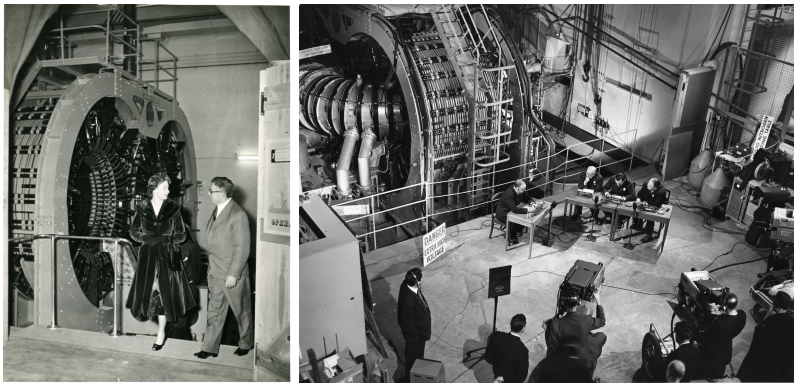

Figure 13: Queen Elizabeth II visits the ZETA facility (still under construction) guided by John Cockcroft (left).
Cockcroft is interviewed in front of ZETA in 1958. During this interview, Cockcroft assessed that he was 90% sure that the measured neutrons were thermonuclear (right).

Nevertheless, on 25 January 1958, the results obtained by ZETA were published on *Nature*, along with the data coming from other British and American devices. The paper did not mention whether the neutrons' origin was actually thermonuclear or not. But John Cockcroft was less cautious, and during a press conference, after being asked several times by the journalists, he declared that he was *«90% certain»* that this was the case. Such a strong statement from a Nobel prize winning scientist was welcomed with huge enthusiasm by the media, and ZETA ended up on all the newspapers, considered a scientific breakthrough superior even to the Russian Sputnik mission. Plans were made to build a follow-on machine, and other countries announced the construction of machines similar to the British one.

But not everyone was convinced. We already mentioned that Spitzer was skeptical about the results, and so were Colgate, Furth and other American

Figure 14: Newspaper articles concerning ZETA.

scientists. Lev Artsimovich's declaration, after reading the *Nature* issue, was just *«Chush sobachi!»* (bulls**t in Russian) [45]. After a series of experiments, it was found that the neutrons were due – as Kurchatov had pointed earlier – to strong electrical potentials generated by plasmas instabilities. Protons were accelerated by these potentials, and then collided with the neutrons already present in the plasma or impacted the walls of the machine, which in turn emitted neutrons via neutron spallation. On 16 May 1958, almost 6 months after his initial declaration, Cockcroft had to publish an embarassing retraction, and plans to build a bigger machine were abandoned [46].

However, every cloud has a silver lining: experimental activity on ZETA gave indeed many major contributions to plasma science, e. g. with the development of the Thomson scattering technique, which is still used today; the same technique was used to assess the results obtained at the T-3 Tokamak after the 1968 Novosibirsk conference (see later). Moreover, it was studying some results obtained with ZETA in 1965 that plasma scientists came up with the Reversed Field Pinch (RFP) concept.

1958 was the year of declassification. As we said, UK and US had released a large amount of data concerning several experiments (British ZETA and Sceptre and Los Alamos' Perhapsatron S-3, Columbus II and Columbus S-2) in January. Some time later, the Kurchatov Institute's papers on CNF were also declassified and collected in four green volumes edited by Leon-

tovich and entitled *Plasma Physics and Problems of Controlled Thermonuclear Reactions* [32]. In September, the goal of declassification was definitively accomplished with the *Second United Nations International Conference on the Peaceful Uses of Atomic Energy*, again in Geneva, at the beginning of which fusion was formally declared declassified by the USA and the UK.

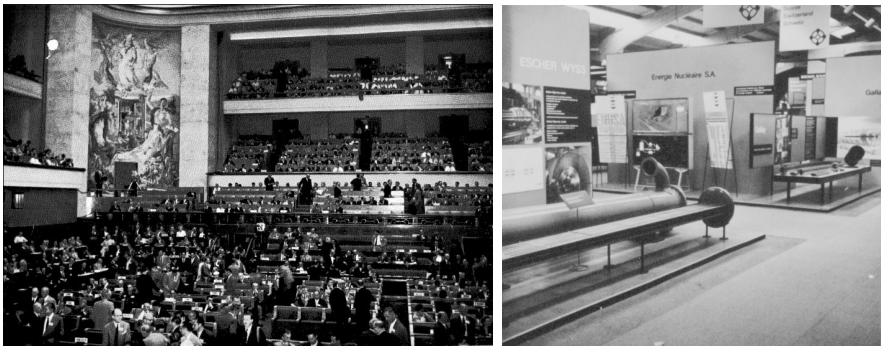

Figure 15: A picture from Geneva 1958 "Atoms for Peace" conference (left). The parallel exhibition of nuclear reactor prototypes at 1958 Atoms for Peace Conference (right).

It was a huge event: 5000 scientists from 67 countries participated to the meeting, held in the *Palais des Nations*, while the first 'nuclear fair' of history took place in an exhibition hall purposedly built to house actual fusion experiments brought along from 13 different countries. 900 journalists from all over the world, 3651 observers from the industry and even more curious auditors took part in the meeting [47]. 105 papers were presented summarising the main results obtained in the field of CNF in the USSR, USA, Uk, Germany and other countries [48]. Lev Artsimovich, who called this conference a *«fair of ideas»* [32], said in his speech [49]:

«A most important factor in ensuring success in these investigations is the continuation and further development of the international cooperation initiated by our conference.»

Scientists at the conference found that they had discovered similar things, although independently and in different countries, and their works shared many common points. Edward Teller said [49]:

«It is remarkable how closely parallel the developments in the different countries are and this, of course, is due to the fact that we all live in the same world and obey the same laws

of nature. [...] It is wonderful that over a large and important area of research we can now all talk and work together freely. I hope that this spirit of cooperation will endure, that it will be generally exercised throughout the world in this field and that be extended also to other fields.»

Figure 16: Afghan commemorative stamp of 1958 conference (left). Lev Artsimovich on a 1974 Russian stamp (right).

But all that glitters is not gold. Teller said also that [43] fusion was at a stage *«similar to the stage at which flying was about 100 years ago»* : technical difficulties were likely to make fusion produced energy *«so costly that an economic exploitation of controlled thermonuclear reactions may not turn out to be possible before the end of the twentieth century»* , showing how scientists at the meeting were far less optimistic than 3 years earlier.

At that time, the magnetic configuration under examination were essentially of two different kinds: linear devices and toroidal devices. Moreover, these machinese could be operated in a pulsed fashion or in steady state. The already cited Lawson criterion [44] had set a lower bound for the product of density and confinement time: pulsed machines, i. e. with short confinement times, had to work at higher densities than steady-state ones. Linear devices were theoretically simpler and exhibited the best performances in terms of plasma temperature rise. Unfortunately, they also suffered from losses at the ends – yielding shorter confinement times – and from various plasma instabilities. In the end, they were judged unsuitable for a commercial reactor, and scientists' attention turned to toroidal machines [17]. However, it was found that plasma transport across magnetic field lines

was much higher than expected. One of the main problems in CNF was the so called *Bohm diffusion*. The results obtained with the first, lossy prototypes of MTR showed that the plasma transport evolved according to a somewhat empirical scaling observed by David Bohm (1917 – 1992) and others while studying isotopes separation by means of magnetic arcs in 1949 [50]. According to this scaling, the diffusion coefficient was inversely proportional to the magnetic field and linear with the plasma temperature. In other words, confinement worsened when warming the plasma. This model predicted loss rates much higher than those of the classical one, which yielded – by random walk arguments – a diffusion coefficient which scaled as $1/B^2$ (meaning that a small increase in the field would have led to a much longer confinement time). Should Bohm's model be correct, building useful magnetic confinement reactors would not be possible. The initial agreement of fusion experiment results with this model led to a stagnation of fusion research during the 60s.

As we said, experiments on what later became the tokamak configuration had started in the USSR in 1951, with tori made of glass, porcelain or metal with insulating inserts. The largest of these machines was the already mentioned TMP. Just to give a rough idea, TMP had a major radius of 0.8 m and a minor radius of 13 cm, with a toroidal magnetic field of 1.5 T and a plasma current of 250 kA [48]. After TMP, many other devices of this kind were built. At the end of 1958, T-1 was the first reactor with a fully metallic vacuum chamber – with no insulation inserts – and can be considered the first actual tokamak. T-2 was built one year later with the purpose of exploring ways to mitigate radiation losses; it had an inner vessel made of corrugated metal which could be heated up to 550°C in order to release trapped gases. TO-1 featured a feedback system for the suppression of MHD instabilities. Experiments on these initial prototypes instilled some hope in the scientists: the confinement did not worsen with the rise of plasma temperature, and experimentally measured values of the energy confinement times exceeded those predicted by the Bohm's formula by an order of magnitude. These

results were later announced in the 2nd IAEA Conference held in Culham in 1965 by Artsimovich, who reported [32]:

«The confinement time in our experiments is almost 10 times the Bohm limit.»

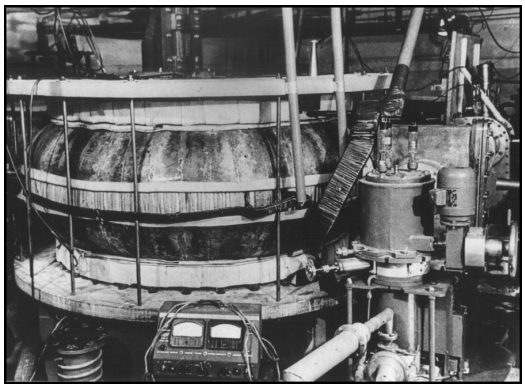

Figure 17: T1, the first tokamak in history, built at the Kurchatov Institute in Moscow in 1958. $R = 0.63$ m, $a = 0.17$ m, $B = 1.5$ T, $I_p = 100$ kA. Copper vacuum vessel, wihout gaps.

But other scientists – notably Spitzer – dismissed these results. In his view, the Bohm limit could still be valid, and the measurements made were not completely reliable. In the already cited review [31] we find:

«The chief problem of toroidal devices is the anomalous loss of particles across the magnetic field, sometimes called "pumpout". The evidence presented at this Conference on the subject of these losses does not add up to an entirely consistent picture. On the other hand, most of the groups working with toroidal plasmas have found that anomalous particle loss is a rather general characteristic of these plasmas. Measurements of the plasma density as a function of time are sometimes not a very reliable indication of plasma loss. When particles escape from a plasma and go to the wall on the millisecond time scale that is customary in most toroidal devices, there is ample time for the particles to return to the discharge and become reionized. To evaluate the intrinsic confinement time one must correct for this recycling by particles that leave the discharge, become neutralized at the walls, and then return to the discharge.
Different groups have used different methods in correcting for this recycling. [...]
These studies all indicate that the diffusion rate agrees in general order of magnitude with the simple diffusion formula given many years ago by Bohm. In the largest Tokamak device the losses reported are less that this theoretical value by about an order of magnitude; in the Model C stellarator the loss rate about equals the Bohm value, while in the smaller stellarators the loss rate was about three times the Bohm formula. I would like to emphasize not the differences between the two groups, as regards the precise ratio of the recycling loss to the Bohm formula, but rather the general agreement that anomalous particle loss is

present and that it is roughly within an order of magnitude of that predicted by the Bohm formula.»

There is no other reference in the rest of the article to the results obtained with the tokamak configuration in terms of confinement time. Moving on to the advancements in additional heating systems, Spitzer dismisses the issue saying that *«the theoretical explanation of pumpout is still a mystery»* .

Incidentally, back in 1958 Spitzer's Stellarator had been considered one of the most interesting prototypes presented during the 1958 Geneva meeting, though the gist of this design was a pretty simple concept. Bending the magnetic field into a torus produces a B gradient which causes the negative charged electrons and the positive nuclei to drift in opposite directions, producing large voltages which in turn cause the plasma ring to expand and eventually touch the walls of the reactor. To compensate this effect, in a tokamak a large current is induced in the plasma, which makes the magnetic field lines twist around the torus: in this way, on the external side of the torus -called Low Field Side (LFS)- due to the drift effect the particles move away from the center of the plasma column, while on the inner side -the High Field Side (HFS)- they move towards it. In a stellarator, this issue is addressed in a different, purely geometric way. The first stellarator, called 'figure-8', had one end flipped with respect to the other. In this way, the drift would reverse its direction every half orbit. In 1958, Spitzer described his design as follows [51]:

«Basically, the confinement scheme in the stellarator consists of modifying the magnetic field so that a single line of force, followed indefinitely, generates not a single circle but rather an entire toroidal surface, called a "magnetic surface".[...]
To produce a rotational transform in a vacuum field it suffices to twist a torus out of a single plane. Virtually any such distortion will remove the degeneracy of the ideal torus and produce a rotational transform. The simplest such system is the figure-eight, historically the first geometry proposed for a stellarator.[...]
A rotational transform angle may be produced in a variety of other ways. When a plasma current is flowing around the simple torus[14], a rotational transform appears, despite its absence in the vacuum field. If steady-state confinement is envisaged, however, a rotational transform must be present in the vacuum field. The most important alternative method

14 i. e. in a tokamak

for producing such a rotational transform is the use of a transverse magnetic field, whose direction rotates with distance along the magnetic axis[15]*.»*

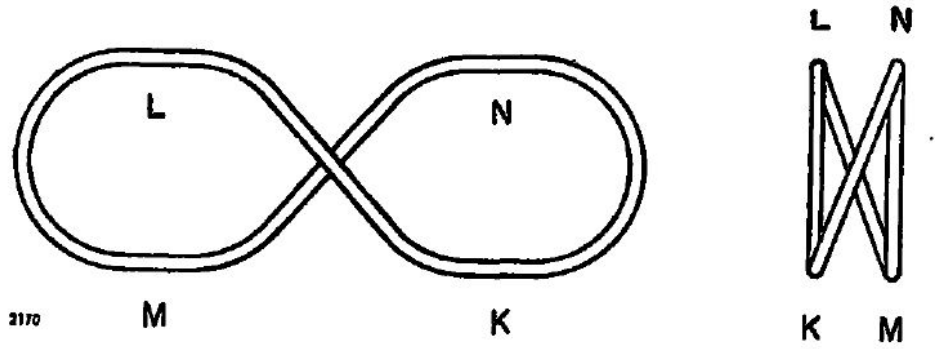

Figure 18: A scheme of the figure-8 stellarator [51].

The stellarator was hence a stationary magnetic system, with the possibility of steady-state operation, ideal for a MTR [16]. After 1958, the Russian also considered the idea of switching to this new concept. In his already cited chronicle of CNF development in the USSR [32], Vitalii Shafranov reports:

«The stellarator affected our research too:

(1) Realizing how important L Spitzer's proposal was, I V Kurchatov prodded N A Yavlinski to change to the stellarator direction instead of continuing the construction of the new tokamak (this was exactly the T-3 tokamak). N A Yavlinski asked S I Braginski and myself to compare this tokamak (this term was not yet in use and here we resort to it for brevity only) with the stellarator. We gave roughly the following arguments in favor of the tokamak. The minor chamber radius is greater in the tokamak than in stellarator of equal chamber length; hence the walls have a smaller effect on the discharge. Further, if heating is achieved by current only (no other methods were available at the time) the advantage lies with the systems with a higher current. This approach helped the tokamak line to survive at the time.

(2) The sword of Damocles of the CNF was the enhanced Bohm diffusion which seemed universal and which was detected both on the 'figure of 8' stellarator and later on the combined 2- and 3-thread stellarator C (with a race track shape). This diffusion caused depression among the researchers. However, theoreticians who tried to decipher the mechanism of this diffusion and 'sifted' a plethora of potential instabilities were able to develop the theory of turbulence and thereby facilitated the progress in plasma physics.

(3) The tokamak – stellarator competition intensified the work on CNF.»

15 See also note 6

16 Incidentally, this is one of the main arguments supporting stellarator research today as well.

But, as we have already seen, the results obtained by the Soviets with the tokamak devices in the 60s were extremely promising, as it seemed that they had finally succeeded in getting rid of the Bohm diffusion. The next breakthrough came with the Third International Conference on the Physics of Hot Plasma and Nuclear Fusion (also called "Plasma Olympics" [52]), held in 1968 at Novosibirsk, in Siberia. During this meeting, it was reported by the Kurchatov team that in the T-3 tokamak a plasma temperature of 1 keV (i. e. 10 million degrees) and a confinement time of 10 ms (an order of magnitude greater than in any other fusion machine) had been achieved [32, 52]. Again, the scientific community looked at these results with a mixture of excitation, suspect and disbelief: had those numbers been true, fusion would have been a huge step closer. But the temperature measurements had been obtained in a rather indirect manner [17]. To remove any doubt, Lev Artsimovich made an unexpected move: in the darkest hour of the Cold War, he proposed to his colleague Sebastian "Bas" Pease (1922 - 2004), the director of the Culham Laboratory for Plasma Physics and Nuclear Fusion, that a delegation of British scientsts came to the Kurchatov Institute to measure themselves the plasma temperature of T-3. In the UK, indeed, a new laser scattering technique (the Thomson scattering) had been developed and applied to fusion plasmas over the last years[17].

The UKAEA team was put together less than 6 months after the conference, and was composed by Nicol Peacock, a renowned spectroscopist, Peter Wilcock, a technical innovator, the laser scattering pioneer Mike Forrest and the 27 years old Derek Robinson, a theoretician with some laser scattering experience, plus the technician Harry Jones. They were nicknamed "The Culham Five" [52].

17 The reader might recall that the ZETA 'missed fusion' affair was caused by a misleading plasma temperature measurement. This explains why, in the aftermath, the British had put so much effort in developing new measurement techniques. As Pease himself wrote on the New Scientist [29]: *«The experiment [ZETA] was perhaps one of the more useful of the pioneering experiments with controlled thermonuclear research.[...] Zeta also provided a major stimulus in diagnostic development: for example, the use of infrared emission and scattering techniques; and in engineering techniques, for example the use of a continuous stainless-steel bellows vacuum chamber.»*

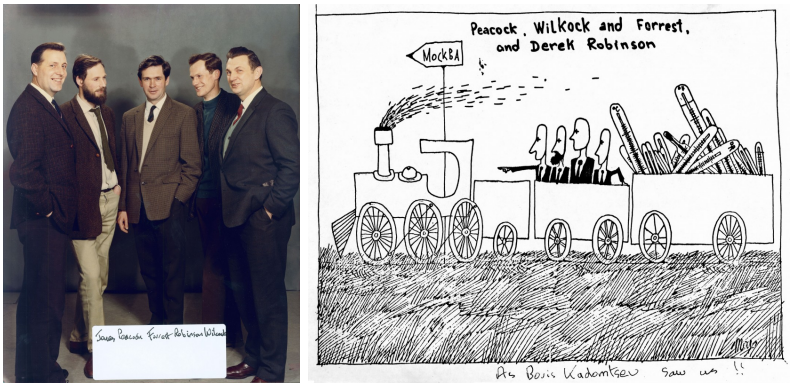

Figure 19: The "Culham five": from left to right, Jones, Peacock, Forrest, Robinson and Wilcock (left).
A cartoon of the "Culham five" expedition to Russia, made by Boris Kadomtsev (1928-1998), who later became the head of the Kurchatov Institute(right).

A first, one week expedition was arranged for Forrest and Wilcock to check what was needed. After that, a semi-permanent base in Russia was set up, and 5 tonnes of equipment were brought to it [52, 53]. By August 1969, under the constant surveillance of the KGB, the team had measured plasma temperature in 88 shots of the T-3 tokamak. The announcement made by Lev Artsimovich at Novosibirsk was confirmed: in the majority of the cases, the temperatures were in the 10 million Kelvin range. The team communicated the results to Culham, which in turn passed them to Washington. Finally, the results were published on Nature in November 1969 [54][18].

Ten years later, an article on the New Scientists reported [39]:

«The world fusion community was slow to accept that with the T3 tokamak the Soviet Union had indeed come up with a system that took the wind out of MHD instabilities.[...] Only when a team of specialists in plasma diagnostics went to the USSR from Culham Laboratory, taking with it a considerable array of laser equipment to try out a brand-new laser diagnostic technique, were the world's plasma physicists, including the Soviets, convinced

18 Dr. Forrest recently commented on his experience [52]: *«Forty years later we feel more than a tinge of pride in our 1969 achievement. After all, we had helped to get tokamaks recognized as the way forward for confined fusion research and, ultimately, to ITER.»* However, his main interest was in laser diagnostics; in fact, he also said: [55]: *«But the important thing was not the Russian thing, really. Developing the first good scattering technique is something I'd be happy to have on my gravestone. It was the first scientific experiment of its kind.»*

that the T3 plasma was as hot as the first crude measurements suggested. The Culham team reported its work in Nature in 1969 (vol 224, p 448), sparking a veritable stampede into tokamak construction around the world.»

The success of T-3 boosted the efforts in CNF research; after 1969, tokamaks were built in many other countries around the world. In 1970, the Model C stellarator at PPPL (the first large-scale stellarator ever built) was converted to the Symmetrical Tokamak (ST), which confirmed the results of T-3.

If, on one hand, the new experiments confirmed that the confinement scaled with the machine size, on the other plasma resistivity was known to be proportional to $T^{-3/2}$ [56], while the current density was limited by the Kruskal-Shafranov limit (see note 6). For this reason, soon ohmic heating was not enough anymore; thus, the next step was to explore different ways to heat up the plasma. Among the others, the tokamak T-10 ($R = 1.5$ m, $a = 0.36$ m, $I_p \leqslant 0.65$ MA, $B_t \leqslant 5$ T) was used in Russia to explore the possibility of using Electron Cyclotron Resonance Heating (ECRH) [57]. The experiments started in 1975, and the machine achieved an electron temperature $T_e = 10$ keV [48]. In the US, ST was followed by the Princeton Large Torus (PLT) in 1975, basically a copy of T-10 equipped with Neutral Beam Injector (NBI) and Lower Hybrid Resonance Heating (LHRH) systems. This machine was built *«to give a clear indication whether the tokamak concept plus auxiliary heating can form a basis for a future fusion reactor»* [58]. It was an incredibly successful experiment, the first to achieve 1 MA plasma current.

With its NBI system, PLT reached a record ion temperature of 60 million degrees in 1978, superior to the theoretical threshold for plasma ignition (about 4keV)[19] [58]. Peak temperatures of 8 keV were reported [32, 59]. Later on, PLT was also the first tokamak to peform a discharge in which

19 To celebrate this achievement, in August 1978 the Russian physicist Katerina Razumova presented the director of PPPL, Mel Gottlieb, with a Russian Firebird. It is believed that a blazing feather from this Firebird can be used to make a dream come true.

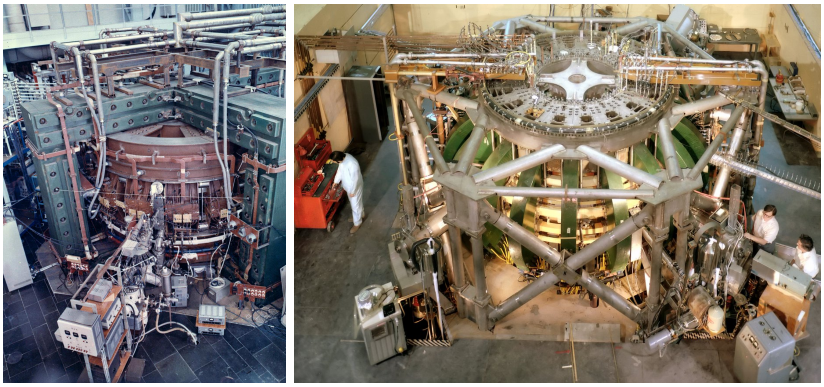

Figure 20: T-10 (left).
PLT (right).

the plasma current was driven entirely by LH radiofrequency waves (in 1981, see [58]).

Figure 21: The Russian Firebird presented by Katerina Razumova after PLT had reached 60 million degrees (right).

From the theoretical point of view, the development of *neoclassical transport* theory led to a deeper understanding of collisional transport in toroidal geometry. One of the main consequences was the discovery of the non-inductive *bootstrap current*, which paved the way to the thriving opportunity of steady-state tokamak operation [60]. Another major breakthrough on the theoretical front was the introduction of elongated cross-section plasmas. In a pioneering article published in 1972 [61], Artsimovich and Shafranov proposed to modify the geometry of the plasma cross-section with the aim of improving the confinement performances of the reactor. This led to a

series of experiments (T-8, T-9, T-12, TBD) which confirmed that a plasma equilibrium with a non-circular cross section was actually possible. In these machines -T-8 entered into operation in 1976- the first divertor configurations were created [48]. Divertor configurations proved to be useful both to handle power exhaust and to lower the amount of impurities entering the plasma due to wall sputtering, and hence they were largely studied in the 80s. In particular, the Axially Symmetric Divertor EXperiment (ASDEX) tokamak ($R = 1.65$ m, $a = 0.4$ m, $I_p \leqslant 0.5$ MA, $B \leqslant 2.8$ T; it entered into operation in 1980) was built in Germany to explore this new configuration [62]. One of the most important moments in modern fusion research came on the 4 February 1982, when the German scientist Fritz Wagner (born 1943) observed an unexpected transition while conducting an experiment on neutral beam heating on ASDEX. As Wagner himself reported [63], *«it wasn't predicted, it just happened»* : suddenly, after being exposed to intense NB heating, edge turbulence of the plasma disappeared, leading to edge pedestals in temperature and density and improving the confinement of a factor 2. It looked as a miracle. In the initial experiments performed on additional heating systems, indeed, it had been found that confinement worsened as the heating power was increased. Scalings based on this depressing finding would have led to unpractically big reactors [17, 43]. This new confinement mode came as manna from heaven. It was called *H-mode* -where the H stands for 'High confinement'- in contrast to the customary *L-mode* plasma discharges which exhibited lower confinement properties[20]. Soon, the H-mode was reproduced on many other devices, and was recognized as a universal phenomenon. Today, the scalings for the ITER are based on this experimentally well-assessed confinement regime. However, there's another side to the coin: along with the H-mode came a new kind of instability: the ELM [66].

20 More details on the H-mode can be found e. g. in [64, 65]. To date, H-mode has not been completely understood yet.

A few years after PLT and T-10, much bigger experiments set off in Europe, Japan, US and in the Soviet Union, aiming at improving the confinement with a 10-fold increase in size.

In the UK, design works for the JET started in 1973. Too expensive for a single laboratory, the machine became a joint European effort[21]. It was completed in 1983 ($R = 2.96$ m, $a = 1.25 - 2.10$ m, $I_p \leqslant 4.8$ MA, $B \leqslant 3.45$ T), and it still is the biggest tokamak in the world. After T-8, JET was one of the first tokamaks in the world designed with a D-shaped vacuum vessel. This had the twofold purpose of improving the safety factor and increasing the mechanical thoughness of the machine. It was known that elongated plasma were vertically unstable; however, simulations of these elongated plasmas showed that the instability could be slowed down by the conducting walls of the reactor to a rate controllable by a feedback system, which was hence included in the design. Later on, the plasma control system of JET was enhanced, in particular with the introduction of plasma current and shape feedback controllers [67], allowing to obtain divertor plasma configurations. In 1986, in the light of the recently discovered H-mode, a test divertor was installed in JET; H-mode was achieved, and the results in terms of confinement performances were promising, encouraging the JET team to install purpose-built divertor [17]. Initially dimensioned for a 3 MA current, which was raised to 4.8 MA during the design phase, the reactor was able – owing to its particularly good design – to reach 7 MA of plasma current.

In response to Europe, the US built the Tokamak Fusion Test Reactor (TFTR) ($R = 2.52$ m, $a = 0.87$ m, $I_p \leqslant 3$ MA, $B \leqslant 6.0$ T). The project was proposed in 1974 and approved in 1976, and the reactor went into operation on December 1982 (a few months before JET, mainly due to a quicker decision on the site) [17, 68]. Both machines had the goal of achieving plasma

21 A political battle set off between Germany and England to house the reactor. Curiously enough, the decision came in October 1977, after a Lufthansa plane was hijacked by the Baader-Meinhof gang and was rescued in Mogadishu with the aid of the British, who provided some special grenades for the operation [17].

break-even. The JET design, as we saw, was focused on a big plasma volume and its D-shaped cross section to increase the confinement time and hence the thermonuclear yield. TFTR, on the other hand, had been designed with a circular cross-section, and did not allow to install a divertor [17]. More emphasis was put on having a powerful NBI system, in order to take advantage of non-thermal beam-plasma reactions [43]. NBI experiments performed on this machine in 1986 produced record ion temperatures of approximately 200 million degrees [58]. This record was raised to 510 million degrees in 1995. TFTR was also the first machine to extensively perform 50/50 D-T experiments, producing in 1993 up to 10 MW of CNF power for 1s, with a Q factor of about 0.3. This result, however, was overcome in 1997, when JET set the current world record for fusion power: 16 MW for ~1s, with a maximum Q of ~0.65. TFTR was closed in 1997 to leave room for a new experiment, the National Spherical Torus eXperiment (NSTX). Since then, JET remained the only operating machine to have the facilities for tritium operation.

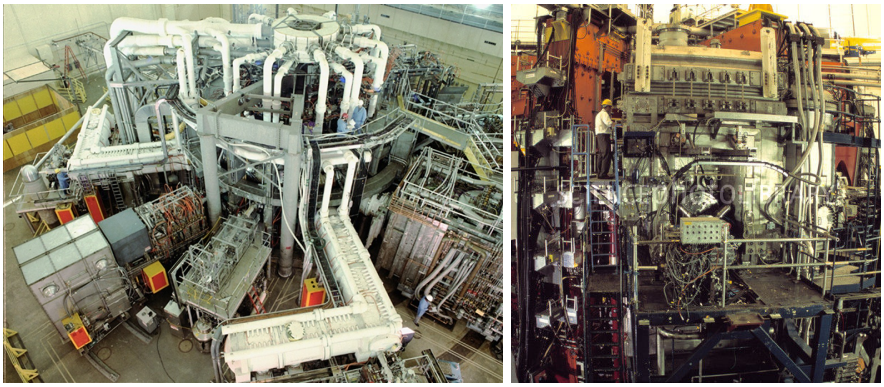

Figure 22: TFTR and JET.

In the USSR, a plan was announced to build a larger tokamak (the project was named T-20), but eventually the decision fell on a smaller design, which was baptized T-15 ($R = 2.43$ m, $a = 0.78$ m, $I_p \leqslant 1$ MA, $B \leqslant 3.6$ T, first plasma in 1988). T-15 was the first tokamak to use superconducting helium-

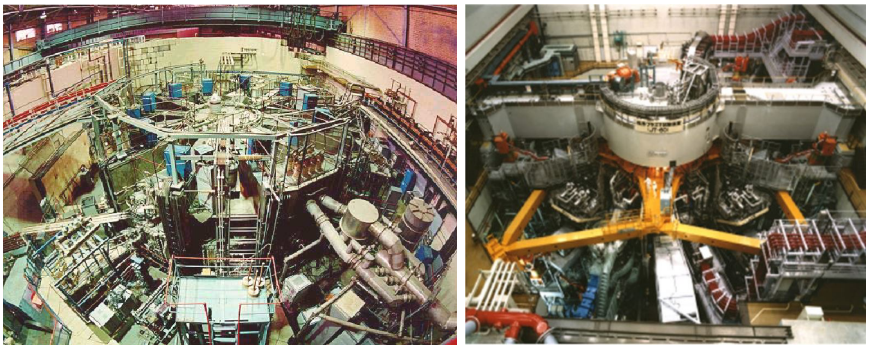

Figure 23: T-15 and Japan Torus-60 (JT-60).

cooled Nb_3Sn coils. Eventually, it was shut down in 1995 due to lack of funds[22].

The last of the big tokamaks built in that period was JT-60 ($R = 3.4$ m, $a = 1.0$ m, $I_p \leqslant 3$ MA, $B \leqslant 4$ T; approved in 1979, 1st plasma in April 1985), in the Ibaraki prefecture of Japan. Differently from JET and TFTR, JT-60 was designed with a divertor since the beginning. Since the first version of the divertor seriously limited the available plasma volume, in 1989 the machine was shut down to install a new one. The upgraded machine (named Japan Torus-60 Upgrade (JT-60U)) came into operation in 1991; it reached plasma currents up to 6 MA [17]. While JET and TFTR focused their efforts on deuterium-tritium operation, JT-60U pushed the performances in D-D experiments. In 1998, this tokamak set the current record for the equivalent fusion energy gain factor Q_{eq}: 1.25 [71]. Currently, the machine is undergoing a new upgrade, named JT-60SA; the installation of superconducting coils is foreseen. The first plasma is planned for September 2020 [72].

With the big tokamaks built and operated in the 1970-1990 season, the achievability of many scientifical and technical goals was demonstrated: reactor-like temperatures, tritium operation (with the subsequent technological implications, e. g. remote handling of the inside components of the reactor) [73], high gain factor [71] have already been discussed. So, what issues remain to be addressed? For a commercial reactor, steady state oper-

22 In 2010, a further upgrade was proposed with the aim of building a hybrid fusion-fission reactor [69]. It should be completed this year [70].

ation is fundamental, as energy has to be produced in a continuous way. For this reason, stellarator research received new impulse, with the construction of devices such as Wendelstein 7-X (W7-X) (first helium plasma in December 2015), which are optimized to reduce particle loss while maintaining stability and confinement properties and feasible coils [68]. W7-X achieved a plasma pulse duration of ~30m during the first operation phase, ended in March 2016[23]. On the other hand, the concept of the *advanced tokamak* was put forward, aiming at increasing the bootstrap current fraction and exploiting non-inductive current drive methods (NBI, Lower Hybrid Current Drive (LHCD) and so on) to supply for the remaining part of the plasma current [68]. In this view, internal profiles tailoring is required to maximise the bootstrap current fraction, feedback control of MHD instabilities is needed, and efficient power exhaust methods become necessary.

If JET, TFTR and JT-60U substantially demonstrated that fusion is scientifically possible, it remains to prove that fusion is also technically feasible; the goal $Q > 1$ is still to be achieved in D-T operation. This will be the main purpose of ITER[24], a machine which is currently being built in Cadarache, in the south of France, as a joint effort of several countries around the world (EU, USA, Russia, Japan, India, China, South Korea). ITER ($R = 6.2$ m, $a = 2$ m, $I_p \leqslant 15$ MA, $B \leqslant 5.3$ T) is expected to achieve Q ~10 at ~500 MW for ~400s, and Q ~5 at ~350 MW for ~2500s. The first plasma is expected for 2025, whereas the machine should enter into proper operation by 2035[25].

23 More details on the machine can be found on the IPP website [74].

24 It is not a coincidence that ITER is also the Latin word for 'pathway', the end of this path being a commercial fusion reactor. Before then, however, a first demonstration power plant should be built. The name by which the preliminary design proposal for such a plant are denoted is DEMOnstration power plant (DEMO) [75].

25 Before ITER, other designs were proposed, such as the Next European Torus (NET) [76] and the INternational TOkamak Reactor (INTOR). The ITER project itself had a troubled gestation, which suffered from political hiccups, long delays and increases in the foreseen cost. For a more detailed review of the history of the ITER project see, for example, [17].

2

CONTROLLED NUCLEAR FUSION

"The whole is ~~greater~~ smaller *than the sum of its parts"*

— Aristotle (?)

2.1 NUCLEAR FUSION

Nuclear fusion is, by definition, a process in which two elements nuclei blend together to form a heavier one. In general, a nucleum composed by N neutrons and Z protons has a mass which is slightly smaller than the sum of the masses of the single nucleons. The missing part, called *mass defect*, is converted into energy according to Einstein's formula:

$$E = mc^2 \tag{1}$$

For light elements, such as the isotopes of hydrogen, fusing into heavier nuclei is energetically favourable, and thus in this case fusion reactions free a certain amount of energy, equal to the difference between the potential energies of the product and the reacting nuclei. This is not the case for heavy elements (e. g. uranium). This can be understood by considering the two main forces involved, i. e. the repulsive Coulomb force and the attractive strong nuclear force. The former acts on a long range (i. e. proportional to the inverse square of the distance), whereas the latter is much stronger but acts over a much shorter distance. When a nucleum exceeds a critical combination of charge (i. e. atomic number) and dimension, the electrostatic repulsion overcomes the attractive effect, hence making the addition of a new nucleon energetically disadvantageous. As it happens, this critical combi-

nation falls in correspondence with Iron-56, where the binding energy of the nucleum reaches a maximum. Fig. 24 shows the binding energy for different elements. A simple qualitative picture of this phenomenon can be found, for instance, in [77].

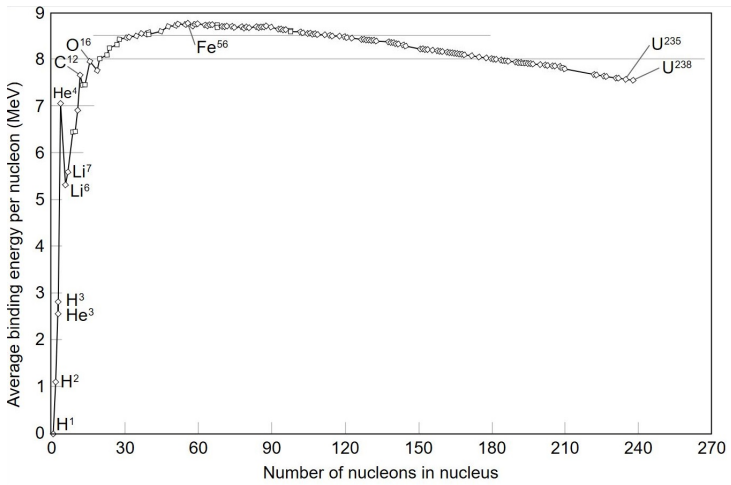

Figure 24: The nuclear binding energy curve.

2.1.1 *Fusion reactions of interest*

Energy production can only occur when moving upwards along the binding energy curve, i. e. by fusing light elements together or by smashing heavy nuclei in fission reactions. But how much energy is produced? Here is a list of some fusion reactions of interest [77]:

Main fusion reactions

1. $D + D \rightarrow He^3 + n + 3.27MeV$
2. $D + D \rightarrow T + p + 4.03MeV$
3. $D + He^3 \rightarrow \alpha + p + 18.3MeV$
4. $D + T \rightarrow \alpha + n + 17.6MeV$
5. ${}_3Li^6 + n(slow) \rightarrow \alpha + T + 4.8MeV$
6. ${}_3Li^7 + n(fast) \rightarrow \alpha + T + n - 2.5MeV$

Let us start by considering reactions 1-4. The probability of occurrence of each reaction can be quantified by an associated *cross section* (σ). This cross section can be seen as the area surrounding a target particle within which the presence of another particle is capable of producing interaction phenomena (see fig. 25).

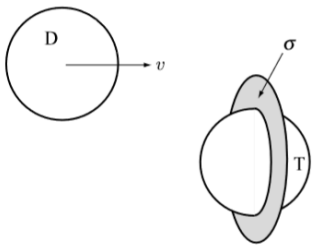

Figure 25: Graphical representation of the cross section concept.

The potential around a nucleum can be obtained by combining the Coulomb potential and the nuclear one, and it has the shape of a deep well surrounded by a barrier (see fig. 26). In order to interact, two particles need to overcome this barrier, and they can only do so if enough kinetic energy is provided to them. It is no surprise, than, that the cross section has a dependence on the temperature of the reactants; this dependence is shown in fig. 27.

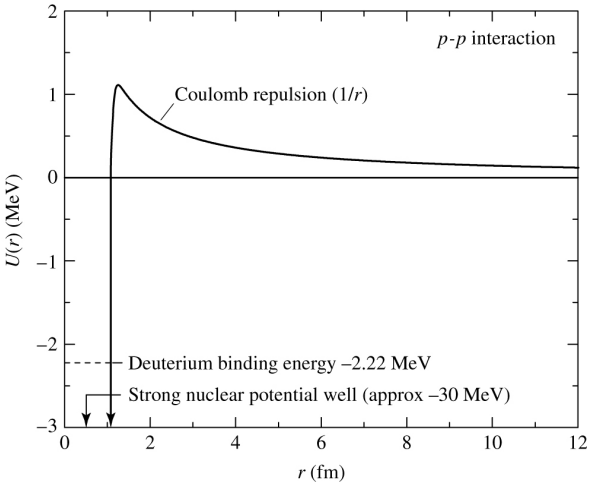

Figure 26: Coulomb barrier in the case of p-p interaction.

As it can be seen, the cross section of the D-T reaction has the highest peak at the lowest temperature (~5 barns at ~100 keV[1]), and thus it is the easiest reaction to initiate. This, together with the big amount of energy released, is one of the reasons why worldwide fusion research is mainly focused on D-T. The other main reason is that, with respect to the other listed reactions, the D-D one is too difficult to trigger, and there is no natural supply of helium-3 on Earth.

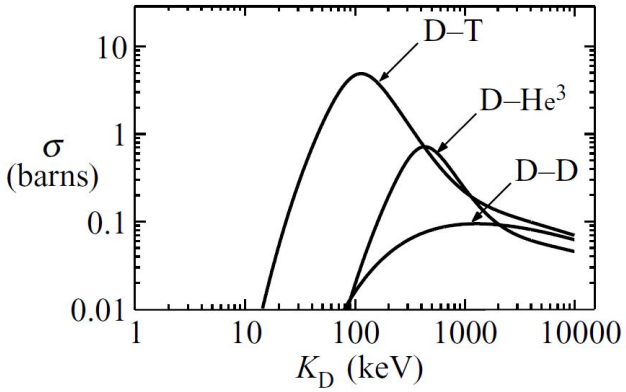

Figure 27: Cross section with respect to temperature for different fusion reactions ($1barn = 10^{-24}cm^2$). The two D-D reactions listed have the same probability of occurrence.

However, the D-T reaction presents some disadvantages, too. First of all, it produces high-energy neutrons[2], which in turn cause material activation and radiation damage; second, it needs tritium, a radioactive and unstable material, which decades into helium-3 with a half-life of 12.33 years[3] and

1 Actually, a classical computation for the Coulomb barrier would yield $E_B = e^2/4\pi\varepsilon_0 d$, i. e. 288 keV for $d = 5 \times 10^{-15} m$. In fact, the peak is shifted towards a lower value due to quantum mechanical effects [77]. However, even ~100 keV correspond to an impractically high temperature of ~1 billion degrees. This value can be further lowered (of about one order of magnitude) taking into account the velocity distribution of the particles -which is assumed to be the Maxwell-Boltzmann one in the case of thermonuclear fusion- and accepting that only the high-energy tail of this distribution satisfies the requirements for the reactions to occur.

2 Incidentally, since one of the products of the reaction is charged while the other is not, it is useful to know how the energy is distributed among the products. By classical arguments (energy and momentum conservation) it is easy to show that the energy of the products is inversely proportional to their masses, yielding: $D + T \rightarrow \alpha(3.5MeV) + n(14.1MeV)$.

3 This is a manageable span of time, especially if compared to the 700 million years half life of U^235 –which is used in fission reactors– and the 4 and a half billion years one of U^238.

is hence practically absent in nature (whereas deuterium can be easily extracted from water). Yet, these setbacks are not enough to abandon fusion research. To have a rough idea of the amount of energy released, we can compare it to the energy obtained by the combustion of fossil fuels. Burning 1 kg of gasoline produces ~40 MJ, enough to move a car for about 10 km. This is quite an impressive number, but it is just a speck of dust compared to fusion energy: 1 kg of D-T mixture could, in principle, release a ten-million higher energy of ~338×10^6 MJ [77]. Tritium can be obtained exploiting the reactions 5-6 mentioned above; in particular, reaction 5 is much easier to initiate, and is hence preferred to reaction 6, even though ${}_3Li^7$ constitutes 92.6% of natural lithium. Technical solutions for neutron handling have been worked out during the years, even though the issue still constitutes an active research topic. However, most present day experimental reactor are meant to explore plasma physics or technological issues, and hence operate without tritium, with very few neutrons produced due to some sporadic D-D reactions occurring.

2.1.2 *Power balance for a fusion reactor*

Now that the main features of the D-T reaction have been described, we can move on to establish some criteria to be met in order to build a useful fusion reactor. [4]. Let us assume that the device is fuelled with a 50/50 mixture of deuterium and tritium. Calling n_D, n_T, n_e the densities of deuterium, tritium and electrons respectively, we have $n_D = n_T = n/2$ and $n_e = n$.

4 The first step in this direction was made by the British engineer and physicist John Lawson in 1955. In his analysis, Lawson derived an energy balance from which he was able to deduce a lower boundary for some parameters of interest. Here we will follow a slightly different path. The interested reader is referred to [44]

The total power density produced by fusion reactions can be estimated by multiplying the energy produced by a single reaction ($w_N = 17.6MeV$) times the *reaction-rate*[5] of D-T:

$$p_N = n_D n_T \langle \sigma v \rangle w_N = \frac{1}{4} n^2 \langle \sigma v \rangle w_N \tag{2}$$

Analogously, the α-particles energy is given by:

$$p_\alpha = \frac{1}{4} n^2 \langle \sigma v \rangle w_\alpha \tag{3}$$

where $w_\alpha = \frac{1}{5} w_N = 3.5MeV$.

The average energy of the particles, at a given temperature T, is given by $\frac{3}{2}T$. The energy per unit volume is hence:

$$w = \frac{3}{2}(n_D + n_T + n_e)T = 3nT \left[eV/m^3 \right] \tag{4}$$

The losses due to heat conduction can be quantified by defining the *energy confinement time* τ_E as the characteristic time over which the system loses energy[6][7]:

Confinement time

$$p_T = \frac{dw}{dt} = \frac{3nT}{\tau_E} \tag{5}$$

Radiation losses, at a temperature of ~1 million K, are mainly due to *Brehmsstralung*, i. e. the radiation emitted by a particle which is decelerated

5 The reaction rate is the number of reactions that occur per unit time and space. Calling $\langle \sigma v \rangle$ the cross section averaged over the velocity distribution, and n_1, n_2 the densities of the reactants, the reaction rate is given by $R_{1,2} = \langle \sigma v \rangle n_1 n_2$ [77].

6 For a correct estimation of the heat flux, the heat conductivity of the plasma and the temperature gradient at its edge should be known. This in general is not easy, mainly due to the complexity of the transport phenomena involved. In practice, τ_E can be estimated by regression analysis over a number of plasma discharges in different conditions, and is in general a function of temperature and pression [77]. For simplicity, we will neglect this dependence for now. On the other hand, a simple way to estimate τ_E can be obtained neglecting the nuclear-generated power and the other source of losses, i. e. $p_H = p_T$, where p_H is the heating power applied to the plasma [78].

7 In his work, Lawson made the simplifying assumption that, in a pulsed machine, the gas is heated instantaneously to a temperature T, which was then hold for a time span τ_E before allowing the gas to cool down. The final result is the same.

when deflected by another charged particle. In his work, Lawson quantified the power density due to this effect as ($Z_i = 1$ for both D and T)[8]: *Brehmsstralung*

$$p_B = 1.4 \times 10^{-38} n^2 Z_i^2 T^{1/2} = C_B n^2 T^{1/2} \left[W/m^3 \right] \tag{6}$$

In his original paper, Lawson supposed that part of the heat produced in the device could be fed back into the machine to heat the reactants, with a given efficiency η (typically, $\eta \leqslant 1/3$). With this assumption, the machine power balance reads: *Power balance*

$$\eta \left(\frac{w_N}{4} \langle \sigma v \rangle n^2 + \frac{3nT}{\tau_E} + C_B n^2 T^{1/2} \right) = C_B n^2 T^{1/2} + \frac{3nT}{\tau_E} \tag{7}$$

From which an explicit dependence of $n\tau_E$ on T can be derived:

$$n\tau_E = \frac{3T}{\left(\frac{\eta}{1-\eta} \langle \sigma v \rangle \frac{w_N}{4} - C_B T^{1/2} \right)} \tag{8}$$

Lawson also defined the *gain factor* as the ratio of the released energy to the supplied one: *Gain factor*

$$Q = \frac{p_N}{p_{Heat}} \tag{9}$$

In his work, Lawson assumed that the energetic fusion products escaped the reactor and hit the walls without interacting with the other particles; thus, at steady state $p_{Heat} = \frac{3nT}{\tau_E} + P_B$. Under this assumption, for a power producing system it must hold that:

$$\eta (Q + 1) > 1 \Rightarrow Q > 2 \tag{10}$$

The condition above is commonly referred to as the *Lawson criterion*, while $Q = 1$ is called *breakeven* condition[9].

8 This relation was obtained by G. Cillie in 1932 [44].

9 Actually, there exist a few different definitions of breakeven. The one proposed here is that of *scientific breakeven*, i. e. $p_N = p_{Heat}$

A rough estimate of the $n\tau_E$ lower bound can be given as follows [78]. Let us assume that only the α-particles re-heat the plasma, while the neutrons escape without interactiong with the D-T ions. Neglecting the brehmsstralung losses[10] and assuming that w_α is completely transferred to the reactants, the power balance becomes:

$$p_{Heat} = \left(\frac{3nT}{\tau_E} - \frac{1}{4} n^2 \langle \sigma v \rangle w_\alpha \right) \tag{11}$$

If we assume that the reactions are sustained only by internal heating (i. e. $p_{Heat} = 0$) we obtain:

Ignition

$$n\tau_E \geqslant \frac{12}{\langle \sigma v \rangle} \frac{T}{w_\alpha} \tag{12}$$

This condition is called *ignition*, and is equivalent to $Q = \infty$.

For a D-T reaction, the relation above has a minimum close to $T = 30keV$, which yields a lower boundary for the Lawson parameter $n\tau_E$ equal to $1.5 \times 10^{20} m^{-3} s$. Since τ_E is function of T, however, we can consider the *triple product* $nT\tau_E$; as it turns out, the optimal temperature is in the 10-20 keV range, and the ignition condition becomes [78]:

Triple product

$$nT\tau_E \geqslant 3 \times 10^{21} m^{-3} keVs \tag{13}$$

2.2 PLASMAS

At the end of sec. 2.1 it was discussed how the optimal temperature for a fusion reactor falls in the 10-20 keV range, equivalent to ~100 million Kelvin. At such a high temperature, any material is in a state known as *plasma*[11]. What is a plasma? A good definition can be found in [79]: *«plasma is quasi-neutral gas with so many free charges that collective electromagnetic phe-*

10 For a more detailed discussion of this assumption and its implications, see [77].
11 See also note 1.

nomena are important to its physical behavior» [12] A good picture is that of a (ideally fully) ionized gas composed by a plethora of microscopic charge carriers (ions and electrons). These carriers constitute two –or more– electrically charged fluids of opposite signs, which tend to arrange in such a way to neutralize the macroscopic charge density. This condition is known as *quasi-neutrality* – the 'quasi' depending on the fact that small deviations from a proper neutrality condition can have significant repercussions on the plasma behaviour. The presence of so many free charges in the plasma makes it an exceptional electrical conductor, especially at high temperatures and low densities. For this reason, plasmas are extremely effective in shielding DC electric fields (whereas magnetic fields can penetrate)[13].

2.2.1 *Basic properties and parameters*

Quasi-neutrality and electrical conductivity are the two basic properties that define a plasma, making it different from a regular gas. In this section, some consequences of these properties will be discussed, leading to the definition of some parameters of interest.

As we said, plasma is very effective in shielding DC electric fields; indeed, the potential generated by a point charge introduced into an otherwise quasi-neutral plasma can be proved to decay in an exponential way. The characteristic length over which this shielding occurs takes the name of *Debye length*, and is equal to [79]:

Debye length

12 Plasma physics is a vast field of study; in this introduction we will just focus on a few of its basic aspects. Among the many different books and sources available, [77] and [78] are probably two of the most widely used, especially in the field of magnetic confinement fusion and tokamak reactors. [79] and [80] give a good general overview on the subject, while more details can be found, for example, in [81] and [82]. Finally, in [83] the MHD model and its application to nuclear fusion are examined in depth.

13 In what follows, temperature will be always expressed in energy units, thus absorbing the Boltzmann's constant.

$$\lambda_D = \sqrt{\frac{\varepsilon_0 T_e}{n_e e^2}} \tag{14}$$

where ε_0 is vacuum permittivity, T_e, e, n_e are electron temperature (in units of energy), charge and equilibrium number density (in absence of the external charge)[14]. For a typical fusion plasma, $\lambda_D \approx 10^{-5} - 10^{-4} m$

Let us now consider the case of a group of electrons which is displaced from its quasi-neutrality position; the Coulomb force pulls them back, acting as a restoring force. It is possible to show that the charge density oscillates at the (electron) *plasma frequency* [78]:

Plasma frequency

$$\omega_{pe} = \sqrt{\frac{n_e e^2}{\varepsilon_0 m_e}} \tag{15}$$

An analogous definition can be given for ions. In a fusion plasma, $\omega_{pe} \approx 10^{11} - 10^{12} s^{-1}$. Just as λ_D is a characteristic length for the plasma, ω_p represents a characteristic frequency: a gas of charged particles can be properly called a plasma only when characteristic lengths much bigger than λ_D and time spans much longer than the period associated to ω_p are considered.

Plasma parameter

Finally, we can define the *plasma parameter* as [77]:

$$\Lambda = \frac{4\pi}{3} n \lambda_D^3 = \frac{4\pi}{3} \frac{\varepsilon_0^{3/2}}{e^3} \frac{T_e^{3/2}}{n^{1/2}} \tag{16}$$

which represents the typical number of particles contained in a sphere of radius λ_D. When $\Lambda \gg 1$, a Debye sphere is typically densely populated. A particle is influenced by all the other particles in her Debye sphere, but this interaction usually does not cause sudden motion changes, and hence long-range collective effects dominate over binary collisions. In this case, the plasma is also said to be *weakly coupled* [82], and can be described in a

14 We dropped the ion contribute by assuming that the ions are much colder than the electrons.

way similar to a gas[15], whereas *strongly coupled* ones are much more difficult to deal with. In a typical tokamak plasma, $\Lambda \approx 10^8 - 10^9$.

2.2.2 *Magnetized plasmas*

A particularly interesting example is that of a charged particle (of mass m and charge q) moving in a uniform magnetic field. Despite its simplicity, it provides some useful insight on the mechanism underlying magnetic confinement. For such a particle, the equation of motion reads:

$$m\frac{dv}{dt} = q\mathbf{v} \times \mathbf{B} \tag{17}$$

If the field points in the z direction:

$$\frac{dv_x}{dt} = \frac{qB}{m}v_y \tag{18}$$

$$\frac{dv_y}{dt} = -\frac{qB}{m}v_x \tag{19}$$

$$\frac{dv_z}{dt} = 0 \tag{20}$$

The quantity *Cyclotron frequency*

$$\omega_c = \frac{qB}{m} \tag{21}$$

15 This can be easily understood by means of a statistical argument: for a continuum fluid model to be valid, the plasma must be subdivided into many small volumes which are much smaller than the typical length of the system but yet contain a great number of particles. This condition can be satisfied when $L \gg \lambda_D$ and $\Lambda \gg 1$ by taking volume elements of a size comparable to the Debye radius.

is the *cyclotron frequency* associated to the particle motion in the field. A solution to equations (18)-(20) is given by [78]:

$$v_x = v_\perp \sin(\omega_c t) \tag{22}$$

$$v_y = v_\perp \cos(\omega_c t) \tag{23}$$

$$v_z = v_{z0} \tag{24}$$

and the particle moves along a helical trajectory around the field lines:

$$x = -r_L \cos(\omega_c t) \tag{25}$$

$$y = r_L \sin(\omega_c t) \tag{26}$$

$$z = z_0 + v_z t \tag{27}$$

Larmor radius

where

$$r_L = \frac{v_\perp}{\omega_C} \tag{28}$$

is called *Larmor radius*.

This *gyro-motion* is the core of the magnetic confinement fusion concept: when a strong magnetic field is applied, the particles are forced to follow helical trajectories of width $2r_L$, and hence transport across the field lines is strongly reduced (since, in principle, particles can deviate from their Larmor trajectories only when a collision happens). For $B = 3T$, $T = 10keV$, the Larmor radii of an electron and a proton are, respectively, 0.11 mm and 4.8 mm, while the gyro-frequencies are $f_{cp} = 2\pi\omega_{cp} = 46GHz$ and $f_{ce} = 2\pi\omega_{ce} = 84GHz$ [78]. For a good confinement, in a fusion plasma the condition $L \gg r_{Li}$ must hold.

The magnetic field's effect on the plasma can be quantified by means of two parameters [82]. The first is the *magnetization parameter*, i. e. the ratio of the gyro radius to the characteristic length of the system:

Magnetization parameter

$$\delta = \frac{r_L}{L} \tag{29}$$

the other is the so called *plasma beta*, which represents the ratio of the thermal energy density $nT \equiv p$ to the magnetic energy density $B^2/2\mu_0$: *Plasma Beta*

$$\beta_s = \frac{2\mu_0 p_s}{B^2} \tag{30}$$

$$\beta = \sum \beta_s \tag{31}$$

where the index s ranges over all the species in the plasma.

2.2.3 *Plasma description*

A plasma can be described at different complexity levels. An exact description requires the solution of the equations of motion for all of the particles. This is an incredibly demanding task, which in most cases can be carried out only by approximations and numerical simulations. Yet, this level of accuracy is needed to analyse some physical phenomena.

A slightly less accurate –but still quite complicated– level of description, consists in characterizing plasma in a statistical way. This can be done by treating the motion of a large number of particles by means of their statistical distribution function in both position and velocity. This is the core of the so called *kinetic theory*, which proves to be useful in many cases (e. g. for the analysis of energy deposition in fusion plasmas associated with various heating methods). We will not cover this argument; more details can be found in [81].

The next step in terms of simplifications is to describe each species in the plasma as a charged fluid[16]. This is the basis of the MHD description. As it usually happens with gases and fluids, in the MHD frame plasma is treated as a continuum, and microscopic fluctuations are neglected in favour of macroscopic parameters such as pressure and temperature. This

16 Macroscopic fluid equations can be derived rigorously by taking the statistical momenta of the velocity distribution function – usually assumed to be Maxwellian – of the particles in the kinetic model and adding some closure conditions. This topic will not covered here; see [78].

is common practice in statistical and fluid mechanics (see, for example, [84]). However, MHD is more complicated than customary fluid equations, due to the interaction between electrically charged fluids and the electromagnetic field.

Finally, a single fluid description can be straightforwardly obtained from the multi-species MHD model. Indeed, for a plasma made of two species (namely electrons and ions), we can define the following quantities:

- $n_i \simeq n_e \simeq n$ number densities of ions and electrons (assumed to be equal due to quasi-neutrality)
- $\rho_i = m_i n_i$, $\rho_e = m_e n_e$, ions and electrons mass densities
- T_i, T_e, ions and electrons temperatures
- $p_i = n_i T_i$, $p_e = n_e T_e$, ions and electrons pressues
- $\mathbf{v_i}$, $\mathbf{v_e}$, ions and electrons fluid velocities

From these, the following single-fluid quantities can be defined [83]:

- $\rho = \rho_i + \rho_e \simeq \rho_i$ (since $m_i \gg m_e$)
- $\mathbf{v} \simeq \mathbf{v_i}$ (momentum is mostly carried by the heavy ions)
- $\mathbf{J} = en(\mathbf{v_i} - \mathbf{v_e})$, current density
- $p = p_e + p_i$
- $T = T_e + T_i$

By adding some further simplifying assumptions (e. g. perfectly conductive plasma, no viscosity, adiabatic behaviour), the *ideal* MHD model is obtained, which describes how the plasma responds to inertial, magnetic and pressure forces in a given magnetic geometry. Ideal MHD will be the starting point for the plasma modelling which will be discussed in the next chapter. Hence, the next section will be devoted to give some physical insight into it.

2.2.4 *Ideal Magnetohydrodynamics*

In a fusion plasma characteristic length, velocity and time are given by $L \sim a$ (the overall plasma dimension, which is usually in the order of meters), $v_i \sim v_{Ti}$ (the thermal velocity of ions, $v_{Ti} = \sqrt{\frac{2T}{m_i}}$, in the order of $10^6 m/s$), $\tau \sim a/v_{Ti}$ (typically in the order of μs). These assumptions lead to the following simplifications [77]:

- $1/\tau \ll \omega_{ce} \sim \omega_{pe}$, hence the electron inertia can be neglected. This is equivalent to assume $m_e \to 0$;
- $v_{Ti} \ll c$, which has two main implications: the first is that the model describes a non-relativistic regime, the second that the displacement current term in Maxwell's equation can be discarded. Furthermore, since $a \gg \lambda_D$, the $\nabla \cdot \mathbf{E}$, yielding the quasi-neutrality relation $n_i \approx n_e$. These simplifications reduce Maxwell's equations to a simpler, Galileian-invariant form. This is equivalent to assume $\varepsilon_0 \to 0$.
- $a \gg \lambda_{DB}$, the De Broglie wavelength associated to the particles, thus quantum effects can also be neglected. [17]

Due to the massive simplification involved, many phenomena are impossible to describe using only the ideal MHD model. Physical aspects such as electromagnetic waves propagation, resonance particle effects, radiation, transport, additional external heating, nuclear reactions and α-particle behaviour, ionization and recombination and a wide range of instabilities are out of the ideal MHD horizon. Nevertheless, the ideal MHD equations cannot be solved analytically in most of the cases. So, why are they so widely used? The reason is that the ideal MHD model succeeds in one fundamental task: describing, at a reasonably manageable level of complexity, the effect of a

17 To cite J. Freidberg [83]: *«regarding physics in general, it has been pointed out that the three major discoveries of modern physics during the last century or so, namely (1) Maxwell's equations with the wave propagation, (2) Relativity, (3) Quantum mechanics are each eliminated in the derivation of MHD.»*

given magnetic geometry on the plasma. The most basic conditions that every magnetic confinement device must satisfy are the equilibrium and stability limits set by this description. As J. Freidberg put it in his famous book on the topic [83], ideal MHD is *«the simplest self-consistent model providing a tractable description of magnetic geometry»* . In addition to that, ideal MHD proves to be useful over a range of conditions which is wider than the one granted by the physical assumptions behind its formulation.

Single-fluid MHD model

Now that the main assumptions behind the ideal MHD model have been discussed, we can move on to the equations. The plasma single-fluid equations can be written as:

$$\frac{\partial \rho}{\partial t} + \nabla \cdot (\rho \mathbf{v}) = 0 \tag{32}$$

$$\rho \left(\frac{\partial \mathbf{V}}{\partial t} + \mathbf{V} \cdot \nabla \mathbf{V} \right) = -\nabla p + \mathbf{J} \times \mathbf{B} - \nabla \cdot \mathbf{\Pi} \tag{33}$$

$$\frac{d}{dt} \left(p \rho^{-\gamma} \right) = \frac{2}{3} \rho^{-\gamma} \left[-\nabla \cdot \mathbf{q} - \mathbf{\Pi} : \nabla \mathbf{v} + \eta J^2 \right] \tag{34}$$

which represent, respectively, mass, momentum and energy conservation. In the 2nd equation, $\mathbf{\Pi}$ represents the viscosity stress tensor; the gravitational force has been neglected. In the 3rd equation, $\gamma = 5/3$ (as for a monoatomic gas), $\mathbf{q}$ represents the heat flux and η is the plasma resistivity.

Ideal MHD

As we said, this fluid model can be further simplified neglecting plasma viscosity and assuming an adiabatic behaviour. Under these assumptions, equations (32)-(34) become:

$$\frac{\partial \rho}{\partial t} + \nabla \cdot (\rho \mathbf{v}) = 0 \tag{35}$$

$$\rho \left(\frac{\partial \mathbf{V}}{\partial t} + \mathbf{V} \cdot \nabla \mathbf{V} \right) = -\nabla p + \mathbf{J} \times \mathbf{B} \tag{36}$$

$$\frac{d}{dt} \left(p \rho^{-\gamma} \right) = 0 \tag{37}$$

The reader may point out that, since the equations above have been obtained starting from a 2-fluid model, some more pieces of information must be available. In particular, these are the charge conservation law:

$$\nabla \cdot \mathbf{J} = 0 \tag{38}$$

and the Ohm's law, which is usually written in the simplified form:

$$\mathbf{E} + \boldsymbol{v} \times \mathbf{B} = \eta \mathbf{J} \tag{39}$$

When $\eta = 0$, the model is called ideal MHD, while the case $\eta \neq 0$ is referred to as *resistive* MHD model.

The equations above must be coupled with the low frequency Maxwell equations:

$$\nabla \times \mathbf{E} = -\frac{\partial \mathbf{B}}{\partial t} \tag{40}$$

$$\nabla \times \mathbf{B} = \mu_0 \mathbf{J} \tag{41}$$

$$\nabla \cdot \mathbf{B} = 0 \tag{42}$$

Since, as we saw, the characteristic MHD time –which is of the order of $1\mu s$– is much smaller than the length of a typical plasma discharge, the latter can be assumed to evolve through a series of equilibrium states. If the external fields and plasma current and pressure are given, steady-state MHD equations can be solved repeatedly to calculate the evolution of the magnetic geometry of the system. In this frame, the ideal MHD model described above is further simplified in order to describe a stationary plasma equilibrium, i. e. $\partial/\partial t = 0$ and $\boldsymbol{v} = 0$. The MHD equilibrium equations read:

MHD equilibrium

$$\nabla p = \mathbf{J} \times \mathbf{B} \tag{43}$$

$$\nabla \times \mathbf{B} = \mu_0 \mathbf{J} \tag{44}$$

$$\nabla \cdot \mathbf{B} = 0 \tag{45}$$

The main properties of this description will be discussed in chapter 3.

2.3 TOKAMAKS

As it was already mentioned in the previous chapter, the tokamak (Russian abbreviation for *toroidal'naya kamera s magnitnymi katushkami* — toroidal chamber with magnetic coils) is a toroidal magnetic confinement system, invented by the Russian scientists Andrej Sacharov and Igor Tamm in 1950 at the Kurchatov Institute. In a tokamak, the confinement is mainly provided by means of a strong toroidal magnetic field, which can range from a few teslas to a maximum of ~15T.

Bending the field lines into a torus has the main advantage of avoiding particle end-losses. However, the plasma ring would tend to naturally expand, and a purely toroidal field is not enough to provide a balancing force. To achieve an equilibrium configuration, a poloidal field is needed in addition to the toroidal one (see note 6, p. 18). In a tokamak, this poloidal field is obtained by inducing a toroidal current into the plasma. As a consequence, in a tokamak the safety factor $q \approx rB_\phi/R_0B_\theta$ is an increasing function of r, and usually it holds that $q > 1$ over the entire plasma due to the strong toroidal field [77].

To date, the tokamak is the most promising fusion reactor concept, and several experiments exist around the world.

2.3.1 *Main components*

The strong toroidal field needed in a tokamak is produced by means of a set of windings, called Toroidal Field Coils (TFC). The maximum achievable field is limited by two main factors, i. e. the maximum forces that the

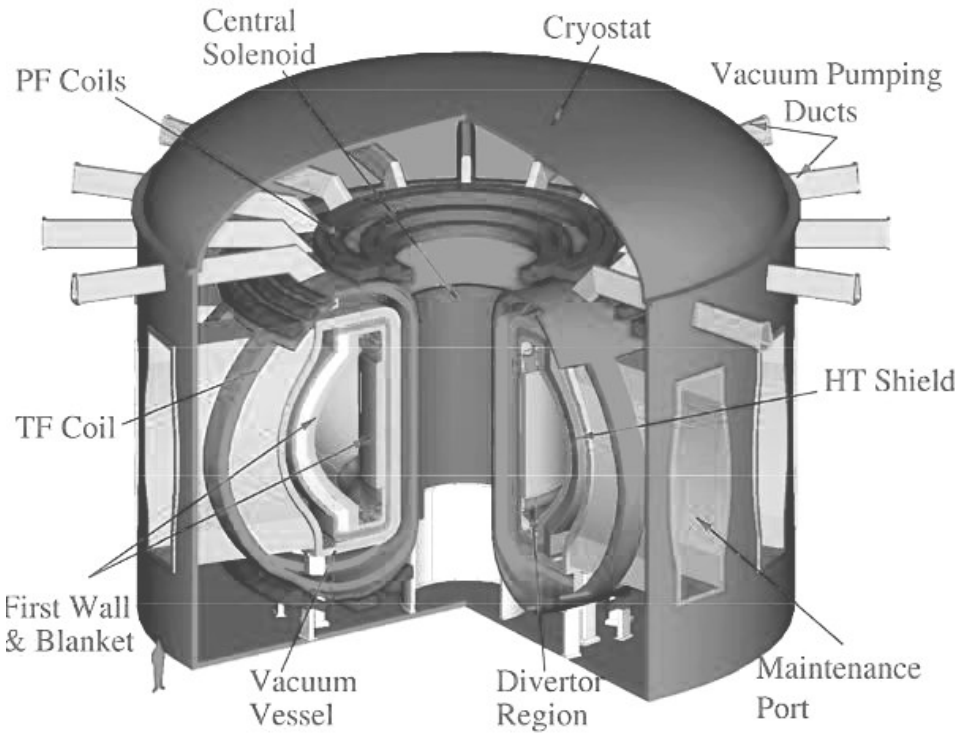

Figure 28: Cutaway of the ARIES-AT tokamak; the main parts are labeled.

coils can bear and the Joule losses. To minimize Joule losses, in particular, superconductive TFC are often adopted in modern devices. [18]

The plasma current needed to produce the poloidal magnetic field is usually induced in the plasma by means of a central primary winding (the Central Solenoid (CS)). To reduce both the required power supply capacity and stray magnetic field lines, the CS often has an iron transformer core (e. g. in JET).

To achieve radial force equilibrium, a vertical field must be supplied by external circuits. Furthermore, it is often desirable to modify the plasma shape to optimize the performances of the machine (for instance, a combination of triangularity and elongation allow higher values of β [77]). Vertical field and shaping circuits (and, in some cases, even the CS) are often col-

18 The need for such a strong field is one of the main disadvantages of the tokamak configuration, due to the technological complications entailed. The other great disadvantage of the tokamak is the intrinsically pulsed operation; a solution could be found in the Advanced Tokamak (AT) concept, based on non-inductive current sources (see 2.3.2.

lected under the common name of PFC, which can be exploited to control the plasma shape and position. Plasma position and shape control algorithms and architectures will be the main focus of this work. Sometimes, further coils are placed inside the vacuum chamber, to provide a faster action on the plasma thanks to the lower magnetic field penetration time; these coils are usually made of copper alloys, since superconductors could not be cooled efficiently enough close to the hot plasma. These are usually referred to as In-Vessel coils, and are often employed to vertically stabilize elongated plasmas.

Using only ohmic heating, plasma temperatures of a few keVs can be achieved. Since plasma conductivity scales as $\sigma \propto T^{3/2}$ [56], Joule losses in the plasma become weaker and weaker as the temperature rises, and thus additional heathing methods are needed in order to reach $T \approx 10keV$. NBIs and RF heating are the main techniques used to address this issue.

In a tokamak, plasma has a very low density, of about 10^{20} particles per cubic meter. To mantain such a low pressure, the plasma is contained inside a vacuum vessel. Impurities in the plasma lead to radiation losses and confinement degradation, thus plasma dilution must be avoided at all costs; for this reason, plasma must be separated from the vacuum chamber walls. Furthermore, the massive heat loads produced by a fusion plasma must be handled appropriately. Both these issues are usually addressed in two main ways: the first is to use a suitable material in the region where the plasma hits the first wall, which constitutes the so called *limiter*; the second is to adopt a magnetic configuration in which the main plasma is separated from the vessel walls. In the second case, the power exhaust is concentrated on a region of the chamber which is called *divertor*.

Finally, in a proper reactor, many other components will be needed, such as diagnostics, vacuum pumps, a cryostat for the superconductive coils, and so on. Among these, a blanket (made of Lithium composites such as Li_2O) capable of slowing down the produced neutrons and breeding tritium is

fundamental. Since not all of the produced neutrons react with the Lithium in the blanket, a neutron multiplier will also be necessary (e. g. Beryllium).

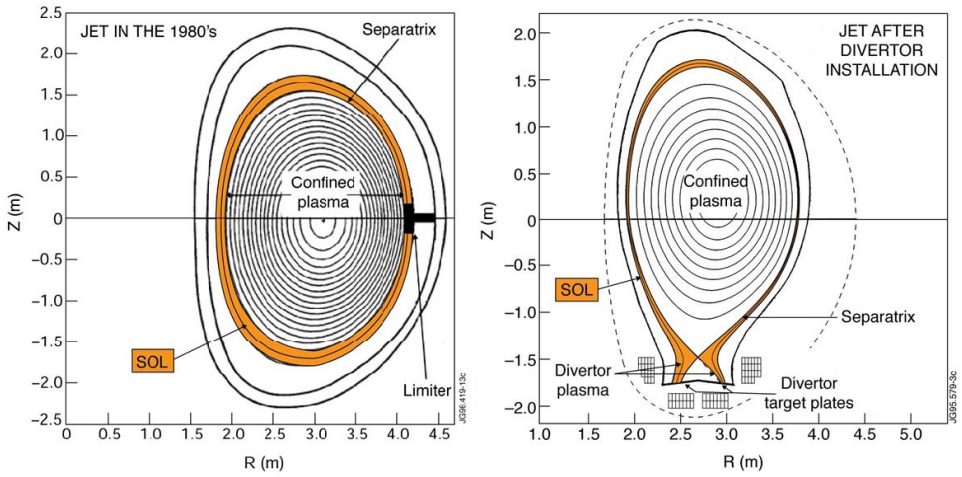

Figure 29: Limiter and divertor plasmas at JET.

2.3.2 *Tokamak operation*

A tokamak is an intrinsically pulsed device. In a typical *scenario*, 5 main phases can be distinguished:

1. *premagnetization*, during which the external coils current increase to a pre-determined value
2. the *breakdown*, in which the plasma is formed, usually inducing a strong electric field in the neutral gas with a fast variation of the CS currents
3. the *ramp-up*, during which the plasma current is increased to a desired value
4. the *flat-top*, during which the plasma current is kept constant
5. the *ramp-down*, during which the plasma current decreases and eventually the plasma dies.

Broadly speaking, designing a tokamak scenario consists in characterizing all of the above mentioned phases, and choosing the appropriate plasma parameters and the external currents to be applied so as to obtain the desired behaviour without meeting operational limits.

Pulsed operation is due to the limited currents that can flow in the external coils. To sustain the plasma current against the resistivity losses, the currents in the external coils (in particular in the CS) have to ramp to induce a desired emf into the plasma. This is one of the main disadvantages of the tokamak configuration, for two main reasons: first, it is ostensibly not desirable for an electrical power station; second, pulsed operation causes thermal fatigue and increases the risks of faults and damages to the machine. To achieve steady state operation, non-inductive current drive sources are hence needed. A possibility is to exploit the transport-induced *bootstrap current*, which arises spontaneously from the non-uniformity of the magnetic field in toroidal geometry and can virtually make up for the 95% of the total current [78]. In practice, for AT operation, a mix of ~75% bootstrap and ~25% external current drive sources -such as NBIs or Radio-Frequency CD- is foreseen [77].

Part II

PLASMA MODELLING AND CONTROL

3

PLASMA MODELLING

"Everything should be made as simple as possible, but not simpler."

— Albert Einstein

In chapter 2 some basic aspects of nuclear fusion and plasma physics have been covered, and the tokamak geometry for magnetic confinement has been presented in its main components. In this chapter, we will move on to introduce plasma electromagnetic modelling and control techniques. The first step consists thus in specializing the MHD equilibrium condition to the case of a tokamak configuration [85–87].

3.1 PLASMA EQUILIBRIUM IN AXISYMMETRIC GEOMETRY

As John Wesson put it [78], tokamak equilibrium consists of two main aspects:

1. the internal balance between the kinetic and magnetic pressure
2. the position and shape of the plasma, determined by the currents flowing in the external coils

As it was discussed in section 2.3, the toroidal field is primarily generated by the TFC system; due to the toroidal geometry, this field is proportional to the inverse of the radius. This simple estimate can be refined by taking into account the diamagnetic effect of the plasma and the ripple due to the non-uniformity of the TFCs along the torus. However, for our purposes it will often suffice to assume that B_ϕ is assigned. Indeed, it will be discussed

how -although in a different form- it will enter as a source term in the equilibrium equation that we are about to derive from (43)-(45).

It is common practice, to simplify the numerical calculations needed to solve the MHD equations, to approximate the tokamak as a perfectly axysimmetric device and to assume a cylindrical set of coordinates (r, z, ϕ). Under this axisymmetry hypothesis, any dependence on the toroidal coordinate ϕ is neglected (i. e. $\partial A/\partial\phi = 0$ for every physical quantity A)[1].

To investigate the equilibrium configurations of the magnetic field, let us start with the definition of the useful *poloidal flux* function $\Psi(r, z)$, i. e. the magnetic flux through the surface enclosed by a circumference $\Gamma(r, z)$ which is coaxial with the torus and passes through the point (r,z) in the poloidal plane. From the definition of Ψ and the divergence-free condition for **B** (eq. (45)), it follows that:

Poloidal flux function

$$\nabla\Psi = 2\pi(rB_z, -rB_r) \tag{46}$$

In the exact same way, a *poloidal current* function $I_{pol}(r, z)$ can be defined, which satisfies (we assumed $\mu = \mu_0$ in the plasma):

Poloidal current function

$$\mu_0 I_{pol} = 2\pi r B_\phi \tag{47}$$

$$\nabla I_{pol} = 2\pi(rJ_z, -rJ_r) \tag{48}$$

1 This is quite a strong hypothesis, since a tokamak is not axially symmetric for many reasons, but it greatly simplifies the analysis and is sufficiently well verified to prove extremely useful in many cases. Methods to couple an axysimmetric plasma with 3D non-axisymmetric surrounding structures have been proposed e. g. in [88, 89].

(eq. (47) comes straightforwardly from Ampère's law). Defining $\psi = \Psi/2\pi$[2] and $f = \mu_0 I_{pol}/2\pi = rB_\phi$[3], equations (46) and (48) can be rewritten as:

$$\nabla\psi = (rB_z, -rB_r) \tag{49}$$

$$\nabla(f/\mu_0) = (rJ_z, -rJ_r) \tag{50}$$

Eq. (49) and (50) allow us to write the poloidal magnetic field and current as

$$\mathbf{B} = \frac{\nabla\psi}{r} \times \hat{e}_\phi + B_\phi \hat{e}_\phi \tag{51}$$

$$\mathbf{J} = \frac{\nabla(f/\mu_0)}{r} \times \hat{e}_\phi + J_\phi \hat{e}_\phi \tag{52}$$

The magnetic field is hence perpendicular to the poloidal flux gradient, which means that the magnetic field lines lie on the surfaces where ψ is constant (whose topology is described by the Grad-Shafranov equation, as we will see shortly). The twist of the field lines on these magnetic surfaces can be characterized by means of the safety factor q introduced in sec. 2.3[4].

2 $\psi = \Psi/2\pi$ is usually referred to as 'poloidal flux per radian', to distinguish it from the poloidal flux function Ψ. However, since we will most often deal with ψ, for brevity the name 'poloidal flux' will be used for ψ.

3 Often, in the literature, the function f is defined without the factor μ_0. However, the present definition proves to be useful when materials with $\mu \neq \mu_0$ are considered, i. e. the ferromagnetic core at the JET tokamak.

4 See also p. 18.

At this point, it is worth to briefly focus on the MHD equilibrium condition $\nabla p = \mathbf{J} \times \mathbf{B}$ (eq. (43)) [5]. From this condition, it immediately follows that:

$$\mathbf{B} \cdot \nabla p = 0 \tag{53}$$

$$\mathbf{J} \cdot \nabla p = 0 \tag{54}$$

Eq. (53) implies that p does not vary along the field lines, and hence the magnetic surfaces are also surfaces of constant pressure. A physical explanation for this can be found observing that the sound speed in a plasma is quite large ($10^5 - 10^6 ms^{-1}$ [78]), thus any pressure imbalance along a field line is rapidly removed. From eq. (54) it follows that also the $\mathbf{J}$ lines lie on the magnetic surfaces. Since p is constant on a surface of constant ψ, it can be expressed (at least locally) as a function $p = p(\psi)$ of the poloidal flux. In a similar way, from equations (50)-(54), it can be found that $\nabla f \times \nabla p = 0$, and thus f can be expressed as a function $f = f(\psi)$ of the poloidal flux as well.

5 It is maybe worth to stress again that, by assuming an equilibrium condition, plasma inertia has been neglected. This can be justified from a physical point of view by the observation that, in a tokamak plasma, the mass density is usually very small(of the order of 10^{-20} particles per cubic meter, i. e. $\sim 10^{-4} g m^{-3}$), while the force density is quite large (a few tonnes per m^{-3}), so in practice it can be assumed that the internal forces must balance. Plasma pressure exerts an outward force, while an inner contribution comes from the poloidal field; the imbalance between the two is taken up by the toroidal field magnetic pressure.
By using Ampère's law (eq. (41)) to eliminate $\mathbf{J}$ and the vector identity:

$$\nabla(\mathbf{F} \cdot \mathbf{G}) = (\mathbf{F} \cdot \nabla)\mathbf{G} + \mathbf{F} \times (\nabla \times \mathbf{G}) + (\mathbf{G} \cdot \nabla)\mathbf{F} + \mathbf{G} \times (\nabla \times \mathbf{F})$$

with $\mathbf{F} = \mathbf{G} = \mathbf{B}$, the $\mathbf{J} \times \mathbf{B}$ term can further be separated in two contributions:

$$\nabla \left(p + \underbrace{\frac{B^2}{2\mu_0}}_{\text{MP}} \right) = \underbrace{\frac{1}{\mu_0} (\mathbf{B} \cdot \nabla) \mathbf{B}}_{\text{MTF}}$$

The former of the two terms represent the magnetic pressure (MP), while the latter is the magnetic tension force (MTF), i. e. the force exerted on the plasma from the magnetic field due to its curvature. It can be rewritten as $\frac{B^2}{\mu_0} \kappa$, where $\kappa = \hat{\mathbf{b}} \cdot \nabla \hat{\mathbf{b}}$ is the magnetic field curvature vector. See [77] for some insightful examples.

Using equations (51)-(52), the force balance condition can be rewritten as:

$$\begin{aligned}\nabla p &= \mathbf{J}_p \times \hat{e}_\phi B_\phi + \hat{e}_\phi J_\phi \times \mathbf{B}_p \\ &= \frac{1}{r}\left(\nabla f \times \hat{e}_\phi\right) \times \hat{e}_\phi B_\phi + \hat{e}_\phi J_\phi \times \frac{1}{r}\left(\nabla\psi \times \hat{e}_\phi\right) \\ &= -\frac{B_\phi}{r}\nabla f + \frac{J_\phi}{r}\nabla\psi\end{aligned}$$

Since:

$$f = f(\psi) \quad \Rightarrow \quad \nabla f = \frac{df}{d\psi}\nabla\psi = f'\nabla\psi$$

$$p = p(\psi) \quad \Rightarrow \quad \nabla p = \frac{dp}{d\psi}\nabla\psi = p'\nabla\psi$$

the toroidal current component can be expressed as:

$$\begin{aligned}J_\phi &= r\frac{dp}{d\psi} + B_\phi\frac{d(f/\mu_0)}{d\psi} \\ &= rp'(\psi) + \frac{1}{\mu_0 r}f(\psi)f'(\psi)\end{aligned}$$

Plugging the above expression into the toroidal component of Ampére's law (eq. (44)):

$$\begin{aligned}\mu_0 J_\phi &= \frac{dB_r}{dz} - \frac{dB_z}{dr} \\ &= -\frac{1}{r}\frac{\partial^2\psi}{\partial z^2} - \frac{\partial}{\partial r}\left(\frac{1}{r}\frac{\partial\psi}{\partial r}\right)\end{aligned}$$

we finally obtain the *Grad-Shafranov equation*:

Grad-Shafranov equation

$$r\frac{\partial}{\partial r}\left(\frac{1}{r}\frac{\partial\psi}{\partial r}\right) + \frac{\partial^2\psi}{\partial z^2} = -\left(\mu_0 r^2 p'(\psi) + f(\psi)f'(\psi)\right) \tag{55}$$

This equation admits solutions in terms of nested magnetic surfaces, which allow to define a magnetic axis and a plasma boundary. Usually, the boundary is defined as the Last Closed Flux Surface (LCFS) for limiter plasmas, i. e. the outermost magnetic surface whose lines do not itersect the walls of the

chamber, while for divertor configurations it is identified with the *separatrix* between open and closed field lines (see fig. 31)[6]. Often, to simplify the notation, the elliptic differential Shafranov operator is introduced

$$\Delta^* \psi = r \frac{\partial}{\partial r} \left(\frac{1}{r} \frac{\partial \psi}{\partial r} \right) + \frac{\partial^2 \psi}{\partial z^2}$$

leading to the more compact form

$$\Delta^* \psi = -\mu_0 r J_\phi \tag{56}$$

By choosing appropriately the expression for the source term, eq. (56) can describe all the structures of a tokamak (see fig. 30). I. e. , in the external conductors[7]:

$$\Delta^* \psi = -\mu_0 r J_{ext}(r, z, \phi) \tag{57}$$

while in the vacuum:

$$\Delta^* \psi = 0 \tag{58}$$

Furthermore, to assure that the solution is unique, a set of boundary condition must be assigned. A set of Dirichlet boundary conditions is given by $\psi = 0$ at the $r = 0$ axis (coming from the definition of poloidal flux) plus a regularity condition $\psi \to 0$ at infinity. In addition, it must hold that $\int_{\Omega_P} J_\phi d\Omega = I_p$ (where Ω_P represents the plasma region).

6 Here it is perhaps worth observing that, with this definition, we are implicitly assuming that the plasma is separated by the surrounding vacuum/containing structures by a sharp boundary, the aim of shape control being that of bringing the position and shape of this boundary towards a desired configuration. It holds clear that, in reality, the plasma does not have such a sharp edge, and this is only a conventional definition.

7 For the external active coils, the current density is obtained in general as NI_{ext}/S, where I_{ext} is the current in the conductor, N is the number of turns and S is the cross section. The current flowing in the passive structures, instead, is often neglected when solving the equilibrium equations. However, the passive structures play a fundamental role in the evolutionary MHD problem, as it will be discussed in what follows.

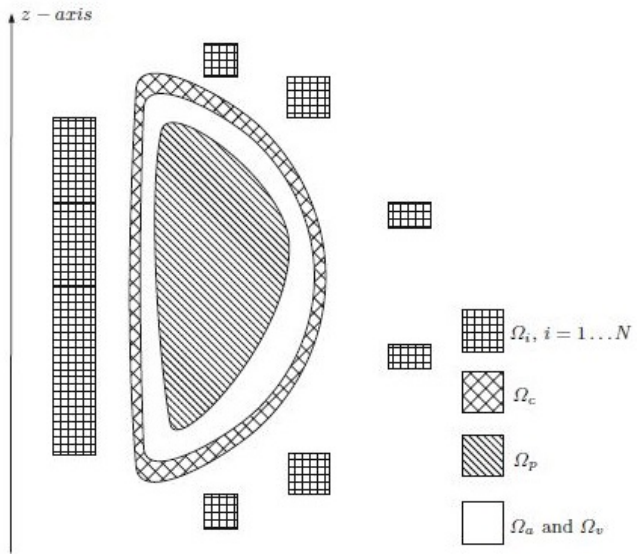

Figure 30: Domain partitioning for the axisymmetric equilibrium problem (the plasma poloidal cross section is denoted by Ω_p, the PFCs by Ω_i, the passive structures by Ω_c, Ω_a and Ω_v represent air and vacuum).

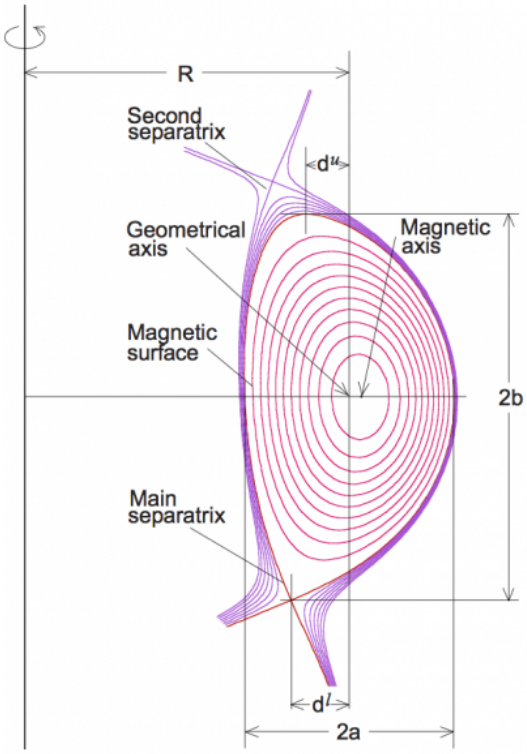

Figure 31: Geometry of the flux surfaces for a divertor configuration).

Evidently, when the plasma is absent the resulting equations are linear. On the other hand, except for trivial choices of the p' and ff' functions -which are not useful for realistic plasma equilibria- and due to the fact that the plasma region boundary depends on the solution itself, the G-S describing a plasma equilibrium equation is strongly non-linear and thus calls for dedicated numerical solution algorithms. Two main problems can be identified:

1. *direct (or forward) equilibrium*: the p' and ff' source terms are assigned together with the currents in the active circuits and the total plasma current. The Grad-Shafranov equation is then solved to find the resulting plasma equilibrium configuration. The solution to the direct problem is useful for prediction or design purposes;

2. *inverse (or backward) equilibrium*: magnetic sensors measurements are available together with a measure of the currents in the active circuits and of the total plasma current. The Grad-Shafranov equation is used as a constraint to find the equilibrium that best fits the experimental data. Usually, for the inverse problem, parameterized forms are used for the p' and ff' profiles (the parameters could be, for instance, the coefficients of a series expansion over a suitable set of basis functions), providing additional degrees of freedom to fit of the available informations[8].

Another distinction can be made between the *stationary* and the *evolutionary* equilibrium problems::

1. the *stationary equilibrium* problem consists in solving the equilibrium equations with assigned plasma current I_p, external currents J_{ext} and plasma profile functions p', ff'.

8 Actually, it is common practice to provide the functions p and ff' in terms of a finite set of parameters even in the forward equilibrium case. See sec. 3.2.1).

2. the *evolutionary equilibrium* problems consists in computing the time evolution of the plasma through a series of equilibrium states (i. e. in the quasi-static approximation). In this view, the functions p', ff' must be provided at every instant t together with initial conditions for the circuits and plasma currents; the evolution of the plasma and external currents is described by the usual circuit equations.

In particular, the solution to the evolutionary MHD equilibrium problem provides the basis for an effective design of the plasma magnetic control system, as it will be discussed briefly in chapter 4 and more extensively in the following parts of this work.

The complexity of the problem and its highly nonlinear nature naturally call for numerical solution methods. A brief overview on the topic will be given in sec. 3.2.

3.2 SOLUTION OF THE PLASMA EQUILIBRIUM PROBLEM

This section deals with the solution to the MHD axisymmetric equilibrium problem. As it is common with partial differential problems, in most cases a closed-form solution to the problem cannot be found, and one must resort to numerical solving methods. Particular emphasis will be put on the choices made for the design of the two codes used in this thesis, namely CREATE-NL [2, 90] and CREATE-L [1].

3.2.1 *Profile functions parameterization*

The first step towards the solution to the problem stated in sec. 3.1 is to quantify the source terms appearing in the Grad-Shafranov equation. The

most general parameterized form of the p' and ff' functions can be written as

$$p' = g_P(\psi; \alpha_P)$$

$$ff' = g_F(\psi; \alpha_F)$$

where g_P and g_F are functions of the poloidal flux ψ and of a chosen set of parameters α_P or α_F; these function are chosen according the guiding criterion of describing the widest possible range of realistic plasma equilibria while preserving the possibility of univocally determine the parameters from the available measurements. The parameters are identified -in the case of the inverse equilibrium reconstruction problem- to obtain a best fit of the available measurements, in general obtained via a possibly nonlinear optimization procedure (e. g. as it is done at ASDEX when the interpretative code CLISTE runs in Slow Mode [91]). However, this approach is in general too slow for real-time equilibrium reconstruction. For this reason, parameterizations of p' and ff' in terms of linear combinations of basis functions depending only on ψ are usually preferred [85, 86, 91], leading to a linear regression form of the problem.

Usually, for what concerns control design purposes, an extremely accurate description of these functions is not needed. Moreover, detailed informations about the current density profile are difficult to obtain starting from external magnetic measurements. Finally, in this case a fast execution is a much more desirable characteristic, from the engineering point of view, than a high degree of accuracy, since the final purpose is that of designing a magnetic control system, which should be robust against parameter variations. Indeed, it will be discussed how that the variations of the source term can be trated as external disturbances. In this view, a simple parame-

terization of the source term $J_\phi = rp' + \frac{1}{\mu_0 r} ff'$ is again chosen. A possibility is [92]

$$J_\phi = \lambda \left[\beta_0 \frac{r}{R_0} + (1 - \beta_0) \frac{R_0}{r} \right] j(\bar{\psi}, \alpha_m, \alpha_n) \tag{59}$$

where $\bar{\psi} = (\psi - \psi_a)/(\psi_b - \psi_a)$ represents a normalized flux, ψ_a and ψ_b are the poloidal flux per radian at the magnetic axis and at the boundary respectively, j is a suitable function and R_0 is a reference length, usually the major radius of the vacuum chamber. This choice has the advantage of depending on a very small number of parameters (i. e. λ, β_0, α_m and α_n) once the function $j(\bar{\psi}, \alpha_m, \alpha_n)$ has been chosen. These parameters can be related to the physical quantities I_p, β_p, l_i and q_0 (i. e. plasma current, poloidal beta, normalized internal inductance and safety factor at the magnetic axis)[9]. The choice made in the CREATE-L code [1] is

$$j = (1 - \bar{\psi}^{\alpha_m})^{\alpha_n}$$

With this choice, the current density at the plasma boundary is automatically zero, I_p is mainly related to λ, β_0 can be linked to β_p and l_i and the safety factor depends on the values of the α_m, α_n parameters. Indeed, λ can be seen as a normalization factor in the equation

$$I_p = \int_{\Omega_p} J_\phi \, d\Omega$$

9 I_p, β_p, l_i can be obtained from external magnetic measurements. In particular, I_p can be obtained directly from a Rogowski loop, or from magnetic field measurements via Ampère's law, while for plasmas with high aspect ratio and circular cross section the sum $\beta_p + l_i/2$ can be computed [93]. Furthermore, β_p and l_i can be separated when the circularity and high aspect ration hypotheses are dropped (see, for example, [92]). Additional informations can be obtained when non-magnetic diagnostics are also used. For a brief historical overview of the problem and more references on the argument, see [94].

while l_i, defined as [10]

$$l_i = \frac{\langle B_p^2 \rangle_{V_P}}{B_p^2(a)}$$

is a measure of the "peakedness"[11] of the profile [92]. Finally, β_p is an adaptation of the β parameter introduced in equations (30)-(31), and is defined as[12]

$$\beta_p = \frac{\langle p \rangle_{V_P}}{\langle B_p^2 \rangle / 2\mu_0}$$

A further simplifications is obtained by considering only three linear combinations of these parameters, neglecting the influence of q_0 on the plasma-external currents interactions. The core idea (as we will discuss in sec. 3.3) is to consider the variations of poloidal beta and internal inductance as external disturbances. For this reason, the parameters α_m, α_n and β_0 are assumed to be constant during the plasma discharge. However, while the toroidal current density is held fixed, the total plasma current may vary, since the evolution of λ is linked to Ohm's law in the plasma region. For this reason, the toroidal current density profile variations are not taken into account in a self-consistent way; however, this is acceptable when dealing with slow changes due to the external currents [1].

10 The internal inductance is defined as the part of the inductance obtained integrating over the plasma volume

$$\frac{1}{2} L_i I_p^2 = \int_{V_P} \frac{B^2}{2\mu_0} d\mathbf{r}$$

The definition of l_i follows by observing that only the poloidal component of the magnetic field B_P is significant in this definition.

11 From the Grad-Shafranov equation, it is clear that the distribution of the magnetic poloidal field is due to the toroidal current density distribution. If this current is driven by an electric field (i. e. in ohmic plasma discharges), the current profile can be assumed to be peaked in the center, since conductivity is proportional to $T^{3/2}$ [56] and the plasma is hotter in the core region. More complicated profiles prove useful in the case of non-inductive current drive sources, especially if these are used to achieve AT scenarios (where internal transport barriers are present, which can be linked to steep pressure gradients at the plasma edge).

12 Actually, different definitions exist in the community for β_p and l_i; see sec. 6.4.2.

A final remark before moving on to discuss the numerical solution to the MHD equilibrium problem. We discussed how J_ϕ is completely characterized, in the plasma region, by the three parameters I_p, β_p, l_i. On the other hand, the toroidal current density in the external conductors is known once that the total currents flowing into the circuits have been assigned. Thus, if the two vectors $\mathbf{x} = (I_1, I_2, ..., I_p)^T$ and $\mathbf{w} = (\alpha_m, \alpha_n, \beta_0)^T$ are assigned, the flux distribution can be computed together with the quantities $\mathbf{q} = (\psi_a, \psi_b, \lambda)$. In this view, $\mathbf{x}$ and $\mathbf{w}$ can be regarded as state variables. This will be useful when the linearized equations for the evolutionary MHD model will be recast into a standard state-space form. Furthermore, as we said, we will focus on the $\mathbf{x}$ vector, treating the variations of $\mathbf{s}$ as external disturbances (whose evolution in time will thus be assumed to be known *a priori*).

3.2.2 *FEM approach*

We saw that the MHD axisymmetric equilibrium can be described by means of the equation

$$L\psi = f(\psi) \tag{60}$$

where

$$L\psi := -\frac{\Delta^*\psi}{r^2} = \nabla \cdot \left(\frac{\nabla\psi}{r^2}\right)$$

is an elliptic differential operator[13] and

$$f := \frac{\mu_0 J_\phi}{r}$$

13 As before, we assumed $\mu_r = 1$ for simplicity. The argument can be extended straightforwardly to the case $\mu_r \neq 1$.

whose expression depends on the considered spatial region. For the active external conductors (again, N represents the number of turns of the conductor, I the current per turn, S the cross section)

$$J_\phi = \frac{NI}{S}$$

while, inside the plasma

$$J_\phi = \lambda \left[\beta_0 \frac{r}{R_0} + (1 - \beta_0) \frac{R_0}{r} \right] (1 - \bar{\psi}^{\alpha_m})^{\alpha_n}$$

The boundary conditions are given by $\psi = 0$ at $r = 0$ and $r \to \infty$ (the second one, in particular, can be approximated by assuming $\psi = 0$ for r "large enough", leading to zero Dirichlet boundary conditions).

A possibility to solve this set of equations is to use a FEM, which allows to turn the considered differential problem into a set of algebraic equations (if starting from a steady-state problem) or Ordinary Differential Equations (if the original problem has a dependence on time). In the second case, the obtained set of equations can then be solved by means a numerical integration scheme (e. g. forward or backward Euler, Crank-Nicholson, Runge-Kutta, etc.). Linearity is preserved, in the sense that the obtained set of equations (algebraic or ODEs) will be linear or not depending on the nature of the original problem. In the case under exam, as it was discussed in sec. 3.1, the problem is highly nonlinear and thus needs dedicated solving methods, the most common being Picard or Newton-Raphson iterations (the latter is the one adopted by CREATE-NL and CREATE-L). This section is intended to give a brief and not rigorous overview of the FEM formulation in order to discuss its benefits and drawbacks. The details are beyond the purpose of this work; interested readers are referred to the classic text [95].

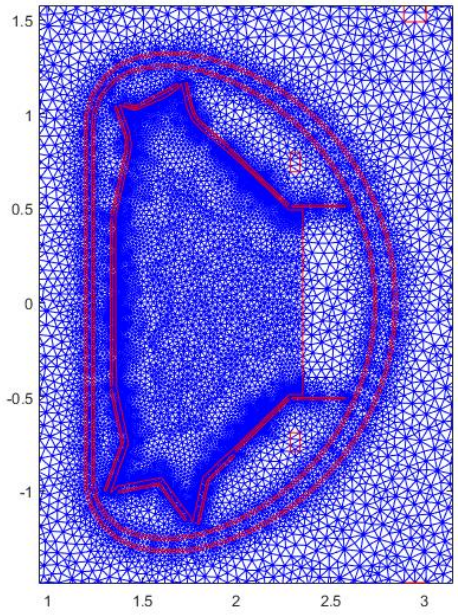

Figure 32: Detail of a FEM mesh for the EAST tokamak.

First, the domain is divided into smaller subdomains (e. g. conductors, passive structures[14], vacuum, plasma, each characterized by different physical properties). Second, each of this regions is further subdivided into finite elements (in our case triangular elements, see figs. 32-33). A set of shape functions $\{v_i\}$ is then chosen (the function v_i is associated to the i-th node of the mesh). These functions are often piecewise polynomials (of 1^{st} and 2^{nd} order in the case of CREATE-L and CREATE-NL respectively), chosen in such a way that each is equal to one in the corresponding i-th node and zero in the adjacent ones (see fig. 33).

14 In what follows, a lumped parameter approach is used for the conducting walls of the machine, which are discretized into a finite number of axisymmetric circuits. The sources of non-axisymmetry (such as ports, tiles, etc.) are usually taken into account using an equivalent section or equivalent parameters for the circuit. See for example [96] for an equivalent axisymmetric description of the iron core of the JET tokamak, an eight-limbed magnetic circuit far from being axisymmetric (see fig. 22).

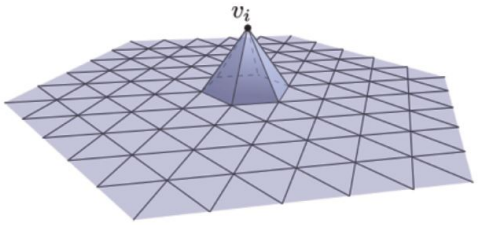

Figure 33: A 1^{st} order finite element over a triangular mesh.

We can recast the differential problem (60) in a so called *weak form* by multiplying both sides of the equation times a test function $u \in H$ and integrating over the domain (this is equivalent to taking the L^2 scalar product $\langle \cdot, u \rangle$):

$$\int\int_\Omega L\psi \, u d\Omega = \int\int_\Omega f \, u d\Omega \tag{61}$$

Integrating by parts, we can move one derivative from the unknown solution to the test function

$$\int\int_\Omega -\left[\nabla \cdot \left(\frac{\nabla\psi}{r^2}\right)\right] u d\Omega = -\oint_{\partial\Omega} \frac{u}{r^2} \nabla\psi \cdot d\mathbf{S} + \int\int_\Omega \frac{\nabla\psi \cdot \nabla u}{r^2} d\Omega$$

In the simple case of zero Dirichlet boundary conditions, we can assume $u, \psi = 0$ on $\partial\Omega$. The surface term in the previous equation vanishes, and a *weak formulation* of eq. (61) is obtained

Weak formulation

$$\int\int_\Omega \frac{\nabla\psi \cdot \nabla u}{r^2} = \int\int_\Omega f \, u d\Omega \tag{62}$$

A *weak solution* to our problem will be a function ψ which satisfies eq. (62) $\forall u \in H$.

The core idea is to set the problem in a Hilbert space[15] (let us call it H), where a scalar product is defined (usually the L^2 product). If we consider a basis $\{\varphi_i\}_{i\in\mathbb{N}}$ for this space H, and denote the scalar product by $\langle \cdot, \cdot \rangle$, we can

15 In particular, ψ and u are supposed to be in the Sobolev space $H_0^1(\Omega)$, while $J_\phi \in L^2(\Omega)$.

decompose any function $h \in H$ into a linear combination of base functions. In particular, it holds

$$\psi = \sum_{i \in \mathbb{N}} \psi_i \varphi_i \qquad\qquad \psi_i = \langle \psi, \varphi_i \rangle$$

Moreover, the condition $\langle L\psi, u \rangle = \langle f, u \rangle \ \forall u \in H$ can be rewritten as $\langle L\psi, \varphi_j \rangle = \langle f, \varphi_j \rangle \ \forall \varphi_j$, since any function $u \in H$ can be written as a linear combination of elements of the base. Hence, the problem becomes

$$\sum_i \psi_i \int\int_\Omega \frac{\nabla \varphi_i \cdot \nabla \varphi_j}{r^2} d\Omega = \int\int_\Omega f \varphi_j d\Omega =: f_j$$

If we approximate the basis $\{\varphi_i\}_{i \in \mathbb{N}}$ with a finite set of functions, we obtain the set of algebraic equations

$$A\boldsymbol{\psi} = \mathbf{f} \tag{63}$$

where $\boldsymbol{\psi}$ is a vector containing the unknown coefficients ψ_i (which represent the value of ψ at the i-th node if linear lagrangian elements are considered), $\mathbf{f}(\psi)$ is a vector containing the terms $\langle f, \varphi_j \rangle$ (which are known if the toroidal current density profile is assigned) and A is the *stiffness matrix* associated to the problem, which in this case is defined by

$$A_{i,j} = \int\int_\Omega \frac{\nabla \varphi_i \cdot \nabla \varphi_j}{r^2} d\Omega$$

The last step is to chose as a base the set of shape functions $\{v_i\}$ defined over the mesh (usually, this set tends to a complete base when the size of the element tends to zero).

As it was already discussed, eq. (63) is nonlinear, and in general has to be solved by iterative procedures (i. e. Newton-Raphson iterations in both CREATE-L and CREATE-NL).

The main advantages of the FEM formulation are the possibility of dealing with complicated geometries and materials with different characteristics, the capability of capturing local phenomena, a good degree of accuracy and the possibility of obtaining an estimate of the error. On the other hand, they require long computation times; furthermore, the geometry of the separatrix is not accurate close to the X-point (which is necessarily a node, which means that the elements must be very small near to the null point) and the accuracy can be poor when the toroidal current density has steep gradients or discontinuities.

3.3 LINEARIZATION

Now that we have a complete formulation of the stationary MHD equilibrium problem under the axisymmetry hypothesis and we know how to solve the equations once that the source terms have been specified, the next step is to move on to discuss the evolutionary equilibrium problem. In particular, our final aim is to obtain a canonical state-space form describing the time evolution of the tokamak system by exploiting a linearization procedure around the considered equilibrium.

The differential operator Δ^* can be characterized in terms of its *free space Green function* $G_0(r,z)$, i. e. the distribution which satisfies

$$\Delta^* G_0(\mathbf{r},\mathbf{r}') = -\mu_0 r \delta(\mathbf{r}-\mathbf{r}')$$

and the boundary conditions

$$\lim_{\mathbf{r}\to\infty} G_0(\mathbf{r},\mathbf{r}') = 0 \quad \text{if} \quad \|\mathbf{r}'\| < M \in \mathbb{R}$$

$$\lim_{\mathbf{r}\to\mathbf{0}} G_0(\mathbf{r},\mathbf{r}') = 0 \quad \text{if} \quad \|\mathbf{r}'\| > M \in \mathbb{R}-\{0\}$$

where δ is the Dirac's delta and $\mathbf{r} = (r, z)$. An expression for G_0 with a detailed derivation can be found in the appendix of [97]. $G_0(\mathbf{r}, \mathbf{r}')$ represents the poloidal flux produced at the location $\mathbf{r}$ by a filamentary toroidal current passing through the point $\mathbf{r}'$.

We can now write the poloidal flux as

$$\begin{aligned}\psi(\mathbf{r}, t) &= \int_{\mathbb{R}^2} J_\phi(\mathbf{r}', t) G_0(\mathbf{r}, \mathbf{r}') d\mathbf{r}' \\ &= \int_{\Omega_m} J_\phi(\mathbf{r}', t) G_0(\mathbf{r}, \mathbf{r}') d\mathbf{r}' + \int_{\Omega_p} J_\phi(\mathbf{r}', t) G_0(\mathbf{r}, \mathbf{r}') d\mathbf{r}' \\ &= \psi_m(\mathbf{r}, t) + \psi_p(\mathbf{r}, t)\end{aligned}$$

where Ω_m and Ω_p are the poloidal cross sections of the conductive structures (including the PFCs, i. e. the union of Ω_c and Ω_i with $i = 1...N$) and of the plasma respectively.

We can express the induced toroidal electric field using Faraday's law as

$$E_i = -\frac{1}{r}\frac{\partial}{\partial t}\psi$$

The toroidal current density can be expressed as

$$J_\phi = \sigma E_\phi = \sigma(E_i + E_m)$$

where E_m is the toroidal component of the electromotive field supplied to the conductors (which is zero for the passive structures) and σ represents the conductivity. From Ampére's law we obtain

$$2\pi r J_\phi = -2\pi\sigma\frac{\partial}{\partial t}\psi + \sigma V \quad \Rightarrow \quad \frac{1}{\sigma}J_\phi = \frac{1}{r}\frac{\partial}{\partial t}\psi + \frac{1}{2\pi r}V \tag{64}$$

where

$$V = \oint_{\Gamma(\mathbf{r})} \mathbf{E_m} \cdot d\mathbf{l} = \int_0^{2\pi} E_m r d\phi$$

Let us start by considering the contribution from the conducting structures. If V is assumed to be constant in each conductor, we can use the characteristic functions of the associated regions to rewrite it as

$$V(t, \mathbf{r}) = \sum_{i=1}^{N} V_i(t) g_i(\mathbf{r})$$

where N is the number of active external circuits and $g_i(\mathbf{r})$ is 1 inside the i-th conductor cross section and 0 outside.

From the finite element formulation of the problem we can recast the J_ϕ term in the form

$$J_\phi(t, \mathbf{r}) = \sum_{h=1}^{n_c} J_h(t) \nu_i(\mathbf{r})$$

where n_c is the number of shape functions. In particular, we will consider the functions ν_h whose supports cover the region Ω_m.

We obtain

$$\begin{aligned}
\psi_m(\mathbf{r}, t) &= \int_{\Omega_m} J_\phi(\mathbf{r}', t) G_0(\mathbf{r}, \mathbf{r}') d\mathbf{r}' \\
&= \sum_{i=1}^{n_c} J_i(t) \int_{\Omega_m} \nu_h(\mathbf{r}') G_0(\mathbf{r}, \mathbf{r}') d\mathbf{r}' \\
&= \sum_{i=1}^{n_c} J_i(t) \tilde{\nu}_h
\end{aligned}$$

Furthermore, by multiplying eq. (64) by a generic shape function ν_h and integrating over the volume V_m obtained by the rotation of Ω_m around the axis of the torus, we have

$$\int_{V_m} \frac{1}{\sigma} J_\phi d\tau = \int_{V_m} \frac{1}{r} \frac{\partial}{\partial t} \psi d\tau + \int_{V_m} \frac{1}{2\pi r} V d\tau \tag{65}$$

The terms appearing in the above equation can be written as

$$\int_{V_m} \frac{1}{\sigma} J_\phi \nu_h d\tau = \sum_{k=1}^{n_c} J_k(t) \int_{V_m} \frac{\nu_k \nu_h}{\sigma} d\tau = \sum_{k=1}^{n_c} R_{hk} J_k(t) \tag{66}$$

$$\int_{V_m} \frac{1}{r} \frac{\partial}{\partial t} \nu_h \psi d\tau = \sum_{k=1}^{n_c} \dot{J}_k(t) \int_{V_m} \frac{\tilde{\nu}_k \nu_h}{r} d\tau = \sum_{k=1}^{n_c} L_{hk} \dot{J}_k(t) \tag{67}$$

$$\int_{V_m} \frac{1}{2\pi r} V \nu_h \psi d\tau = \frac{1}{2\pi} \sum_{l=1}^{N} V_l \int_{V_m} \frac{g_l \nu_h}{r} d\tau = \sum_{l=1}^{N} S_{hl} V_l \tag{68}$$

(the dot indicates a time derivative).

Putting together equations (65)-(68) we obtain

$$\sum_{k=1}^{n_c} \left[R_{hk} J_k(t) + L_{hk} \dot{J}_k(t) \right] = \sum_{l=1}^{N} S_{hl} V_l$$

or, in matrix form

Plasmaless circuit equations

$$R\mathbf{I}(t) + L\dot{\mathbf{I}}(t) = S\mathbf{V} \tag{69}$$

The equations have the form of the usual circuit equations, where L is the inductance matrix (the element on the diagonal are the self inductances while the off-diagonal ones are the mutual inductances) and R is the (diagonal) resistance matrix. Considering the elements contained in the cross-section of each poloidal conductor and assuming the current distribution in each of the conductors to be constant, eq. (69) can be rewritten in such a way that the terms in the $\mathbf{I}$ vector correspond to the physical currents flowing into the active and passive circuits (see [97]). Generally speaking, the vector $\mathbf{I}$ contains ~100-200 elements, depending on how the passive structures have been discretized. The S matrix, instead, is usually exploited to keep track of the sign between the voltage and the current for each circuit; in what follows, we will assume that it is the identity matrix.

When the effect of the plasma is taken into account, an additional term appears in eq. (69)

$$R\mathbf{I}(t) + L\dot{\mathbf{I}}(t) + \dot{\boldsymbol{\psi}}_{\mathbf{p}} = S\mathbf{V}$$

$\dot{\boldsymbol{\psi}}_{\mathbf{p}}$ is a vector whose elements are

$$\dot{\psi}_p h := 2\pi \int_{\Omega_m} \psi_p \nu_h d\Omega$$

The value of $\dot{\boldsymbol{\psi}}_{\mathbf{p}}$ can be computed solving the nonlinear equilibrium problem presented in sec. 3.1, and will be a function of the external currents (which we indicated with $\mathbf{x}$), the total plasma current I_p and the vector $\mathbf{w} = (\beta_p, l_i)$

$$\dot{\boldsymbol{\psi}}_{\mathbf{p}}(\mathbf{r}, t) = \gamma(\mathbf{r}, \mathbf{x}(t), \mathbf{w}(t), I_p(t))$$

Finally, defining

$$\mathbf{I} = \mathbf{I_0} + \delta\mathbf{I}$$

$$\mathbf{w} = \mathbf{w_0} + \delta\mathbf{w}$$

$$\mathbf{I_p} = \mathbf{I_{p0}} + \delta\mathbf{I_p}$$

$$\mathbf{V} = \mathbf{V_0} + \delta\mathbf{V}$$

(where the subscript 0 refers to the reference equilibrium) a linearized plasma response model can be obtained as

Linearized plasma response

$$\left(L + \left[\frac{\partial}{\partial \mathbf{I}}\gamma\right]_0\right)\delta\dot{\mathbf{I}} + \left[\frac{\partial}{\partial I_p}\gamma\right]_0 \delta\dot{I}_p \left[\frac{\partial}{\partial \mathbf{w}}\gamma\right]_0 \delta\dot{\mathbf{w}} + R\delta\mathbf{I} = S\delta V \tag{70}$$

The final step is to put the model into the standard *state-space* form

$$\delta\dot{\mathbf{x}} = A\delta\mathbf{x} + B\delta\mathbf{u} + E\delta\dot{\mathbf{w}} \tag{71}$$

$$\delta\mathbf{y} = C\delta\mathbf{x} + D\delta\mathbf{u} + F\delta\dot{\mathbf{w}} \tag{72}$$

If we define

$$\delta\mathbf{x} = (\delta\mathbf{I} \quad \delta I_p)^T$$

$$L^* = \left(L + \left[\left[\frac{\partial}{\partial\mathbf{I}}\gamma\right]_0 \left[\frac{\partial}{\partial I_p}\gamma\right]_0\right]\right)$$

$$LE = \left[\frac{\partial}{\partial\mathbf{w}}\gamma\right]_0$$

$$\delta\mathbf{u} = \delta\mathbf{V}$$

Eq. (70) becomes

$$L^*\delta\dot{\mathbf{x}} + R\delta\mathbf{x} + LE\delta\dot{\mathbf{w}} = S\delta\mathbf{u} \tag{73}$$

The state-space equations (71)-(72) can be obtained putting

$$A = -L^{*-1}R$$

$$B = L^{*-1}S$$

$$E = -L^{*-1}LE$$

The C and F matrices can be obtained by perturbing the plasma equilibrium evaluating how the chosen outputs (i. e. plasma centroid, geometrical descriptors of the shape, X-point(s) position, simulated magnetic measurements, etc.) are modified by a variation of one of the state variables. The D matrix is usually the zero matrix. The only difficulty left is that the plasma current variation here appears as an input parameter; however, since it is one of the variables that need to be controlled, a relation between δI_p and

the variation of the other state variables must be established. This can be done, for example, taking into account the conservation of some physical quantity and neglecting the plasma resistance (see [97]).

In practice, the resistance matrix is usually a known parameter, while the inductance matrix L can be computed starting from the geometry of the machine. L^* is a modified inductance matrix that takes into account the effect of the plasma (which is a non-fixed deformable conductor). The S matrix can be subdivided into two blocks, corresponding to the identity matrix (linking the voltages applied to the active circuits to the corresponding currents) and the zero matrix (on the rows corresponding to the passive circuits). It must be kept in mind that, although in principle $\delta\mathbf{w}$ should be part of the system state, our description of the evolution of β_p and l_i is not self-consistent. Thus, their variation will be considered as an exogenous disturbance to be rejected by the control system. Finally, until now we neglected the plasma resistance. An estimate of the overall resistive losses can be obtained by taking into account the flux consumption (i. e. during an experiment with similar plasma conditions). This estimate may take into account also the effect of external current drive sources. Both CREATE-L and CREATE-NL can provide linearized models around a given equilibrium. In particular, CREATE-L exploits an analytical procedure, while the linearization is carried out in a purely numerical way by CREATE-NL. Interested readers are referred to [1, 90] for further details.

4

ELECTROMAGNETIC CONTROL

"Trust is good, control is better."

— Vladimir Ilic Ul'Janov (Lenin)

Broadly speaking, the control problem in a tokamak reactor can be separated into two major aspects: electromagnetic control and kinetic control.

Kinetic control mainly deals with the exploitation of particle feed rates and/or auxiliary heating and current drive systems to modify the plasma internal profiles in terms of density, temperature, pressure, current density. Although some basic problems in kinetic control have been solved (e. g. the control of plasma density, the use of additional heating systems to achieve H-mode, etc.), other are still an open research topic, and become particularly important in view of AT scenarios. However, plasma kinetic control is beyond the purpose of this thesis; an overview on the subject can be found in [98].

On the other hand, electromagnetic control -or just *magnetic control*, as it is often referred to- consists in the exploitation of the PFC system to mantain or modify the plasma current, position and shape. Along with these primary tasks, some additional requirements need to be met, i. e. vertical stabilization in the case of elongated plasmas and an effective control of the currents flowing in the PFCs. Magnetic control is a a core aspect of plasma control, and it has reached a good degree of maturity over the last years. A good overview on the subject can be found in [97].

The main objectives of magnetic control are:

- *Vertical stabilization*: since the first pioneering article by Artsimovich and Shafranov [61] was published in 1972, vertically elongated plas-

mas have been adopted in many fusion devices to improve the achievable performances in terms of MHD stability. However, these plasmas are not vertically stable, posing a limit to the maximum elongation of the plasma. Indeed, it can be shown by simple arguments that they are unstable against $n = 0$ axysimmetric perturbations (i. e. a uniform vertical displacement)[1]. Imagine the plasma as a wire kept in equilibrium by two equally spaced conductors (see fig. 34). The elongated cross section results from the forces exerted by these conductors on the plasma, which pull upwards and downwards respectively. When a small vertical displacement of the plasma is considered, a net vertical force in the same direction of the displacement is produced.

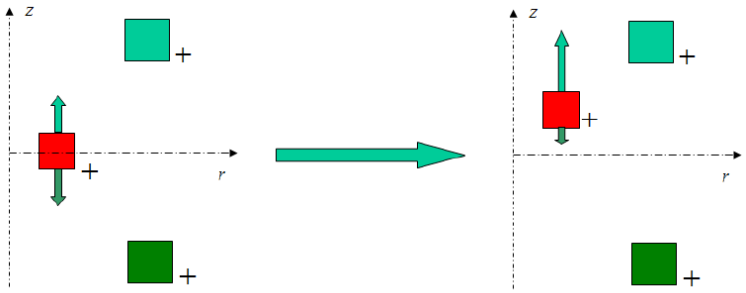

Figure 34: Simplified physical picture of elongated plasmas vertical instability.

In principle, this instability could be eliminated by surrounding the plasma with a perfectly conducting wall. However, in practice resistive walls are only able to slow down the instability[2] (which in this case goes under the name of Resistive Wall Mode (RWM)), and active stabilization methods are necessary. The simplest model of a vertically unstable plasma which can be used for control design is the *rigid displacement model* [99, 100], which is obtained by treating the plasma

1 A more detailed physical picture can be found in [77].

2 Which would be otherwise uncontrollable. As it was discussed at in sec. 3.1, plasma inertia is very small; in fact, the characteristic time scales -usually referred to as Alfvén time- are of the order of $1 - 10\mu s$ for large tokamaks; this allowed us to assume a quasi-stationary evolution of the plasma. The other side of the coin is that the Alfvén time scale is also characteristic of the axisymmetric vertical instability, which is extremely fast in the no-wall limit.

as a filamentary current-carrying wire. However, it was shown [101] that this model leads to uncorrect estimates of the instability growth rate and inaccurate modelling of the magnetic diagnostics used for the stabilization. A more complete description of the vertically unstable plasma can be obtained by means of a perturbed equilibrium approach.

- *Plasma current control*: the ohmic drop of the plasma is compensated by means of ramping currents in the surrounding coils (especially in the CS), which are usually preprogrammed before the discharge. However, plasma resistance may vary during the pulse, due to modifications in plasma conditions (e. g. temperature); furthermore, the switching on of an external current drive during the pulse may result into a reduction of the fraction of inductive plasma current of an amount which may be difficult to estimate *a priori*. For these reasons, a feedback control is necessary to keep the plasma current at the desired value. The plasma current is usually measured by means of a dedicated Rogowski coil [102] or integrating magnetic measurements along the vacuum chamber.

- *Position control*: the position of the plasma centroid is adjusted by means of suitable currents in the PFCs. This is a very basic way of controlling the plasma, often used for circular cross sections or in the early phases of a discharge. The centroid position is often estimated as a linear combination of magnetic diagnostics, which sense the perturbation of the magnetic field due to plasma displacement. The combination of plasma current and position control is often referred to as *RZIp* control.

- *Shape control*: controlling the shape of the LCFS has many benefits. As we said, MHD stability could be improved by an elongated cross section. An accurately shaped LCFS may result into improved confinement of energy and particles [103]. Moreover, sweeping the strike

points position on the divertor plates could spread more evenly the power deposition [104, 105]. The distributed nature of the problem is usually tackled by defining a discrete set of variables to be controlled by means of model-based multivariable techniques. The two main shape control approaches are *gap control*, where the controlled variables are plasma-wall gaps, and *isoflux control*, where the X-point position is controlled and the differences between the poloidal flux at a set of desired boundary points and the flux at the target X-point position are regulated to zero. An additional complication arises due to the fact that the shape of the LCFS cannot be measured directly, and must be estimated by means of reconstruction codes from the available magnetic measurements [85–87].

5

PROPOSAL FOR A PLASMA MAGNETIC CONTROL ARCHITECTURE

"The yielding overcomes the stiff."

— Lao Tzu

In chapter 4 the main problems related to plasma magnetic control were presented. A possible control architecture is shown in fig. 35; the proposed solution contains a dedicated block for each of the control problems listed.

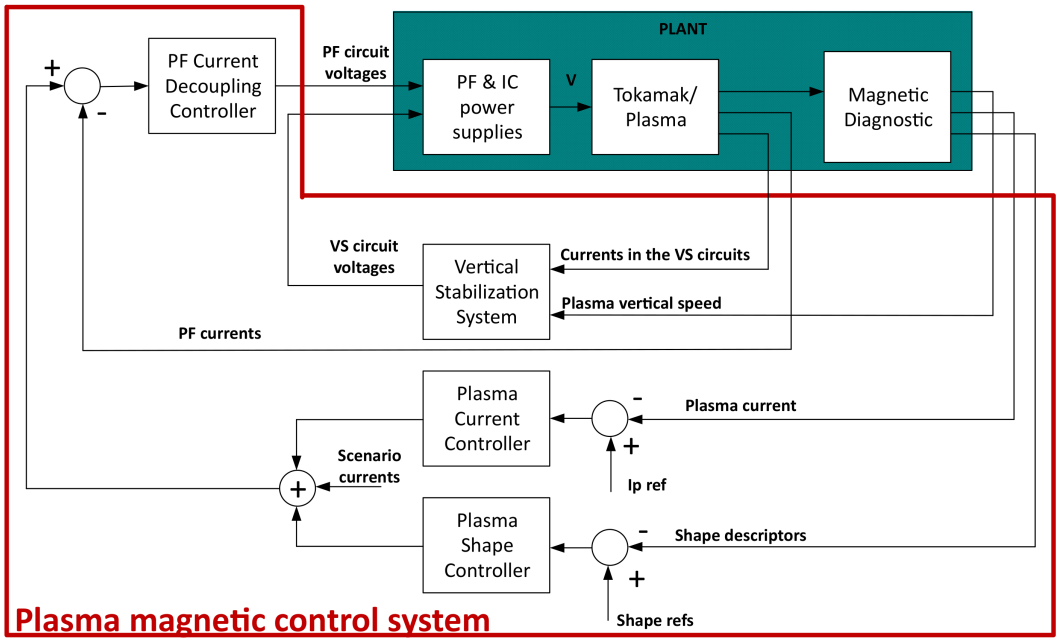

Figure 35: Proposed architecture for the magnetic control system. The main blocks are shown. The scenario currents represent the PF nominal currents (courtesy of prof. G. De Tommasi).

In particular, the proposed control system consists of

- a **Vertical Stabilization System**, which takes care of stabilizing the elongated plasma. In modern tokamaks, this system usually exploits a set of dedicated circuits as actuators, which often includes at least a pair of in-vessel coils. In order to separate the vertical stabilization from the position/shape controller, only the vertical velocity of the plasma is fed back to this system, i. e. the plasma is only stopped by the Vertical Stabilization (VS), while the task of bringing it to its desired vertical position is left to the position/shape control;

- a **PF Current Decoupling Controller**, which constitutes the inner control loop of a nested architecture that includes the plasma current and position/shape controllers as outer loops. This controller takes care of tracking the PFC current references, obtained as the sum of the preprogrammed scenario current and of the corrections computed by the outer loops. This controller is designed in a Multi-Input-Multi-Output (MIMO) fashion, with the aim of decoupling the dynamic response of the PFCs;

- a **Plasma Current Controller**, which tracks the plasma current reference by generating additional requests for the PFC Decoupling Controller;

- a **Plasma Shape Controller**, which controls the shape of the LCFS by generating additional requests for the PFC Decoupling Controller. This block could be replaced by a simpler **Position Controller**, i. e. in the early phases of a discharge.

More details on the control algorithms proposed for each of the main blocks shown in fig. 35 are given in the rest of this chapter.

5.1 VERTICAL STABILIZATION

Generally speaking, the vertical stabilization problem is solved by driving suitable currents into a set of dedicated circuits. Often, in modern devices, these circuits are in-vessel copper coils, which are capable of providing a faster control action since they are not shielded by the conductive structures surrounding the plasma. The current driven in these circuits must produce a radial magnetic field in order to influence the vertical movement of the plasma, so often these coils are connected in anti-series. A general control law for the VS system is given by

$$V_{IC_{ref}}(s) = F_{VS}(s) \cdot (K_V \cdot I_{p_{ref}} \cdot V_c(s) + K_{IC} \cdot I_{IC}(s)) \tag{74}$$

where $V_{IC_{ref}}$ is the voltage request to the in-vessel circuits power supplies, I_{IC} is the current flowing in the in-vessel coil and V_c is the plasma vertical speed. The controller parameters are the *current gain* K_{IC} and the *velocity gain* K_V, along with the transfer function $F_{VS}(s)$, which represents a dynamic compensator (usually a lead network [106, Section 2.6.5]) that can be adjusted so as to improve the controller performances. The K_V gain is multiplied times the plasma current reference $I_{p_{ref}}$ in order to adapt to different plasma conditions (it is assumed that the plasma current controller is capable of tracking its reference with a small steady-state error).

In some cases, additional ex-vessel coils are used in order to satisfy the control requirements. This is true, for example, for the ITER tokamak, where the use of an additional ex-vessel coil is foreseen. In this case, the control law for this coils is chosen as

$$V_{EC}(s) = K_{EC} \cdot I_{IC}(s) \tag{75}$$

It can be seen how the slower ex-vessel coil is used to reduce the current request to the internal coils, which in turn are in charge of controlling the vertical speed of the plasma.

It is worth to remark that the proposed VS system consists of a first order Multi-Input-Single-Output (MISO) controller, whose output is the voltage request to the in-vessel coils. The quite simple structure of this solution opens up the possibility of implementing adaptive algorithms and/or effective noise rejection strategies. The controller can be designed on the basis of the state-space model (71)-(72). Further details on the VS system design will be given in sec. 7.1.

5.2 POLOIDAL FIELD COILS CURRENT CONTROLLER

Usually, the starting point for the design of this controller is a plasma-less model of the device, which can be written in the following form

$$L\dot{x}(t) + Rx(t) = u(t)\,, \tag{76}$$

L and R are the inductance and resistance matrices, $x(t)$ is the state vector, containing the current in the circuits (both active and passive) and $u(t)$ is the input vector, which contains the voltages applied to the circuits (assumed equal to zero for the passive structures; see also sec. 3.3, eq. (69)).

For the design of the controller, a modified version $\widetilde{L}_{PF} \in \mathbb{R}^{n_{PF}} \times \mathbb{R}^{n_{PF}}$ of the inductance matrix is considered, where only the n_{PF} active PF circuits are taken into account, while the effect of the passive structures is neglected. In order to minimize the control effort, in each row of $\widetilde{L}_{PF}$, the mutual inductance terms lower than a given threshold (chosen equal to the 10% of the corresponding circuit self-inductance) are also neglected. In this way, the current in each circuit will be controlled by acting only on the coils which have a stronger coupling to it. This device prevents situations in which a high control effort -which may turn into voltages saturation- is applied to obtain a very low effect on the controlled current, without any practical improvement in the controller performances.

5.2.1 *Proportional control*

Let us start by considering the simple case of a purely proportional controller. Given the time constants τ_{PF_i} for the response of the i-th circuit, we can define the matrix

$$\Lambda = \begin{pmatrix} 1/\tau_{PF1} & 0 & \dots & 0 \\ 0 & 1/\tau_{PF2} & \dots & 0 \\ \dots & \dots & \dots & \dots \\ 0 & 0 & \dots & 1/\tau_{PF_n} \end{pmatrix}$$

Note that, in order to have the same dynamic response on all the PF circuits, the time constants τ_{PF_i} should all be equal to the same value. The voltage requests for the PFC power supplies can be then computed as

Proportional PFC current controller

$$V_{PF}(t) = K_{PF} \cdot \left(I_{PF_{ref}}(t) - I_{PF}(t)\right) + \widetilde{R}_{PF} I_{PF}(t) \tag{77}$$

where $\widetilde{R}_{PF} \in \mathbb{R}^{n_{PF} \times n_{PF}}$ is estimated matrix of the PF circuit resistances, and the control gain matrix K_{PF} is given by

$$K_{PF} = \widetilde{L}_{PF} \cdot \Lambda$$

The estimation of the PFC resistances can be usually performed with good accuracy, which means $\widetilde{R}_{PF} \cong R_{PF}$. Plugging (77) into (76) and assuming $\widetilde{L}_{PF} = L_{PF}$, we obtain the closed loop behaviour

$$\dot{I}_{PF}(t) = \Lambda \cdot \left(I_{PF_{ref}}(t) - I_{PF}(t)\right) .$$

which in terms of error dynamics (if a constant reference is assumed, i. e. $\dot{I}_{PF_{ref}} \cong 0$) means

$$\dot{e}_{PF}(t) = -\Lambda \cdot e_{PF}(t) \tag{78}$$

Since Λ is diagonal, the control law (77) assures the desired decoupling.

It is worth to notice that, if the resistance estimate is accurate, the feed-forward compensation term $\widetilde{R}_{PF} I_{PF}(t)$ allows to treat the behaviour of any coil as that of a superconductor. Furthermore, when the decoupling action provided by the $\widetilde{L}_{PF}$ matrix is taken into account, the dynamic response of the coils becomes that of pure integrators (as it appears clearly from eq. (78)). The possibility of tuning the controller on a simple transfer function such as that of an integrator (i. e. $1/s$) makes the design much easier; furthermore, the extremely simple description of this inner control loop simplifies dramatically the design of the outer ones (as it will be discussed in sec. 5.5).

5.2.2 *PID control*

The architecture proposed in sec. 5.2.1 can be slightly modified in order to provide more flexibility. A diagonal matrix $PID(s)$ containing the parameters of a set of Proportional-Integral-Derivative (PID) controllers can be applied to the PFC current errors, in order to impose a desired dynamic to the controlled circuits. In general, the derivative action is not necessary, i. e.

$$PID(s) = PI(s) = \begin{pmatrix} K_{p,1} + \frac{K_{i,1}}{s} & 0 & \dots & 0 \\ 0 & K_{p,2} + \frac{K_{i,2}}{s} & \dots & 0 \\ \dots & \dots & \dots & \dots \\ 0 & 0 & \dots & K_{p,n_{PF}} + \frac{K_{i,n_{PF}}}{s} \end{pmatrix}$$

The control law becomes

$$V_{PF}(t) = \widetilde{L}_{PF} \cdot PI(s) \cdot \left(I_{PF_{ref}}(t) - I_{PF}(t) \right) + \widetilde{R}_{PF} I_{PF}(t) \tag{79}$$

Another possibility is to implement the control law

$$V_{PF}(t) = diag(\widetilde{L}_{PF}) \cdot PI(s) \cdot \left(I_{PF_{ref}}(t) - I_{PF}(t)\right) + \widetilde{M}_{PF} \cdot \dot{I}_{PF}(t) + \widetilde{R}_{PF} I_{PF}(t) \quad (80)$$

where $diag(\widetilde{L}_{PF})$ is the diagonal matrix containing the PFC self inductances and $\widetilde{M}_{PF} = (\widetilde{L}_{PF} - diag(\widetilde{L}_{PF}))$ contains the off diagonal terms. With this approach, the cross-coupling term in the circuit equation is directly compensated by means of the term $M\dot{I}_{PF}$. This control method has the main disadvantage of needing an evaluation of the time derivative of the PFC currents, which needs a suitable filtering strategy in order to avoid large control voltages due to noisy measurements.

A third possibility, which summarizes the previous two, is to adopt the control law

General PFC current controller with PIDs

$$V_{PF}(s) = G_1 \cdot PI(s) \cdot (I_{PF_{ref}}(s) - I_{PF}(s)) + sG_2 I_{PF}(s) + G_3 I_{PF}(s) \quad (81)$$

By setting

$$G_1 = \widetilde{L}_{PF}\,,\ G_2 = 0\,,\ G_3 = \widetilde{R}_{PF}$$

eq. (79) is recovered, while by setting

$$G_1 = diag(\widetilde{L}_{PF})\,,\ G_2 = \widetilde{M}_{PF}\,,\ G_3 = \widetilde{R}_{PF}$$

we recover eq. (80).

5.3 PLASMA CURRENT CONTROLLER

The Plasma Current Controller is the first of the feedback loops that generate requests to the PFC current controller. It receives as input the plasma current and the corresponding reference waveform, and it computes the PF current deviations needed to obtain the desired I_p.

Let $\mathbf{k}_{p_{curr}} \in \mathbb{R}^{n_{PF}}$ be the vector of PFC currents which causes a unitary flux variation along a closed line containing the foreseen plasma boundary; the elements in $\mathbf{k}_{p_{curr}}$ can be obtained via an optimization procedure based on the plasmaless model (76).

This combination of currents influences the plasma current while keeping the effect on the shape small. For this reason, the elements in $\mathbf{k}_{p_{curr}}$ are often called *transformer currents*. It follows that the $\mathbf{k}_{p_{curr}}$ vector can be used to design a plasma current control algorithm that has a loose coupling with the plasma shape controller. In particular, this objective can be achieved by considering the following Single-Input-Multiple-Output (SIMO) control law

$$\delta I_{PF}(s) = \mathbf{k}_{p_{curr}} \cdot F_{I_p}(s) \cdot (I_{p_{ref}}(s) - I_p(s)) \tag{82}$$

where $F_{I_p}(s)$ is the controller transfer function, which has a Single-Input-Single-Output (SISO) structure. Usually a PID regulator is chosen, the integral action assuring zero steady state error at the flat-top; different choices for $F_{I_p}(s)$ can be considered when special requirements need to be met[1]. If an iron core is present (i. e. as in the JET tokamak), the transformer field is usually obtained by driving the current in the central solenoid, thus the $\mathbf{k}_{p_{curr}}$ becomes a scalar and the control law (82) simplifies to a SISO one [108].

5.4 PLASMA POSITION CONTROLLER

To influence plasma vertical and radial position, radial and vertical fields are needed respectively. A possible approach to plasma position control is to choose linear combinations of currents which provide these two field separately; this proves particularly convenient for up-down symmetric devices.

1 For instance, for ITER it is important to track the reference with zero error also during the ramp-up and ramp-down phases; for this reason, $F_{I_p}(s)$ must be designed with a double integral action [107].

In this way, the vertical and radial position control problems can be naturally decoupled, and simple SIMO controllers can be designed for both the centroid coordinates, in a way similar to what has been discussed in sec. 5.3 for the plasma current. Plasma position can be estimated on the basis on magnetic measurements, hence a reconstruction code is not needed for this kind of control[2].

5.5 PLASMA SHAPE CONTROLLER

From the linearized model output equation (72) it follows that the shape descriptors variations can be linked to the PFC currents variations by the static relation

$$\delta\mathbf{Y}(s) = C\delta\mathbf{I}_{PF}(s)$$

where $\delta\mathbf{Y}(s)$ contains the variations of the n_G shape descriptors (which can include flux differences, gaps, X-point(s) coordinates, etc.). The additional current references to be sent to the PFC current controller can be computed as

$$\delta\mathbf{I}_{PF_{ref}} = C^{\dagger}\delta\mathbf{Y}$$

where $C^{\dagger}$ denotes the pseudo-inverse of the output matrix C. The pseudo-inverse matrix[3] can be computed starting from the Singular Value Decomposition (SVD)

$$C = USV^{T}$$

2 Alternatively, an approach similar to the one proposed in sec. 5.5 could be considered, which may include also the plasma current control.

3 It is good practice to include the row relative to the plasma current in the C matrix when designing the controller and removing the corresponding column from the pseudo-inverse matrix. In this way, the shape controller will be automatically decoupled from the plasma current.

where $U \in \mathbb{R}^{n_G \times n_G}$ and $V \in \mathbb{R}^{n_{PF} \times n_{PF}}$ are two orthogonal matrices $S \in \mathbb{R}^{n_G \times n_{PF}}$ is a diagonal matrix. In particular:

- the columns of U are the *left singular vectors* of C, i. e. the eigenvectors of CC^T;
- the columns of V are the *right singular vectors* of C, i. e. the eigenvectors of C^TC;
- the elements on the diagonal of S are the *singular values* of C, i. e. the eigenvalues of CC^T and C^TC

Two additional diagonal matrices can be introduced to assign different weights to some of the shape descriptors or to some of the actuators

$$\tilde{C} = QCR$$

In this case, the SVD of the $\tilde{C}$ matrix can be considered[4]

$$\tilde{C} = USV^T$$

The proposed algorithm can control up to n_{PF} linear combinations of shape descriptors. However, in principle the number of these descriptors might be greater than the number of available actuators, i. e. $n_G > n_{PF}$. In this case, it can be shown that the controlling to zero the error on the n_{PF} linear combinations $C^\dagger \delta Y$ is equivalent to minimizing the steady-state performance index[5]

$$J_{XSC} = \lim_{t \to +\infty} (\delta \mathbf{Y}_{ref} - \delta \mathbf{Y}(t))^T Q^T Q (\delta \mathbf{Y}_{ref} - \delta \mathbf{Y}(t)) \tag{83}$$

where $\delta \mathbf{Y}_{ref}$ are constant references for the geometrical descriptors. The performance index (83) reduces to the least square error when $Q = \mathbb{I}_{n_G}$.

4 With a slight abuse of notation, we will use the same symbols for the matrices appearing in the SVDs of both C and $\tilde{C}$. The difference will be clear from the context.

5 The argument is the same used to prove that a pseudo-inverse matrix can be used to minimize the mean square error in a linear regression problem.

In order to avoid large control actions, a truncated SVD can be considered by neglecting the singular values which are lower than a given threshold (in a way similar to what has been done for the $\widetilde{L}_{PF}$ matrix in sec. 5.2; see also sec. 7.4.2 for an example).

The argument above holds for the steady-state performance of the controller. For what concerns the dynamic behaviour, when a PFC decoupling controller like the one proposed in sec. 5.2 is considered, the closed loop dynamics of the PFC currents is known

$$\delta I_{PF_i}(s) = G_i(s)\ \delta I_{PF_{ref,i}}(s)$$

where $G_i(s)$ is the closed loop transfer function for the i-th PF coil obtained with the PFC current control. If all of the PFCs' responses are characterized by the same transfer function (i.e. $G_i(s) = G(s) \quad \forall i = 1, \ldots, n_{PF}$), for the shape descriptors it holds that

$$\delta \mathbf{Y}(s) = C\ \delta \mathbf{I}_{PF}(s) = C\ G(s)\ \delta \mathbf{I}_{PF_{ref}}(s)$$

Thus, all the quantities in $\delta\mathbf{Y}(s)$ have the same dynamics of the PFC currents; furthermore, the transfer function describing these dynamics is the same for all of the elements in $\delta\mathbf{Y}(s)$ and has a simple form (in general that of a 1st or 2nd order system) yielded by the choice of the PFC regulator.

The response of the PFCs can be further adjusted by an additional set of n_{PF} PID controllers, as shown in fig. 36.

If we collect these controllers into a transfer matrix $PID(s)$, we obtain

$$\delta \mathbf{I}_{PF_{ref}} = PID(s)\ C^{\dagger}\ (\delta \mathbf{Y}_{ref}(s) - \delta \mathbf{Y}(s))$$

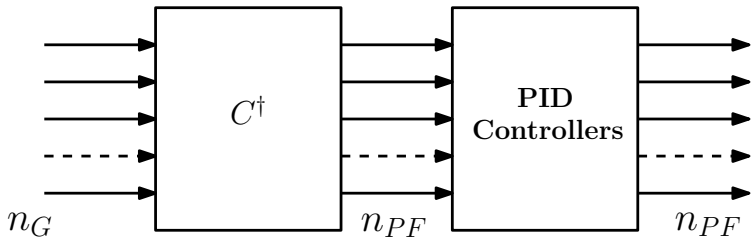

Figure 36: Block diagram of an XSC-*like* shape controller. The pseudo-inverse $C^{\dagger}$ is usually computed using the largest singular values that result from the SVD of the C matrix.

However, if the PID controllers are all equal, they can be treated as a scalar and moved to the right of the $C^{\dagger}$ matrix, yielding

$$\begin{aligned}\delta\mathbf{Y}(s) &= G(s)\ C\ C^{\dagger}\ PID(s)\ \delta(\delta\mathbf{Y}_{ref}(s) - \delta\mathbf{Y}(s)) \\ &= G(s)PID(s)(\delta\mathbf{Y}_{ref}(s) - \delta\mathbf{Y}(s))\end{aligned}$$

In this way, the loop function for each of the shape descriptors is given by the simple SISO transfer function $G(s)PID(s)$, which can be adjusted by choosing the PID parameters on the basis classical control engineering techniques.

The adopted approach owes to that of the eXtreme Shape Controller (XSC), implemented and tested at JET; interested readers are referred to [4, 109–112].

Part III

APPLICATIONS

6

THE EAST TOKAMAK

"If a craftsman wants to do good work,
he must first sharpen his tools."

— Confucius

6.1 MOTIVATION

One of the main technical challenges for the successful operation of a proper fusion plant resides in the problem of power exhaust handling. Nowadays, the technological limit for the heat flux over a tokamak's divertor plates is $5 - 10 MW m^{-2}$; however, in the current optimal scenario for a reactor such as DEMO, heat fluxes on the divertor plates up to $50 MW m^{-2}$ are foreseen. One of the goals of the ITER project is to assess the possibility of mitigating the heat loads on the divertor targets by increasing core plasma radiation or producing detached divertor conditions. However, a risk remains that these solutions might not scale up to DEMO. For this reason, the investigation of alternative solutions to the divertor power exhaust problem has been included in the EFDA roadmap to fusion electricity [113]. One possibility is to exploit alternative magnetic divertor configurations, such as the snowflake [114, 115] or the super-X [116] divertor. In the roadmap document we read:

> *«Some concepts are already being tested at proof-of-principle level in* $\leqslant$ 1MA *devices (examples are super-X, snowflake, liquid metals). These concepts will need not only to pass the proof-of-principle test but also an assessment of their technical feasibility [...]. The goal is to bring at least one of the alternative strategies (or a combination of baseline and some alternative strategy) to a sufficient level of maturity by 2030 [...].»*

With this perspective, in 2014-2015 the possibility of realizing and controlling a two-null-points divertor configuration was explored at the EAST tokamak [117]. During these preliminary experiments, a heat flux reduction on the divertor plates was observed; however, the position of the secondary null point was not controlled in feedback. To conduct further studies, the need for a dedicated feedback control system arose; this need led to the opportunity of improving the existing EAST magnetic control system in order to make the closed-loop control of alternative divertor configurations possible.

6.2 DESCRIPTION OF THE MACHINE

EAST is an experimental fusion device site in Hefei, China. It entered into operation in 2006, and it is the first tokamak operating with both poloidal and toroidal superconducting coils, aiming to reach a pulse duration of ~1000s. It has a D-shaped poloidal cross section, a double layer vacuum vessel, a major radius of 1.85 meters, a minor radius of 0.45 meters and a toroidal field of 3.5 Teslas. EAST experiments are conducted by the Hefei-based institute of Plasma Physics under the Chinese Academy of Sciences.

The EAST device is equipped with 14 PFCs driven by 12 individual power supplies; coil pairs PF7/PF9 and PF8/PF10 are connected in series and treated as a single circuit. The PF coils are designed to fulfill both the plasma current and the position/shape control tasks; this approach brings along the drawback of an additional challenge in the controller design. Moreover, two copper coils (named IC1 and IC2) connected in anti-series are installed inside the vacuum vessel in order to provide a faster control action for the plasma vertical stabilization. The coils layout is shown in the fig. 37.

Fig. 37 shows also the position of the magnetic diagnostics: EAST is equipped with 37 flux loops and 38 poloidal field sensors, which can be exploited for magnetic control purposes.

EAST has many technical similarities with the ITER tokamak (e.g. the same distribution of toroidal and poloidal field coils and a similar vessel structure); this makes the experience achieved on this machine relevant in order of a future reuse in the control of ITER[1].

6.3 ELECTROMAGNETIC MODELING

As a preliminary step, plasma equilibria and linearized models of the EAST tokamak were obtained by means of the CREATE-L and CREATE-NL codes and validated in open loop against experimental data.

The first validation step aimed at assessing the goodness of the relation between the current variations in the active circuits and the outputs (i. e. shape descriptors, magnetic probes, X-point position, etc.), taking into account also the dynamics of the eddy currents. To do so, it was necessary to slightly modify the linearized model (equations (73)-(71)-(72)) to accept the active coils currents as inputs[2]. This state transformation will prove useful also for the simulation of the *fast Z* controller (see sec. 7.1.1).

The $\mathbf{I}$ current vector can be split as

$$\mathbf{I}(t) = [\mathbf{I}_{VD}^T \; \mathbf{I}_{CD}^T]^T , \tag{84}$$

where $\mathbf{I}_{VD}$ and $\mathbf{I}_{CD}$ indicate the currents in the voltage driven and current driven circuits respectively. The voltage driven circuits also include the

1 The experimental data obtained at EAST are stored on a MDSplus [118, 119] server and are freely accessible. Informations on the stored data can be found in an online handbook, available at [120].

2 For simplicity, the S matrix in eq. (73) has been assumed to be the identity matrix, and the voltages applied to the passive circuits have been assumed to be equal to zero.

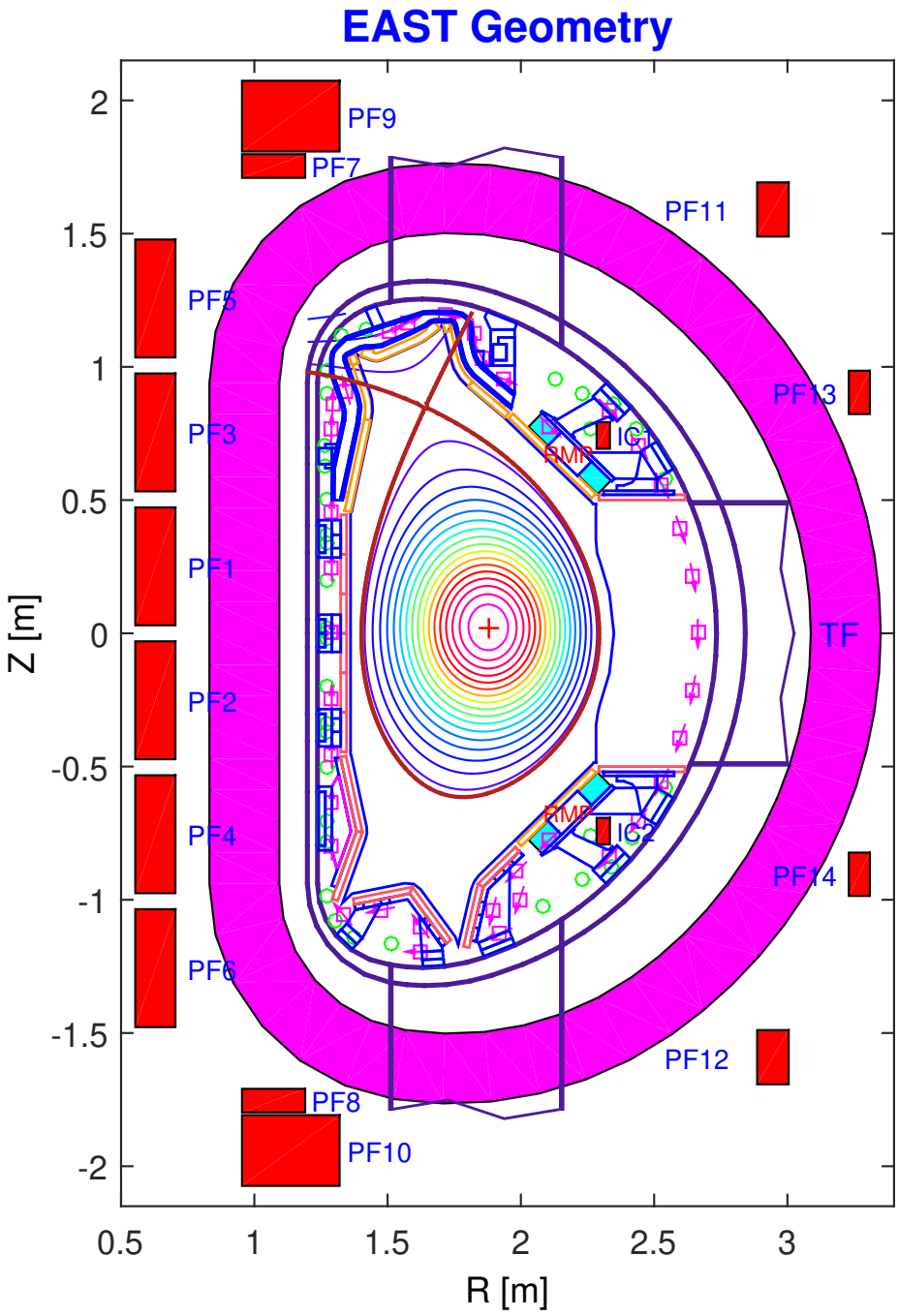

Figure 37: EAST poloidal cross-section. PF coils are shown in red. The green circles indicate the position of the flux loops, while the pink squares show position and orientation of the poloidal magnetic field probes.

plasma[3] and the passive elements where $V = 0$. Plasma-circuit equation can be then rewritten as

$$\begin{bmatrix} L_{11} & L_{12} \\ L_{21} & L_{22} \end{bmatrix} \begin{bmatrix} \dot{\mathbf{I}}_{VD} \\ \dot{\mathbf{I}}_{CD} \end{bmatrix} = - \begin{bmatrix} R_{11} & 0 \\ 0 & R_{22} \end{bmatrix} \begin{bmatrix} \mathbf{I}_{VD} \\ \mathbf{I}_{CD} \end{bmatrix} + \begin{bmatrix} \mathbf{V}_{VD} \\ \mathbf{V}_{CD} \end{bmatrix} . \tag{85}$$

For the sake of simplicity, the disturbances have been neglected in this discussion; they can be easily included in the input vector applying simple matrix algebra to the equations (71), (72). Experimental traces of β_p and l_i are available in EAST's EFIT database [121].

Let us introduce now the magnetic fluxes $\boldsymbol{\Psi} = L\mathbf{I}$, as the new state variables. $\mathbf{I}_{CD}$ will be the new input vector, and $\boldsymbol{\Psi}$ can be written as

$$\boldsymbol{\Psi} = L_{11}\mathbf{I}_{VD} + L_{12}\mathbf{I}_{CD} \quad \Rightarrow \quad \mathbf{I}_{VD} = L_{11}^{-1}\Psi - L_{11}^{-1}L_{12}\mathbf{I}_{CD} . \tag{86}$$

Plugging (86) in (85) we get:

$$\dot{\boldsymbol{\Psi}} = -R_{11}L_{11}^{-1}\boldsymbol{\Psi} + R_{11}L_{11}^{-1}L_{12}\mathbf{I}_{CD} + \mathbf{V}_{VD} \Rightarrow \dot{\boldsymbol{\Psi}} = A\boldsymbol{\Psi} + B \begin{bmatrix} \mathbf{V}_{VD} \\ \mathbf{I}_{CD} \end{bmatrix} , \tag{87}$$

where:

- $A = -R_{11}L_{11}^{-1}$;
- $B = \begin{bmatrix} \mathbb{I} & R_{11}L_{11}^{-1}L_{12} \end{bmatrix}$ ($\mathbb{I}$ is the identity matrix);

For the output equation, substituting (86) into (72) we get:

$$y(t) = C_1\mathbf{I}_{VD} + C_2\mathbf{I}_{CD} + D_1\mathbf{V}_{VD} \quad \Rightarrow \quad y(t) = C\boldsymbol{\Psi} + D \begin{bmatrix} \mathbf{V}_{VD} \\ \mathbf{I}_{CD} \end{bmatrix} , \tag{88}$$

where:

3 The possibility to apply a "virtual" voltage to the plasma can be useful to simulate current drive effects.

- $C = C_1 L_{11}^{-1}$;
- $D = \begin{bmatrix} D_1 & C_2 - C_1 L_{11}^{-1} L_{12} \end{bmatrix}$.

This form of the state-space equations allows to use the measured currents in the active circuits as inputs to the linearized model, and to compare the obtained output variations with the experimental data.

With the perspective of plasma shape control design and validation, a grid of 30×30 virtual flux loops placed all over the chamber has been included among the outputs of the system. This allows to reconstruct in simulation the complete poloidal flux and field maps[4] together with a set of ancillary quantities, such as the X-points position. In fact, in the linearized models only the position of one X-point is available, whereas we are interested in dealing with magnetic configurations characterized by multiple null points (see sec. 6.1). In principle, the X-points could be identified with the locations of the chamber where both the poloidal field components are zero; however, since the poloidal flux is known only in a discrete set of positions, some further calculation is needed to obtain an accurate result.

In the surroundings of a null point, the flux can be approximated by a quadratic expansion

$$\psi(r, z) = a^2 r + brz + cz^2 + dr + ez + f\,.$$

To determine the coefficients vector $[a \;\; b \;\; \cdots \;\; f]^T$, the points of the grid surrounding the expected X-point position have been considered. Since the

4 The reader might recall that the poloidal field is linked to the poloidal flux ψ by eq. (46).

poloidal flux values at these locations are known quantities, the estimation of the coefficients can be treated as a standard linear regression problem

$$\begin{bmatrix} r_1^2 & r_1 z_1 & z_1^2 & r_1 & z_1 & 1 \\ r_2^2 & r_2 z_2 & z_2^2 & r_2 & z_2 & 1 \\ \dots & \dots & \dots & \dots & \dots & \dots \\ r_n^2 & r_n z_n & z_n^2 & r_n & z_n & 1 \end{bmatrix} \begin{bmatrix} a \\ b \\ c \\ d \\ e \\ f \end{bmatrix} = \begin{bmatrix} \psi(r_1, z_1) \\ \psi(r_2, z_2) \\ \dots \\ \psi(r_n, z_n) \end{bmatrix} \Rightarrow$$

$$\Rightarrow \begin{bmatrix} a \\ b \\ c \\ d \\ e \\ f \end{bmatrix} = \begin{bmatrix} r_1^2 & r_1 z_1 & z_1^2 & r_1 & z_1 & 1 \\ r_2^2 & r_2 z_2 & z_2^2 & r_2 & z_2 & 1 \\ \dots & \dots & \dots & \dots & \dots & \dots \\ r_n^2 & r_n z_n & z_n^2 & r_n & z_n & 1 \end{bmatrix}^{\dagger} \begin{bmatrix} \psi(r_1, z_1) \\ \psi(r_2, z_2) \\ \dots \\ \psi(r_n, z_n) \end{bmatrix},$$

where $[\cdot]^{\dagger}$ denotes the Moore-Penrose pseudoinverse. The null point coordinates (r_{xp}, z_{xp}) must satisfy the condition

$$\nabla\psi(r_{xp}, z_{xp}) = \left.\frac{\partial\psi}{\partial r}\right|_{\substack{r=r_{xp} \\ z=z_{xp}}} \hat{r} + \left.\frac{\partial\psi}{\partial z}\right|_{\substack{r=r_{xp} \\ z=z_{xp}}} \hat{z} = 0\,,$$

which yields

X-point position estimation

$$\begin{bmatrix} 2a & b \\ b & 2c \end{bmatrix} \begin{bmatrix} r_{xp} \\ z_{xp} \end{bmatrix} + \begin{bmatrix} d \\ e \end{bmatrix} = \begin{bmatrix} 0 \\ 0 \end{bmatrix} \Rightarrow \begin{bmatrix} r_{xp} \\ z_{xp} \end{bmatrix} = - \begin{bmatrix} 2a & b \\ b & 2c \end{bmatrix}^{-1} \begin{bmatrix} d \\ e \end{bmatrix}.$$

The above equations also allow to compute the flux and the poloidal magnetic field at the null point. In fig. 38 the results of this procedure applied to EAST Double Null (DN) pulse #46530 are shown. For this test, a 5×5 grid of virtual sensor spaced by ~5 cm has been placed in the region containing

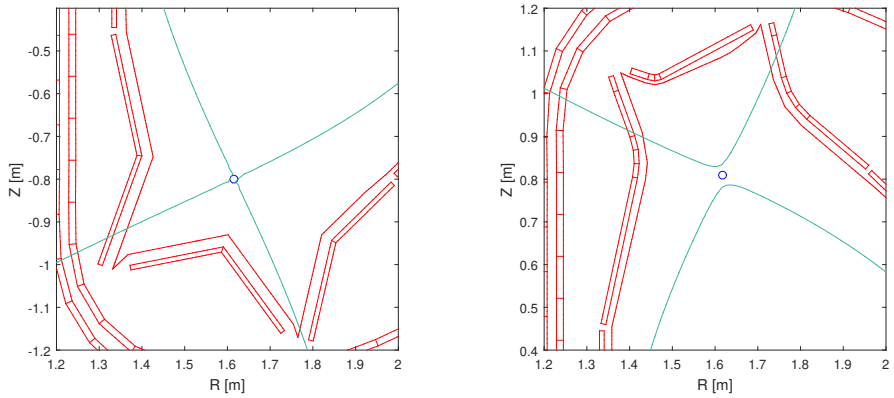

Figure 38: Static identification of active (left figure) and non active (right figure) X-points for for EAST DN pulse #46530. The EFIT plasma boundary is shown in blue (courtesy of dr. A. Castaldo).

the expected X-point position, and the flux map reconstruction provided by the EFIT [121] code has been used. The resulting error between boundary reconstruction performed by EFIT and the X-point position estimation obtained with the above method is less than 1 mm for both the active and non-active X-points (see fig. 38). [5]

To conclude this section, experimental and open loop simulated plasma current, radial and vertical position of plasma centroid, radial and vertical position and flux of both active and non active X-point, magnetic field and flux measurements and fluxes on control segments are shown in figs. 39-44. Besides the currents on the active circuits, the open-loop system has been fed the experimental poloidal beta and internal inductance variations. An equivalent plasma voltage is also available among the system inputs, which can be useful to take into account the effect of non inductive current drive systems. Since elongated plasmas are vertically unstable (see chap. 4), the unstable mode has been treated separately and simulated backwards in

5 It is worth to mention that the proposed method fails in the case of alternative configurations with very close null points, such as the snowflake divertor. Indeed, in this case a quadratic expansion is not sufficient to properly fit the flux map in the vicinity of the null points. An alternative solution, which involves a higher order approximation of the poloidal flux, has been proposed in [122] and used in [123].

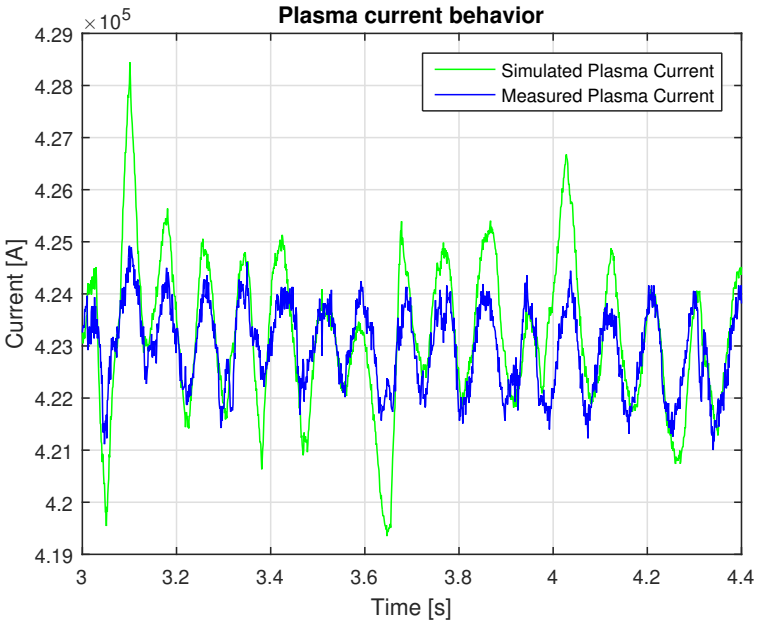

Figure 39: Comparison between simulated plasma current (green solid line) and experimental plasma current (blue solid line) for pulse #69449 (courtesy of dr. A. Castaldo).

time (in this way, the sign of the unstable eigenvalue is reversed. See [124]). The slight mismatch between simulated and experimental results is related to the estimation of the eddy currents in the passive structures and hence to the estimated resistivity of the discretized vessel elements [125]

6.4 PLASMA CONTROL SYSTEM

Fig. 45 shows a simplified block diagram of the EAST Plasma Control System (PCS). The PCS has been adapted from the DIII-D one and is continuously updated to satisfy growing experimental needs [126–129]. The control system has an inner PFC current control loop, which is in charge of tracking the current references produced by other external controllers, which are summed to the preprogrammed scenario currents. In addition to that, a so called *fast Z* control is employed in order to vertically stabilize the elongated plasma.

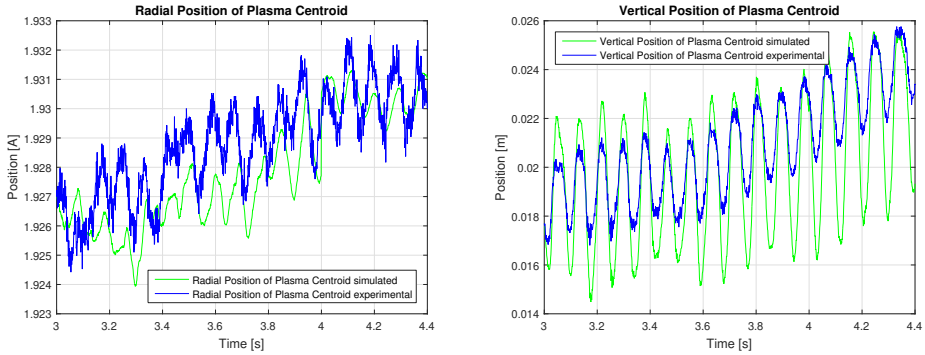

Figure 40: Comparison between simulated (green solid line) and experimental (blue solid line) plasma centroid radial (left figure) and vertical (right figure) position for pulse #69449 (courtesy of dr. A. Castaldo).

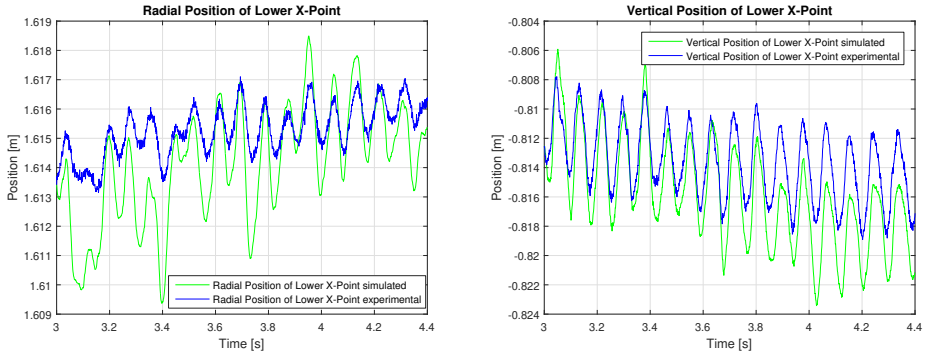

Figure 41: Simulated (green solid line) and experimental (blue solid line) plasma Lower X-point radial (left) and vertical (right) position for pulse #69449 (courtesy of dr. A. Castaldo).

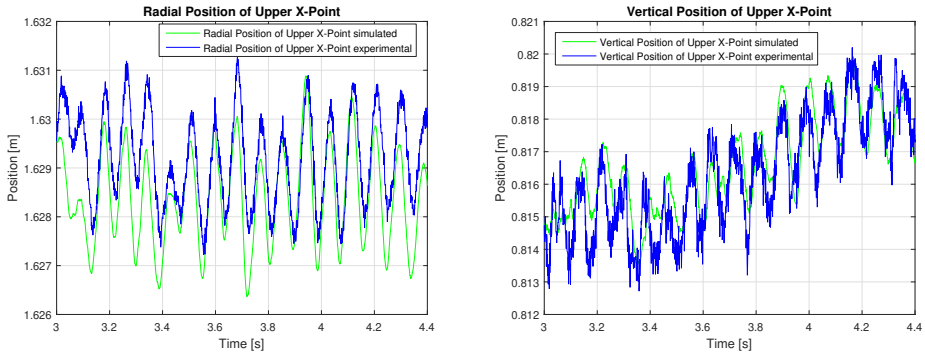

Figure 42: Simulated (green solid line) and experimental (blue solid line) plasma Upper X-point radial (left) and vertical (right) position for pulse #69449 (courtesy of dr. A. Castaldo).

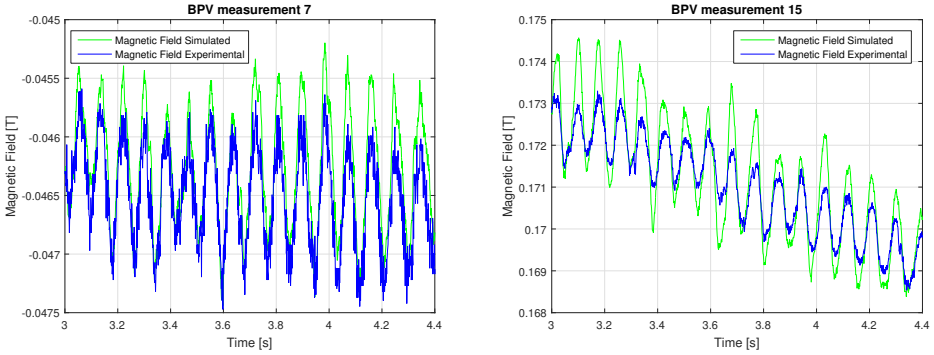

Figure 43: Simulated (green solid line) and experimental (blue solid line) magnetic measurements BPV 7 (left) and BPV 15 (right) for pulse #69449 (courtesy of dr. A. Castaldo).

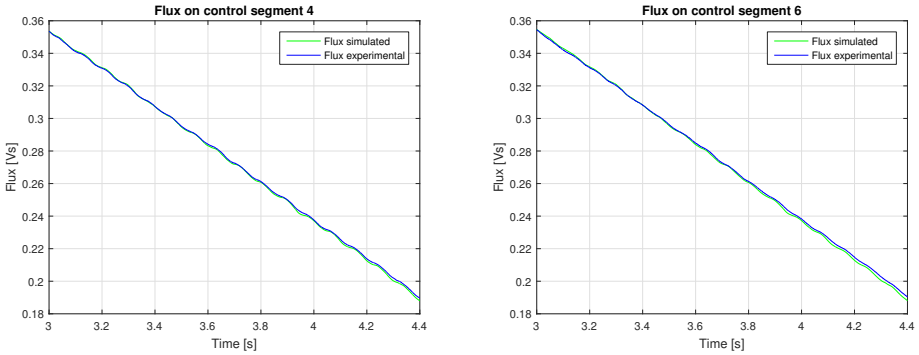

Figure 44: Simulated (green solid line) and experimental (blue solid line) magnetic flux for control segment 4 (left) and 6 (right) for pulse #69449 (courtesy of dr. A. Castaldo).

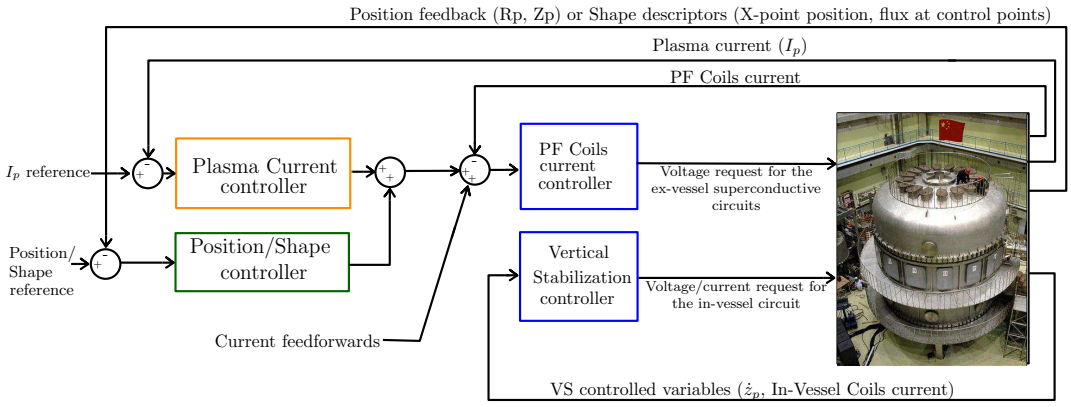

Figure 45: Simplified block diagram of the EAST Plasma Control System (PCS).

6.4.1 *Modeling and open loop validation*

Since the final aim of the models described in the previous section is the design of new control algorithms for the EAST plasma, it is necessary to assess their reliability when performing closed loop simulations. In order to carry out this task, it is then fundamental to reproduce correctly the EAST PCS control algorithms. In particular, the two main control logics adopted at EAST are:

- *RZIP*: in this operation mode, the controlled quantities are the plasma current (I_p) and the radial and vertical position of the plasma centroid (R, Z).

- *Isoflux*: this operation mode aims at controlling the plasma shape by regulating to zero the difference between the flux at the null-point and the flux at some target positions; the fluxes are estimated by means of a real-time reconstruction code (RT-EFIT [85] or PEFIT [87]). In addition, the plasma current and the null-point position are controlled to a desired value; alternatively, instead of controlling the X-point position, the magnetic field at a given location can be regulated to zero. For DN plasmas, the position of the 2^{nd} null and the distance at the midplane between the isoflux surfaces passing through the two nulls (dr_{sep}) are also controlled; however, for the purposes of this discussion, we will focus on Single Null (SN) plasmas.

Both control logics generate references for the inner PFC current control loop. Usually, a EAST plasma discharge starts in the RZIP control mode; after the limiter-divertor transition, the controller switch to the isoflux phase. During the switching, a convex combination of the references generated by the two controllers is fed to the internal current control loop, with a transition time of the order of ~0.1 s. Finally, a vertical stabilizing controller is needed. At EAST, this controller usually actuates the IC coils in current driven mode. The architecture of the PCS is shown in Fig. 46.

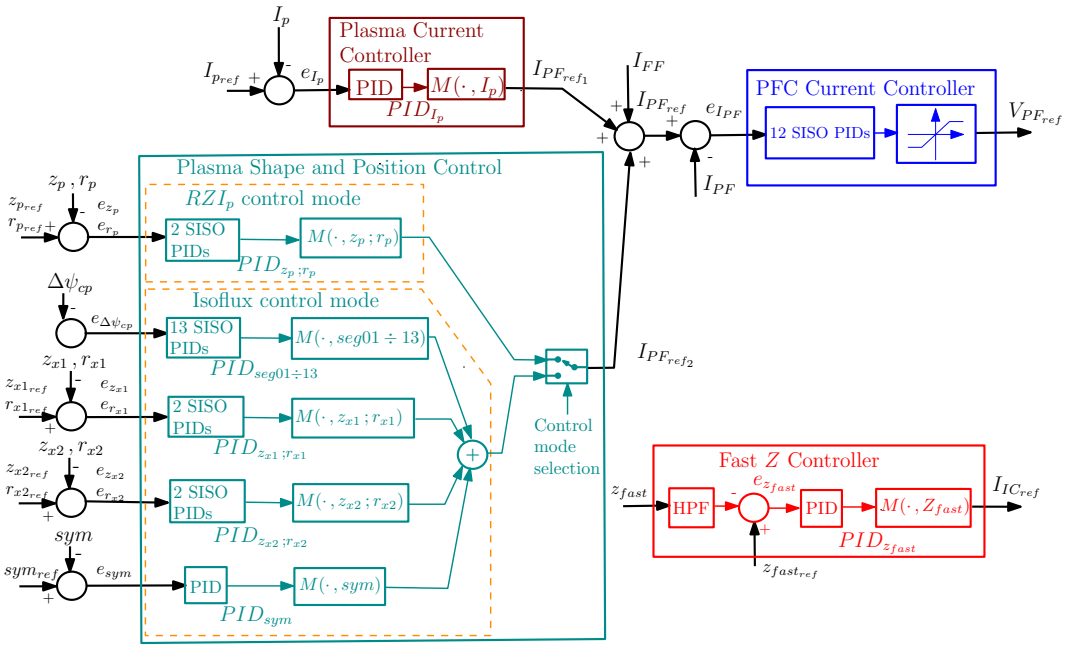

Figure 46: Architecture of the EAST PCS (the 'sym' signals refer to the *symmetry* control loop, which controls dr_{sep} in DN plasmas). The M matrix is used to spread the contribution of each control loop among the 12 available PF circuits. The PF current requests are then tracked by the PFC current controller.

As it can be seen in fig. 46, most of the controllers employed in the EAST PCS contain PID regulators. The standard PID available in the EAST PCS library [130] is equipped with an input low pass filter, i. e.

$$U(s) = \frac{1}{1 + sT_p} \cdot \left(K_p + K_i \frac{1}{1 + sT_i} + K_d \frac{sT_d}{1 + sT_d} \right) \cdot E(s) \,, \tag{89}$$

where $U(s)$ and $E(s)$ denote the controller output and the input error respectively.

The parameters for each of the controllers are stored on the EAST PCS dedicated server, and can be made accessible via MDSplus. Knowing these parameters, all the controllers can be tested in open loop, feeding in the experimental errors and comparing the simulated outputs with the experi-

mental ones. An example is shown in fig. 47 for pulse #74104.

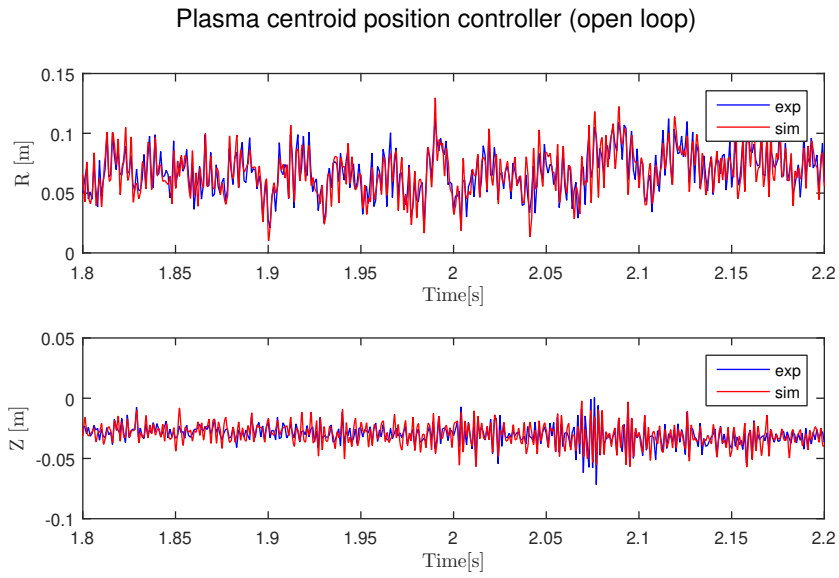

Figure 47: Plasma centroid position controller output for pulse #74104. The small discrepancies are due to a sub-sampling of the experimental error signal.

Each of the controller's outputs is post-multiplied by a column vector which distributes opportunely the control action to the PFCs; these vectors are all collected in a single matrix, called M-*matrix* in the PCS jargon, as it can be seen from fig. 46. Each row of the M-matrix corresponds to one circuit: by summing the plasma current, position and/or shape controllers outputs weighted by the M-matrix elements and suitable feedforwards, the current references for the PF Current controller are obtained.

On the other hand, the vertical stabilization loop (called *fast Z* controller) is separated from the other ones, and relies on a couple of in-vessel coils, connected in anti-series. This loop takes as a feedback a linear combination of magnetic sensors placed along the chamber walls, which is processed by a high pass filter in the form

$$Y_d(s) = \frac{sT_f}{1 + sT_f} Y(s) \tag{90}$$

Usually, the time constant T_f is kept fixed to 0.1 s. In fact, this linear combination is quite different from the vertical position feedback; nevertheless, the vertical velocity estimation yielded is acceptable (see fig. 48).

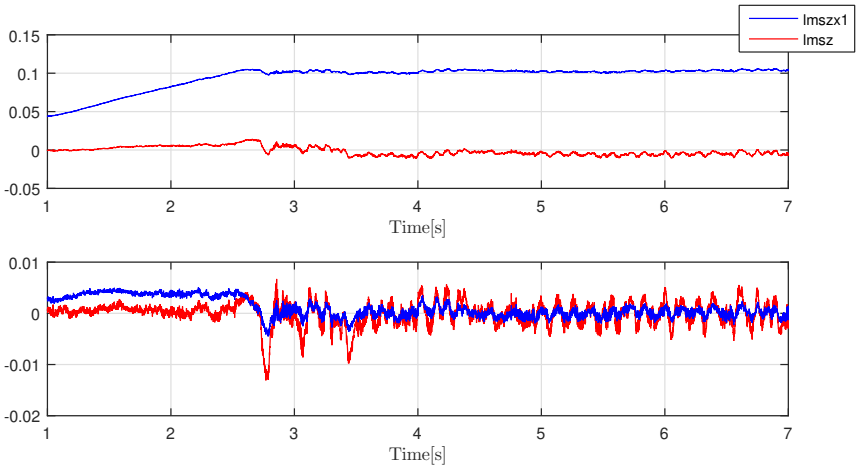

Figure 48: Comparison between the z_p feedback (red) and the magnetic probes combination used by the vertical stabilization controller (pulse #74104). The upper plot shows the two signals, while the lower one their derivatives obtained by means of a high pass filter of the form (90).

The controller output is the current reference for the IC circuit; when the *fast Z* controller is active, the in-vessel coils are usually operated in current-driven mode, as the power supply takes care of tracking the requested currents[6].

6.4.2 *Closed loop simulation*

Once the reliability of both the plasma linearized model and the control system algorithms has been assessed, actual EAST experiments can be reproduced by means of closed loop simulations. The pulse is simulated using the experimental control parameters, references and disturbances

6 For the simulations, the IC coils power supplies were treated as ideal actuators when the in-vessel circuit was in current mode.

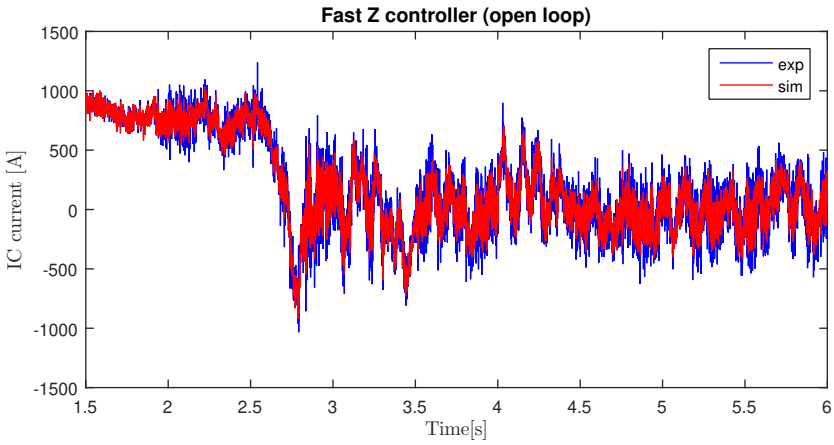

Figure 49: Fast Z controller (including the high pass filter) output for pulse #74104. The small discrepancies are due to a subsampling of the experimental feedback signal.

(β_p and l_i). In particular, since the disturbances definition between EFIT and the CREATE codes is different, some preliminary operations need to be done. These definitions are

$$\beta_{p,\mathrm{CREATE}} = \frac{W_p}{W_m} \tag{91}$$

$$l_{i,\mathrm{CREATE}} = \frac{4W_m}{\mu_0 R_0 I_p^2} \tag{92}$$

$$\beta_{p,\mathrm{EFIT}} = \frac{4W_p}{\mu_0 \bar{R} I_p^2} \tag{93}$$

$$l_{i,\mathrm{EFIT}} = \frac{4W_m}{\mu_0 \bar{R} I_p^2} \tag{94}$$

W_p is the average kinetic pressure, W_m is the average magnetic pressure, R_0 is the plasma major radius and $\bar{R}$ is defined as

$$\bar{R} = \frac{2V_p}{l_p^2}\,, \tag{95}$$

where V_p is the plasma volume and l_p is the plasma perimeter[7].

7 $\bar{R}$ approaches R_0 in the large aspect ratio approximation.

As it can be seen from equations (91)-(94), the value of poloidal beta adopted by CREATE-L is related to the EFIT definition via the following relation

$$\beta_p = \frac{\beta_{p,EFIT}}{l_{i,EFIT}} . \tag{96}$$

The definition of the internal inductance adopted by EFIT, instead, is different from the one adopted by CREATE-L by a factor of $\bar{R}/R_0$ in (92)-(94). This factor is related to the shape of the plasma and may change during the pulse. In the hypothesis that the plasma shape is almost constant during the flat top phase, a good approximation is given by

$$l_i = l_{i,EFIT} \cdot \bar{R}_{equil}/R_{0,equil} , \tag{97}$$

The equilibrium values $\bar{R}_{equil}$ and $R_{0,equil}$ are a direct output of the equilibrium code. $\bar{R}$ and R_0 could be estimated online during the simulation; however, since these disturbances are only used to test the robustness of the different control architectures, this level of accuracy is not needed.

An example of closed loop simulation for pulse #74104 is shown below in Figs. 50-55. The simulated traces of the controlled variables (i.e. plasma current, null point position, current in the in-vessel coils, controlled flux differences) and the plasma shape at $t = 7, 8$ and 9 s are plotted against the experimental ones.

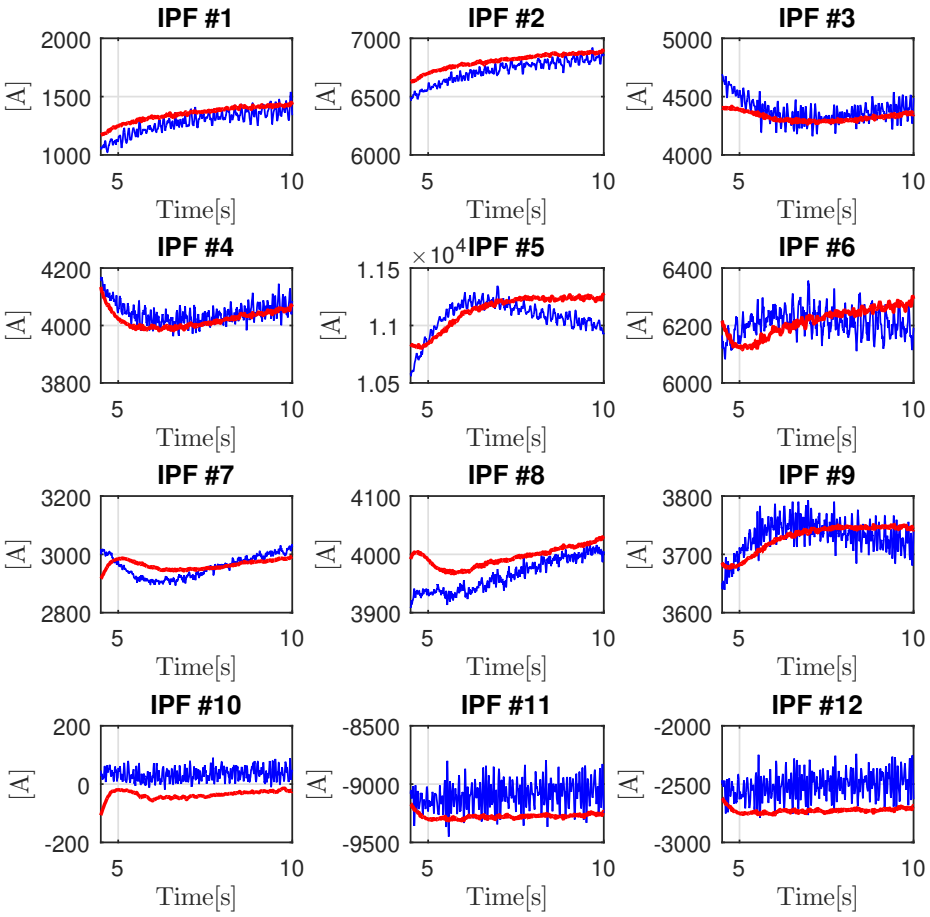

Figure 50: Simulated and experimental PFC currents for pulse #74104, obtained with the existing EAST controller. The experimental signal is shown in blue, while the simulated one is in red.

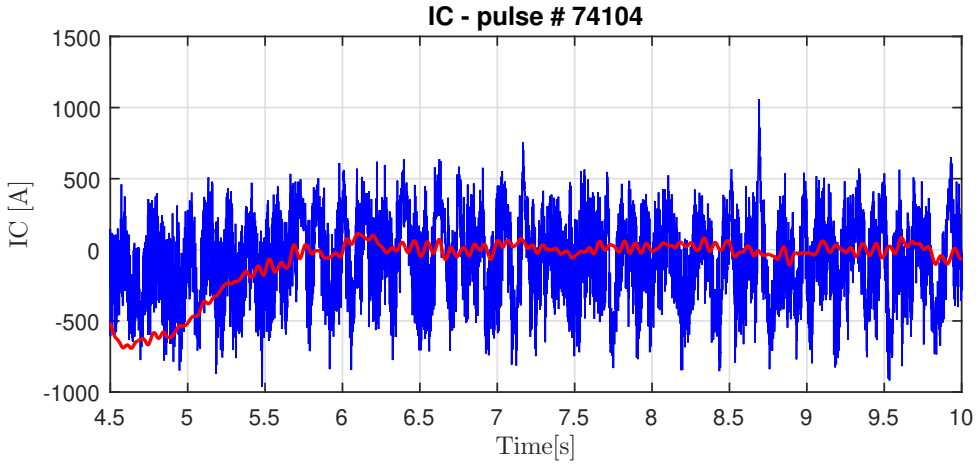

Figure 51: Simulated and experimental in-vessel circuit current for pulse #74104, obtained with the existing EAST controller. The experimental signal is shown in blue, while the simulated one is in red.

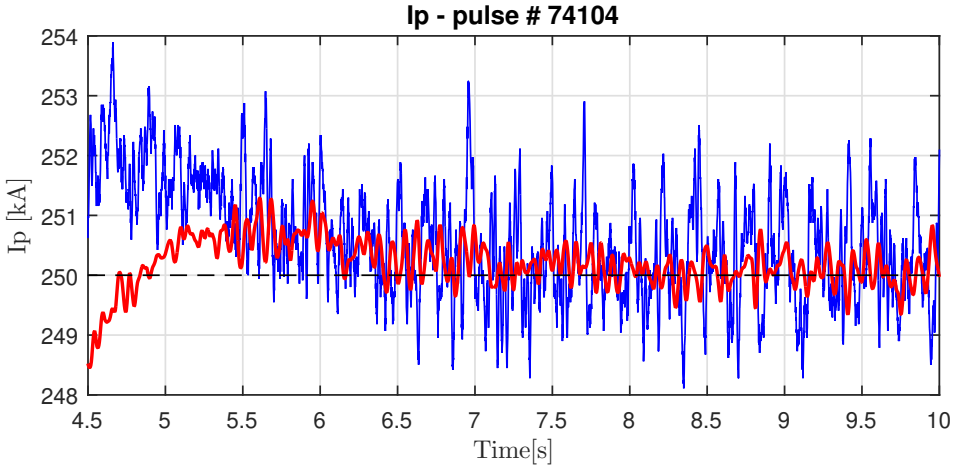

Figure 52: Simulated and experimental plasma current for pulse #74104, obtained with the existing EAST controller. The experimental signal is shown in blue, while the simulated one is in red. The dashed black line shows the reference signal.

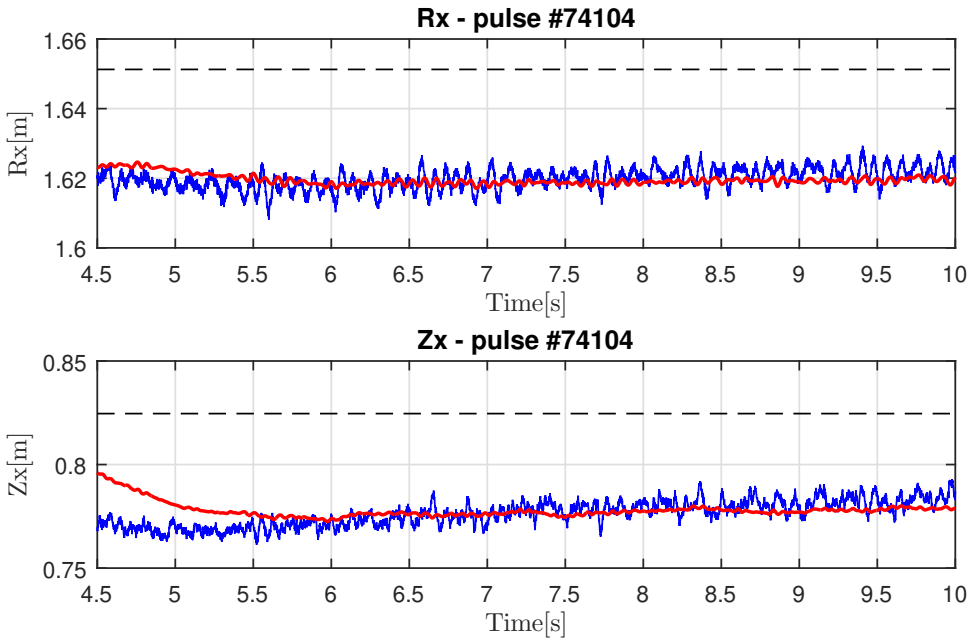

Figure 53: Simulated and experimental x-point position for pulse #74104, obtained with the existing EAST controller. The experimental signal is shown in blue, while the simulated one is in red. The dashed black line shows the reference signal.

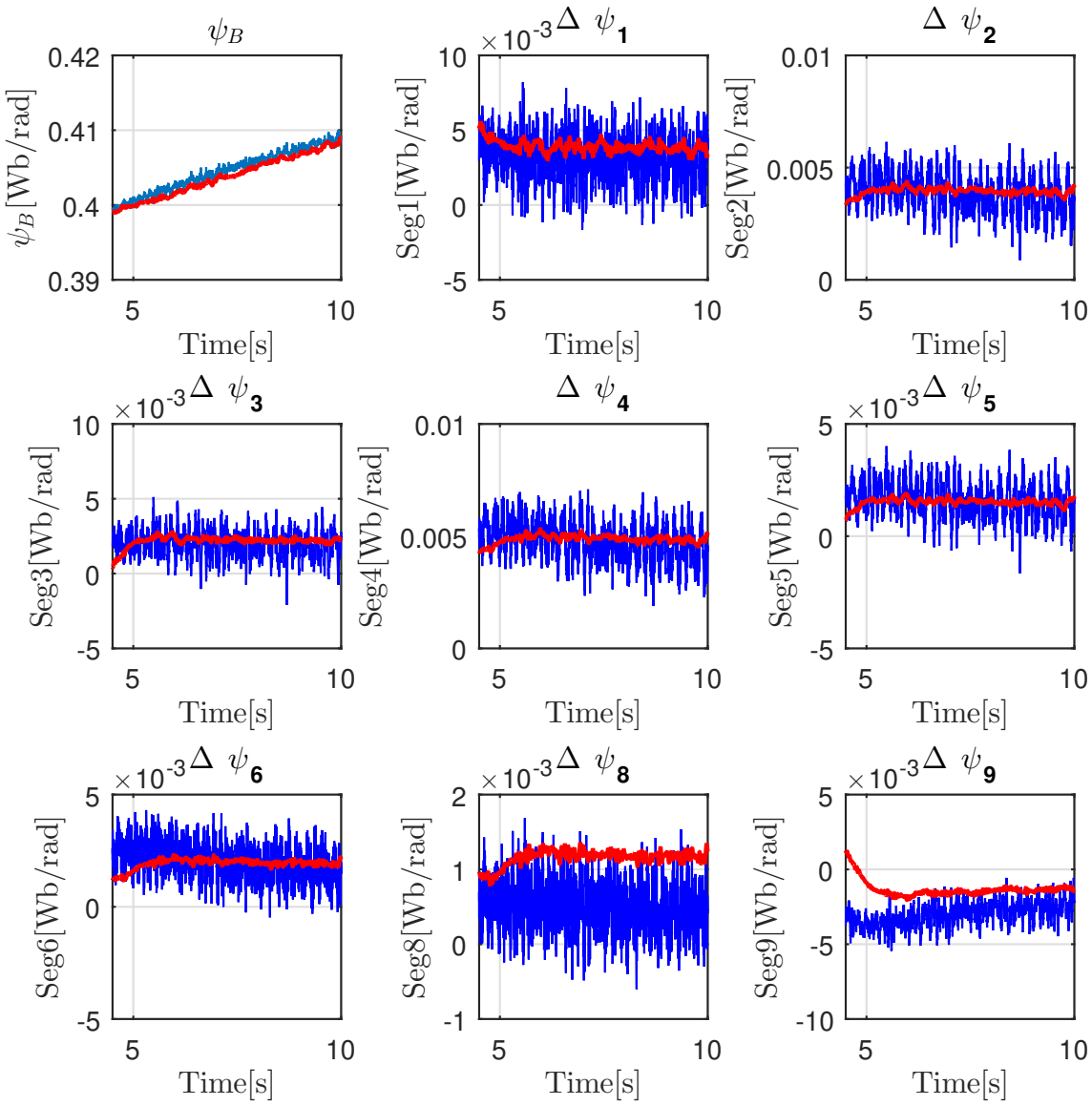

Figure 54: Simulated and experimental boundary flux and controlled flux differences for pulse #74104, obtained with the existing EAST controller. The experimental signal is shown in blue, while the simulated one is in red.

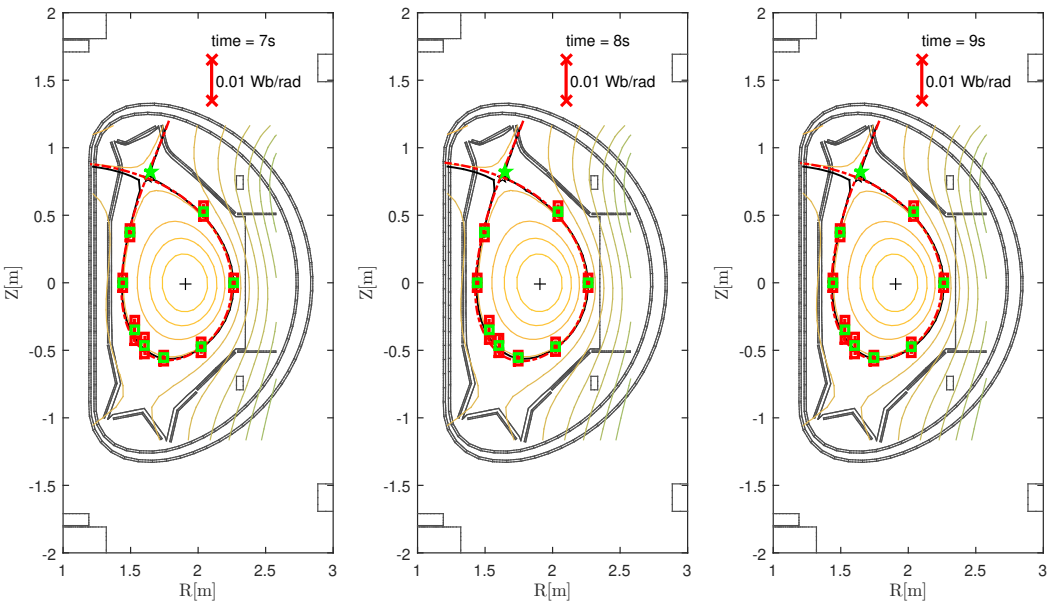

Figure 55: Reconstruction of flux map and plasma contour for pulse #74104 at 7, 8 and 9 s. In all the above snapshots, the green markers represent the reference shape, while the red bars show the flux error at the control points. The experimental separatrix, reconstructed by EFIT, is shown by the red dashed line, while the one obtained in simulation using the existing EAST controller is shown in solid black.

7

MAGNETIC CONTROL AT THE EAST TOKAMAK

"From land,
it is necessary to take thought for sailing,
if one is able and has the means,
but when one is upon the sea,
necessity runs to the present."

— Alcaeus of Mytilene

This chapter reports on the experimental activity carried out at EAST during the 2016-2018 period. Almost every block of EAST's plasma magnetic control system has been redesigned in order to meet the experimental requirements for advanced magnetic configurations control, according to the general architecture proposed in chapter 5. Each of sections 7.1-7.4 describes the issues related to one of the controllers and the proposed solutions. The design has been carried out in such a way to have a minimum impact on the PCS software architecture, so as to require a minimum programming effort. Two exceptions to this philosophy are represented by the VS system and the PFC MIMO decoupling controller, which needed some dedicated coding (even though they largely rely on functions and routines which were already available in the existing software).

The proposed approach, which is largely *model based*, prompts also the significant advantage of requiring -once all the modeling tools have been well assessed- a very small number of experiments for parameters tuning. Indeed, as it was discussed in part II, the controllers can be designed exploiting plasma-circuits numerical models and classical control engineering techniques. Additional experiments, when needed, are mainly devoted to solv-

ing practical implementation problems. The approach previously adopted at EAST was instead mainly based on a trial and error procedure, requiring entire experimental sessions dedicated to the tuning of the control parameters.

To conclude this chapter, some further results obtained in simulation are presented. In particular, sec. 7.5 presents some preliminary results for the control of poloidal flux expansion in the divertor region. In sec. 7.6, instead, the possibility of exploiting a Kalman filter approach for the estimation of the eddy currents and for plasma boundary identification is presented.

7.1 VERTICAL STABILIZATION: AN ITER-LIKE APPROACH

As it was already discussed in sec. 6.1, the final aim of the work presented in this thesis is to develop a plasma magnetic control system which is capable of dealing with advanced magnetic configurations. In this view, decoupling the VS system and the plasma shape and position control becomes an essential feature.

Tipically, the decoupling between the VS system and the other controllers is achieved by means of a frequency separation approach, which allows to design the plasma current, position and/or shape controllers assuming that the plasma is vertically stable [131]. This decoupling strategy prompts an extremely attractive simplification in the design phase of these controllers, since otherwise the VS system should be explicitly taken into account.

As it will be discussed shortly, the pre-existing EAST VS [127, 129] was not decoupled from plasma current, position and shape control. For this reason, as a preliminary step towards the development of a new magnetic control architecture, the VS algorithm proposed in [132, 133] for the ITER tokamak

has been adapted to EAST[1]; the proposed architecture is compliant to the one described in chapter 5.

7.1.1 *Analysis of the* fast Z *controller*

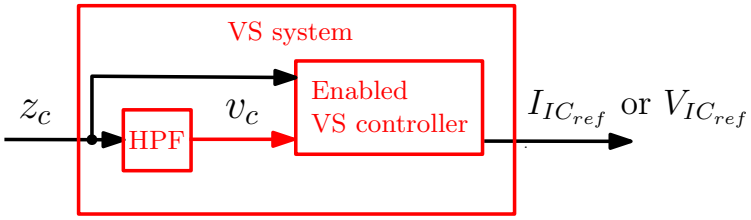

Figure 56: Simplified block diagram of the pre-existing EAST VS system. The controller output can be either a voltage or a current request to the power supply of the IC circuit, depending on the selected control algorithm.

The pre-existing EAST VS system (fig. 56) takes as input the estimated plasma vertical position z_c, and estimates its time derivative $\dot{z}_c = v_c$ by means of the high pass filter (90)[2]. The Laplace transform of the estimated plasma vertical speed is given by

$$V_c(s) = \frac{s\tau_z}{1 + s\tau_z} Z_c(s)\,,$$

where the time constant τ_z is usually set equal to 100 ms. Plasma vertical position and speed are processed by the VS controller, which can generate either a current or a voltage request to the IC power supply, depending on the enabled algorithm. Three different control algorithms are available:

1 To distinguish between the pre-existing controller and the new one, in what follows the former will be often referred to as *fast Z* controller, while the latter as *ITER-like VS*.

2 Actually, as it was already discussed in sec. 6.4.1, the plasma vertical position estimate used for the VS is not particularly accurate. Nevertheless, the velocity estimate is acceptable. For simplicity, in the following we will refer to the linear magnetic combination used for the VS system as z_c. When designing the new VS algorithm (see sec. 7.1.2), the same linear combination of magnetic measurements was used, in order to minimize the impact of the new design on the PCS.

(vs1) *PID control with IC in current-driven mode*: the estimate of the plasma vertical speed is taken as input by an extended PID[3] in the form (89); the velocity setpoint is zero, so in this case $E(s) = -V_c(s)$. The current target $I_{IC_{ref}}$ is tracked by the local controller of the IC power supply.

(vs2) *PID control with IC in voltage-driven mode*: this algorithm is similar to **(vs1)**, but the PID output is the voltage request $V_{IC_{ref}}$ to the IC power supply.

(vs3) *Bang-bang control with IC in voltage-driven mode*: both the vertical position and speed estimates are used as inputs. In this control mode, a bang-bang approach is used to drive the IC voltage when the control error on the position exceeds a given threshold; otherwise, a voltage-driven PID controller is used [129].

It is worth to remark that, besides controlling the plasma vertical velocity to zero, all of the VS algorithms listed above can -at least in principle- influence the plasma vertical position, either directly (as for the bang-bang controller) or not (e. g. via PID integral action on v_c). This, in turn, would imply an undesired coupling with the plasma position control. On the other hand, by controlling only the vertical plasma velocity, a stable controller cannot stabilize the plasma (i. e. the plant is not *strongly stabilizable*). This issue will be discussed in more detail in sec. 7.1.2.

From the analysis of the control algorithms **(vs1-vs3)**, it resulted that they do not guarantee the required decoupling between vertical stabilization and plasma shape control.

As an example, let us consider EAST pulse #56603, a SN plasma at $I_p \cong 235$ kA. At $t = 2.6$ s, the current-driven PID **(vs1)** is enabled, while plasma

3 It is worth to notice that, in the *extended* PID (89), the integral action is obtained by means of a low-pass filter, whose time constant τ_I is usually set to a value that is greater than the duration of the whole discharge. On the other hand, the value of τ_p in the VS system's PID is usually set to a value corresponding to a cut-off frequency which is greater than the bandwidth of the VS system itself.

current and position are controlled by means of the RZIP algorithm (see sec. 6.4). Exploiting a plasma linearized model produced by means of the CREATE codes (see sec. 3.3), it is possible to estimate the plasma growth rate and how the unstable eigenvalue is modified -and eventually stabilized- by the EAST magnetic control system; linearized models which accept the I_{IC} current as input can be obtained by means of the procedure described in sec. 6.3. The estimated growth rate γ at $t = 2.6$ s (obtained using CREATE-L) is $\gamma \cong 574\ s^{-1}$. As it turns out, by closing only the current-driven PID the growth rate is slowed down to $\gamma \cong 6.16\ s^{-1}$; hence using the **(vs1)** algorithm (which is the most used at EAST, as far as the author is aware), the VS system alone is not capable to vertically stabilize the plasma. Overall vertical stabilization can be achieved by closing also the RZIP loop. In this way, the maximum eigenvalue of the closed loop system is equal to $\sim -1.5 \times 10^{-4}$, which implies a -rather marginal- closed loop stability. It was also possible to verify that vertical stabilization is achieved by the joint action of the PID on the IC circuit and the plasma centroid vertical position loop embedded in the RZIP controller. With these two controllers alone, the resulting maximum eigenvalue in closed loop is $\sim -5 \times 10^{-3}$. Hence, within the existing architecture of the EAST magnetic control, plasma vertical stabilization is achieved by the joint action of plasma position and shape controller and the VS system. As it turns out, the two system are strongly coupled, and the design of the plasma shape controller cannot be carried out without explicitly taking into account the VS system[4].

As a further example, let us consider EAST pulse #69516 at $t = 2.5$ s. In this pulse the enabled VS algorithm was the voltage-driven PID **(vs2)**, with the same RZIP controller used in pulse #56603. In this case, the open loop system has a growth rate of $\gamma \cong 547\ s^{-1}$. When the voltage-driven PID is

4 In the experiment, the plasma shape control switched from RZIP to isoflux shortly after a single null configuration had been reached (i. e. at 2.7 s). However, during pulse #56603 the VS system and plasma shape control were strongly coupled even in the isoflux phase. Indeed, in simulation it was not possible to simply modify the isoflux controller gains without affecting the overall stability [12].

closed on the plasma linearized model, two unstable poles appear in ~$1.7 \pm i\,1650$. For this specific plasma equilibrium, the closed loop system remains unstable even when the RZIP loop is closed; indeed, the two unstable poles remain almost unchanged (~$1.32 \pm i\,1645$). They yield an estimated natural frequency equal to $\omega \cong 1645$ rad/s. The model-based analysis (carried out with the CREATE-L linear model) seems to be confirmed by the experiment. Fig. 57 shows the time evolution of z_c. As it was predicted by the model, once the plasma is sufficiently elongated (i. e. right after $t = 2.45$ s) an oscillatory unstable mode appears, with a frequency of ~ 1256 rad/s. The difference between the estimated value and the experimental one for the natural frequency of the unstable mode is significant; however it should be remarked that, being the closed loop system unstable, the linearized plasma model around the equilibrium (generated at $t = 2.5$ s) just gives a rough estimation of this natural frequency, since during the unstable transient the plasma may be far from the reference configuration.

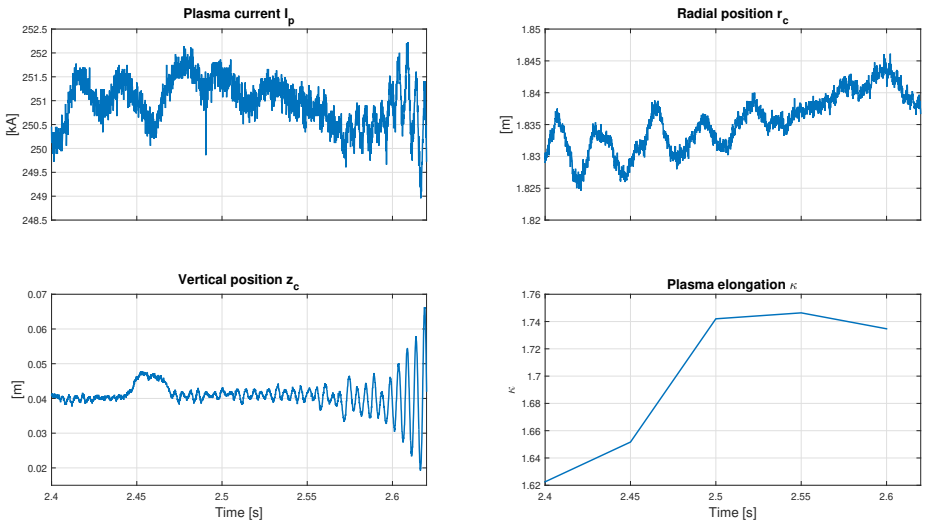

Figure 57: Time evolution of plasma current I_p, plasma centroid position (r_c, z_c), and plasma elongation κ during EAST pulse #69516.

Finally, a brief remark on the bang-bang control algorithm **(vs3)**. In [129], it is described how this controller, developed in 2015, represents an improvement with respect to the previous solutions. However, this algorithm aims at controlling directly the vertical position, causing thus -as it was discussed- a coupling with the shape and position loops. Furthermore, it has been designed according to a rigid displacement model, and hence it suffers from the drawbacks described in chapter 4.

7.1.2 *Design of the VS system*

A simplified block diagram representing the structure of the proposed VS controller is shown in fig. 58.

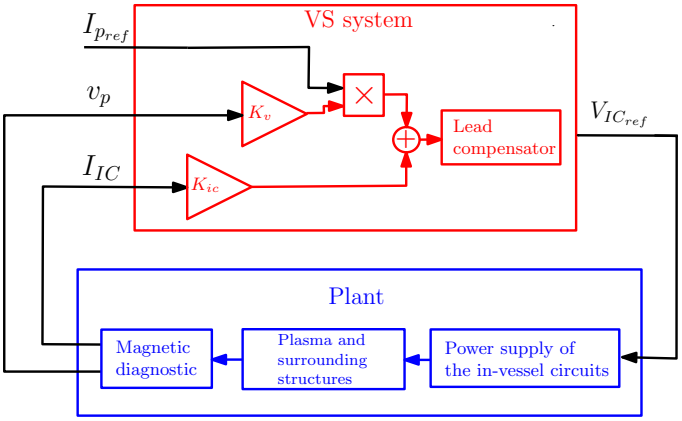

Figure 58: Simplified block diagram of the ITER-like VS deployed at EAST. Only the plasma vertical velocity v_c is fed back; the current flowing in the IC circuit is also controlled, in order to minimize the Joule losses in the copper in-vessel coils. The speed gain K_v is multiplied times the target waveform for the plasma current $I_{p_{ref}}$.

The voltage request $V_{IC_{ref}}$ is obtained as *ITER-like VS*

$$V_{IC_{ref}}(s) = \frac{1+s\tau_1}{1+s\tau_2} \cdot \left(K_v \cdot I_{p_{ref}} \cdot \frac{s}{1+s\tau_z} \cdot Z_c(s) + K_{IC} \cdot I_{IC}(s) \right) \tag{98}$$

This control law can be obtained straightforwardly from eq. (74) when $F_{VS}(s)$ is chosen as a lead compensator. The following parameters need to be chosen:

- K_v: plasma speed gain, scaled by $I_{p_{ref}}$;
- K_{IC}: IC current gain;
- τ_1 and τ_2: time constants of the lead compensator. Such a compensator is needed to adjust the closed loop parameters of the VS system, in order to obtain the desired values for the stability margins and the closed loop bandwidth [134]. Note that, in order to have a lead compensator, it must hold $\tau_1 > \tau_2$.

In order to design the controller, the state-space model (71)-(72) can be used to derive an input-output relation in the form

$$Y(s) = \begin{pmatrix} Y_1(s) \\ Y_2(s) \end{pmatrix} = W_p(s) \cdot \widetilde{V}_{IC}(s) = \begin{pmatrix} W_{p_1}(s) \\ W_{p_2}(s) \end{pmatrix} \cdot \widetilde{V}_{IC}(s)\,, \tag{99}$$

where $\widetilde{V}_{IC}(s)$ is the actual voltage applied to the IC circuit by the power supply, $Y_1(s) = Z_c(s)$ is the plasma vertical position and $Y_2(s) = I_{IC}(s)$ is the current in the IC circuit (all the quantities are expressed in the Laplace domain). The transfer matrix (99) models the behavior of the plasma and of the surrounding conductive structures. In addition, when designing the VS system, models of both the power supply and the relevant magnetic diagnostic should be taken into account; indeed, these two components usually have a major impact on the performance of the closed loop system. The power supply of the IC circuit has been modelled as a first order filter with a delay, i. e.

$$\widetilde{V}_{IC}(s) = \frac{e^{-\delta_{ps} s}}{1 + s\tau_{ps}} \cdot V_{IC_{ref}}(s)\,, \tag{100}$$

whose parameters can be estimated from dry-run pulses; the obtained values are $\tau_{ps} = 100\ \mu s$ and $\delta_{ps} = 550\ \mu s$. On the other hand, the same reconstruction method adopted by the PCS -i. e. a linear combination of simulated magnetic diagnostics- has been implemented to build the feedback signal to the VS system (see also sec. 6.4.1); simulated magnetic diagnostic measurements can be obtained as outputs of the CREATE linearized models, as described in 3.3. Furthermore, to estimate the vertical speed of the plasma, a derivative filter has been applied on the measured vertical position of the centroid $Z_c(s)$, i. e.

$$V_c(s) = \frac{s}{1 + s\tau_v} \cdot Z_c(s)\,, \tag{101}$$

whose time constant has been set equal to $\tau_v = 1$ ms. The plant model results from the series of (99)-(101), and is equal to

$$W_{plant}(s) = \begin{pmatrix} W_{p,1}(s) \\ \frac{s}{1+s\tau_v} W_{p,2}(s) \end{pmatrix} \cdot \frac{e^{-\delta_{ps} s}}{1 + s\tau_{ps}}\,. \tag{102}$$

The reader may have noticed from fig. 58 that, counterintuitively, to achieve plasma stabilization the controller must be closed in positive feedback on the plant. This can be justified as follows. In order to make the use of a root locus design approach possible for (98), the 550 μs time delay of the IC power supply has been replaced by its third order Padé approximation [106, Section 4.1.6], that is

$$e^{-\delta_{ps} s} \cong \frac{-(s - 8444)(s^2 - 1.34 \cdot 10^4 s + 8.54 \cdot 10^7)}{(s + 8444)(s^2 + 1.34 \cdot 10^4 s + 8.54 \cdot 10^7)}\,. \tag{103}$$

With this approximation, and by exploiting the Paring Interlacing Property (PIP) [135]:

Theorem: A linear plant $W(s)$ is strongly stabilizable *if and only if* the number of poles of $W(s)$ between any pair of real zeros in the right-half-plane is even. ■

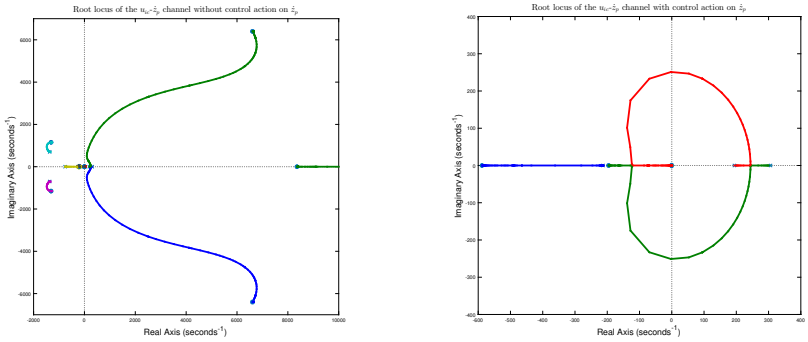

(a) Root locus of the $V_{IC} - V_c$ channel, when the loop on the IC current provided in (98) is closed.

(b) Root locus of the $V_{IC} - V_c$ channel, when both the loops provided in (98) are closed.

Figure 59: Root locus of the $V_{IC} - V_c$ channel when the controller (98) is used and the plasma model for the EAST pulse #60938 at $t = 6$ s is considered. The root locus diagrams have been obtained considering a reduced model of order 10 for the plant (102) (see [136, Ch. 7]) (courtesy of prof. G. De Tommasi).

it can be shown that, given the plant model (102), it is not possible to stabilize the plasma by feeding back only the vertical speed V_c. Indeed, given the two positive zeros introduced by the delay of the power supply (103), for the PIP an additional pole in the Right Half Plane (RHP) is required in the open loop transfer function of the $V_{IC} - V_c$ channel; without it, there is no way to move the plasma's unstable pole to the Left Half Plane (LHP) using a stable controller. The additional pole can be placed in the RHP by closing a positive feedback on Z_c (i. e. using an integral action on V_c) on I_{IC}. However, the first solution would be equivalent to feeding back also the vertical position Z_c, which is what we decided to avoid in the first place; for this reason, the (positive) feedback term on I_{IC} has been added in (98). By closing the loop on I_{IC} another unstable pole is added in the $V_{IC} - V_c$ channel, as it is shown in fig. 59a. At this point, the closed loop system can be stabilized by a proportional loop on V_c, as shown in fig. 59b (the sign of the K_v gain depends on the relation between I_{IC} and Z_c).

7.1.3 *Robustness analysis*

The CREATE-L plasma linearized models have been also exploited in order to assess the robustness of the proposed approach, which can be evaluated by using the Nichols chart [134] of the SISO transfer function obtained by opening the control loop in correspondence with the VS system output.

In [7], the proposed controller was tested against different plasma configurations in order to assess its robustness. Here we report the results obtained for four different equilibria (see table 1 and fig. 63a), using the VS parameters (see sec. 7.1.4)

$$K_v = 2.15 \cdot 10^{-4}\,, K_{IC} = 5.3 \cdot 10^{-2}\,, \tau_1 = 1.7 \text{ ms}\,, \tau_2 = 0.01 \text{ ms}\,, \qquad (104)$$

Fig. 63a shows the corresponding plasma cross sections. This initial analysis, which led to the charts shown in fig. 60, was performed by considering a pure delay model for the power supply of the IC circuit with $\delta_{PS} = 550$ μs.

As it can be seen from the graphs, the proposed ITER-like VS is able to provide plasma stabilization for all the four different configurations considered. In three cases out of four, the phase margin is greater than 40 degrees, and also the upper and lower gain margins guarantee robustness against either a doubling or a halving of the open loop gain. However, the margins significantly worsen for the equilibrium #64204 at $t = 3.5$ s (which is a Lower Single Null (LSN) plasma and has the highest growth rate among the ones listed in table 1). In fact, when the full power supply model (100) is considered, the closed loop system for this equilibrium becomes unstable. To provide the desired robustness with respect to this configuration, the controller parameters can be modified *ad hoc*. As an example of this, fig. 61 compares the Nichols diagram obtained with the VS parameters (104) for

pulse #64204 with the one obtained for the same plasma equilibrium using the following set of parameters

$$K_v = 2.0 \cdot 10^{-4}\,, K_{IC} = 4.5 \cdot 10^{-2}\,, \tau_1 = 1.0 \text{ ms}\,, \tau_2 = 0.01 \text{ ms}\,. \tag{105}$$

However, in the 2016-2018 experimental campaigns, Upper Single Null (USN) and DN plasmas were generally preferred to LSNs, mainly due to technical reasons related to the lower divertor. For this reason, the set of parameters (104) has also been tested against several plasma equilibria obtained starting from 2016-2018 experiments (see table 2 and fig. 63b), showing good performances; the results are reported in fig. 62.

Finally, a multiobjective optimization procedure was also set up to find a set of parameters capable of optimizing the stability margins of the VS system with respect to a set of different plasma configurations. For the sake of brevity, it will not be discussed here in detail; interested readers are referred to [8]. A more general solution may include an adaptive algorithm capable of adjusting the VS gains according to the experiment.

Table 1: Main plasma parameters for the four equilibria considered in fig. 60, i. e. the ones proposed in [7, 8]. The values reported for the growth rate γ, the elongation κ, the poloidal beta β_p, and the internal inductance l_i have been computed with the CREATE-NL equilibrium code.

Reference pulse	Configuration	$I_{p_{eq}}$ [kA]	γ [s^{-1}]	κ	β_p	l_i
46530 at t = 3 s	Double-null	281	137	1.66	0.30	1.27
52444 at t = 3 s	Limiter	230	92	1.35	0.26	1.34
60938 at t = 6 s	Upper single-null	374	194	1.77	0.78	0.95
64204 at t = 3.5 s	Lower single-null	233	512	1.61	0.02	2.19

7.1.4 *Experimental results*

In this section, some experimental results are presented and discussed.

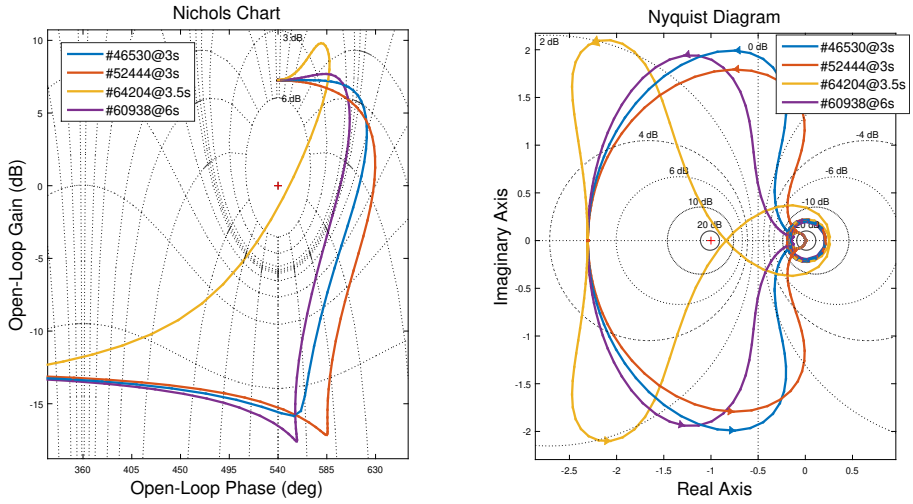

(a) Nichols diagrams of the open loop transfer function at the output of the VS system shown in fig. 58 for the equilibria in table 1.

(b) Nyquist diagrams of the open loop transfer function at the output of the VS system shown in fig. 58 for the equilibria in table 1.

Figure 60: Robustness analysis for the VS system.

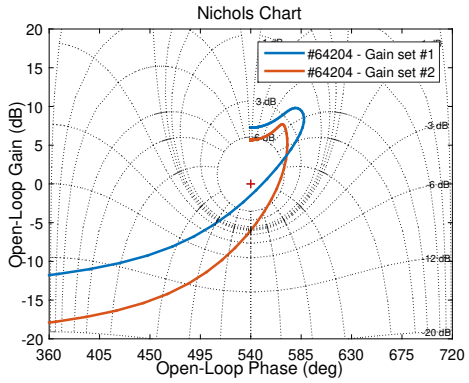

Figure 61: Nichols diagrams for the equilibrium #64204 at $t = 3.5$ s. The blue trace is the diagram obtained with the parameters in (104), while the red trace is the diagram for the parameters specified in (105).

The first presented experiment aims at proving that the control algorithm (98) is capable alone to vertically stabilize the plasma column, as predicted by the model-based analysis presented in sec 7.1.2. In this view, during pulse #70799, the ITER-like VS was enabled from 2.1 s to 3.3 s. During

Table 2: Main plasma parameters for the three equilibria considered in fig. 62. The values reported for the growth rate γ, the elongation κ, the poloidal beta β_p, and the internal inductance l_i have been computed with the CREATE-NL equilibrium code.

Reference pulse	Configuration	$I_{p_{eq}}$ [kA]	γ [s^{-1}]	κ	β_p	l_i
74104 at t = 1.7 s	Limiter	249	97	1.34	0.44	1.15
77472 at t = 2.65 s	Upper single-null	299	273	1.69	0.28	1.20
79295 at t = 3 s	Upper single-null	299	178	1.65	0.69	1.36

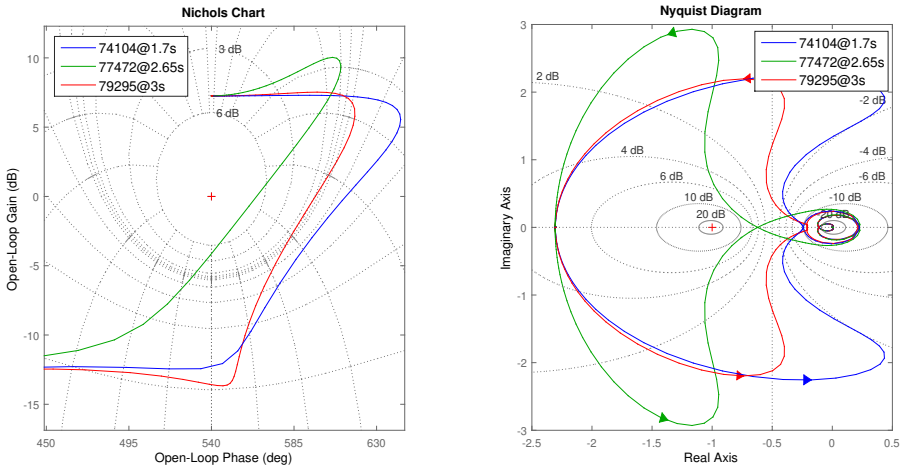

(a) Nichols diagrams of the open loop transfer function at the output of the VS system shown in fig. 58.

(b) Nyquist diagrams of the open loop transfer function at the output of the VS system shown in fig. 58

Figure 62: Robustness analysis for the VS system.

the same time window, only I_p and r_c were controlled in closed loop using the RZIP algorithm, while z_c was purposely left uncontrolled.

The experimental result for this pulse are shown in fig. 64, where the time traces for I_p, r_c, z_c, $V_{IC_{ref}}$, and I_{IC} are reported. After an initial transient, z_c does not exhibit any exponential drift, meaning that stabilization is achieved without directly controlling the position. Moreover, the current in the control circuit is kept small.

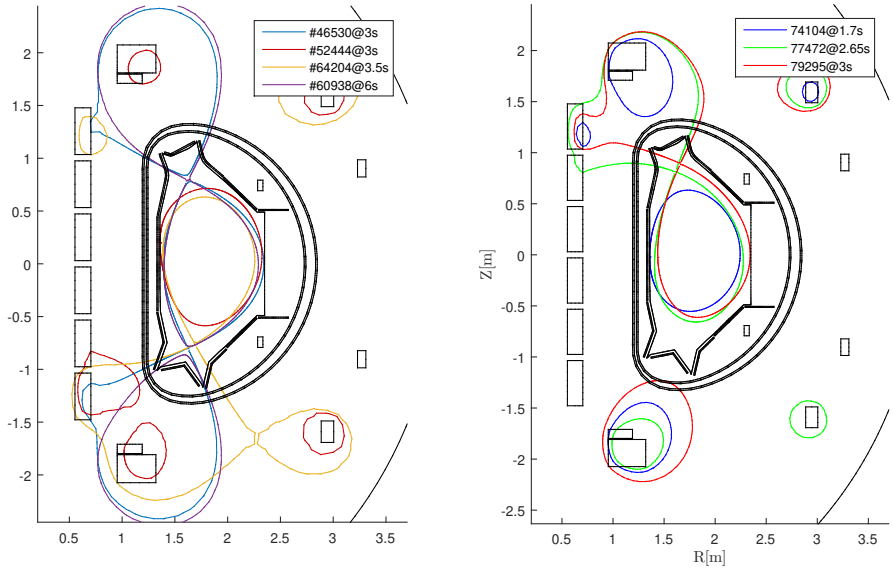

(a) Plasma cross section for the equilibria in table 1, obtained by means of CREATE-NL.

(b) Plasma cross section for the equilibria in table 2, obtained by means of CREATE-NL.

Figure 63: Plasma poloidal cross section for the plasma equilibria in tables 1-2.

During a second experiment, pulse #70799 was repeated, and the controller parameters of the VS were finely tuned to reduce the amplitude of the oscillations on both z_c and I_{IC}. The new set of parameters was set equal to (104) (i. e. to the values used to draw most of the conclusions of this section), and was tested during the EAST pulse #71423. A comparison between pulses #70799 and #71423 is shown in fig. 65; as in pulse #70799, the ITER-like VS was enabled from 2.1 s to 3.3 s. In fig. 65, a bump on the plasma current trace can be seen in pulse #74123; this bump was induced by the transition between the two different controllers, which was implemented without a proper bumpless transfer strategy. Nevertheless, the overall closed loop behavior exhibit less oscillations and succeeds in recovering from the unexpected disturbance.

In a third experiment, the vertical position loop of the RZIP controller was redesigned (since, with the new VS, it was not needed to achieve verti-

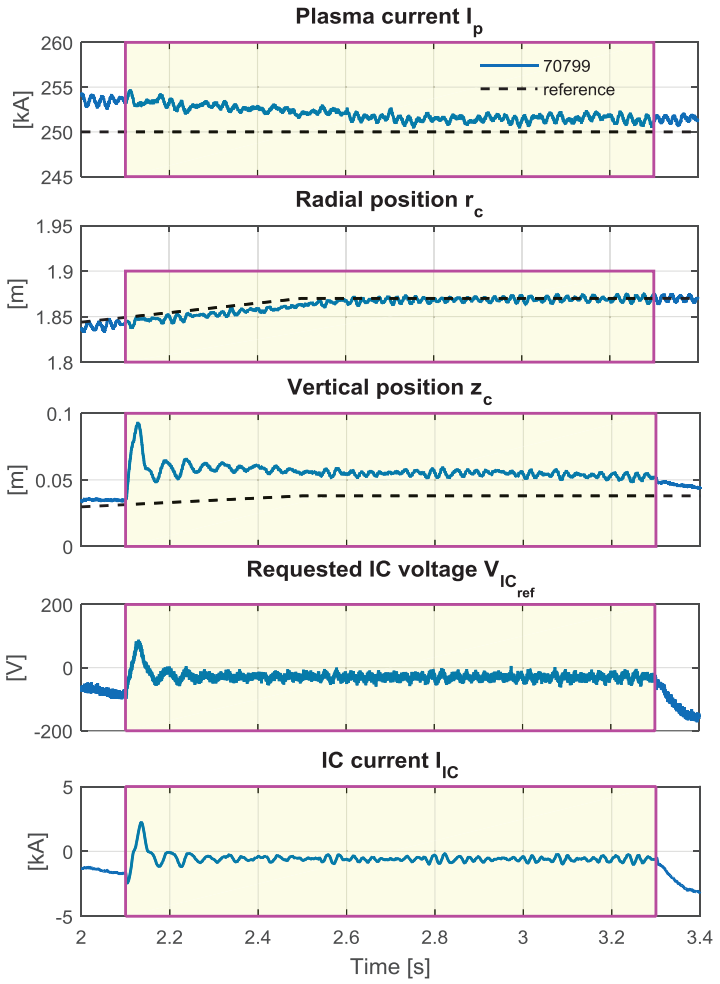

Figure 64: EAST pulse #70799. During this pulse the new VS system was enabled for 1.2 s starting from $t = 2.1$ s. In this time window only the plasma current I_p and the radial position of the centroid r_c were controlled in closed loop, while z_c was not controlled (indeed, for z_c the dashed black reference is not tracked).

cal stabilization anymore) and the vertical position of the plasma centroid was controlled in feedback. Fig. 67 shows the experimental results obtained during pulse #70131, where the VS was enabled from $t = 2.1$ s until the end of the pulse, and the controller parameters were set equal to (104). It can be seen that, regardless the disturbance due to the plasma current bump, the z_c reference is tracked by the controller.

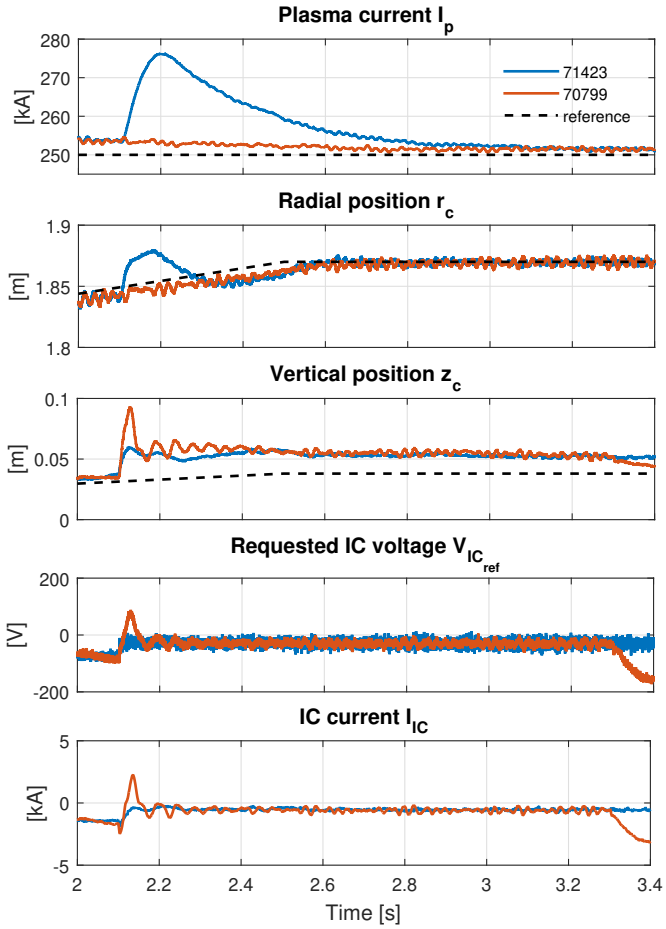

Figure 65: Tuning of the VS controller. This figure shows a comparison between EAST pulses #70799 and #71423. The control parameters in (98) used for the pulse #71423 were tuned exploiting the CREATE linear model, with the aim of reducing the amplitude of the oscillations on both z_c and I_{IC}.

Finally, during pulse #77472, due to wrong PCS settings all the controllers were unintentionally switched off, with the exception of the VS system and of the plasma current controller. The pulse lasted up to 7.3 s, proving again the capability of the new VS to independently guarantee plasma vertical stability.

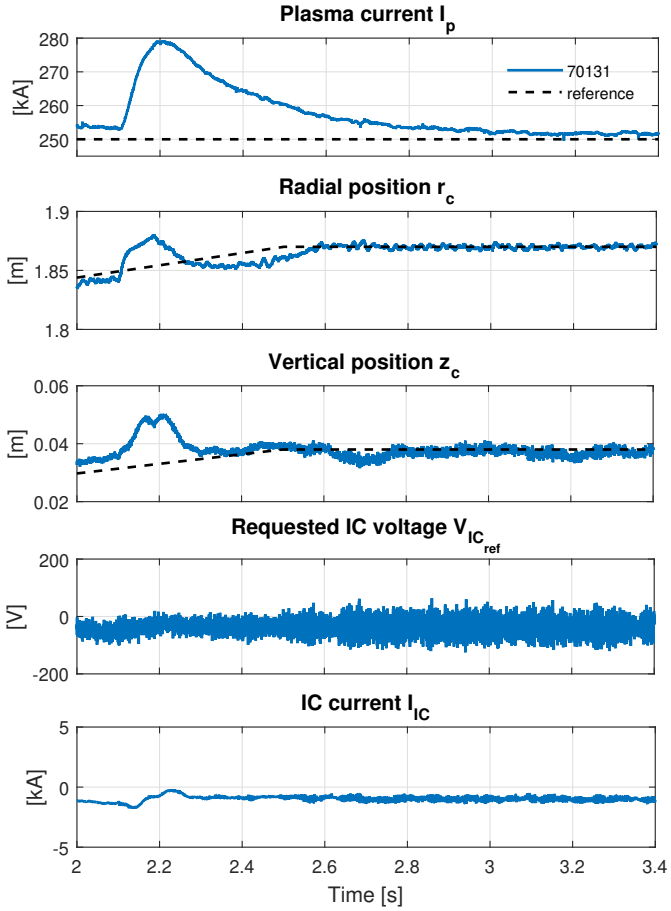

Figure 66: EAST pulse #70131. During this pulse the vertical position of the plasma centroid z_c was also controlled.

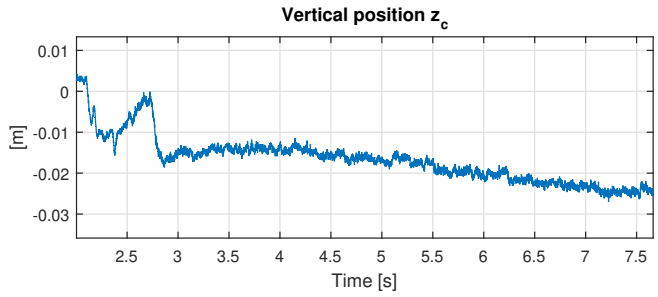

Figure 67: Plasma centroid vertical position for EAST pulse #77472.

7.2 POLOIDAL FIELD COILS DECOUPLING CONTROLLER

In the proposed architecture, the outputs of the plasma current, position and shape controllers are used to adjust the current requests to the PFCs. The inner PFC currents control loop is in charge of tracking these requests, by generating proper voltage requests to be sent to the power supplies. In fact, the pre-existing PFC currents controller of EAST was able of guaranteeing quite good performances; however, also this block was re-designed, since the proposed approach for the shape controller relies on the assumption that the PFC currents all have (almost) the same dynamic response, as it will be discussed in sec. 5.5[5]. Furthermore, the design of a new control algorithm for the PFC current controller provided a good way to further validate the reliability of the exploited electromagnetic models.

The new PFC current controller was designed according to the criteria discussed in sec. 5.2. In particular, it has the form (81); however, most of the experiments have been conducted with a controller equivalent to (79).

7.2.1 *Analysis and simulations*

The simulated response to a 1 kA step on PF1 for a purely proportional controller (77) with $\tau_i = 45$ ms for all the circuits is shown in fig. 68.

Furthermore, in order to test the effectiveness of the decoupling in the presence of plasma, the proposed controller has been tested in closed loop with a linearized model obtained from pulse (USN) #78289 at $t = 3$ s. In fig 69 the Bode diagrams for both the diagonal and off-diagonal channels are reported, showing how the PFC exhibit almost the same dynamics and the coupling effects are suppressed by the controller.

5 As for the VS, a frequency separation approach is adopted also for the PFC current controller, whose response should be faster than that of the plasma current, position and shape control loops.

As it was discussed at the end of sec. 5.2.1, the feedforward compensation term $\widetilde{R}_{PF} I_{PF}(t)$ allows to treat the behaviour of any coil as that of a superconductor. Even for truly superconducting coils, a residual resistivity could still be present, i. e. due to the connections to the power supplies. In the case of EAST, the superconductivity assumption seems to be well verified, and thus we chose to put $\widetilde{R}_{PF} = \mathbb{O}_{n_{PF} \times n_{PF}}$ in the last experimental campaign ($\mathbb{O}$ represent the zero matrix).

Furthermore, although it might look as an oversimplification, the approximation of the PFC behaviour with that of pure integrators (see again sec. 5.2.1, eq. (78)) is very well verified experimentally, as it can be seen from figs. 70-71 (sec. 7.2.2).

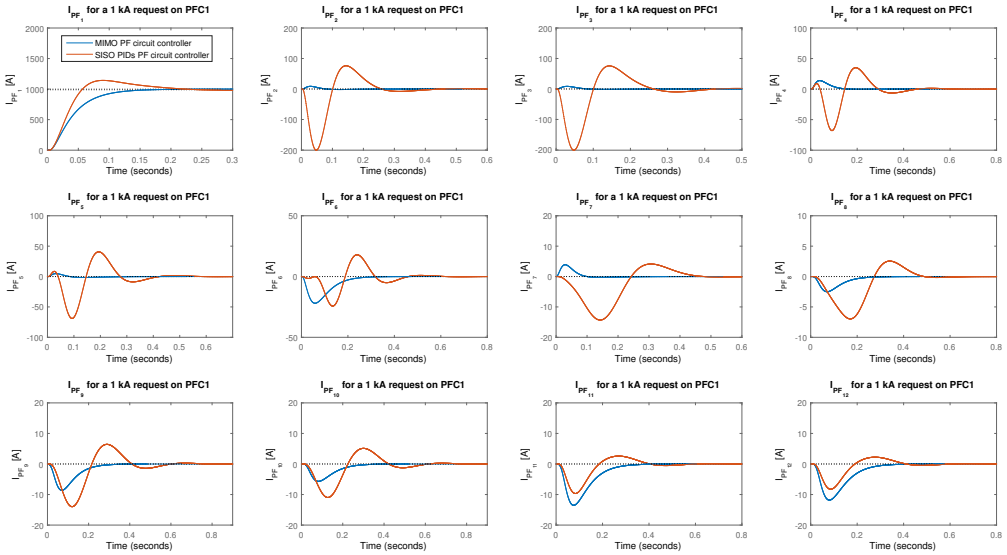

Figure 68: Simulation showing a comparison between the PFC-MIMO decoupling controller (77) with $\tau_i = 45$ ms for all the PF circuits and EAST's SISO PID controllers when a 1 kA request is applied to PF1. It can be seen how the proposed controller is able to reduce the effect of the variation of I_{PF1} on the other coils.

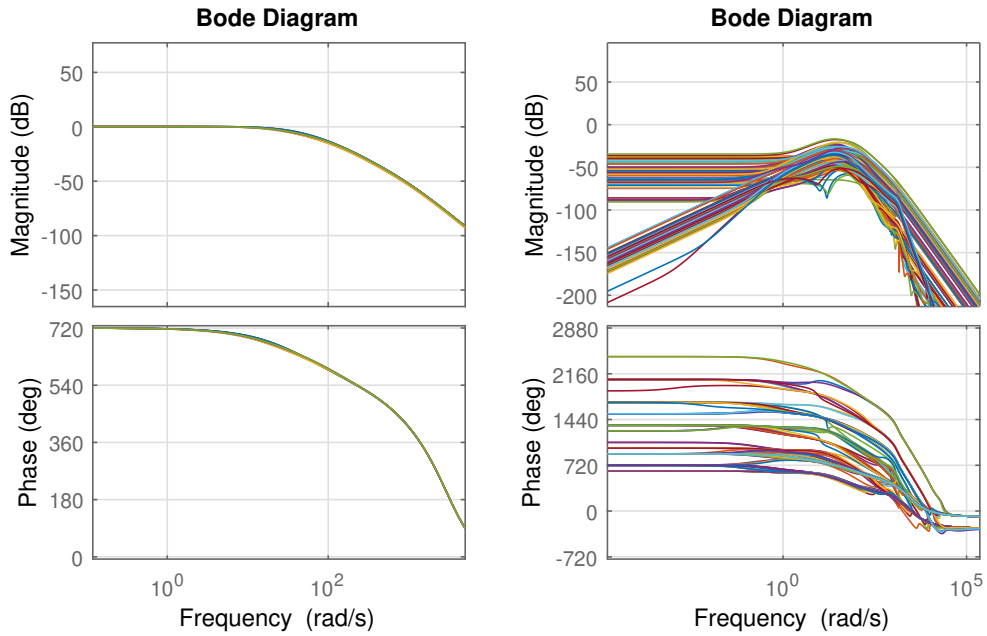

Figure 69: Bode diagrams of the closed loop system obtained with the PFC-MIMO decoupling controller (77) with $\tau_i = 45$ ms for the equilibrium #78289 at $t = 3$ s. On the left the diagonal channels, which show the response of the PF circuits to a reference applied to the same circuit; on the right, the response of the PFC to a reference applied on a different coil. Although the inductance matrix in (76) is modified by the presence of the plasma, the decoupling remains effective.

7.2.2 *Experimental results*

In this section, some experimental results are presented. The controller performances were assessed during a series of plasmaless pulses. The results obtained with the purely proportional controller presented in sec. 5.2.1 are shown in fig. 70. For this experiment, a value of $\tau_i = 45$ ms was chosen for all the PF circuits.

In fig. 71, the results obtained with a PI controller (79) are shown. The controller parameters are $Kp = 40$, $Ki = 4000$, $Kd = 0$, $\tau_P = -$ (i.e. not used), $\tau_I = 10$ s, $\tau_D = -$. These parameters were chosen in order to assign a desired settling time and damping factor to the closed loop system.

Simulated results are also presented along with the experimental ones. Their agreement with the experiments is satisfactory, proving the reliability of the modeling tools. For comparison, in the figures, the results obtained when the dynamics of the PFCs are approximated by pure integrators are also shown.

Finally, figs. 72-75 show a comparison between the proposed MIMO decoupling controller and the previous SISO one.

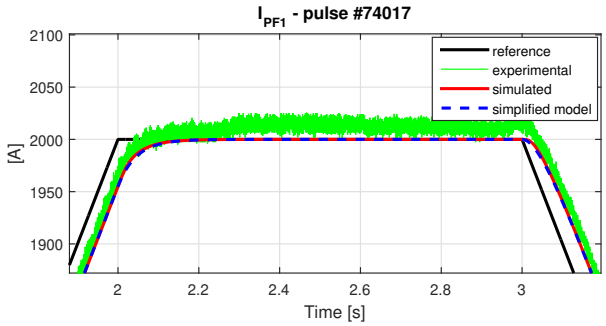

Figure 70: Comparison between simulated and experimental response to a trapezoidal reference signal for EAST plasmaless pulse #74107. Controller (77) was used with $\tau_i = 45$ ms for all the PF circuits. The dashed blue line represents the simulated output when the control loop is closed on a pure integrator. The dynamics show a good agreement with the experiment, while the small steady state error is due to an imperfect compensation of the coils resistances.

7.3 DESIGN OF AN ALTERNATIVE RZIP CONTROL

Once the alternative approach to VS described in sec. 5.1 was successfully commissioned, it was possible to tune the plasma centroid position control system. Indeed, the parameters of the PIDs used to control both the horizontal (r_c) and vertical (z_c) position of the plasma centroid were optimized in order to provide good performance when coupled to the new VS. This activity was carried out before the implementation of the MIMO PFC controller described in sec. 5.2.

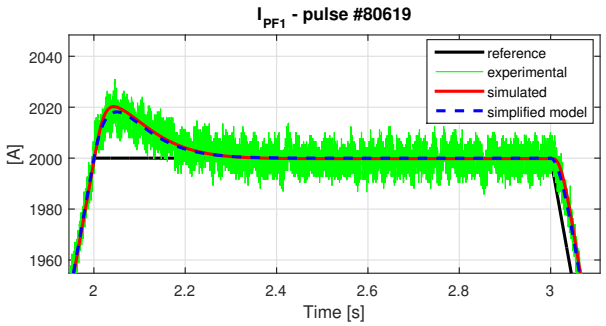

Figure 71: Comparison between simulated and experimental response to a trapezoidal reference signal for EAST plasmaless pulse #80619. Controller (79) was used withPID parmeters $Kp = 40$, $Ki = 4000$, $Kd = 0$, $\tau_P = -$ (i. e. low pass filter not used), $\tau_I = 10$ s, $\tau_D = -$. The steady-state error is compensated by the integral action; however, the presence of a zero in the controller's transfer function causes a small overshoot in the response. The dashed blue lines represents the simulated current when the control loop is closed on a pure integrator.

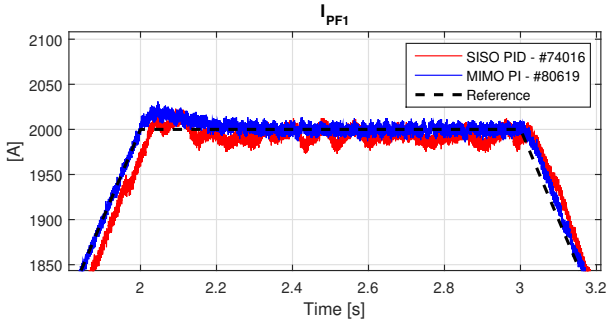

Figure 72: Comparison between PF1 measured currents during EAST plasmaless pulses #74016 (SISO PID) and #80619 (MIMO PI).

By exploiting the linear model (71)-(72), and by explicitly taking into account both the VS and the SISO PFC controller, a MIMO closed loop system from the current requests to the plasma centroid position was obtained. By taking into account also the *M-matrix* of the (r_c, z_c) controller, two SISO transfer functions were obtained, one for each of the two coordinates. In fact, the *M-matrix* that was customarily used at EAST for the control of the plasma centroid position turned out to be capable of providing a good

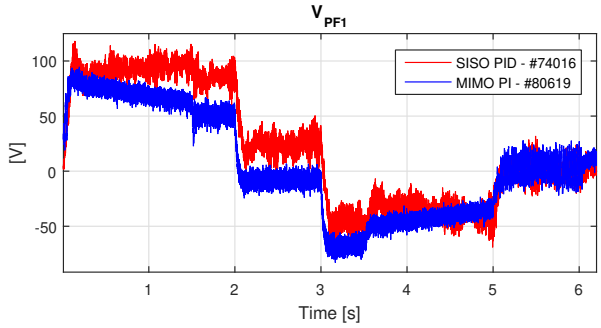

Figure 73: Comparison between PF1 voltage requests during EAST plasmaless pulses #74016 (SISO PID) and #80619 (MIMO PI). The control actions are comparable.

decoupling of the two controlled variables, and thus it was not modified[6]. At this point, the controller parameters could be tuned on the obtained transfer functions, and then tested in closed-loop simulations to assess the controller performances.

With the introduction of the PFC MIMO controller, the design of the centroid position controller became much easier. Indeed, after the PFC current controller was succesfully implemented and tested, a new RZIP control was also designed on the basis of a simplified model (see end of sec. 5.2.1). Experimental tests of this new controller are expected by the end of 2018.

A brief remark on the plasma current control to conclude this section. One of the main issues encountered in the early phases of this work was the lack of a proper bumpless transfer strategy when passing from RZIP to isoflux control. In fact, RZIP and isoflux are defined as two separate *control phases* in the PCS software, which means that the isoflux controller starts processing the control error only after the switch; thus, at the switching instant, all the integrators in the PID controllers were unloaded. In partcular, this was true of the Ip controller, which initially was embedded in the RZIP/isoflux one. When switching from one to another, the integral action

6 It is worth to remark that the PFC system of EAST is up-down symmetric (see sec. 5.4).

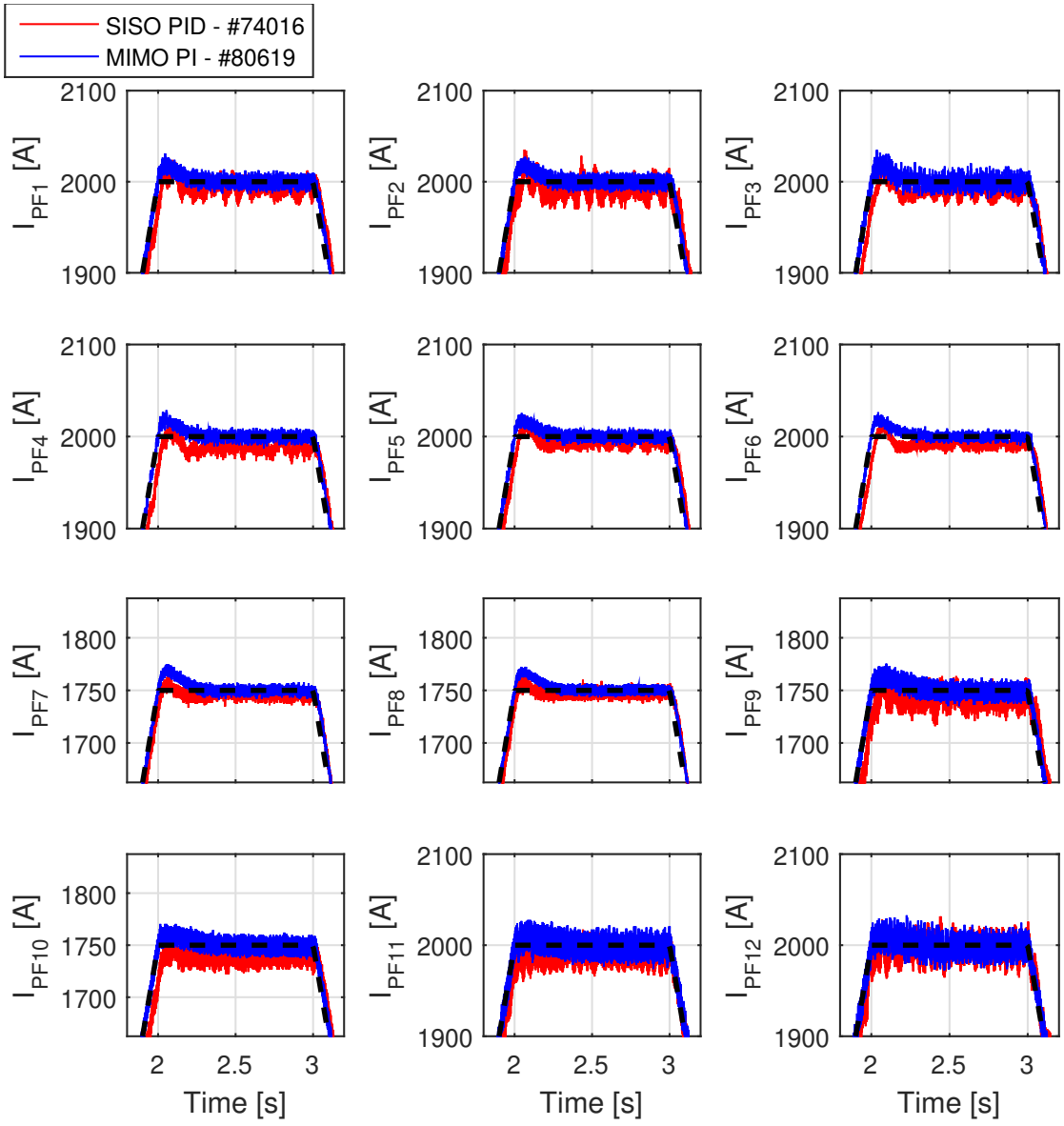

Figure 74: Comparison between PF1-12 measured currents during EAST plasmaless pulses #74016 (SISO PID) and #80619 (MIMO PI).

of the plasma current control loop was reset, yielding considerable bump which had a catastrophic effect on the overall control architecture performance (this also happened at the transition from one RZIP controller to another; see, for example, fig. 67). Actually, the transition from RZIP to

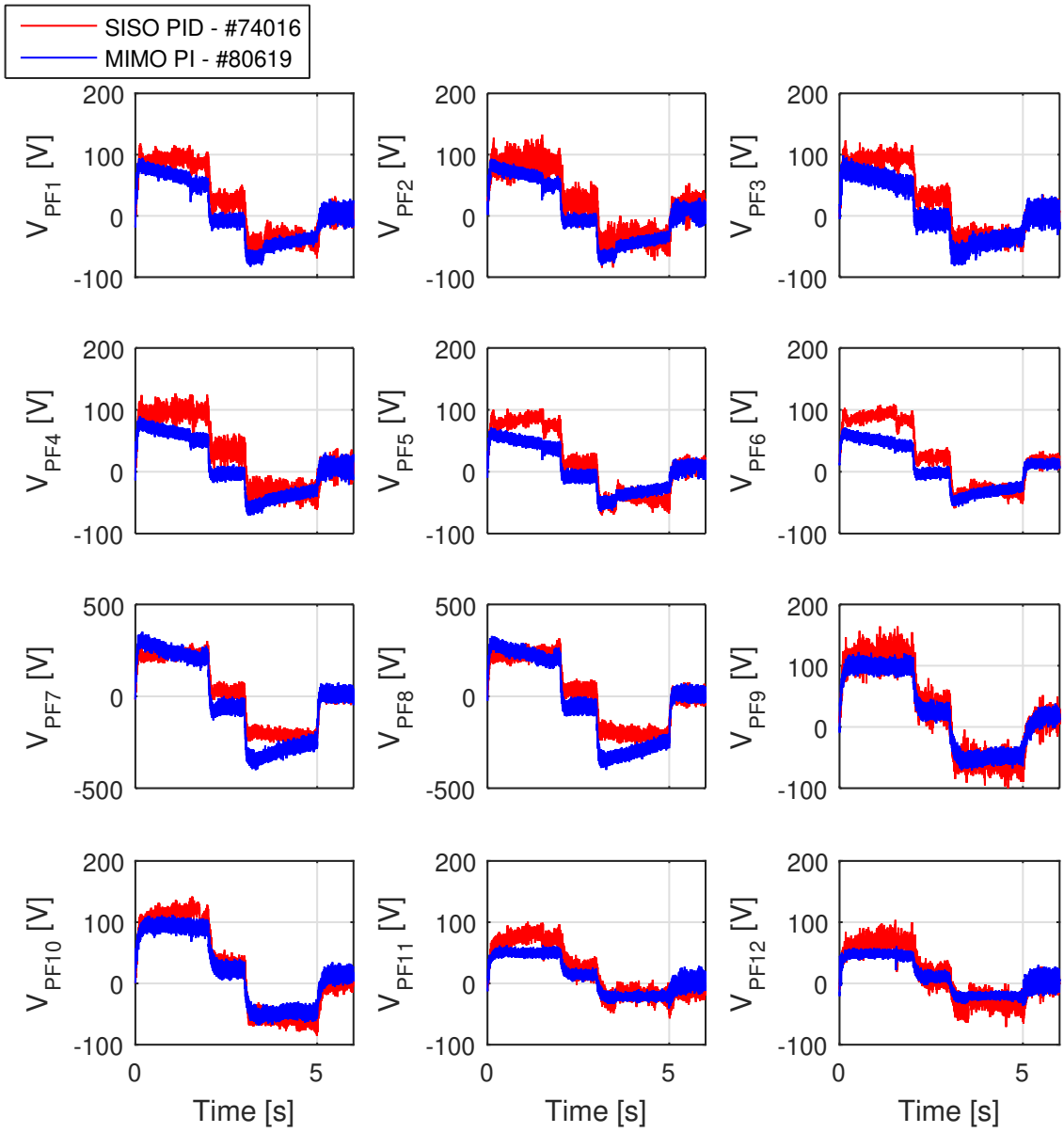

Figure 75: Comparison between PF1-12 voltage requests during EAST plasmaless pulses #74016 (SISO PID) and #80619 (MIMO PI). The control actions are comparable.

isoflux took place over a finite time interval $[t_i, t_f]$ (whose length is usually set to 0.05 to 0.1 s), i. e. as

$$u(t) = \frac{t - t_i}{t_f - t_i} u_{isoflux}(t) + \frac{t_f - t}{t_f - t_i} u_{RZIP}(t)$$

However, this device was not enough to solve the issue. The problem has been partially solved by defining a separated *control category* for the I_p controller which is active during all the discharge in parallel to the position/shape control; in this way, the reset of the integral action of the I_p controller after the switch was avoided. A further improvement was achieved after the introduction of PEFIT, since the isoflux error was also made to go smoothly from zero to the actual value at the beginning of the isoflux phase. Nevertheless, the lack of a bumpless transfer procedure and of an anti-windup logic for the PIDs has been of the main obstacles to the completion of this work.

7.3.1 *Experimental results*

In this section some experimental results are reported.

Fig. 76 shows the results obtained in pulse #70800, where a model-based RZIP controller was active from 2.14 s to 3.3 s, together with the ITER-like VS presented in sec. 5.1. A bump on the plasma current due to the transition to the new RZIP controller can be seen in the first plot.

Similar considerations hold for pulse #70131. The results were shown in fig. 67 (sec. 7.1.4).

7.4 A MIMO ARCHITECTURE FOR PLASMA SHAPE CONTROL

As it was discussed at the beginning of this chapter, the main aim of the experimental activity carried out at EAST was that of developing an efficient strategy for plasma shape control. This issue was faced with a shape controller design similar to the one proposed in sec. 5.5.

The previously existing control approach is discussed in sec. 7.4.1. Sec. 7.4.2 briefly describes the proposed MIMO decoupling algorithm. Finally, sec. 7.4.3 reports on some experimental results.

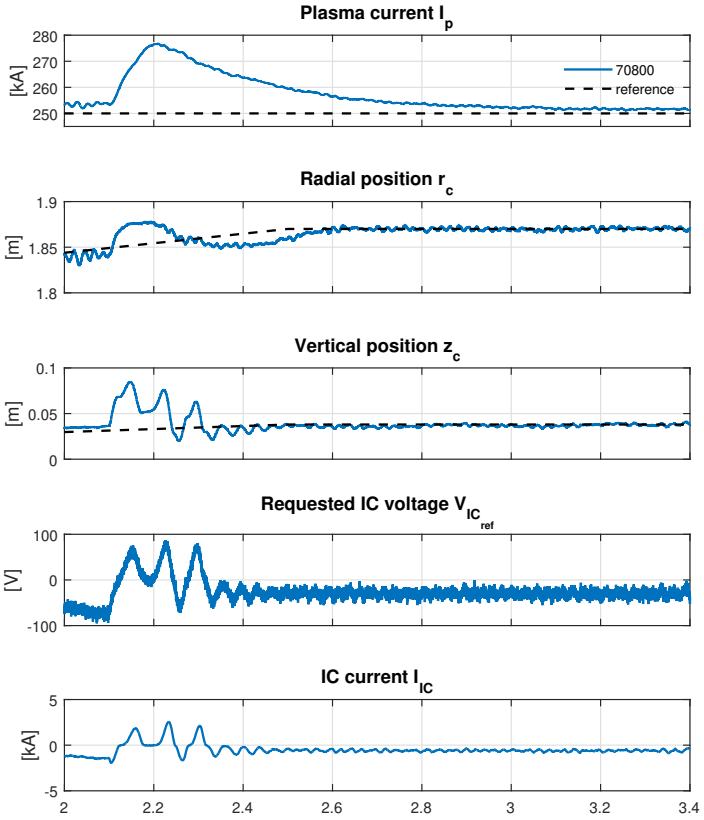

Figure 76: Time traces for the EAST pulse #70800, during which both the new VS and the model-based centroid position control were enabled from t = 2.1 s to t = 3.3 s.

7.4.1 *Isoflux control at EAST*

As it was discussed in chapter 4, one of the tasks that must be accomplished by plasma magnetic control consists in controlling the shape of the plasma boundary, which can be identified with the LCFS. This is usually done in two ways:

- *Isoflux control*: a finite set of points is chosen along the desired plasma boundary. The value of the poloidal flux in these points is controlled the one estimated at the desired X-point/limiter point location. Equivalently, the difference between the poloidal flux at these points and

at the null/limiter point can be regulated to zero. In addition, the X-point/limiter point position is also controlled, either by closing a loop directly on the radial and vertical coordinates or by controlling the poloidal field in that point to zero. Multiple X-points can be controlled, e. g. for magnetic configurations such as double-null plasmas;

- *Gap control*: the distance between the LCFS and the first wall along a given set of straight segments is controlled to a desired value.

The shape control problem at EAST is usually tackled with an *isoflux* approach (even though a gap controller was under development during the experimental campaign of summer 2018). During a pulse, up to 13 flux differences between a set of given boundary points and the X-point can be controlled by the PCS, but in general only 7-8 of them are actually controlled. The controlled boundary points are placed at the intersection of the desired boundary with a set of *control segments*, defined in the PCS; for this reason, in what follows we will refer to them as control points or control segments equivalently.

It is worth to remark that, since the poloidal flux at the control points cannot be directly measured, a real-time reconstruction code is needed. The codes used at EAST are RT-EFIT [85] and, more recently, the more accurate PEFIT [87][7]; in particular, PEFIT is a parallelized version of EFIT which relies on the CUDA architecture, allowing to solve the Grad-Shafranov equation over a much finer grid (129×129 points with respect to the 33×33 of RT-EFIT). From the point of view of the magnetic control system, the outputs of RT-EFIT are the desired flux differences and the X-point(s) position, while PEFIT also provides the magnetic field at the null-point target position[8]. Furthermore, after the introduction of PEFIT, a smooth transition procedure was also implemented, which gradually brings the errors seen from the shape controller from zero to their actual value (usually with a

7 The offline version of EFIT [121] is used instead for post-discharge analyses.
8 Controlling to zero the two components of the magnetic field at a desired location is equivalent to controlling the position of a null point.

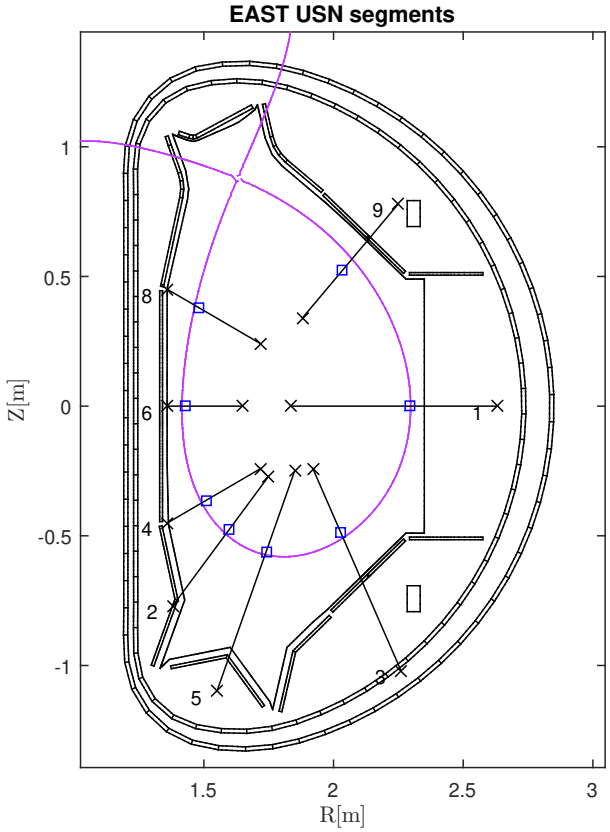

Figure 77: Control segments for a USN configuration (pulse #78289). The control points are indicated by the blue squares. The figure shows only the segments that are actually controlled by the PCS.

transition time of ~0.3 s). This device solved some of the bumpy transfer issues that were common when the controller switched from RZIP to isoflux in the previous experiments.

The controller consists of a set of PIDs; one (or sometimes two) PFCs are used to control each segment or X-point coordinate/poloidal field component, in a SISO (or SIMO) fashion.

7.4.2 *MIMO Isoflux control*

To enhance the performances of EAST's shape controller, a MIMO control algorithm was designed and deployed, following the approach described

in sec. 5.5. In order to avoid large control actions, a truncated SVD can be considered by neglecting the singular values which are lower than a given treshold (see also sec. 5.5). In fig. 78 $C\tilde{C}^{\dagger}$ is reported when the three lowest singular values are removed.

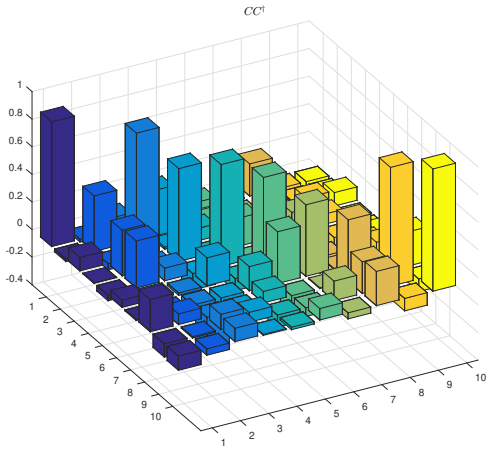

Figure 78: Matrix multiplication C $\tilde{C}^{\dagger}$ when 3 singular values are removed.

The shape controller has been designed with an isoflux approach (see chapter 4). Furthermore, when all the regulators have the same transfer function (see sec. 5.5) the controller structure is the same used by the EAST PCS, i.e. a set of PIDs followed by a matrix which distributes the control actions to the PF coils. Hence, the controller can be implemented without additional programming; the only differences are that now the *M-matrix*[9] is not sparse anymore, and the PID controllers need to be equal on all the control channels.

7.4.3 *Experimental results*

Figs. 79-80 show a comparison between the previous SISO shape controller (pulse #78140) and the proposed MIMO shape control (pulse #79289). Both pulses are ohmic USN discharges at $I_p = 250$ kA. During pulse #78140

9 See fig. 46.

the X-point position was directly controlled, while during pulse #78140 the null point position control was achieved by regulating to zero the poloidal field at the target location. During the proposed experiment, the PFC MIMO controller commissioning was not complete, and thus the SISO PID controller was used to track the PF currents. However, the argument discussed above still holds partially if we assume that the internal PFC current control loop is fast enough with respect to the shape controller, i. e. $\delta \mathbf{I}_{\mathrm{PF}} \cong \delta \mathbf{I}_{\mathrm{PF}_{\mathrm{ref}}}$. The only difference is that a simple tuning of the controller parameters as described in sec. 7.4.2 in principle is not possible, and thus it must be carried out experimentally or taking into account more detailed models of the inner control loop behavior.

Experiments which make use of the new PFC current controller are expected by the end of 2018.

7.5 CONTROL OF ALTERNATIVE DIVERTOR CONFIGURATIONS

As it was discussed in 6.1, the final aim of the proposed magnetic control architecture is to provide a sound and flexible framework for the feedback control of alternative divertor magnetic configurations. Some preliminary results are presented in this section.

One possibility to achieve this goal is to directly control the magnetic configuration of the plasma in order to increase the *flux expansion* in the divertor region. In order to get a simple physical picture, let us consider two flux surfaces separated by a given flux difference $\delta\psi$. We can imagine the Scrape-Off Layer (SOL) region between these two magnetic surfaces as a flux tube, in which the particles are forced to flow due to the magnetic confinement. If the section of this flux tube increases, the hot gas which flows towards the divertor expands; as a consequence, it cools down and deposits the heat flux over a wider divertor area. One possibility to increase the distance between two flux surfaces is to directly shape the poloidal cross section of the isoflux surfaces in the region of interest by controlling a set

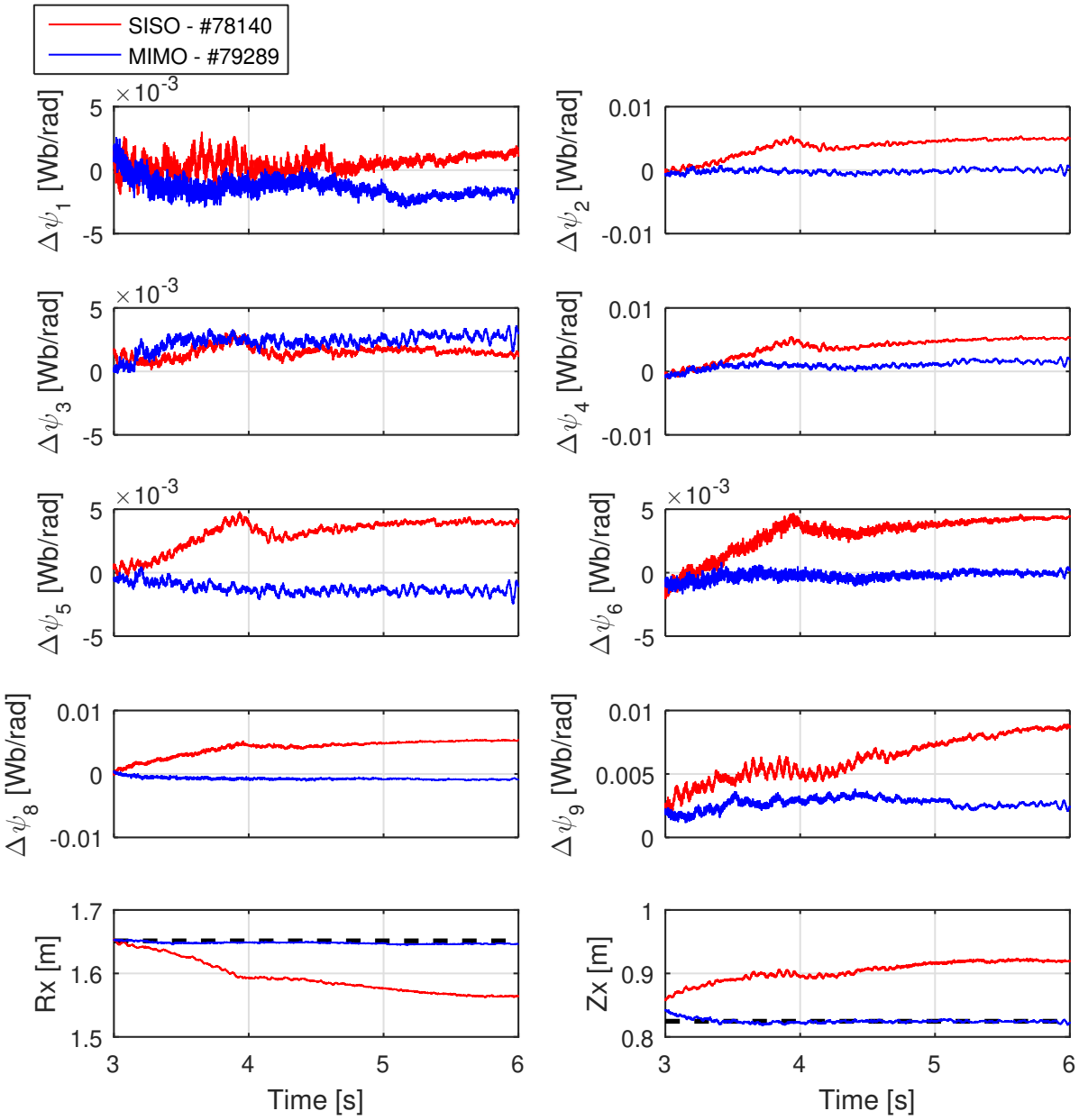

Figure 79: Comparison between the SISO and MIMO shape controllers (pulses #78140 and #79289). The new decoupling strategy provides a dramatic improvement of the controller performances. The dashed black line in the last two plots represents the X-point position reference.

of flux differences to a desired value (which, in this case, may be different

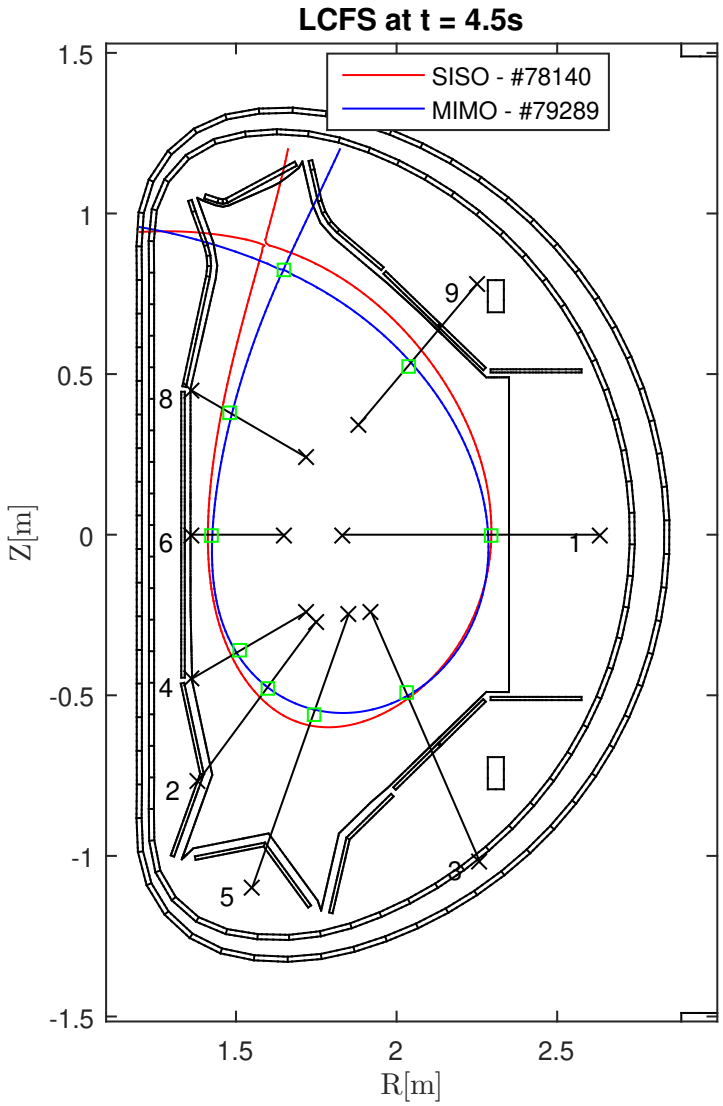

Figure 80: Comparison between the SISO and MIMO shape controllers (pulses #78140 and #79289). The LCFS at t = 4.5 s is shown together with the control points and the target X-point position.

from zero). As an example, consider fig. 81. A possible set of flux differences is given by

$$\chi_1 = \psi'_O - \psi_O \,, \tag{106a}$$

$$\chi_2 = \psi'_P - \psi_P \,, \tag{106b}$$

$$\chi_3 = \psi'_Q - \psi_Q \,. \tag{106c}$$

The new flux differences can be easily included among the controlled outputs exploiting an SVD-based procedure similar to the one described in sec. 7.4.2.

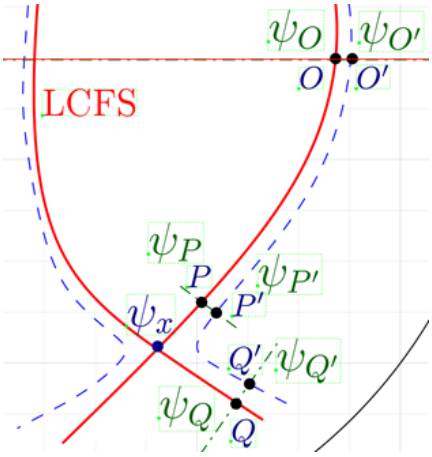

Figure 81: Reference scenario for the control of the flux expansion using isoflux control. The plasma shape controller should be able of regulating the flux differences $\chi_1 = \psi'_O - \psi_O$, $\chi_2 = \psi'_P - \psi_P$ and $\chi_3 = \psi'_Q - \psi_Q$, to a given value while controlling simultaneously the overall shape.

In what follows, a simple simulation example will be presented. Starting from the plasma configuration of pulse #78290 (fig. 82) -an USN discharge where the MIMO shape controller proposed in 5.5 was used- an additional control point has been placed in the surroundings of the X-point, as it is shown in fig. 83. This control point was chosen at the same vertical coordinate of the equilibrium X-point, but in a position corresponding to the 99% of the equilibrium boundary flux (the corresponding isoflux line is shown in red in fig. 83). Let us call this new control point P. The flux difference $\delta\psi_P = \psi_X - \psi_P$ obtained from the equilibrium has been used as a constant non-zero reference for the isoflux controller on the channel relative to $\delta\psi_P$; this choice is justified by the fact that the poloidal flux generally exhibits a linear behaviour during a plasma discharge. To achieve the desired flux expansion, the new control point has been moved radially outward of 3 cm between $t = 4$ s and $t = 5$ s. The simulation has been performed using the experimental feedforwards and reference signals (except for the new

control point), but including the new MIMO PFC controller 79 (in the experiment, the SISO PFC current control was used). The plasma current controller was also, since the old one was not compatible with the new PFC current controller. The experimental values of β_p and l_i were also considered in the simulation, in order to test the robustness of the controller with respect to the action of the disturbances. The results are shown in figs. 84-88; the experimental values of the experiment -i. e. without the additional control point- are also shown in blue for comparison. [10].

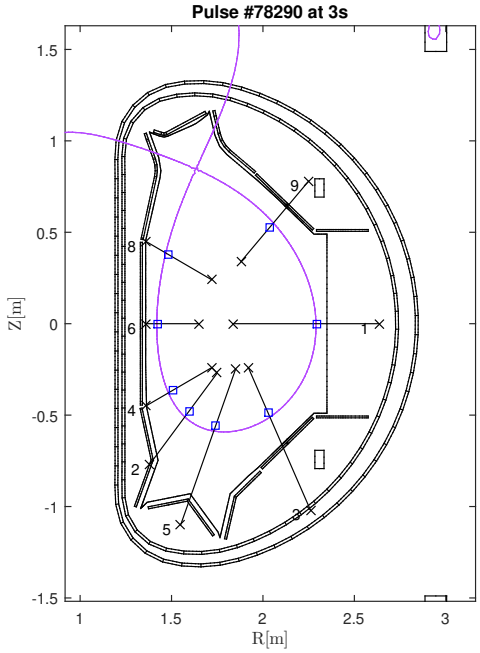

Figure 82: Plasma equilibrium for EAST USN pulse #78290 at $t = 3$ s. The control segments used in the experiment and the target boundary points are also shown.

10 A procedure similar to the one proposed in this section was presented in [12]. Another possibility is to control the position of a secondary null-point, in order to bring the plasma configuration closer to a snowflake one; this kind of configurations is called Quasi-SnowFlake (QSF). Feedback control of QSF configurations is one of the goals to be achieved in the next experimental campaigns. However, the procedure is -at least in principle- equivalent to the one proposed here, since the X-point can be controller in the same way, i. e. by adding it to the output vector in the SVD procedure described in 7.4.2

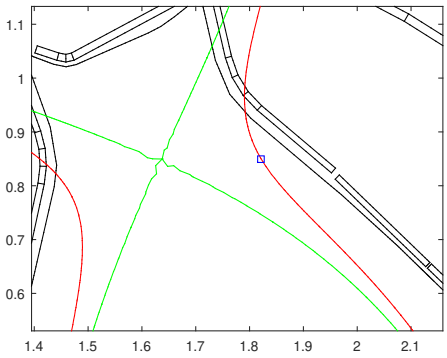

Figure 83: Additional control point added; the equilibrium has been obtained from pulse #78290 at t = 3 s. The green and red lines represent the LCFS and an isoflux line corresponding to the 99% of the boundary flux value.

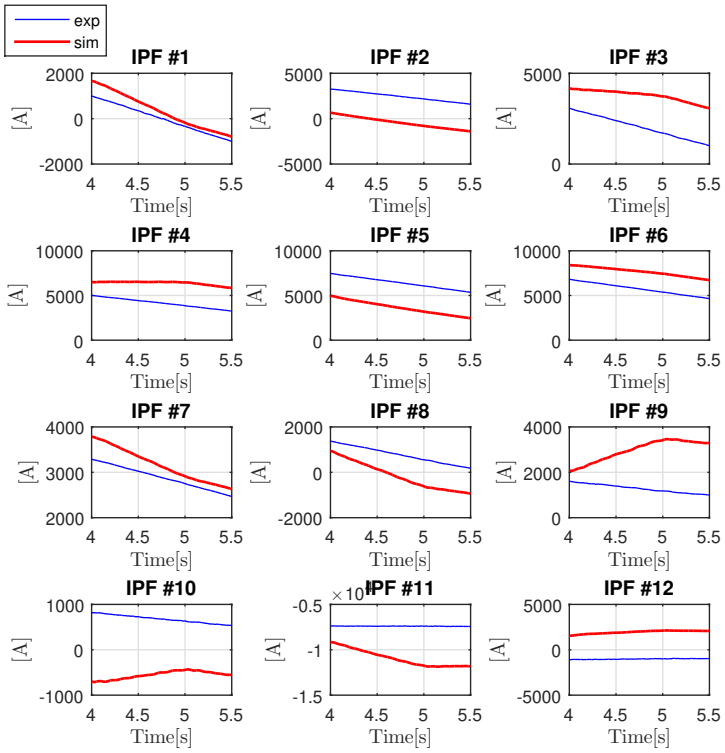

Figure 84: Requested PFC currents.

7.6 EDDY CURRENT ESTIMATION AND SHAPE RECONSTRUCTION VIA KALMAN FILTERING

To conclude this chapter, a possible procedure for the estimation of the eddy currents flowing in the passive structures surrounding the plasma

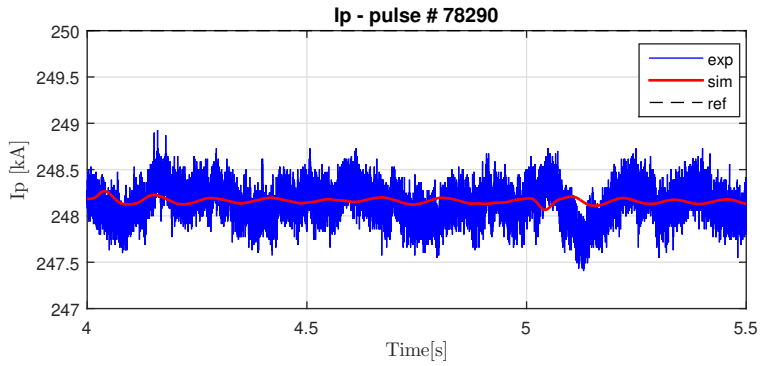

Figure 85: Plasma current.

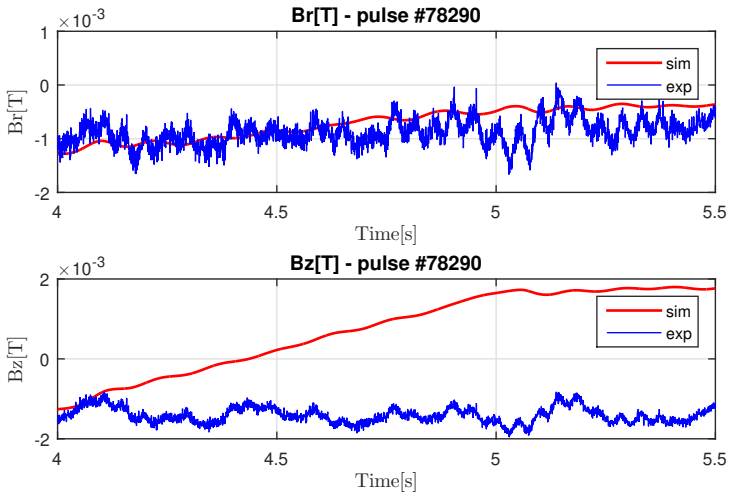

Figure 86: Poloidal field at the X-point reference position.

will be presented. This approach is based on the well known *Kalman filter* optimal observer, and has the advantage of allowing a fast identification of the plasma boundary.

7.6.1 *Introduction*

A fast and reliable algorithm for the reconstruction of the poloidal flux map is a crucial issue for plasma magnetic control, as it was discussed in sec. 7.4.1. Most of the strategies adopted to face this problem entail a real-time solver of the Grad-Shafranov equation. Due too the non-linearity of

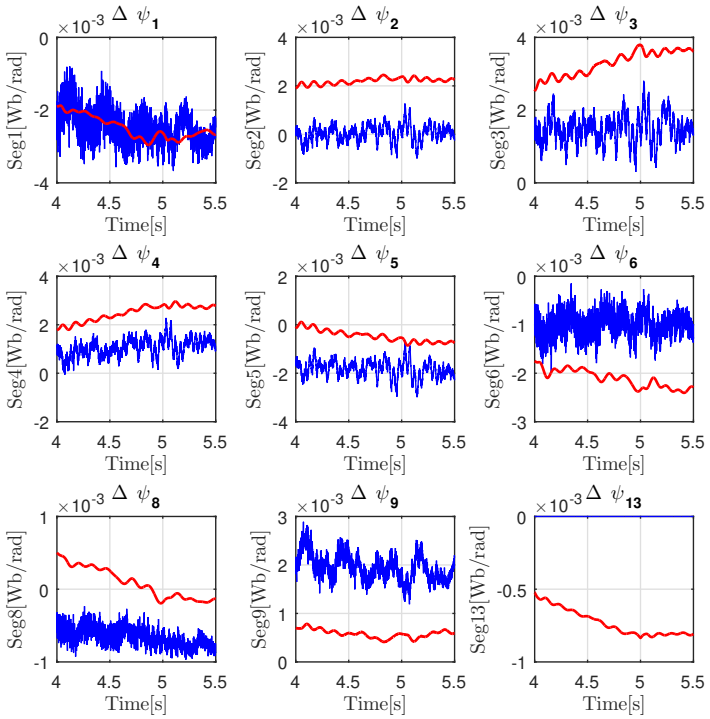

Figure 87: Errors on the controlled flux differences. It can be seen how, adding a new controlled variable, the overall performances worsen. The new controlled flux difference was added on segment #13 (which was not controlled in the experiment). The imposed reference for this new variable is $\sim 4 \cdot 10^{-3}$ Wb/rad.

this equation[11], the solution is usually obtained by means of iterative methods, which can become slow depending on the desired accuracy and the difference between the initial guess and the actual plasma shape. For these reasons, a number of real-time versions of the main reconstruction codes have been realized, which exploit different methods in order to make the reconstruction fast enough. Some examples are RT-EFIT [85], PEFIT [87] and LIUQE [86]. In practice, all of these algorithm only perform one iteration, starting from the solution computed at the previous time instant. Ostensibly, this approach can fail when very fast changes in the plasma are considered. Furthermore, since the eddy currents induced in the pas-

11 See chapter 3 for a detailed discussion of the Grad-Shafranov equation and of the issues related to its solution.

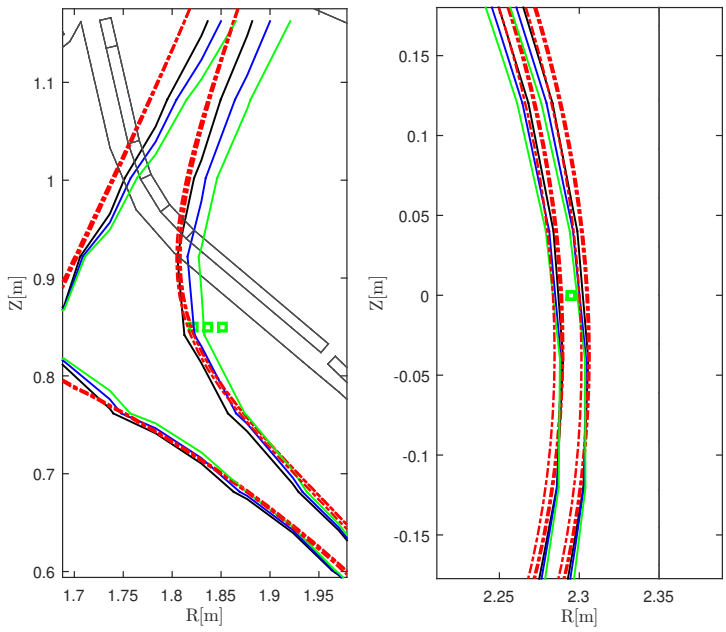

Figure 88: Plasma shape in the divertor region and at the midplane at t = 4, 4.5, and 5 s (black, blue and green lines respectively). It can be seen how the flux surfaces expand in the divertor region, while they are almost unchanged at the midplane. The isoflux lines are not very close to the control points, despite the small ($\sim 10^{-4} Wb/rad$) error (see fig. 87). This is due to the fact that the flux gradient is small near the X-point. The boundaries obtained with EFIT for the experiment (pulse #78290) are also shown for comparison.

sive structures are not directly measurable, these codes often neglect them when solving the Grad-Shafranov equation, renouncing to some significant information. However, this issue has already been addressed at the DIII-D tokamak, where Kalman filtering theory has been used in order to estimate the eddy currents and include them in the real-time equilibrium reconstruction performed by the EFIT code [137].

A possible extension to this approach is proposed here. As it was discussed in sec. 3.3 accurate linearized models for the plasma-circuits interaction can be obtained exploiting the CREATE equilibrium codes [1], [96]. These models can be used as the starting point for a state observer design, which allows to estimate the currents induced in the passive structures.

Furthermore, the output equations (72) yields a static relation between the currents (including plasma) and the flux map. By placing a grid of virtual flux probes over the vacuum chamber, this approach brings along a fast and accurate reconstruction of the plasma shape, which can be exploited for magnetic control purposes.

Possible extensions to the preliminary approach proposed here can be considered. To achieve better performances in a real-time implementation, the matrices of the linearized model used by the filter could be updated during the pulse (e.g. by considering different snapshots of the plasma scenario and scheduling the matrices to be used according to the respective linearized models). Furthermore, an extended Kalman filter could be used to take into account some nonlinear effects. Finally, the effect of β_p and l_i variations have been neglected here; an estimate of these quantities could be used to further increase the amount of information available to the observer.

7.6.2 *Recursive Kalman filter*

The Kalman filter [138] is an algorithm which is used to estimate the state of a dynamical system starting from known inputs to the system and output measurements affected by uncertainty. The filter provides an efficient state estimation for systems with modeling uncertainties and measurement noise, and is proved to be optimal when the model perfectly matches the actual system, the entering noise is white and gaussian and the covariance matrices of the noise are known. At every step, the filter combines the previous estimate of the state with the inputs/outputs to the system in order to give a best guess of its internal state: indeed, the filter works in a recursive fashion. The structure is similar to that of the classical Luenberger Observer, but the observer gain is chosen on the basis of the noise covariance matrices (i.e., the filter "trusts more" the measurements which are affected by a lower uncertainty).

Given a linear dynamical system in the form:

$$\dot{x}(k+1) = Ax(k) + Bu(k) + v_x(k) \tag{107}$$

$$y(k) = Cx(k) + v_y(k) \tag{108}$$

with $v_x(k)$ and $v_y(k)$ gaussian, uncorrelated and with zero average, and

$$Q = var[v_x] \qquad R = var[v_y] \qquad N = var[v_x, v_y]$$

it can be demonstrated that the optimal bayesian linear estimator of the state variables is given by

$$L(k) = P(k|k-1)C^T \left[CP(k|k-1)C^T + R\right]^{-} 1 \tag{109}$$

$$\hat{x}(k|k) = \hat{x}(k|k-1) + L(k)\left[y(k) - C\hat{x}(k|k-1)\right] \tag{110}$$

$$P(k|k) = [I - L(k)C]\, P(k|k-1) \tag{111}$$

$$\hat{x}(k+1|k) = A\hat{x}(k|k) + Bu(k+1) \tag{112}$$

$$P(k+1|k) = AP(k|k)A^T + BQB^T \tag{113}$$

Equation (109) gives the expression for the Kalman filter gain at the time instant k. Equations (110) and (111), instead, represent the *measurement update* phase, where the new estimate of the state variables is generated. Finally, equations (112) and (113) constitute the *time update* phase, during which the prediction of the state variables and the error covariance matrix P are projected one time step forward (from k to $k+1$).

It is important to remark that a tokamak plasma is far from being a linear system. Nevertheless, in the neighborhood of a given equilibrium, the plasma behavior can be well approximated by a linearized model in the form (70).

7.6.3 *Application to the EAST tokamak*

To test the proposed algorithm, a collection of 10 EAST *quasi-snowflake* USN pulses has been used [139]. The reference numbers of these experiments are 7130, 71308, 71309, 71372, 71375, 71379, 71380, 71381, 71382, 71464. A single linearized model was generated using the data related to pulse 71307 at 4 s and then used for all the other pulses, in order to verify that the same model provides a good response even for different plasma discharges. In this way, in a realistic control-room situation, the linearized model obtained using data from the designed scenario (or from a similar discharge done before) should work also for a new experiment, provided that the controller succeeds in keeping the plasma parameters near to the desired values.

On the EAST tokamak, 43 field measurements and 35 poloidal flux probes are available. Of these, the ones used for the simulation are shown in Fig. 89 (some of the field sensors were removed because their measurements were judged unreliable).

The inputs to the filter were the output vector (magnetic probes and plasma current) and the measured PFC and IC currents. The PFC and In-Vessel circuits can be treated as if they were current-driven by the procedure described in sec. 6.3. Actually, the plasma current can be treated both as an input current or as a measured output; both strategies proved to be effective. The covariance matrices R, Q were estimated starting from the experimental data of pulse 73107.

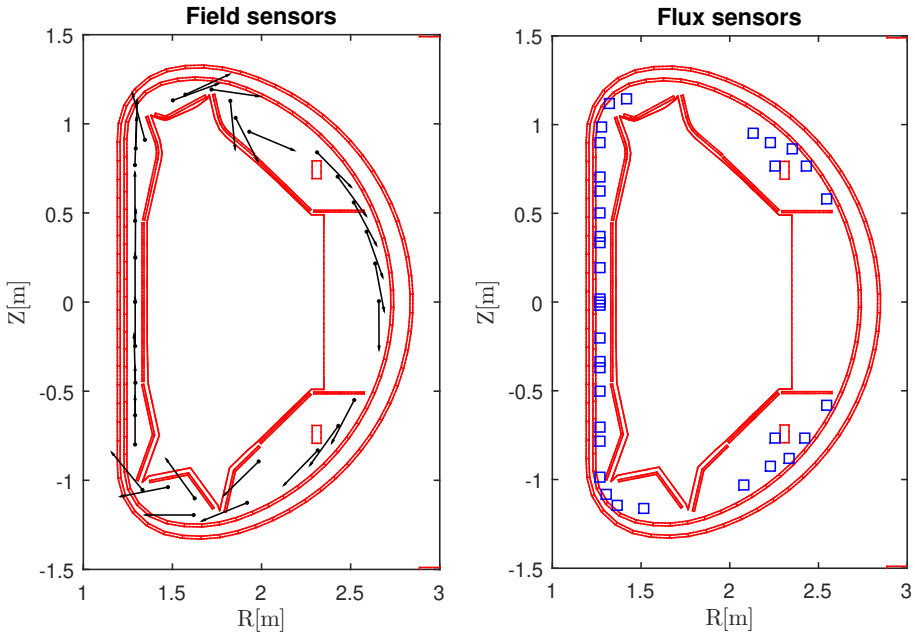

Figure 89: Field and Flux sensors used for the simulations.

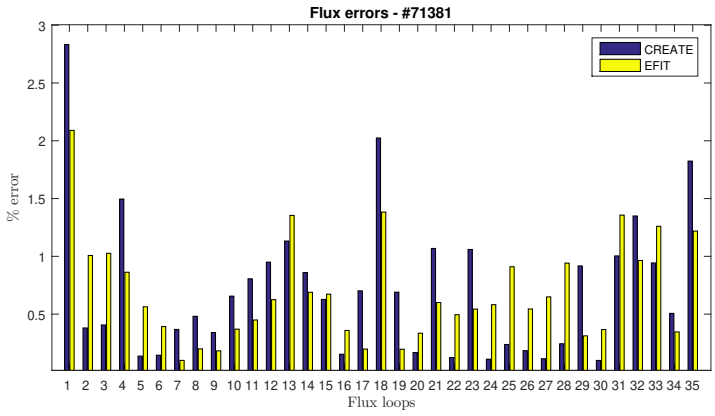

Figure 90: Mean error between the experimental the flux probes traces and the estimates of EFIT and the approach proposed here (labeled as CREATE in the figure). The errors are comparable and always under the 3% of the total poloidal flux.

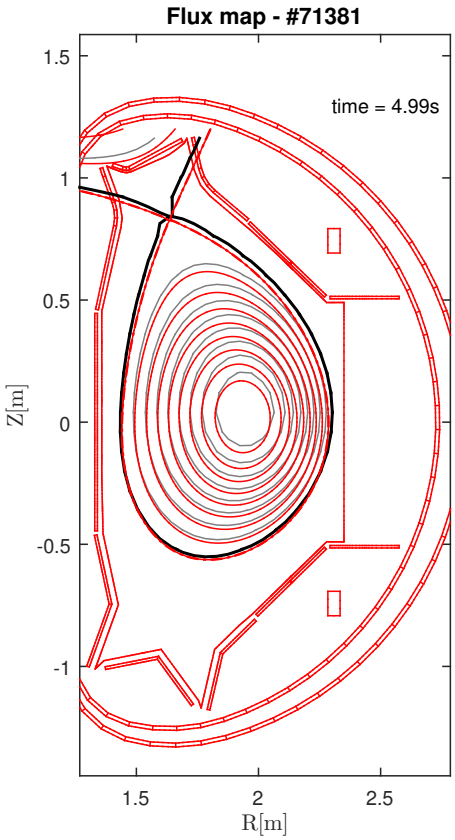

Figure 91: Comparison between the estimated flux map (in gray) and the one computed by EFIT (in red) for pulse #71381 at t $\cong$ 5 s.

8

PRELIMINARY STUDIES FOR THE JT-60SA TOKAMAK

"The thing to judge in any Jazz artist is,
does the man project and does he have ideas. "

— Miles Davis

Japan and the European Union stipulated an agreement, named Broader Approach (BA)[140], with the aim of accelerating the realization of fusion energy by carrying out R&D and by developing some advanced technologies for future demonstration fusion power plants. The main project under the BA agreement is the Satellite Tokamak Programme (STP), which includes the construction of the JT-60SA superconductive tokamak and its exploitation as an ITER satellite facility [141, 142]. The STP is expected to develop operating scenarios and address key physics issues to support ITER's start-up and experimentation. In fact, it is expected that the operation of JT-60SA will complement that of ITER in the areas of fusion R&D which are necessary to proceed towards the design and realization of DEMO[143].

European scientists are actively contributing to the definition of the JT-60SA research plan [144], and an active involvement of a European team in the operation of this forthcoming tokamak is foreseen. For this reason, the European fusion community is carrying out preliminary studies related to the exploitation of the device in different research fields. Besides a participation in the physics experiment, the EU also aims at giving engineering support to the operations [144, 145].

In this context, several tools for the design and validation of control systems are being developed in Europe; this is true also for what concerns magnetic axisymmetric control. Within a dedicated Eurofusion workpackage, the CREATE tools have been exploited to perform preliminary studies on plasma magnetic control at JT-60SA.

8.1 DESCRIPTION OF THE MACHINE

The JT-60SA tokamak is currently under construction in Naka, in the Ibaraki Prefecture of Japan. Its plasma will have a major radius of 2.96 m and a minor radius of 1.18 m, with an overall plasma volume of 132 m^3 [141]; the maximum foreseen plasma current is 5.5 MA for a plasma with a relatively low aspect ratio (elongation $\kappa = 1.93$ and triangularity $\delta = 0.53$), and 4.6 MA for an *ITER-shaped* plasma ($\kappa = 1.8$ and $\delta = 0.43$). JT-60SA pulses will last up to a few hundreds of seconds [143, 146].

After the machine upgrade is completed, JT-60SA will be equipped with a PFC system consisting of two sets of superconductive coils. The first is composed by the six Niobium-Titanium (NbTi) Equilibrium Field Coils (EFC), while the second is made up of four independent Niobium-Tin (Nb_3Sn) coils, which constitute the CS. Furthermore, two in-vessel copper Fast Plasma Position Coils (FPPC) will also be installed. Fig. 92 shows the PFC layout of JT-60SA.

8.2 CONTROLLER DESIGN

The control architecture described in chapter 5 and applied to the EAST tokamak in chapter 7 has been adapted to the JT-60SA device. A simplified block diagram is shown in fig. 93.

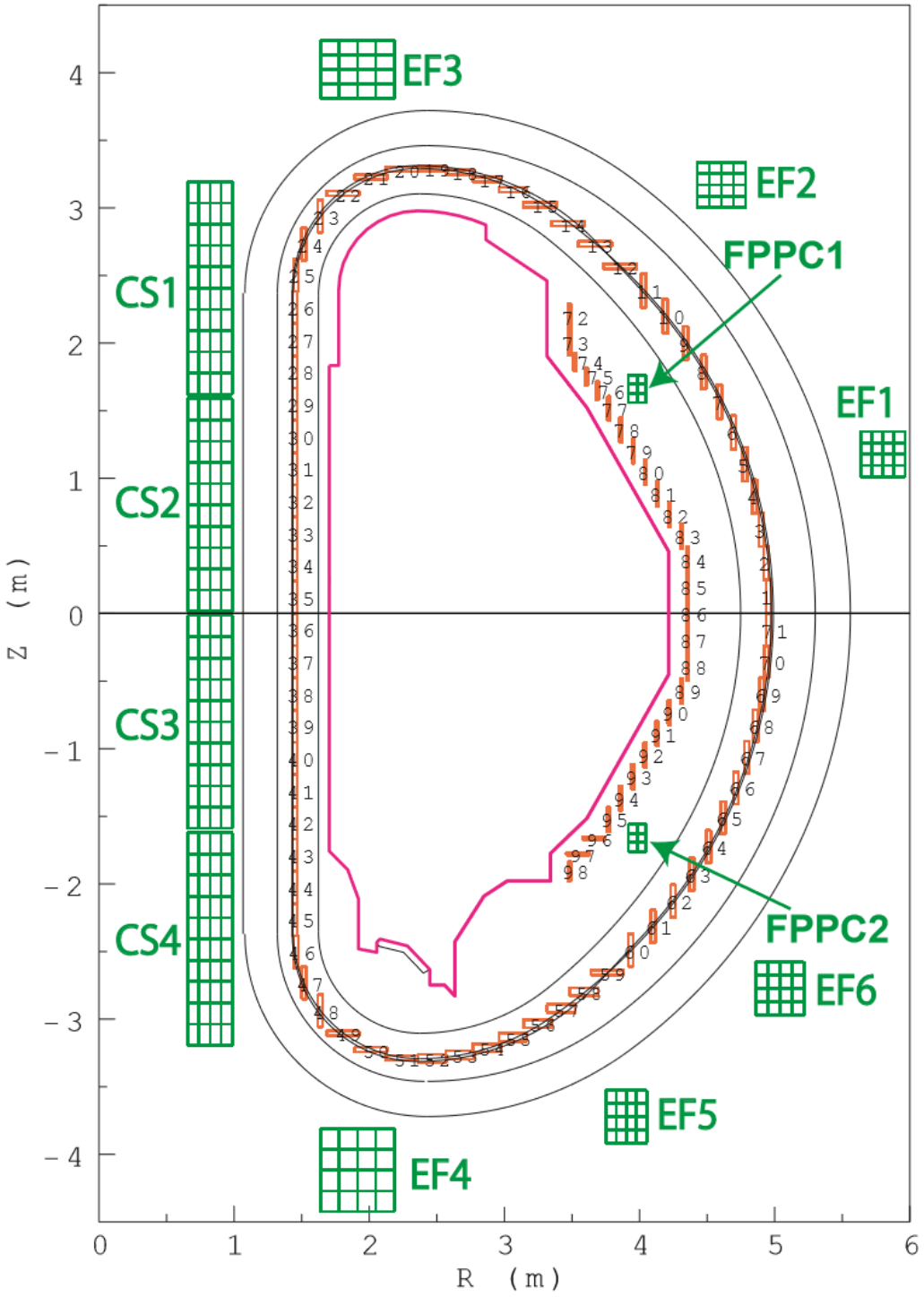

Figure 92: JT-60SA poloidal cross-section and layout of the PFC system.

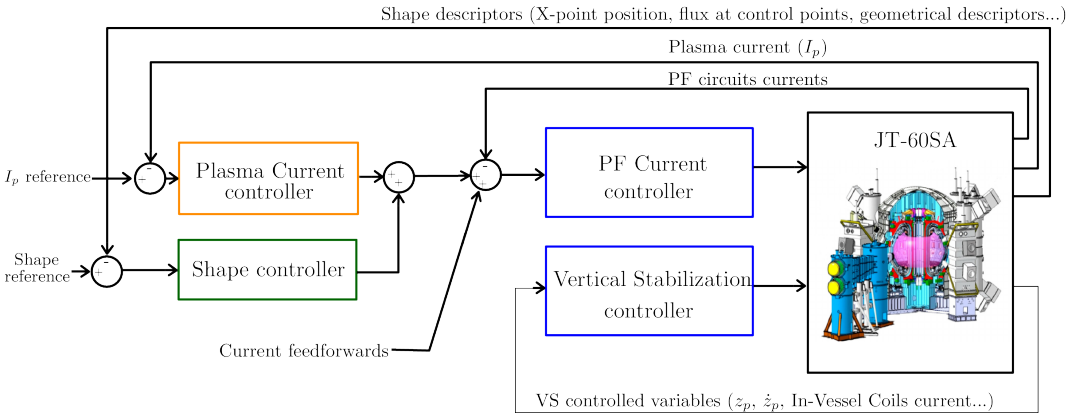

Figure 93: Proposed magnetic control architecture for the JT-60SA tokamak.

8.2.1 *Vertical Stabilization system*

The VS system computes the voltage requests to the FPPC coils as a linear combination of the vertical velocity of the plasma and of the FPPC *imbalance* current. As in EAST, the two in-vessel coils are up-down symmetric and driven in anti-series. For this reason, the VS system can consider the FPPC coils as a single circuit, where $I_{FPPC}(t)$ is the imbalance current between the two coils, and $V_{FPPC_{ref}}(t)$ is the voltage, which must be applied with opposite signs to the coils.

The resulting control law is

$$V_{FPPC_{ref}}(t) = k_1 I_{FPPC}(t) + k_2 \dot{z}_p(t) \tag{114}$$

As it was discussed in sec. 7.1, the controller aims at regulating to zero the plasma vertical velocity while maintaining the imbalance current $I_{FPPC}(t)$ far from the saturation limits.

Again, the controller parameters do not need to be changed from one scenario to another; furthermore, in this case the lead compensator was not necessary. As usual, the only exception is the gain k_2, which must be scaled according to the plasma current reference $I_{p_{ref}}$.

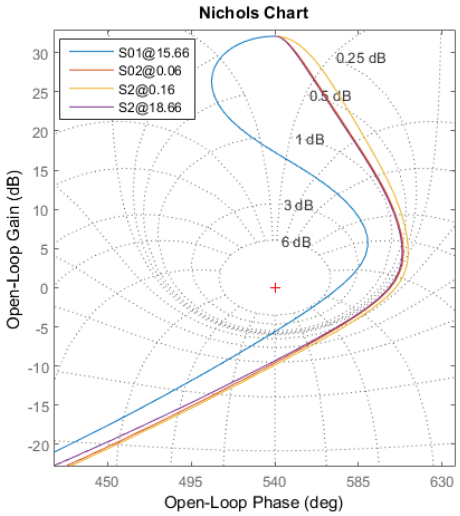

Figure 94: Nichols plots for the VS system for Scenario 1 and Scenario 2.

To assess the robustness of the VS system, the open-loop transfer function between $V_{FPPC}(t)$ and the linear combination $k_1 I_{FPPC}(t) + k_2 \dot{z}_p(t)$ has been considered, in the same way discussed in sec. 7.1.3. As an example, the Nichols plots obtained with linearized models of *Scenario 1* at $t = 15.66$ s, and of *Scenario 2* at $t = 0.06$, 0.16 and $t = 18.66$ s [146, Sec. 1.2] are shown in fig. 94. As it can be seen, the gain margin stays in the range $[5.58, 9.83]$ dB, while the phase margin is in the interval $[34.4, 65.0]$ degrees.

The possibility of using a near-time-optimal VS controller has also been explored. For brevity, it will not be discussed here; interested readers are referred to [14].

8.2.2 *PF Currents Decoupling Controller*

A PFC current decoupling controller like (77) has been tested for JT-60SA. No integral action was included in the design of the controller, since the PFC have been supposed to be perfectly superconducting. In real operation, the integral action can be included easily; alternatively, the ohmic drop can be compensated via a feedforward action (see sec. 5.2).

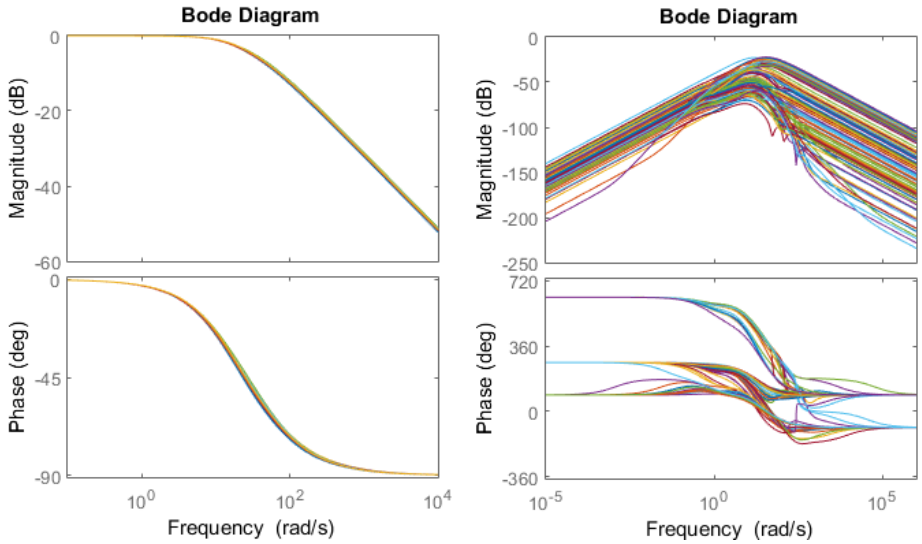

Figure 95: Bode diagrams of the closed loop system obtained with the PFC-MIMO decoupling controller (77). The diagonal channels (from the $i-th$ voltage to the $i-th$ current) exhibit very similar dynamic responses, while the off-diagonal channels have a much lower magnitude, proving the effectiveness of the decoupling.

The bode diagrams of the closed loop PF coils current control system are shown in fig. 95.

8.2.3 *Plasma Current controller*

The Plasma Current control problem has been solved adopting a simple PID control logic. The current references for the CS and EFC coils are calculated as

$$\mathbf{I}_{PF}(s) = \mathbf{K}_{p_{curr}} \left(k_P + k_I \frac{1}{1+s\tau_I} + k_D \frac{s\tau_D}{1+s\tau_D} \right) I_{p_e}(s)\,, \tag{115}$$

where $I_{p_e}(s) = I_{p_{ref}}(s) - I_p(s)$ is the Laplace transform of the plasma current control error, while $\mathbf{K}_{p_{curr}}$ is the vector containing the *transformer currents*, obtained via an optimization procedure, based on a plasmaless model of the machine (see sec. 5.3).

Similarly to what has been seen for the vertical stabilization algorithm (114), the PID parameters in (115) can be tuned using SISO control design tools on the basis of open-loop transfer function between the considered linear combination of PFC currents and the plasma current.

8.2.4 *Shape controller*

The controller design procedure is the same described in sec. 5.5. Both *isoflux* and *gap* control have been tested. The results are discussed in sec. 8.3.

8.3 SIMULATION RESULTS

8.3.1 *Isoflux control*

In this section some results obtained with the *isoflux* shape controller are discussed. A set of 10 control points was chosen, including the two strike points on the divertor plates (see fig. 96). A linearized model has been generated for Scenario 2 at the Start Of Flat-top (SOF) (i.e. $t = 18.66$ s, $I_p = 5.5$ MA, $\beta_p = 0.53$, $l_i = 0.85$) [146, Sec. 1.2]. The PFC and FPPC power supplies have been modelled as first order systems with a 3 ms time constant, a pure delay of 1.5 ms and a voltage saturation.

A transition from the configuration described above and that of Scenario 2 at the End Of Flat-top (EOF) (i.e. $t = 116.46$ s, $I_p = 5.5$ MA, $\beta_p = 0.80$, $l_i = 0.75$) has been considered. In the simulation, this transition takes place between $t = 0$ s and $t = 5$ s. The PFC feedforwards have been chosen as ramps which start from the nominal currents of the first configuration and approach those of the second one at the end of the transition time interval; after $t = 5$ s, the scenario currents are kept constant. Furthermore, the plasma current reference drops from 5.5 MA to 5.0 MA over the same transition time interval. The initial time for the simulation was set to -3 s, in order to eliminate the initial spurious transients. The initial and final ref-

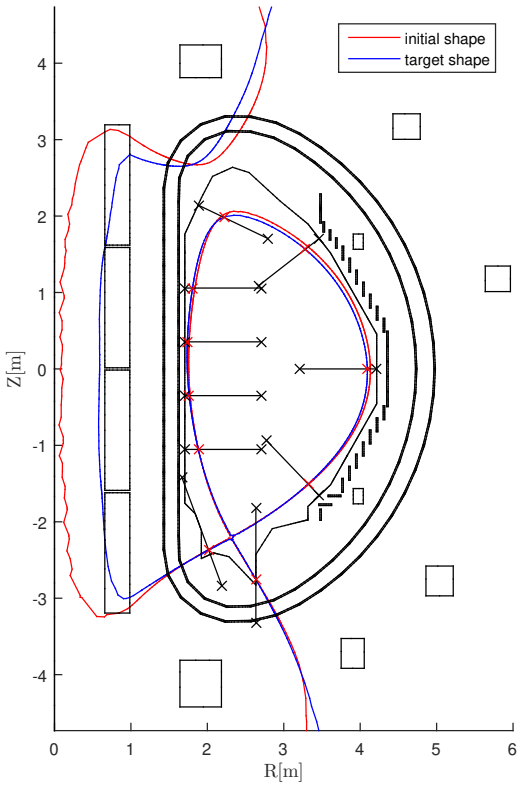

Figure 96: Initial and final plasma configurations for the simulation shown below. The black lines represent the used control segments (including the strike points).

erence shapes are shown in fig. 96, while the traces for β_p and l_i are shown in fig. 97. Figs. 98-102 show the obtained results in terms of PFC currents, plasma current, null-point position, controlled flux differences and plasma shape.

To conclude this section, it is worth to notice that, all the controlled variables have been obtained from the CREATE linearized model. However, in the future a block containing the actual machine reconstruction code could be easily included in the simulink architecture, in order to take into account the nonlinearities due to the reconstruction when validating the control algorithms (see [111]).

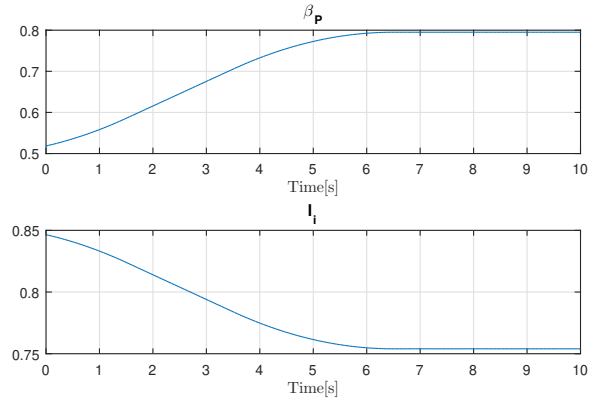

Figure 97: Time traces of β_p and l_i.

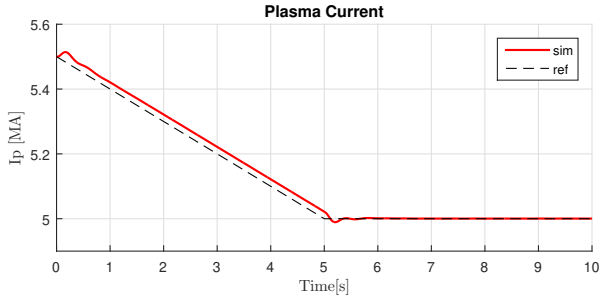

Figure 98: Simulated plasma current.

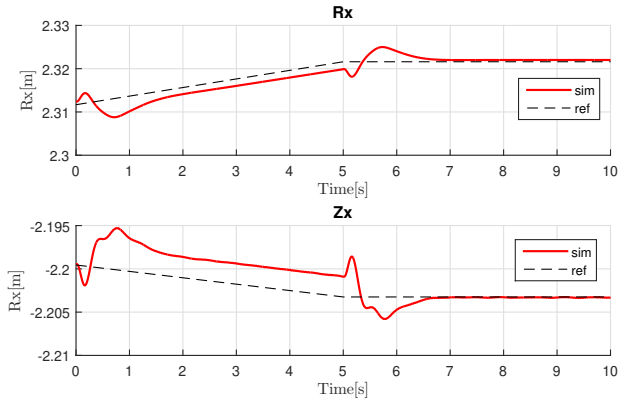

Figure 99: Simulated X-point position.

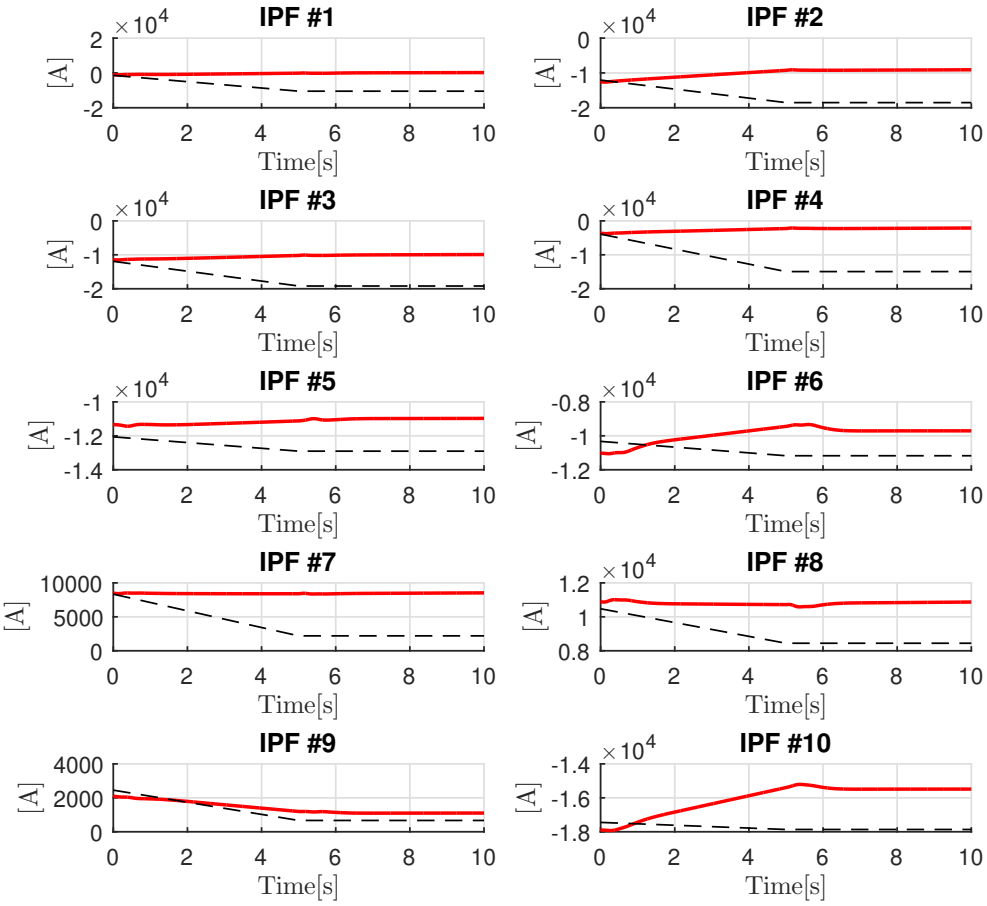

Figure 100: Simulated PFC currents; the dashed black lines are the current feedforwards.

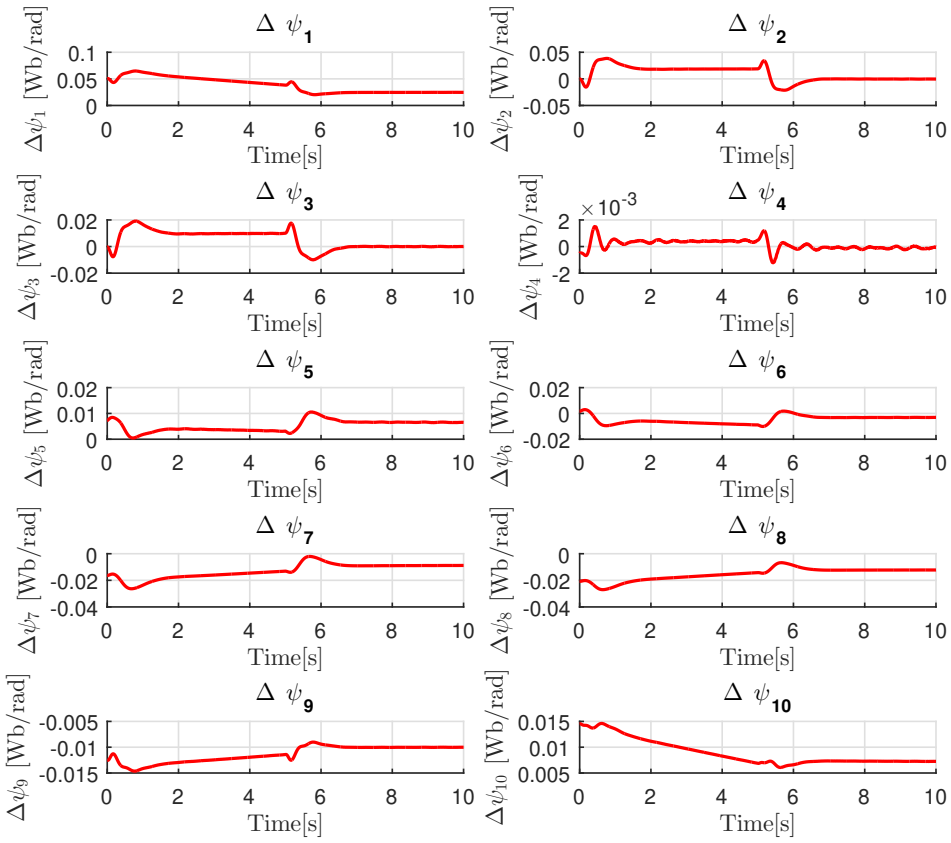

Figure 101: Simulated controlled flux differences.

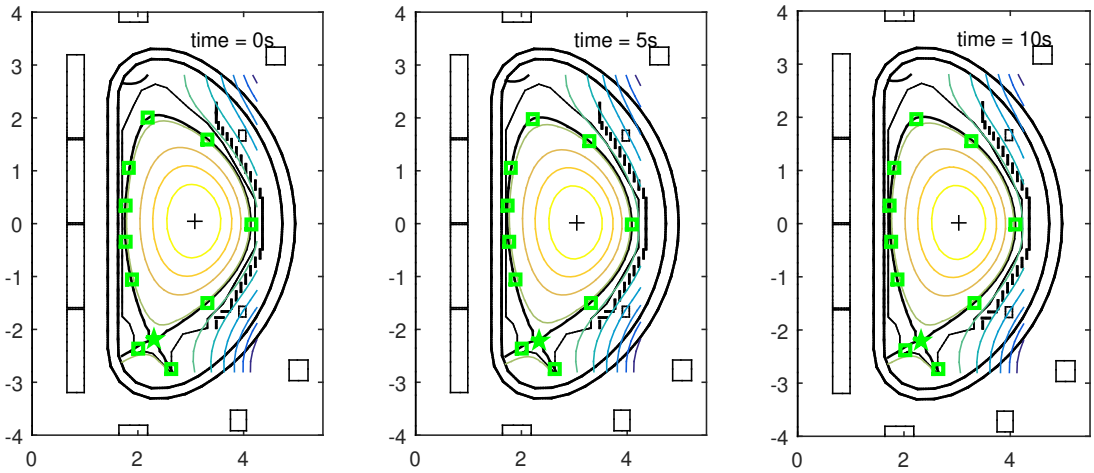

Figure 102: Plasma shape at different time instants.

8.3.2 *Gap control*

The same procedure described in sec. 5.5 can be used to design a gap controller. This controller was tested as an alternative to the *isoflux* one, and some preliminary results are discussed in this section.

The considered plasma scenario was again Scenario 2 [146, Sec. 1.2], which was already discussed in sec. 8.3.1. A linearized model of this scenario at the SOF has been used to design the proposed gap-based shape controller and to simulate its behavior. To assess the controller performances, the following set of disturbances –modelled as variations of β_p and l_i– have been considered (see fig. 103):

- **Disturbance #1** refers to the behavior of β_p and l_i soon after the current flattop is reached (at $t \sim 16$ s), as modelled in [147] on the basis of the foreseen plasma density and temperature spatial profiles.
- **Disturbance #2** simulates the occurrence of an ELM. As described in [146, p. 34], during the flattop an instantaneous drop in β_p of $0.05\ \beta_{p_{eq}}$ is followed by and exponential recovery with a time constant of 0.05 s with a frequency 10 Hz; l_i does not change.
- **Disturbance #3** models a *compound ELM*, commonly referred to as a series of multiple clearly distinguishable crash events which cause large energy losses [148]. The time trace of β_p is the same as in the case of Disturbance #2, while l_i is characterized by an instantaneous drop of $0.06\ (l_{i_{eq}} - 0.5)$ followed by and exponential recovery with a time constant of 0.05 s with a frequency 10 Hz [146, p. 34].
- **Disturbance #4** models a *minor disruption*; it consists in an instantaneous drop in l_i of $0.2\ (l_{i_{eq}} - 0.5)$ without recovery, simultaneous with a drop on β_p of $0.2\ \beta_{p_{eq}}$ followed by a recovery exponential time of 1 s [146, p. 34].

Moreover, a reference tracking case has also been included, In particular, a transition from the Scenario 2 reference shape to the one shown in black in fig. 104 has been considered, to be performed in a time span of 1 s.

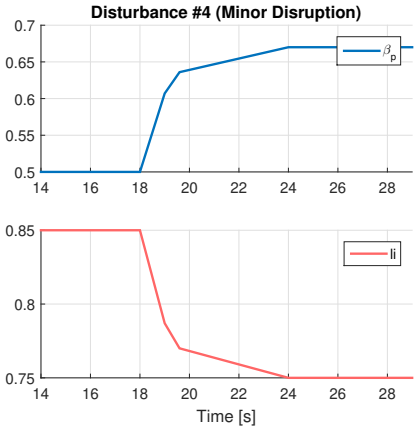

(a) Disturbance #1 - soon after the plasma current flattop is reached (at t ~ 16 s), as in [147].

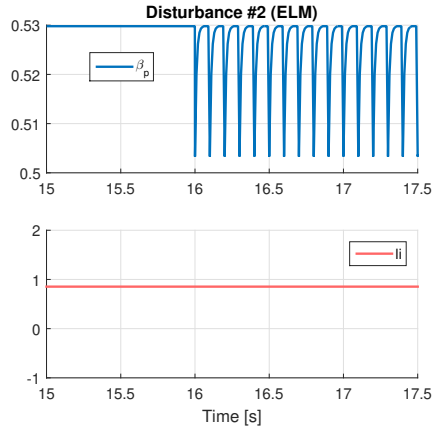

(b) Disturbance #2 - ELM.

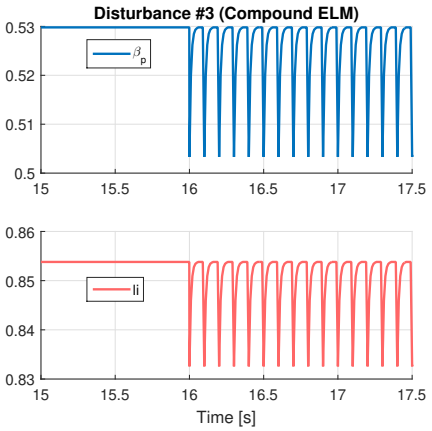

(c) Disturbance#3 - Compound ELM.

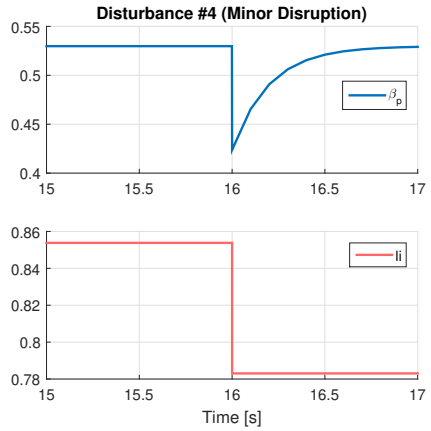

(d) Disturbance#4 - minor disruption.

Figure 103: Poloidal beta and internal inductance time traces for the considered disturbances (courtesy of drs. D. Corona).

An analysis was carried out with the aim of choosing a set of controlled gaps capable of providing a good trade-off between performances and number of controlled variables. In this view, an equally spaced distribution of 85 gaps was initially considered, as shown in fig. 105a. Other than the whole

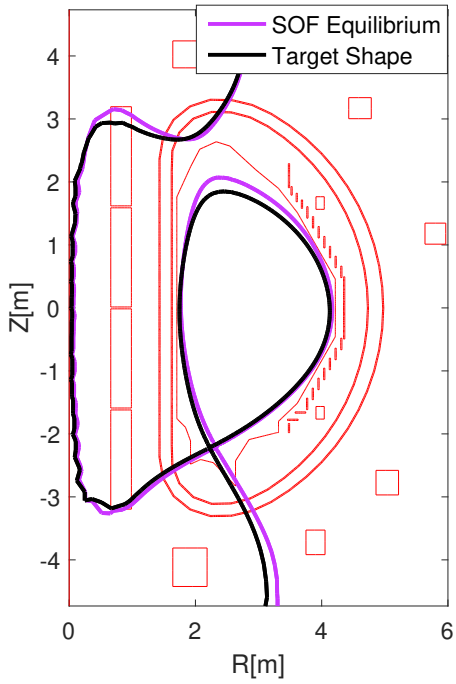

Figure 104: LCFS at the SOF for reference Scenario 2 (purple) and the modified plasma shape considered (black). The transition time between the two configurations is 1 s (courtesy of drs. D. Corona).

set of 85 gaps, three additional choices are discussed in the following. The first one is shown in fig. 109, and consists of 20 gaps equally spaced along the first wall. Moreover, the selections of 8 and 6 gaps corresponding to the isoflux control segments considered in [149] and [150] respectively have been also considered (figs. 108-107).

It is worth to remark that all of these choices include the two vertical gaps in the divertor zone, which can be used to control the strike-points (and consequently the X-point).

Fig. 106 shows the time trace of the Root-Mean-Square Error (RMSE) for the different test cases considered, computed over all the 85 available gaps. Periodic disturbances (i. e. ELMs and compound ELMs) were supposed to act for a finite time window of 1.55 s and removed afterwards, allowing the

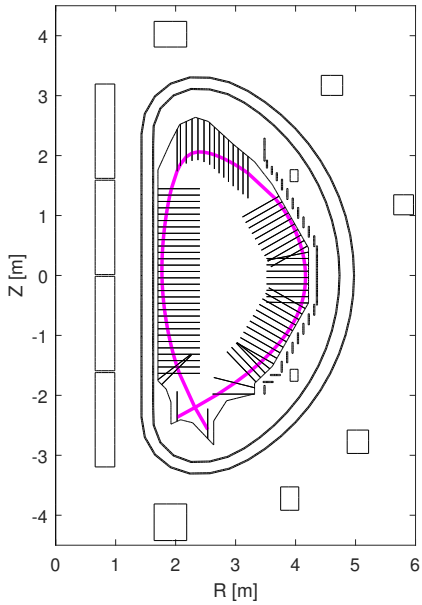

(a) The 85 gaps used to assess the performance of plasma shape controller.

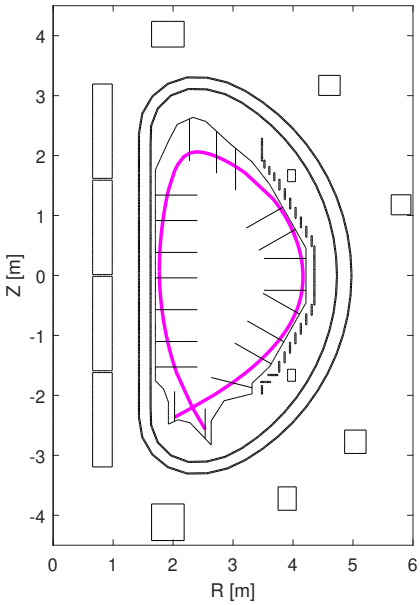

(b) The 20 gaps used to assess the performance of plasma shape controller

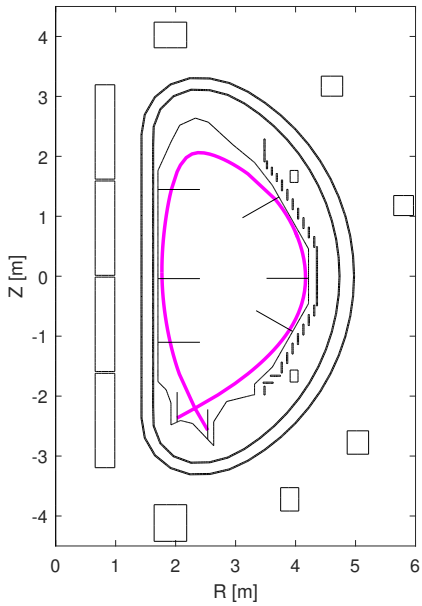

(c) The 8 control segments by the isoflux controller proposed in [149].

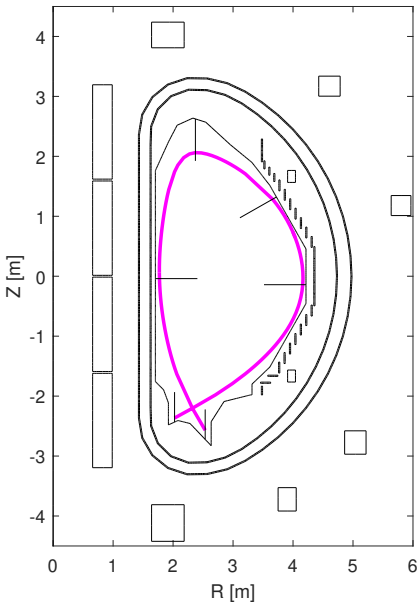

(d) The 6 control segments used by the isoflux controller proposed in [150].

Figure 105: Different choices for the set of controlled gaps (courtesy of drs. D. Corona).

system to evolve towards a steady-state. In particular, it is worth to notice that, with respect to the reference shape change test case, the controller shows a considerable transient error when the 8 gaps choice is considered. This is mostly due to the fact that this selection does not include any gap in the top region of the plasma, which is the one that is most affected by the shape change.

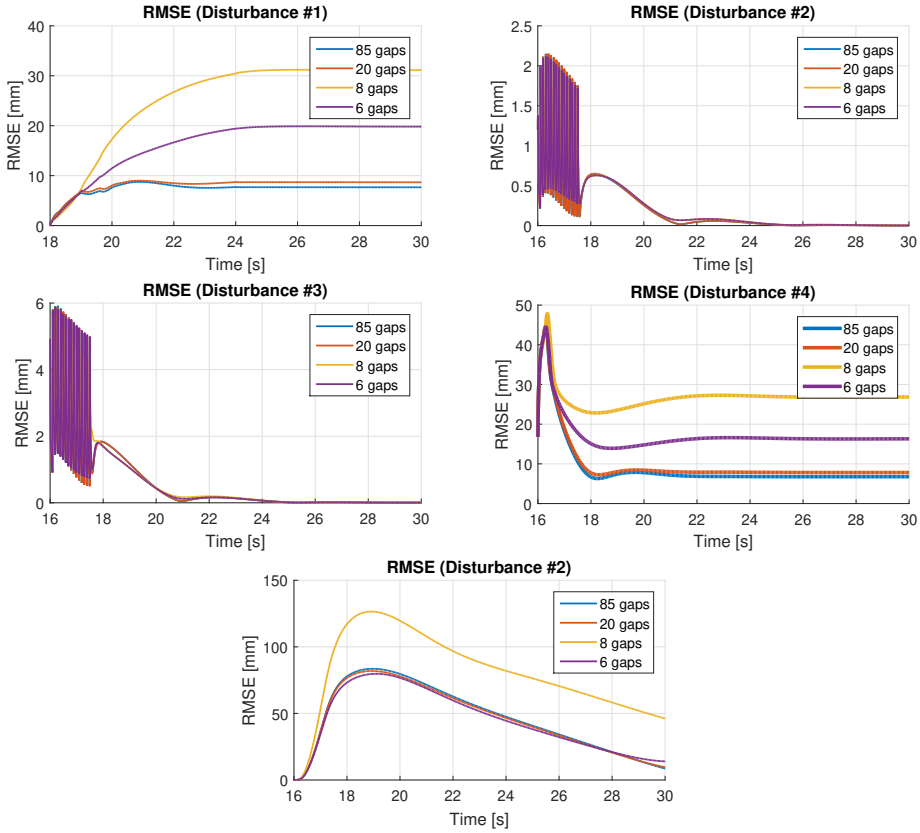

Figure 106: RMSE time trace for Disturbances #1-#4 and for the shape tracking case with 6, 8 and 20 gaps (courtesy of drs. D. Corona).

The obtained results are summarized in table 3, which shows the RMSE between the reference and the obtained shapes at steady-state, after the occurrence of the disturbance or the reference change. As it turns out, for all the considered cases, the sets of 85 and 20 gaps provide a considerable better steady-state RMSE in comparison with those of 8 or 6 gaps.

Apart from the shape tracking, it can be seen that the worst case corresponds to the selection of 8 gaps with the presence of Disturbance #4. Some

Steady-state RMSE [mm]				
	85 Gaps	20 Gaps	8 Gaps	6 Gaps
Disturbance #1	7.7	8.7	31.2	19.8
Disturbance #2	~0	~0	~0	~0
Disturbance #3	~0	~0	~0	~0
Disturbance #4	6.1	7.8	48.5	32.5
Reference shape tracking	5.6	8.4	40.6	14.7

Table 3: RMSE values for different choices of controlled gaps for the proposed test cases (courtesy of drs. D. Corona).

details regarding the results obtained for Disturbance #4 with the different gaps choices proposed are shown in figs. 107-110.

Finally, it is worth to observe that there is no practical difference between the reference shape and the one attained at steady-state in all the proposed test cases when the two options with 85 and 20 equally spaced gaps are considered. Hence, among the considered configurations, the 20 gaps selection represents the *optimal* choice for the set of gaps to be controlled assuming a XSC-like control approach.

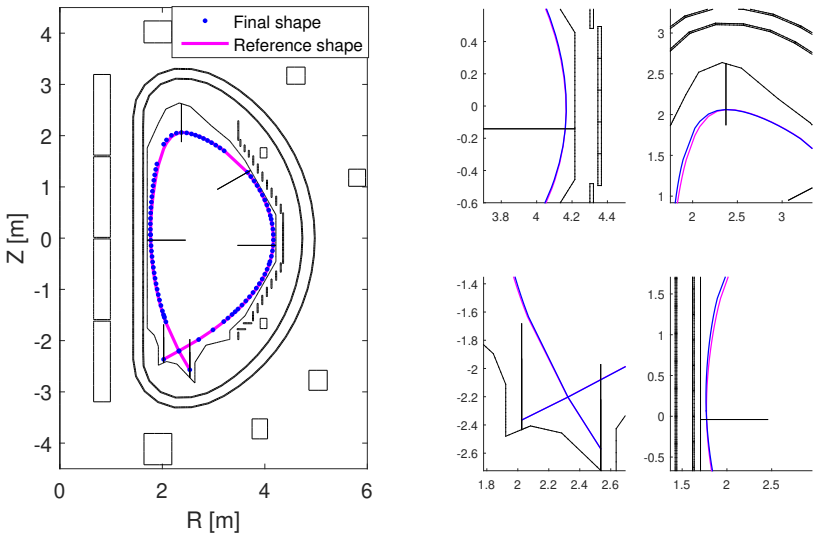

(a) Reference and obtained shape at steady state with 6 gaps.

(b) Detail.

Figure 107: Steady-state plasma shape when controlling 6 gaps in presence of Disturbance #4 (courtesy of drs. D. Corona).

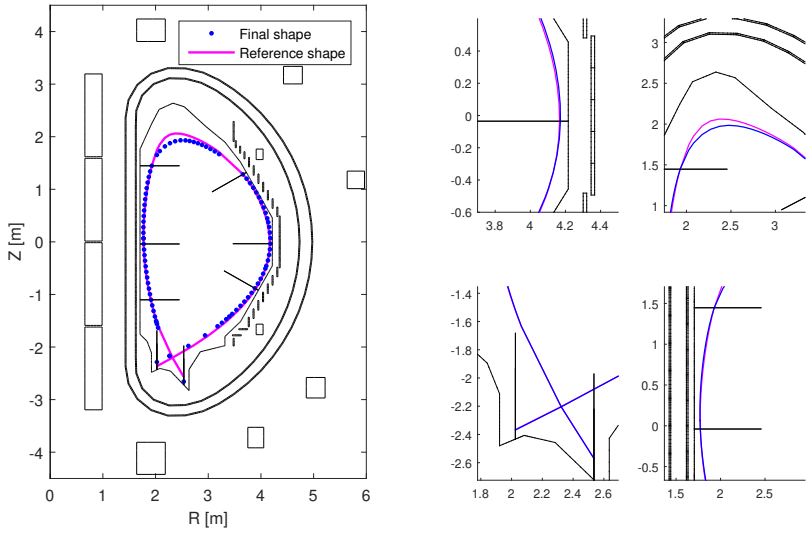

(a) Reference and obtained shape at steady state with 8 gaps.

(b) Detail.

Figure 108: Steady-state plasma shape when controlling 8 gaps in presence of Disturbance #4 (courtesy of drs. D. Corona).

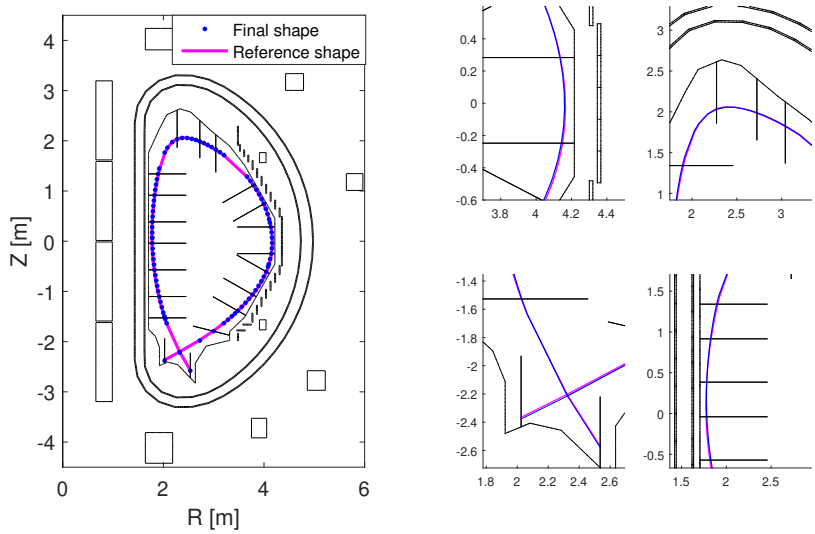

(a) Reference and obtained shape at steady state with 20 gaps.

(b) Detail.

Figure 109: Steady-state plasma shape when controlling 20 gaps in presence of Disturbance #4 (courtesy of drs. D. Corona).

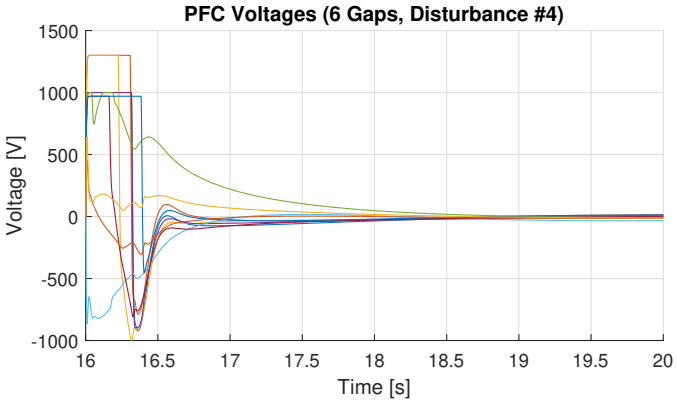

(a) PFC voltages for Disturbance #4 with 6 gaps.

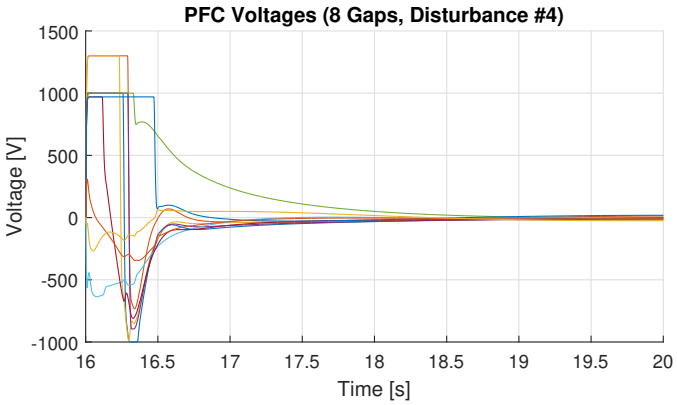

(b) PFC voltages for Disturbance #4 with 8 gaps.

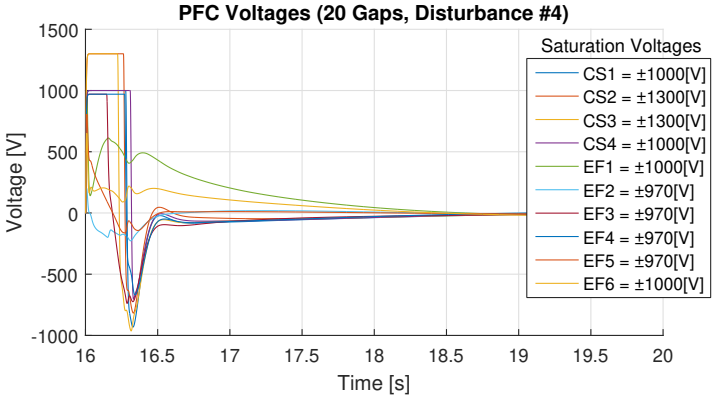

(c) PFC voltages for Disturbance #4 with 20 gaps.

Figure 110: PFC voltages for Disturbance #4 for different gap choices (courtesy of drs. D. Corona).

Part IV

CONCLUSIONS

9

CONCLUSIONS

In this work, a flexible architecture for plasma magnetic control in tokamak reactors has been proposed. This architecture includes all the control loops which are customarily present on a modern tokamak magnetic control system, and prompts the advantage of allowing to easily include additional controlled variables. Once a set of modelling tools has been assessed and validated for the target machine, the control design procedures can be carried out almost automatically; moreover, it becomes possible to test the controller in simulation before using it in an actual plasma discharge. In this way, the experimental time needed to tune and validate the controller is greatly reduced, together with the number of failed discharges, which could damage the machine. The proposed architecture could also –at least in principle– be used during the plasma start-up phases (i. e. breakdown, burn-through and ramp-up). This can be done by substituting the external shape control loop with adequate current feedforwards or with an alternative controller which acts on the magnetic field in a number of control point in the null region, producing current requests to the PFC system.

The proposed solution has been applied to the EAST reactor in order to enhance the shape control performances, with the final aim of making feedback control of alternative divertor configurations possible. In particular, exploiting the CREATE-L and CREATE-NL codes a set of modelling and simulation tools was set up and validated against the experimental data (see chapter 6). These tools proved to be able of providing a sufficiently detailed description of the physical behaviour of the machine, although being simple enough to be useful for the purposes of controller design. Once assessed, this simulation environment was extensively used both to

re-design EAST's existing magnetic controllers and to propose new ones (see sec. 7.1-7.5). The developed simulation tools were also used to design an optimal state observer for the reactor; this observer estimates the eddy currents in the passive structures and provides a shape reconstruction based on a superposition of a first order perturbation over the equilibrium shape (see sec. 7.6). Experiments are still ongoing, and additional results are expected by the beginning of 2019. Starting in 2019, a machine upgrade is also foreseen; this upgrade includes the installation of new In-Vessel coils, paving the way to a more efficient control of magnetic configurations such as the snowflake divertor. With this upgrade, the tools proposed hereby are expected to be exploited again in order to achieve an effective feedback control of such alternative configurations. However, some advances in this direction are already foreseen during the next experimental campaign, in the scope of which the control of secondary null points or other physically meaningful quantities such as the poloidal flux expansion are among the main goals to be achieved. In this view, the simulation results discussed in sec. 7.5 represent a first step.

Furthermore, the proposed control architecture was also applied to the JT-60SA reactor, whose first plasma is foreseen in 2020. The development of reliable and flexible modelling and control tools allows to propose different solutions in order to meet the requirements for the magnetic control system (see chapter 8). It is worth to remark that the same simulation and design environment was used for both EAST and JT-60SA, proving to represent an effective and flexible resource for the design of magnetic controllers in tokamak reactors. A full magnetic control system was designed and tested in simulation, including either an isoflux or a gap-based shape controller. The integration of the proposed tools with the codes provides by the Japanese research unit, in particular the Cauchy Condition Surface (CCS) reconstruction routine, is currently ongoing. The availability of CCS in the proposed simulation environment will also make it possible to assess the impact of

magnetic sensors measurement noise on both the plasma boundary reconstruction and the plasma magnetic control system.

In the near future, studies on the application of the solution proposed in this thesis to the Divertor Tokamak Test (DTT) facility design are also foreseen, in particular for what concerns the feedback control of alternative divertor configurations such as the Snowflake, X and Super-X divertor configurations. Experiments with the proposed control solution on the Tokamak à Configuration Variable (TCV) facility have also been proposed.

BIBLIOGRAPHY

[1] R. Albanese and F. Villone. «The linearized CREATE-L plasma response model for the control of current, position and shape in tokamaks.» In: *Nuclear Fusion* 38 (1998), p. 723.

[2] M. Mattei et al. «CREATE-NL+: a robust control-oriented free boundary dynamic plasma equilibrium solver.» In: *28th Symp. on Fusion Technology, P1.036)*. San Sebastian, Spain, 2014.

[3] R. Albanese et al. «Overview of modelling activities for Plasma Control Upgrade in JET.» In: *Fusion Engineering and Design* 86.6–8 (2011), pp. 1030–1033.

[4] R. Albanese et al. «Design, implementation and test of the XSC extreme shape controller in JET.» In: *Fus. Eng. Design* 74.1-4 (Nov. 2005), pp. 627–632.

[5] M. Ariola et al. «A Modern Plasma Controller Tested on the TCV Tokamak.» In: *Fusion Technology* 36 (1999), pp. 126–138.

[6] A. Castaldo et al. «Simulation Suite for plasma magnetic control at EAST tokamak.» In: *Fusion Engineering and Design* (2018).

[7] R. Albanese et al. «ITER-like Vertical Stabilization System for the EAST Tokamak.» In: *Nuclear Fusion* 57.8 (Aug. 2017), p. 086039.

[8] G. De Tommasi, A. Mele, and A. Pironti. «Robust plasma vertical stabilization in tokamak devices via multi-objective optimization.» In: *International Conference on Optimization and Decision Science (ODS2017)*. Sorrento, Italy, Sep. 2017.

[9] G. De Tommasi, A. Mele, Z. P. Luo, A. Pironti, and B. J. Xiao. «On plasma vertical stabilization at EAST tokamak.» In: *2017 IEEE Conf. Contr. Tech. Appl.* Kohala Coast, Hawaii, 2017, pp. 511–516.

[10] G. et al. De Tommasi. «Model-based plasma vertical stabilization and position control at EAST.» In: *Fusion Engineering and Design* 129 (Apr. 2017), pp. 152–157.

[11] R. Albanese et al. «MIMO shape control at EAST tokamak: simulations and experiments.» In: *30th Symposium on Fusion Technology (SOFT'18)*. Giardini di Naxos, Italy, Sep. 2018.

[12] R. Albanese et al. «A MIMO architecture for integrated control of plasma shape and flux expansion for the EAST tokamak.» In: *Proc. of the 2016 IEEE Multi-Conf. Syst. Contr.* Buenos Aires, Argentina, Sep. 2016, pp. 611–616.

[13] A. Mele et al. «Shape reconstruction and eddy current estimation via Kalman filter at the EAST tokamak.» In: *45th EPS Conference on Plasma Physics (EPS2018)*. Prague, Czech Republic, Jul. 2018.

[14] N. Cruz et al. «Control-oriented tools for the design and validation of the JT-60SA magnetic control system.» In: *Control Engineering Practice* 63 (Jun. 2017), pp. 81–90.

[15] D. Corona et al. «Plasma shape control assessment for JT-60SA using the CREATE tools.» In: *30th Symposium on Fusion Technology (SOFT'18)*. Giardini di Naxos, Italy, Sep. 2018.

[16] A. S. Eddington. «The Internal Constitution of the Stars.» In: *The Scientific Monthly* 11.4 (11 Oct. 1920), pp. 297–303.

[17] G. McCracken and P. Stott. *Fusion: the energy of the Universe.* Elsevier Academic Press, 2012.

[18] R. d Escourt Atkinson and F. G. Houtermans. «Zur Frage der Aufbaumöglichkeit der Elemente in Sternen.» In: *Zeitschrift für Physik* 54.9-10 (1929), 656–665.

[19] «USE OF THE ENERGY IN ATOM HELD NEAR; Dr. Compton Says New Experiments Show Its Practical Use May Be Possible.» In: *The New York Times* March 30 (30 Mar. 1934), p. 22.

[20] M. L. E. Oliphant, P. Harteck, and E. Rutherford. «Transmutation Effects Observed with Heavy Hydrogen.» In: *Proceedings of the Royal Society* 144 (1934), pp. 692–703.

[21] A. Moyal. *Portraits in Science*. Canberra: National Library Australia, 1994.

[22] H. A. Bethe and R. F. Bacher. «Nuclear Physics A. Stationary States of Nuclei.» In: *Reviews of Modern Physics* 8.82 (Apr. 1936), 82–229.

[23] H. A. Bethe. «Nuclear Physics B. Nuclear Dynamics, Theoretical.» In: *Reviews of Modern Physics* 9.3 (Apr. 1937), 69–244.

[24] S. M. Livingstone and H. A. Bethe. «Nuclear Physics C. Nuclear Dynamics, Experimental.» In: *Reviews of Modern Physics* 8.82 (Jul. 1937), pp. 245–390.

[25] S. S. Schweber. *Nuclear Forces: The Making of the Physicist Hans Bethe.* Cambridge, Massachusetts: Harvard University Press, 2012.

[26] S. S. Schweber. *In the Shadow of the Bomb: Bethe, Oppenheimer, and the Moral Responsibility of the Scientist.* Princeton University Press, 2000.

[27] W. H. Bennett. «Magnetically Self-Focussing Streams.» In: *Physical Review* 45.12 (1934), pp. 890–897.

[28] G. P. Thomson and M. Blackwell. *British Patent No 817681*. 1946.

[29] R. S. Pease. «Fusion research 25 years after Zeta.» In: *New Scientist* (20 Jan. 1983).

[30] R. Hermann. *Fusion: the search for endless energy.* Cambridge University Press, 1990.

[31] L. Spitzer Jr. «Controlled nuclear fusion research, September 1965: review of experimental results.» In: *Plasma Physics and Controlled Nuclear Fusion Research*. Vol. I - Conference proceedings Culham 6-10 September 1965. IAEA. Vienna, Austria, 1966.

[32] V. D. Shafranov. «The initial period in the history of nuclear fusion at the Kurchatov Institute.» In: *Physics Uspekhi* (2001).

[33] R. Rhodes. *Dark Sun: The Making of the Hydrogen Bomb*. New York: Simon & Schuster, 1995.

[34] R. Arnoux. «"Proyecto Huemul:" the prank that started it all.» In: *ITER newsline* (2011).

[35] J. J. Saldaña. *Cross Cultural Diffusion of Science: Latin America*. Berkeley, California, 1987. Chap. The Perón-Richter Fusion Program: 1948-1953 (R. Cabral).

[36] M. Cardona, M. L. Cohen, and S. G. Louie. «Leopoldo Maximo Falicov.» In: *Biographical Memoirs* 83 (2003).

[37] I. Nauka. «Oleg Lavrentiev a top secret physicist.» In: (2003).

[38] R. Arnoux. «The "Kremlin letter" that started it all.» In: *ITER newsline* 56 (2008).

[39] M. Kenward. «Fusion research - the temperature rises.» In: *New Scientist* (24 May 1979).

[40] «It is now two minutes to midnight.» In: *Bulletin of the Atomic Scientists* (25 Jan. 2018). Ed. by J. Mecklin.

[41] D. Eisenhower. *Atoms for Peace Speech*. URL: https://www.iaea.org/about/history/atoms-for-peace-speech.

[42] J. F. Pilat, R. E. Pendley, and C. K. Ebinger, eds. *Atoms for Peace: An Analysis After Thirty Years*. Boulder, CO: Westview Press, 1985. Chap. Appendix C.

[43] J. Jacquinot. «Fifty years in fusion and the way forward.» In: *Nuclear Fusion* 50 (2010).

[44] J.D. Lawson. «Some criteria for a useful thermonuclear reactor.» In: *Proc. Phys. Soc.* 70, pt.1.445 (1957), pp. 6–10.

[45] R. Herman. *Fusion: the search for endless energy*. Cambridge University Press, 1990.

[46] K. Love. «H-BOMB UNTAMED, BRITAIN ADMITS.» In: *The New York Times* (17 May 1958).

[47] S. Griffith. «IAEA celebrates 50 years of magnetic confinement fusion research.» In: *ITER newsline* 54 (2008).

[48] V. P. Smirnov. «Tokamak foundation in USSR/Russia 1950–1990.» In: *Nuclear Fusion* 50 (2009).

[49] S. Griffith. «Two weeks in September, 1958: Atoms for Peace conference in Geneva.» In: *ITER newsline* 47 (2008).

[50] D. Bohm. *The characteristics of electrical discharges in magnetic fields*. Ed. by A. Guthrie and R. K. Wakeling. New York: McGraw-Hill, 1949.

[51] L. Spitzer Jr. «The Stellarator Concept.» In: *Physics of Fluids* 1.4 (1958).

[52] R. Arnoux. «Off to Russia with a thermometer.» In: *ITER newsline* 102 (2009).

[53] WalesOnline. «The Valleys boy who broached the Iron Curtain to convince the USA that Russian Cold War nuclear fusion claims were true.» In: *WalesOnline* (3 Nov. 2011).

[54] N. J. Peacock, D. C. Robinson, M. J. Forrest, P. D. Wilcock, and V. V. Sannikov. «Measurement of the Electron Temperature by Thomson Scattering in Tokamak T3.» In: *Nature* 224 (1969), pp. 488–490.

[55] M. J. Forrest. *Lasers Across the Cherry Orchards*. 2011.

[56] R. S. Cohen, L. Spitzer Jr., and P. McR. Routly. «The Electrical Conductivity of an Ionized Gas.» In: *Physical Review* 80.2 (15 Oct. 1950).

[57] V. S. Strelkov. «History of the T-10 Tokamak: Creation and Development.» In: *Plasma Physics Reports* 27.10 (2001), pp. 819–824.

[58] PPPL. *Timeline*. URL: https://www.pppl.gov/about/history/timeline.

[59] H. Eubank et al. «Neutral-Beam-Heating Results from the Priceton Large Torus.» In: *Physical Review Letters* 43.4 (23 Jul. 1979).

[60] R. J. Bickerton, J. W. Connor, and J. B. Taylor. «Diffusion Driven Plasma Currents and Bootstrap Current.» In: *Nature Physical Science* 229 (25 Jan. 1971).

[61] L. A. Artsimovich and V. D. Shafranov. «Tokamak with non-round section of the plasma loop.» In: *Soviet Phys. - JETP Letters* 13.72 (1972).

[62] M. Keilhacker and the ASDEX Team. «The ASDEX divertor tokamak.» In: *Nuclear Fusion* 25.9 (1985).

[63] R. Arnoux. «How Fritz Wagner "discovered" the H-Mode.» In: *ITER newsline* 86 (19 Jun. 2009).

[64] F. Wagner et al. «Regime of Improved Confinement and High Beta in Neutral-Beam-Heated Divertor Discharges of the ASDEX Tokamak.» In: *Physical Review Letters* 49.19 (8 Nov. 1982).

[65] F. Wagner. «A quarter-century of H-mode studies.» In: *Plasma Physics and Controlled Fusion* 49 (14 Nov. 2007).

[66] M. Bécoulet et al. «Edge localized mode physics and operational aspects in tokamaks.» In: *Plasma Physics and Controlled Fusion* 44 (10 Nov. 2003).

[67] J. Wesson. *The Science of JET*. 2000.

[68] D. Meade. «50 years of fusion research.» In: *Nuclear Fusion* 50 (30 Dec. 2010).

[69] R. Arnoux. «The second life of Tokamak T-15.» In: *ITER newsline* 152 (5 Nov. 2010).

[70] *Upgraded Russian tokamak T-15 launch in 2018*. URL: https://bashny.net/t/en/295165.

[71] T. Fujita et al. *High performance experiments in JT-60U reversed shear discharges*. IAEA-CN-69/EX1/2.

[72] Japan Atomic Energy Agency. *The JT-60SA project introduction*. URL: http://www.jt60sa.org/b/index_nav_1.htm?n1/introduction.htm.

[73] A. Gibson and the JET team. «Deuterium–tritium plasmas in the Joint European Torus (JET): Behavior and implications.» In: *Physics of Plasmas* 5 (27 Apr. 1998).

[74] Max Planck Institute for Plasma Physics. *Wendelstein 7-X*.

[75] Max Planck Institute for Plasma Physics. *DEMO demonstration power plant*.

[76] R. Toschi. «The Next European Torus.» In: *Nuclear Engineering and Design. Fusion* 3.4 (1986).

[77] J. P. Freidberg. *Plasma Physics and Fusion Energy*. Cambridge, MA, USA: Cambridge University Press, 2007.

[78] J. Wesson. *Tokamaks*. 3rd ed. Clarendon Press - Oxford, 2004.

[79] E. Kilpua and H. Koskinen. *Introduction to Plasma Physics*. 2015. URL: https://mycourses.aalto.fi/pluginfile.php/438830/mod_resource/content/2/PlasmaIntro_KilpuaKoskinen.pdf.

[80] M. Gedalin. *Introduction to Plasma Physics*. URL: http://physweb.bgu.ac.il/COURSES/PlasmaGedalin/introplasma.pdf.

[81] N. A. Krall and A. W. Trivelpiece. *Principles of Plasma Physics*. 1973.

[82] R. Fitzpatrick. *Plasma Physics*. University of Texas at Austin. URL: http://farside.ph.utexas.edu/teaching/plasma/Plasma/Plasmahtml.html.

[83] J. P. Freidberg. *Ideal Magnetohydrodynamics*. Cambridge, MA, USA: Plenum publishing, 1987.

[84] P. K. Kundu and I. M. Cohen. *Fluid Mechanics*. 2nd ed. Academic Press, 2002.

[85] J.R. et al. Ferron. «Real time equilibrium reconstruction for tokamak discharge control.» In: *Nuclear Fusion* 38 (Nov. 1998), p. 1055.

[86] J. M. Moret, B. P. Duval, H. B. Le, S. Coda, F. Felici, and H. Reimerdes. «Tokamak equilibrium reconstruction code LIUQE and its real time implementation.» In: *Fusion Engineering and Design* 91 (2015), pp. 1–15.

[87] Y. Huang et al. «Implementation of GPU parallel equilibrium reconstruction for plasma control in EAST.» In: *Fus. Eng. Des.* 112 (2016), pp. 1019–1024.

[88] F. Villone, A. Chiariello, S. Mastrostefano, and S. Pironti A.and Ventre. «GPU-accelerated analysis of vertical instabilities in ITER including three-dimensional volumetric conducting structures.» In: *Plasma Physics and Controlled Fusion* 54.8 (2012).

[89] F. Villone, L. Barbato, S. Mastrostefano, and S. Ventre. «Coupling of nonlinear axisymmetric plasma evolution with three-dimensional volumetric conductors.» In: *Plasma Physics and Controlled Fusion* 55.9 (2013).

[90] R. Albanese, R. Ambrosino, and M. Mattei. «CREATE-NL+: A robust control-oriented free boundary dynamic plasma equilibrium solver.» In: *Fus. Eng. Des.* 96-97 (Oct. 2015), pp. 664–667.

[91] P. J. McCarthy, P. Martin, and W. Schneider. *The CLISTE Interpretative Equilibrium Code*. May 1999. URL: http://pubman.mpdl.mpg.de/pubman/item/escidoc:2130737/component/escidoc:2130736/IPP_5_85.pdf.

[92] J. Luxon and B. Brown. «Magnetic analysis of non-circular cross section tokamaks.» In: *Nuclear Fusion* 22.6 (1982), p. 813.

[93] V. D. Shafranov. «Determination of the parameters β_p and l_i in a Tokamak for arbitrary shape of plasma pinch cross-section.» In: *Plasma Physics* 13.9 (1971), p. 757.

[94] J. Blum, C. Boulbe, and B. Faugeras. «Reconstruction of the equilibrium of the plasma in a Tokamak and identification of the current density profile in real time.» In: *Journal of Computational Physics* 231 (2012), pp. 960–980.

[95] A. Quarteroni. *Numerical models for differential problems*. 2nd ed. Springer, 2013.

[96] R. Albanese, G. Calabrò, M. Mattei, and F. Villone. «Plasma response models for current, shape and position control at JET.» In: *Fusion Engineering and Design* 66–68 (Sep. 2003), pp. 715–718.

[97] M. Ariola and A. Pironti. *Magnetic Control of Tokamak Plasmas*. 2nd. Springer, 2016.

[98] F. Felici. «Real Time Control of Tokamak Plasmas: from Control of Physics to Physics-Based Control.» PhD thesis. École Polytechnique Fédérale de Lausanne, 2011.

[99] S. C. Jardin and D. A. Larrabee. «Feedback stabilization of rigid axisymmetric modes in tokamaks.» In: *Nuclear Fusion* 22 (1982), pp. 1095–1098.

[100] E. A. Lazarus, J. B. Lister, and G. H. Neilson. «Control of the vertical instability in tokamaks.» In: *Nuclear Fusion* 30 (1990), pp. 111–141.

[101] R. Albanese, E. Coccorese, and G. Rubinacci. «Plasma modelling for the control of vertical instabilities in tokamaks.» In: *Nuclear Fusion* 29 (1989), pp. 1013–1023.

[102] W. Rogowski and W. Steinhaus. «Die Messung der magnetischen Spannung.» In: *Archiv für Elektrotechnik* 1, pt.4 (1912), pp. 141–150.

[103] J. M. Moret et al. «Influence of Plasma Shape on Transport in the TCV Tokamak.» In: *Phys. Rev. Lett.* 79.11 (1997), 2057–2060.

[104] A. Pironti, F. Sartori, G. Ambrosino, G. Ariola M. De Tommasi, F. Piccolo, F. Villone, and JET EFDA contributors. «A New Algorithm for Strike-Point Sweeping at JET.» In: *Proceedings of the 34th EPS Conference on Plasma Physics*. Warsaw, Poland, 2007.

[105] G. Ambrosino, M. Ariola, G. De Tommasi, A. Pironti, F. Sartori, E. Joffrin, and F. Villone. «Plasma strike-point sweeping on JET tokamak with the eXtreme Shape Controller.» In: *IEEE Transactions on Plasma Science* 36.3 (Jun. 2008), pp. 834–840.

[106] S. Skogestad and I. Postlethwaite. *Multivariable feedback control: analysis and design*. Wiley, New York, 2007.

[107] R. Ambrosino et al. «Design and nonlinear validation of the ITER magnetic control system.» In: *Proc. of the 2015 IEEE Multi-Conf. Syst. Contr.* Sydney, Australia, Sept. 2015, pp. 1290–1295.

[108] F. Sartori, G. De Tommasi, and F. Piccolo. «The Joint European Torus.» In: *IEEE Control Sys. Mag.* 26.2 (2006), pp. 64–78.

[109] M. Ariola and A. Pironti. «The design of the eXtreme Shape Controller for the JET tokamak.» In: *IEEE Control Syst. Mag.* 25 (2005), pp. 65–75.

[110] M. Ariola G. Ambrosino and A. Pironti. «Optimal steady-state control for linear non-right-invertible systems.» In: *IET Control Theory & Applications* 1.3 (May 2007), pp. 604–610.

[111] G. De Tommasi et al. «XSC Tools: a software suite for tokamak plasma shape control design and validation.» In: *IEEE Trans. Plasma Sci.* 35.3 (2007), pp. 709–723.

[112] G. De Tommasi et al. «Shape control with the XSC during plasma current ramp-up and ramp-down at the JET tokamak.» In: *Proc. of the* 52nd *IEEE Conf. on Decision and Control*. Florence, Italy, 2013, pp. 366–371.

[113] EFDA. *Fusion Electricity - A roadmap to the realisation of fusion energy*. Jul. 2015. URL: https://www.euro-fusion.org/fileadmin/user_upload/EUROfusion/Documents/Roadmap.pdf.

[114] D. D. Ryutov. «Geometrical properties of a "snowflake" divertor.» In: *Physics of Plasmas* 14.6 (Jun. 2007).

[115] and V. A. Soukhanovskii D. D. Ryutov. «The snowflake divertor.» In: *Physics of Plasmas* 22.116 (Nov. 2015).

[116] M. Kotschenreuter, P. Valanju, B. Covele, and S. Mahajan. «Magnetic geometry and physics of advanced divertors: The X-divertor and the snowflake.» In: *Physics of Plasmas* 20.10 (Oct. 2013).

[117] G. Calabrò et al. «EAST alternative magnetic configurations: modelling and first experiments.» In: *Nucl. Fus.* 55.8 (Aug. 2015).

[118] G. Manduchi et al. «MDSplus evolution continues.» In: *Fusion Engineering and Design* 87.4 (Dec. 2012), pp. 2095–2099.

[119] *MDSplus Wiki*. URL: http://www.mdsplus.org/index.php/Introduction.

[120] *EAST Handbook*. URL: http://202.127.204.26/eastwiki/index.php/EAST_Handbook.

[121] L. L. Lao, H. St John, R. D. Stambaugh, A. G. Kellman, and W. Pfeiffer. «Reconstruction of current profile parameters and plasma shapes in tokamaks.» In: *Nuclear fusion* 25.11 (1985), p. 1611.

[122] D. D. Ryutov, M. A. Makowski, and M. V. Umansky. «Local properties of the magnetic ield in a snowflake divertor.» In: *Nuclear Fusion* 52.10 (Aug. 2010).

[123] E. Kolemen et al. «Initial development of the DIII-D snowflake divertor control.» In: *Nuclear Fusion* 58.6 (Apr. 2018).

[124] Albanese, R. and Artaserse, G. and Maviglia, F. and Sartori, F. «Identification of Vertical Instabilities in JET Tokamak.» In: *IEEE Trans. Magnetics* 44.6 (2008), pp. 1650–1653.

[125] S. L. Chen, F. Villone, B. J. Xiao, L. Barbato, Z. P. Mastrostefano S. Luo, Y. Guo, and L. Liu. «Equivalent axisymmetric plasma response models of EAST.» In: *Plasma Physics and Controlled Fusion* 58 (2016).

[126] B. J. Xiao et al. «The web-based user interface for EAST plasma control system.» In: *Fusion Engineering and Design* 83.2-3 (Apr. 2008), pp. 181–187.

[127] Q. P. Yuan et al. «Plasma current, position and shape feedback control on EAST.» In: *Nuclear Fusion* 53 (2013), p. 043009.

[128] R. R. Zhang, B. J. Xiao, Q. P. Yuan, F. Yang, Y. Zhang, R. D. Johnson, and B. G. Penaflor. «The web-based user interface for EAST plasma control system.» In: *Fusion Engineering and Design* 89.5 (May 2014), pp. 558–562.

[129] B. J. Xiao et al. «Enhancement of EAST plasma control capabilities.» In: *Fusion Engineering and Design* 112 (2016), pp. 660–666.

[130] D. A. Humphreys et al. «DIII-D Integrated plasma control solutions for ITER and next-generation tokamaks.» In: *Fus. Eng. Des.* 83.2–3 (Apr. 2008), pp. 193–197.

[131] G. De Tommasi; et al. «Current, position, and shape control in tokamaks.» In: *Fusion Sci. Technol.* 59.3 (2011), pp. 486–498.

[132] G. Ambrosino et al. «Design of the Plasma Position and Shape Control in the ITER Tokamak Using In-Vessel Coils.» In: *IEEE Transactions on Plasma Science* 37.7 (Jul. 2009), pp. 1324–1331.

[133] G. Ambrosino, M. Ariola, G. De Tommasi, and A. Pironti. «Plasma Vertical Stabilization in the ITER Tokamak via Constrained Static Output Feedback.» In: *IEEE Trans. Contr. Sys. Tech.* 19.2 (Mar. 2011), pp. 376–381.

[134] G. Franklin, J. D. Powell, and A. Emami-Naeini. *Feedback Control of Dynamic Systems*. 7th. Pearson, 2015.

[135] D. C. Youla, J. J. Bongiorno Jr., and C. N. Lu. «Single-loop feedback-stabilization of linear multivariable dynamical plants.» In: *Automatica* 10.2 (1974), pp. 159–173.

[136] K. Zhou and J. C. Doyle. *Essentials of robust control*. Vol. 104. Prentice hall Upper Saddle River, NJ, 1998.

[137] Y. Ou, M. L. Walker, E. Schuster, and J. R. Ferron. «Equilibrium reconstruction improvement via Kalman-filter-based vessel current estimation at DIII-D.» In: *Fusion Engineering and Design* 82 (2007), pp. 1144 –1152.

[138] R. E. Kalman. «A New Approach to Linear Filtering and Prediction Problems.» In: *Transactions of the ASME–Journal of Basic Engineering* 82.Series D (1960), pp. 35–45.

[139] B. J. Xiao et al. «Integrated plasma control for long pulse advanced plasma discharges on EAST.» In: *Fus. Eng. Des.* 128 (2018), pp. 90–94.

[140] T. Tsunematsu. «Broader Approach to fusion energy.» In: *Fusion Engineering and Design* 84 (2009), pp. 122–124.

[141] W. R. Spears. «JT-60SA Construction Status.» In: *IEEE Transactions on Plasma Science* 42 (3 Mar. 2014), pp. 427–431.

[142] H. Shirai, P. Barabarschi, and Y. Kamada. «Progress of JT-60SA Project: EU-JA joint efforts for assembly and fabrication of superconducting tokamak facilities and its research planning.» In: *Fusion Engineering and Design* (2016).

[143] JT-60SA Research Unit. *JT-60SA Research Plan - Research Objectives and Strategy*. Tech. rep. http://www.jt60sa.org/pdfs/JT-60SA_Res_Plan.pdf.

[144] G. Giruzzi et al. «Physics and operation oriented activities in preparation of the JT-60SA tokamak exploitation.» In: *Proc. of the 26th IAEA Fusion Energy Conf.* Kyoto, Japan, 2016.

[145] P. Innocente et al. «Requirements for tokamak remote operation: Application to JT-60SA.» In: *Fusion Engineering and Design* 96–97 (2015), pp. 799–802.

[146] JT-60SA. *Plant Integration Document (PID), v3.8*. Tech. rep.

[147] H. Urano et al. «Development of operation scenarios for plasma breakdown and current ramp-up phases in JT-60SA tokamak.» In: *Fusion Engineering and Design* 100 (2015), pp. 345–356.

[148] H. et al. Meyer. «Overview of progress in European medium sized tokamaks towards an integrated plasma-edge/wall solution.» In: *Nuclear Fusion* 57 (2017). ISSN: 17414326. DOI: 10.1088/1741-4326/aa6084.

[149] Y. Miyata et al. «Study of JT-60SA Operation Scenario using a Plasma Equilibrium Control Simulator.» In: *Plasma and Fus. Res.* 8 (2013), pp. 2405109–2405109.

[150] Y. Miyata, T. Suzuki, S. Ide, and H. Urano. «Study of Plasma Equilibrium Control for JT-60SA using MECS.» In: *Plasma and Fus. Res.* 9 (2014), pp. 3403045–5.

Part V

APPENDIX

A

LIST OF PUBLICATIONS

(* corresponding/presenting author)

A.1 CONFERENCES AND SEMINARS

[C1] G. Calabrò, B. J. Xiao, J. G. Li, Z. P. Luo, Q. P. Yuan, L. Wang, K. Wu, R. Albanese, R. Ambrosino, A. Castaldo, F. Crisanti, G. De Tommasi, X. Z. Gong, Y. Huang, P. Innocente, H. Q. Liu, R. Lombroni, C. Meineri, A. Mele, S. Minucci, A. Pironti , J. P. Qian, G. Ramogida, N. Vianello, T. Zhang, "Developing steady state ELM-absent H-mode scenarios with advanced divertor configuration in EAST tokamak," in 27th IAEA Fusion Energy Conference, Ahmedabad, India, October 2018

[C2] S. Clement-Lorenzo, J. F. Artaud, G. De Tommasi, J. Farthing, G. Giruzzi, H. Kubo, N Hayashi, O. Hemming, A. Hynes, F. Imbeaux, S. Ide, Y. Ishii, G. Manduchi, M. Matsukawa, M. Mattei, A. Mele, Y. Miyata, N. Nakajima, H. Nakanishi, J. Noe, O. Naito, S. Ohira, T. Ozeki, A. Rigoni, F. Robin, F. Sartori, Y. Sugie, T. Totsuka, H. Urano, V. Vitale, M. Wheatley, K. Yamanaka, "Verification tests for remote participation at ITER REC," in 27th IAEA Fusion Energy Conference, Ahmedabad, India, October 2018.

[C3] G. De Tommasi, F. Villone, T. Bolzonella, D. Corona, N. Cruz, E. Joffrin, M. Mattei, G. Matsunaga, A. Mele, Y. Miyata, A. Pironti, T. Suzuki, H. Urano, "2D and 3D modelling of JT-60SA for disruptions and plasma start-up", in 27th IAEA Fusion Energy Conference, Ahmedabad, India, October 2018.

[C4] D. Corona, N. Cruz, G. De Tommasi, H. Fernandes, E. Joffrin, M. Mattei, A. Mele, Y. Miyata, A. Pironti, H. Urano, T. Suzuki, F. Villone, "Plasma shape control assessment for JT-60SA using the CREATE tools," in 30th Symposium on Fusion Technology (SOFT'18), Giardini di Naxos, Italy, September 2018.

[C5*] A. Mele, R. Albanese, R. Ambrosino, A. Castaldo, G. De Tommasi, Z. P. Luo, A. Pironti, Q. P. Yuan, B. J. Xiao, "MIMO shape control at EAST tokamak: simulations and experiments," in 30th Symposium

on Fusion Technology (SOFT'18), Giardini di Naxos, Italy, September 2018.

[C6*] A. Mele, G. De Tommasi, A. Pironti, B.J. Xiao "Shape reconstruction and eddy current estimation via Kalman filter at the EAST tokamak," in 45th EPS Conference on Plasma Physics (EPS2018), Prague, Czech Republic, July 2018.

[C7] G. De Tommasi, A. Mele, Z. P. Luo, A. Pironti, B. J. Xiao, "On plasma vertical stabilization at EAST tokamak," in 2017 IEEE Conference on Control Technology and Applications (IEEE CCTA'17), Kohala Coast, Hawai'i, August 2017, pp. 511-516.

[C8] J. Farthing, T. Ozeki, S. L. Clement, N. Nakajima, F. Sartori, G. De Tommasi, G. Manduchi, P. Barbato, A. Rigoni, V. Vitale, G. Giruzzi, M. Mattei, A. Mele, F. Imbeaux, J. -F. Artaud, F. Robin, E. Joffrin, A. Hynes, O. Hemming, M. Wheatley, S. Ohira, S. Ide, Y. Ishii, M. Matsukawa, H. Kubo, T. Totsuka, H. Urano, O. Naito, N. Hayashi, Y. Miyata, M. Namekawa, A. Wakasa, T. Oshima, H. Nakanishi, K. Yamanaka, "Status of ITER Remote Experimentation Centre," in 11th IAEA Technical Meeting on Control, Data Acquisition, and Remote Participation for Fusion Research, Greifswald, Germany, May 2017.

[C9] B. J. Xiao, R. Albanese, R. Ambrosino, A. Castaldo, G. De Tommasi, Z. P. Luo, A. Mele, A. Pironti, Q. P. Yuan, "Model-based plasma vertical stabilization and position control at EAST," in 11th IAEA Technical Meeting on Control, Data Acquisition, and Remote Participation for Fusion Research, Greifswald, Germany, May 2017.

[C10] G. De Tommasi, A. Mele, A. Pironti, "Robust plasma vertical stabilization in tokamak devices via multi-objective optimization," in International Conference on Optimization and Decision Science (ODS2017), Sorrento, Italy, September 2017.

[C11*] F. Amato, G. De Tommasi, A. Mele, A. Pironti, "New conditions for Annular Finite-time Stability of Linear Systems," in 55th IEEE Conference on Decision and Control (CDC'16), Las Vegas, Nevada, December 2016.

[C12] G. Giruzzi, E. Joffrin, J. Garcia, D. Douai, J. -F. Artaud, B. Pégourié, P. Maget, Y. Kamada, M. Yoshida, S. Ide, N. Hayashi, G. Matsunaga, T. Nakano, K. Shinohara, S. Sakurai, T. Suzuki, H. Urano, M. Enoeda, H. Kubo, K. Kamiya, M. Takechi, Y. Miyata, A. Isayama, T. Kobayashi, S. Moriyama, K. Shimizu, K. Hoshino, H. Kawashima, A. Bierwage,

D. McDonald, C. Sozzi, L. Figini, S. Nowak, A. Moro, P. Platania, D. Ricci, G. Granucci, T. Bolzonella, P. Bettini, P. Innocente, D. Terranova, L. Pigatto, F. Villone, A. Pironti, S. Mastrostefano, G. De Tommasi, M. Mattei, A. Mele, F. Orsitto, D. Dunai, T. Szepesi, E. Barbato, V. Vitale, M. Romanelli, L. Garzotti, A. Boboc, S. Saarelma, M. Wischmeier, P. Lauber, P. Lang, R. Neu, C. Day, C. Gleason-Gonzalez, M. Scannapiego, R. Zagorski, K. Galazaka, W. Stepniewski, N. Cruz, E. De La Luna, M. Farcia-Munoz, J. Vega, S. Clement-Lorenzo, F. Sartori, S. Coda, T. Goodman, S. Soare, "Physics and operation oriented activities in preparation of the JT-60SA tokamak exploitation," in 26th IAEA Fusion Energy Conference, Kyoto, Japan, October 2016.

[C13] R. Albanese, R. Ambrosino, G. Calabró, A. Castaldo, F. Crisanti, G. De Tommasi, L. Liu, Z. Luo, A. Mele, A. Pironti, B. J. Xiao, Q. Yuan, "A MIMO architecture for integrated control of plasma shape and flux expansion for the EAST tokamak," in 2016 IEEE Multi-Conference on Systems and Control (MSC'16), Buenos Aires, Argentina, September 2016, pp. 611-616.

A.2 PUBLICATIONS AND CONTRIBUTIONS

[1*] [https://doi.org/10.1016/j.fusengdes.2018.05.068] A. Castaldo, A. Mele, R. Albanese, R. Ambrosino, G. De Tommasi, Z. P. Luo, A. Pironti, B. J. Xiao, Q. P. Yuan, "Simulation suite for plasma magnetic control at EAST tokamak," Fusion Engineering and Design, vol. 133, pp. 19-31, August 2018.

[2] [https://doi.org/10.1016/j.fusengdes.2018.02.020] G. De Tommasi, B. J. Xiao, R. Albanese, R. Ambrosino, A. Castaldo, Z. P. Luo, A. Mele, A. Pironti, Q. P. Yuan, "Model-based plasma vertical stabilization and position control at EAST", Fusion Engineering and Design, Volume 129, pp. 152-157, April 2018.

[3] [https://doi.org/10.1016/j.fusengdes.2018.02.004] J. Farthing, T. Ozeki, S. L. Clement, N. Nakajima, F. Sartori, G. De Tommasi, G. Manduchi, P. Barbato, A. Rigoni, V. Vitale, G. Giruzzi, M. Mattei, A. Mele, F. Imbeaux, J. -F. Artaud, F. Robin, E. Joffrin, A. Hynes, O. Hemming, M. Wheatley, S. Ohira, S. Ide, Y. Ishii, M. Matsukawa, H. Kubo, T. Totsuka, H. Urano, O. Naito, N. Hayashi, Y. Miyata, M. Namekawa, A. Wakasa, T. Oshima, H. Nakanishi, K. Yamanaka, "Status of ITER Remote Experimentation Centre," Fusion Engineering and Design, vol. 128, pp. 158-162, March 2018.

[4] [https://doi.org/10.1088/1741-4326/aa7962] G. Giruzzi, M. Yoshida, J.F. Artaud, Ö. Asztalos, E. Barbato, P. Bettini, A. Bierwage, A. Boboc, T. Bolzonella, S. Clement-Lorenzo, S. Coda, N. Cruz, C. Day, G. De Tommasi, M. Dibon, D. Douai, D. Dunai, M. Enoeda, D. Farina, L. Figini, M. Fukumoto, K. Galazka, J. Galdon, J. Garcia, M. Garcia-Munoz, L. Garzotti, C. Gil, C. Gleason Gonzàlez, T. Goodman, G. Granucci, N. Hayashi, K. Hoshino, S. Ide, R. Imazawa, P. Innocente, A. Isayama, K. Itami, E. Joffrin, Y. Kamada, K. Kamiya, Y. Kawano, H. Kawashima, T. Kobayashi, A. Kojima, H. Kubo, P. Lang, P. Lauber, E. de la Luna, P. Maget, G. Marchiori, S. Mastrostefano, G. Matsunaga, M. Mattei, D. McDonald, A. Mele, Y. Miyata, S. Moriyama, A. Moro, T. Nakano, R. Neu, S. Nowak, F. Orsitto, G. Pautasso, B. Pegourie, L. Pigatto, A. Pironti, P. Platania, G. Pokol, D. Ricci, M. Romanelli, S. Saarelma, S. Sakurai, F. Sartori, H. Sasao, M. Scannapiego, K. Shimizu, K. Shinohara, J. Shiraishi, S. Soare, C. Sozzi, W. Stepniewski, T. Suzuki, Y. Suzuki, T. Szepesi, T. Manabu, K. Tanaka, D. Terranova, H. Urano, J. Vega, F. Villone, V. Vitale, T. Wakatsuki, M. Wischmeier, R. Zagorski, "Physics and operation oriented activities in preparation of the JT-60SA tokamak exploitation", Nuclear Fusion, vol. 57, no. 8, pp. 085001, August 2017.

[5] [https://doi.org/10.1088/1741-4326/aa7a78] R. Albanese, R. Ambrosino, A. Castaldo, G. De Tommasi, Z. Luo, A. Mele, A. Pironti, B. Xiao, Q. Yuan, "ITER-like Vertical Stabilization System for the EAST Tokamak", Nuclear Fusion, vol. 57, no. 8, pp. 086039, August 2017.

[6*] [https://doi.org/10.1016/j.conengprac.2017.03.009] N. Cruz, G. De Tommasi, M. Mattei, A. Mele, Y. Miyata, A. Pironti, T. Suzuki, "Control-oriented tools for the design and validation of the JT-60SA magnetic control system," Control Engineering Practice, vol. 63, pp. 81-90, June 2017.